

Numerical Analysis of Flux Reconstruction



William Trojak

Supervisors:

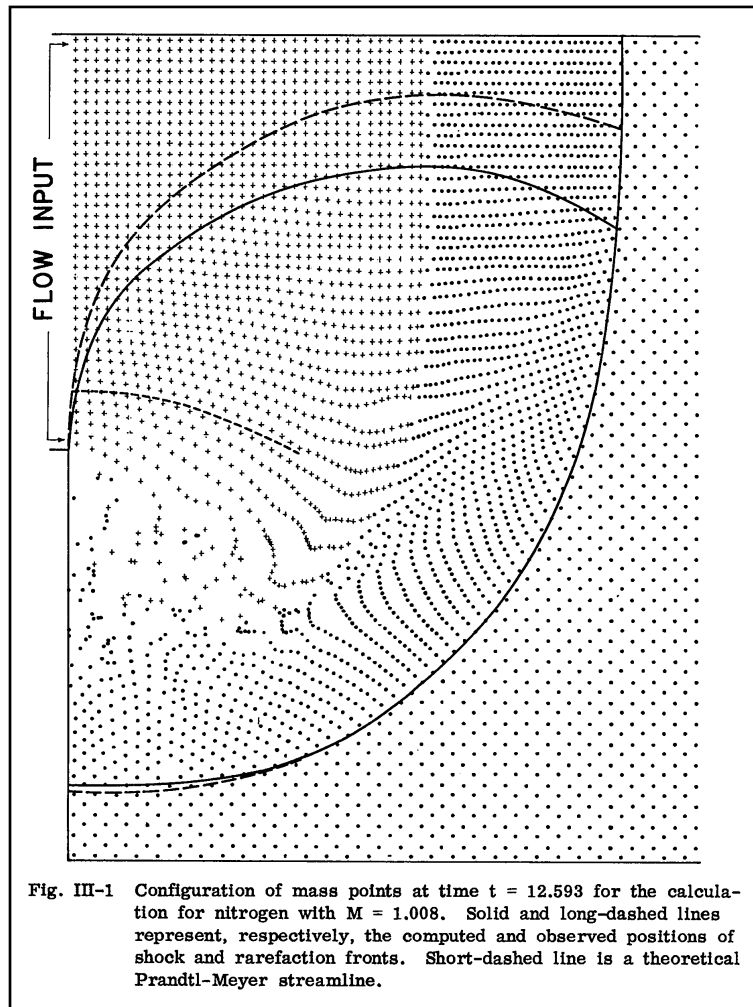
Prof. P. G. Tucker and Prof. R. S. Cant

Department of Engineering

University of Cambridge

This dissertation is submitted for the degree of
Doctor of Philosophy

Numerical Analysis of Flux Reconstruction



Harlow's particle-in-cell method used to simulate shocks in supersonic flow, Harlow 1959. One of the earliest 2D inviscid flow calculations performed on a computer.

William Trojak

Numerical Analysis of Flux Reconstruction

A Ph.D Thesis




William Trojak 
Department of Engineering
Trumpington Street
CB2 1PZ
wt247@cam.ac.uk

Mathematics Subject Classification (2010): 46E_{xx}, 65J_{xx}, 65M_{xx}, 65N_{xx}, 65Y_{xx}, 65Z_{xx}

Typeset using Krishna Kumar thesis class, modified by Will Trojak

© June 2019 William Trojak

This work is licensed under the Creative Commons Attribution-NonCommercial-NoDerivatives
4.0 International (CC BY-NC-ND 4.0) License. 

Declaration

I hereby declare that except where specific reference is made to the work of others, the contents of this dissertation are original and have not been submitted in whole or in part for consideration for any other degree or qualification in this, or any other university. This dissertation is my own work and contains nothing which is the outcome of work done in collaboration with others, except as specified in the text and Acknowledgements. This dissertation contains fewer than 65,000 words including appendices, bibliography, footnotes, tables and equations and has fewer than 150 figures.

William Trojak

June 2019

Abstract

Numerical Analysis of Flux Reconstruction

William Trojak

High-order methods have become of increasing interest in recent years in computational physics. This is in part due to their perceived ability to, in some cases, reduce the computational overhead of complex problems through both an efficient use of computational resources and a reduction in the required degrees of freedom. One such high-order method in particular – Flux Reconstruction – is the focus of this thesis. This body of work relies and expands on the theoretical methods that are used to understand the behaviour of numerical methods – particularly related to their real-world application to industrial problems.

The thesis begins by challenging some of the existing dogma surrounding computational fluid dynamics by evaluating the performance of high-order flux reconstruction. First, the use of the primitive variables as an intermediary step in the construction of flux terms is investigated. It is found that reducing the order of the flux function by using the conserved rather than primitive variables has a substantial impact on the resolution of the method. Critically, this is supported by a theoretical analysis, which shows that this mechanism of error generation becomes increasingly important to consider as the order of accuracy increases.

Next, the analysis of Flux Reconstruction was extended by analytically and numerically exploring the impact of higher dimensionality and grid deformation. It is found that both expanding and contracting grids – essential components of real-world domain decomposition – can cause dispersion overshoot in two dimensions, but that FR appears to suffer less than comparable Finite Difference approaches. Fully discrete analysis is then used to show that, depending on the correction function, small perturbations in incidence angle can cause large changes in group velocity. The same analysis is also used to theoretically demonstrate that Discontinuous Galerkin suffers less from dispersion error than Huynh’s FR scheme – a phenomenon that has previously been observed experimentally, but not explained theoretically.

This thesis concludes with the presentation of a robust theoretical underpinning for determining stable correction functions for FR. Three new families of correction functions are presented, and their properties extensively explored. An important theoretical finding is introduced – that stable correction functions are not defined uniquely by a norm. As a result, a generalised approach is presented, which is able to recover all previously defined correction functions, but in some instances via a different norm to their original derivation. This new super-family of correction functions shows considerable promise in increasing temporal stability limits, reducing dispersion when fully discretised, and increasing the rate of convergence.

Taken altogether, this thesis represents a considerable advance in the theoretical characterisation and understanding of a numerical method – one which, it has been shown, has enormous potential for forming the heart of future computational physics codes.

Acknowledgements

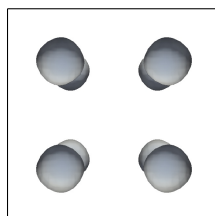
I would firstly like to thank Dr Rob Watson for initially sparking my interest in CFD and his continued help and support throughout my Masters and PhD. Even after his move to Queen's University Belfast he was more than willing to offer help when I needed it. I would also like to thank Prof. Paul Tucker, throughout my PhD, Paul has had his own battles but has continued to give as much assistance as he was able to, which was always greatly appreciated. Paul was also willing to frequently indulge my curiosity, principally by allowing me to undertake a PhD for which I am very grateful. Finally, I would like to thank the assistance of Prof. Stewart Cant who was ready and willing to provide his opinion on a range of subjects, and this made our discussions thoroughly enjoyable. I would like to dedicate this thesis to Damaris, because if listening to me talk about CFD wasn't enough, now she gets to read about it too.

Contents

List of Contributions	xvii
List of Figures	xix
Nomenclature	xxv
1 Introduction	1
1.1 Motivation for High-Order Methods	1
1.2 Motivation For The Current Study	3
1.3 Literature Review	5
1.3.1 Development of High-Order Methods	5
Finite Difference	5
Finite Volume	7
Element Based	9
Temporal Integration Schemes	10
1.3.2 Computational Considerations	11
1.3.3 Flux Reconstruction	12
1.3.4 PDEs Characteristic of Industry	13
Advection Equations	13
Diffusion Equations	14
1.3.5 Correction Functions	15
1.4 Conclusions	16
2 Flux Reconstruction Methodology	19
2.1 Preliminaries	19
2.2 One-Dimensional Approach for First-Order PDEs	20
2.3 Two-Dimensional Approach for Second-Order PDEs	23
3 Effect of Flux Function Order and Working Precision	27
3.1 Introduction	27

3.2	Discrete Error Mechanism	29
3.3	Primitive and Conserved Variables	33
3.3.1	Euler's Equations	33
	Conserved Variable Computation	33
	Inviscid Flux Computation	34
3.3.2	Navier–Stokes Equations	35
3.4	Isentropic Convecting Vortex	38
3.5	Taylor–Green Vortex	40
3.5.1	Effect of Flux Function Order	40
3.5.2	Effect of Working Precision	47
3.6	Conclusions	49
4	Flux Reconstruction for First-Order PDEs on Stretched Grids	51
4.1	Introduction	51
4.2	Two-Dimensional Von Neumann Analysis	52
4.3	Two-Dimensional Convergence Analysis	57
4.4	Analytical Findings	59
4.4.1	Review of 1D Grid Expansion	59
4.4.2	Semi-Discrete Dispersion and Dissipation	60
4.4.3	Error and Convergence	67
4.4.4	CFL Limits	70
4.4.5	Fully Discrete Dispersion and Dissipation	70
4.5	Non-linear Navier–Stokes Equations with Deformed Grids	74
4.5.1	Randomised Grids	75
4.5.2	Curved Grids	81
4.6	Conclusions	84
5	Novel Correction Functions	85
5.1	Introduction	85
5.2	Stability Definition	86
5.2.1	Preliminaries	86
5.2.2	Sobolev Norm	87
5.2.3	Weighted Sobolev Norm	88
5.2.4	Generalised Sobolev Norm	90
5.2.5	Lebesgue Norm	91
5.3	Finding Stable Correction Functions	92
5.3.1	Original Stable Flux Reconstruction	92
5.3.2	Generalised Jacobi Stable Flux Reconstruction	92

Spectral Difference Schemes	95
5.3.3 Generalised Sobolev Stable Flux Reconstruction	97
$p = 2$	100
$p = 3$	100
$p = 4$	101
5.3.4 Generalised Lebesgue Stable Flux Reconstruction	103
5.4 Analytical Findings	106
5.4.1 Generalised Jacobi Results	109
5.4.2 Generalised Sobolev Results	114
5.4.3 Generalised Lebesgue Results	117
5.5 Numerical Experiments	121
5.5.1 Linear Homogeneous Problems — GSFR	121
5.5.2 Linear Heterogeneous Problems — GSFR	122
5.5.3 Isentropic Convecting Vortex — GSFR	125
5.5.4 Taylor–Green Vortex	126
GJFR Results	127
GLSFR Results	129
5.6 Conclusions	132
5.6.1 Generalised Jacobi	132
5.6.2 Generalised Sobolev	133
5.6.3 Generalised Lebesgue	133
6 Conclusions	135
6.1 Conclusions	135
6.2 Future Work	136
References	139
Appendix A Introductory Theory of Orthogonal Polynomials	153
A.1 Legendre Polynomials	155
A.2 Jacobi Polynomials	157
Appendix B Extended Range of Energy Stable Flux Reconstruction Correction Functions	159
Appendix C Additional Generalised Sobolev FR Derivation Details	161
Appendix D Burgers’ Turbulence and GJFR	165



Appendix E	Correction Function Pseudo Code	169
E.1	Generalised Sobolev Stable FR	169
E.2	Generalised Lebesgue Stable FR	170

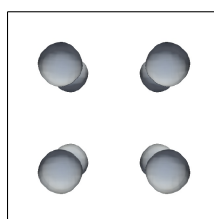
List of Contributions

Journal Papers

1. W. Trojak. Generalised Sobolev Stable Flux Reconstruction. *Journal of Computational Physics*, Transferred March 2019.
ArXiv: 1804.04714
2. W. Trojak, A. Scillitoe, and R. Watson. All Equalities are Equal, but Some are More Equal Than Others: The Effect of Implementation Aliasing on the Numerical Solution of Conservation Equations. *Computers and Fluids*, Submitted January 2019.
ArXiv: 1901.08884
3. W. Trojak, and F.D. Witherden. A New Family of Weighed One-Parameter Flux Reconstruction Schemes. *Computer Methods in Applied Mechanics and Engineering*, Revised March 2019.
ArXiv: 1809.07846
4. W. Trojak, R. Watson, A. Scillitoe, and P.G. Tucker. Effect of Mesh Quality on Flux Reconstruction in Multi-Dimensions. *Journal of Scientific Computing*. Revised January 2019.
ArXiv: 1809.05189
5. W. Trojak, R. Watson, and P.G. Tucker. High Order Flux Reconstruction on Stretched and Warped Meshes. *AIAA Journal*, Vol. 57, No. 1 (2019), pp. 341-351.
DOI: 10.2514/1.J056341.

Conference Papers

1. J. Tyacke, R. Watson, W. Trojak, and P.G. Tucker. High Fidelity Turbomachinery Simulation. *12th International ERCOFTAC Symposium on Engineering Turbulence Modelling and Measurements*, Montpellier France, Sept 2018.



2. W. Trojak, R. Watson, and P.G. Tucker. Temporal Stabilisation of Flux Reconstruction on Linear Problems, Paper AIAA-2018-4263, *Fluid Dynamics Conference, AIAA AVIATION Forum*, Atlanta Georgia, June 2018.
3. R. Watson, W. Trojak, and P.G. Tucker. A Simple Flux Reconstruction Approach to Solving a Poisson Equation to Find Wall Distances for Turbulence Modelling, Paper AIAA-2018-4261, *Fluid Dynamics Conference, AIAA AVIATION Forum*, Atlanta Georgia, June 2018.
4. W. Trojak, R. Watson, and P.G. Tucker. High Order Flux Reconstruction on Stretched and Warped Meshes, Paper AIAA-2017-0521, *55th AIAA Aerospace Sciences Meeting*, Grapevine Texas, Jan 2017.

Oral Presentations

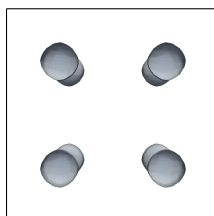
1. W. Trojak, R. Watson, and P.G. Tucker. Temporal Stabilisation of Flux Reconstruction on Linear Problems, Paper AIAA-2018-4263, *Fluid Dynamics Conference, AIAA AVIATION Forum*, Atlanta Georgia, Jun 2018.
2. W. Trojak, R. Watson, and P.G. Tucker. High Order Flux Reconstruction on Stretched and Warped Meshes, Paper AIAA-2017-0521, *55th AIAA Aerospace Sciences Meeting*, Grapevine Texas, Jan 2017.

Pending

1. W. Trojak. Generalised Lebesgue Stable Flux Reconstruction.
ArXiv: 1805.12481

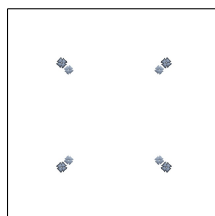
List of Figures

0	Harlow’s particle-in-cell method used to simulate shocks in supersonic flow, Harlow 1959. One of the earliest 2D inviscid flow calculations performed on a computer.	iv
1.1	Ratio of theoretical double precision FLOPs to memory bandwidth for several CPUs and GPUs. Data courtesy of Karl Rupp under CC BY 4.0 license.	2
1.2	An example stencil of a Compact FD scheme, showing the interconnection between node and how this can be leveraged to give a far wider stencil.	7
1.3	Schematic of cell vertex finite volume grid, with dual generated via connecting centroids.	8
2.1	Point layout in $\hat{\Omega}$ for $p = 4$ and example of flux correction.	23
3.1	Variation of error in ICV density with time for FR, $p = 4$, using methods A, B and D on $16 \times 16 \times 2$ and $20 \times 20 \times 2$ element grids.	39
3.2	Variation in total kinetic energy of the ICV, FR $p = 4$, for two grid resolutions. using methods A, B, and D.	40
3.3	Enstrophy of the Taylor–Green Vortex with $R_e = 1600$, $p = 4$ and 80^3 degrees of freedom for storage methods A-D.	43
3.4	Enstrophy of the Taylor–Green Vortex with $R_e = 1600$, $p = 3$ and 80^3 degrees of freedom.	44
3.5	Enstrophy of the Taylor–Green Vortex with $R_e = 3000$, $p = 4$ and 80^3 degrees of freedom.	45
3.6	Enstrophy of the Taylor–Green Vortex with $R_e = 400$, $p = 4$ and 40^3 degrees of freedom.	46
3.7	Taylor–Green Vortex Enstrophy $R_e = 1600$, $p = 4$ and 80^3 DoF for different variable storage precisions.	48
3.8	Taylor–Green Vortex Enstrophy error $R_e = 1600$, $p = 4$ and 80^3 DoF for different variable storage precisions.	48



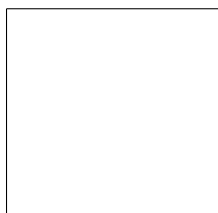
4.1	Example mesh slice from low pressure turbine calculation	52
4.2	Linear advection schematic for two and three dimensions.	55
4.3	Upwinded 1D FR, for various orders with NDG correction functions. . .	60
4.4	Primary mode dispersion for 2D upwinded FR, with Huynh g_2 corrections, at various orders. Normalised wavenumber as radial distance (markers at $\pi/4$ intervals), and element angle of incidence as azimuthal distance. . .	61
4.5	Primary mode dissipation for 2D upwinded FR, with Huynh g_2 corrections, at various orders. Normalised wavenumber as radial distance (markers at $\pi/4$ intervals), and element angle of incidence as azimuthal distance.	62
4.6	Two dimensional upwinded FR, $p = 3$ with Huynh g_2 corrections, for different grid expansion factors. Normalised wavenumber as radial distance (markers at $\pi/4$ intervals), and element angle of incidence as azimuthal distance.	64
4.7	Two dimensional upwinded FR, $p = 3$, with Huynh g_2 corrections at selected incident angles and stretching.	65
4.8	Two dimensional upwinded FR, $p = 3$ with NDG corrections, for different grid expansion factors. Normalised wavenumber as radial distance (markers at $\pi/4$ intervals), and element angle of incidence as azimuthal distance.	66
4.9	Semi-discrete error of FR, $p = 3$, with upwinded interfaces on a uniform grid for $\theta = 45^\circ$	67
4.10	Grid spacing rate of convergence of FR, $p = 3$, with upwinded interfaces on a uniform grid for $\theta = 0^\circ$	68
4.11	Grid spacing rate of convergence of FR, $p = 3$, with upwinded interfaces on a uniform grid.	69
4.12	Semi-discrete error of FR, $p = 3$, upwinded interfaces with: $\gamma_x = 1$, $\gamma_y = 1.1$, and $\theta = 30^\circ$. Here Huynh's g_2 correction function has been applied.	69
4.13	Dispersion and dissipation of upwinded FR, $p = 3$, with Huynh g_2 corrections, explicit RK44 temporal integration, and $CFL = 0.8CFL_{\max}$. The radial distance is the normalised wavenumber (including the effect of angle), and the azimuthal distance is the angle of incidence to the element.	72
4.14	Dispersion and dissipation of upwinded FR, $p = 3$, with NDG corrections, explicit RK44 temporal integration, and $CFL = 0.8CFL_{\max}$. The radial distance is the normalised wavenumber (including the effect of angle), and the azimuthal distance is the angle of incidence to the element.	73

4.15	Example slices through a 3D hexahedral mesh to illustrate the mesh quality metric.	76
4.16	Effect of jitter on turbulent kinetic energy dissipation of the TGV ($R_e = 1600$) for FR, $p = 2$, with Huynh g_2 correction functions on a 120^3 DoF mesh. Explicit time step size is $\Delta t = 1 \times 10^{-3}$	76
4.17	Effect of jitter on turbulent kinetic energy dissipation of the TGV ($R_e = 1600$) for FR, $p = 4$, with Huynh g_2 correction functions on a 120^3 DoF mesh. Explicit time step is $\Delta t = 1 \times 10^{-3}$	77
4.18	Comparison of TGV ($R_e = 1600$) enstrophy for 120^3 degree of freedom grid with similar q_h	78
4.19	Comparison of polynomial and RBF methods for point placement on jittered meshes. This is for a TGV, $R_e = 1600$, $p = 4$, 120^3 DoF, RK44, and $\Delta t = 10^{-3}$. A jitter factor of $j_f = 0.3$ and 0.2 gives $q_h = 0.7157$ and 0.7199 respectively.	78
4.20	Comparison of Huynh g_2 correction functions with NDG for jittered meshes. This is for a TGV, $R_e = 1600$, $p = 4$, 120^3 DoF, RK44, and $\Delta t = 10^{-3}$. A jitter factor of $j_f = 0.3$ gives $q_h = 0.7157$	79
4.21	Dispersion and Dissipation relation for 1D upwinded FR, $p = 1$, with DG correction function.	80
4.22	Comparison of FR, $p = 1$ with DG correction functions with a second order central FV scheme with L2 Roe smoothing both with 170^3 degrees of freedom and $\Delta t \approx 5 \times 10^{-4}$. A reference DNS solution is provided by Brachet et al. [21].	81
4.23	Comparison of FR, $p = 1$ with DG correction functions with a second order KEP FV scheme with L2 Roe smoothing both with 170^3 degrees of freedom and $\Delta t \approx 5 \times 10^{-4}$. A reference DNS solution is provided by Brachet et al. [21].	82
4.24	Example 120^3 DoF curved grid for $p = 4$, $A = 0.4$, and $k_g = 4$. Here a sub-sample of every 10^{th} point is shown.	83
4.25	TGV results for FR, $p = 4$, on a curved grid with 120^3 DoF. RK44 explicit time stepping is used with $\Delta t = 10^{-3}$	83
5.1	Selected Gauss-Jacobi quadratures for $n = 4$	98
5.2	Comparison of OSFR, ESFR and GSFR correction functions, $p = 3$. . .	103
5.3	Variation of the rate of error convergence with grid for qDG, $p = 4$	110
5.4	CFL limit of various temporal integration methods for upwinded qDG, $p = 4$	111
5.5	Example qGD, $p = 4$, correction function.	112



5.6	Variation of the rate of error convergence with grid for Jacobi-SD correction functions, $p = 4$	112
5.7	Variation of error with time and normalised wavenumber ($\hat{k} = k/(p + 1)$) for SD correction functions with optimal convergence from Figure 5.6, $p = 4$, $\Delta_x = 1$	113
5.8	CFL limit of various temporal integration methods for Jacobi SD with upwinded interfaces, $p = 4$	114
5.9	Dispersion and dissipation relations of convergence optimal Jacobi-SD and qDG correction function, $p = 4$	115
5.10	CFL limit for upwinded FR with GSFR correction functions, $p = 3$, and RK44 temporal integration on a regular grid.	115
5.11	Dispersion and dissipation for selected $p = 3$ GSFR correction functions with interface upwinding.	116
5.12	CFL limit for upwinded FR with GSFR correction functions, $p = 4$, and RK44 temporal integration on a regular grid. ($t_1 = 1 \times 10^{-5}$).	117
5.13	Example GLSFR, $p = 4$, correction function with arbitrary weights and wave propagating characteristics.	118
5.14	Maximum stable CFL number for GLSFR [$c = 1, \nu = 0$], with RK44 temporal integration.	119
5.15	Linear advection dispersion and dissipation comparison of spatial and temporal-spatial (T/S) analysis for upwinded GLSFR, $p = 4$	119
5.16	Linear advection dispersion relations for central interface flux GLSFR, $p = 4$	120
5.17	Maximum stable CFL number for GLSFR [$c = 10, \nu = 1$], with RK44 temporal integration.	120
5.18	Order of accuracy of GSFR, $p = 3$, applied to linear advection.	122
5.19	L^2 energy error of GSFR, $p = 3$, applied to linear advection.	125
5.20	Error in the domain integrated kinetic energy of the ICV for FR, $p = 3$, for various GSFR correction functions.	125
5.21	Jacobi-SD TGV dissipation and enstrophy comparison with OSFR correction function.	127
5.22	Jacobi SD, $p = 4$, time averaged dissipation and enstrophy error for TGV	128
5.23	Quasi-DG, $p = 4$, time averaged dissipation and enstrophy error for TGV	130
5.24	GLSFR $p = 4$, TGV dissipation rate error.	130
5.25	Optimal GLSFR $p = 4$ correction function dissipation rate for the TGV	131
5.26	Euler diagram to show the interconnection of the spaces of FR correction functions	132

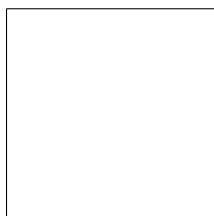
D.1	Burgers' turbulence energy spectra of FR, $p = 4$, with SD correction functions $\alpha = \beta = 0$, DoF = 1200, $\Delta t = 2 \times 10^{-5}$	166
D.2	Burgers' turbulence parametrisation for FR, $p = 4$, at $t = 0.1$ for various correction functions.	167



Nomenclature

Roman Symbols

a	linear advection convective velocity
$b_p^{(\alpha,\beta)}$	the value of the p^{th} derivative of $J_p^{(\alpha,\beta)}$
\mathbf{C}_\bullet	interface correction matrix
C^n	unbounded n^{th} derivative continuity space
C_0^n	bounded n^{th} derivative continuity space
\mathbf{D}_η	differentiation matrix operator in η
\mathbf{D}_ξ	differentiation matrix operator in ξ
e_a	aliasing error
\mathbf{F}	aggregate flux vector, used in one equation formulation
\mathbf{f}	x dimension flux vector
\mathbf{f}, \dots	conservative flux in x, \dots
$\mathbf{f}^{\text{inv}}, \dots$	conservative inviscid flux in x, \dots
$\mathbf{f}^{\text{vis}}, \dots$	conservative viscous flux in x, \dots
\mathbf{G}	Jacobian matrix
\mathbf{g}	y dimension flux vector
\mathbf{G}_n	Jacobian matrix for the n^{th} element
h	correction function
J_n	determinant of the n^{th} element's Jacobian matrix



$J_i^{(\alpha,\beta)}$	i^{th} order Jacobi polynomial, with control variables (α,β)
k	wavenumber
\hat{k}	Nyquist normalised wavenumber, k/k_{nq} ($[0,\pi]$ by convention)
k_{nq}	Nyquist wavenumber
$l_i(\xi)$	i^{th} Lagrange polynomial basis function in ξ
L_p	p^{th} Lebesgue space
M_a	Mach Number
P_r	Prandtl Number
Q	semi-discretised spatial scheme matrix
Q_c	vector of conserved variables
$\nabla\mathbf{Q}_c$	gradient of conserved variables
Q_{c+p}	vector of conserved variables, with E substituted with p
$q_n^{(\alpha,\beta)}$	the value of $(J_n^{(\alpha,\beta)})^2$ integrated over $[-1, 1]$ w.r.t the weight function w .
Q_p	vector of primitive variables
$\nabla\mathbf{Q}_p$	gradient of primitive variables
R	temporal update matrix
R_e	Reynolds Number
R	specific gas constant
u	primitive column vector
V	vector of velocity components
v	eigenvector
W_2^u	l_2 Sobolev space of u and $u^{(p)}$
$W_2^{u,w}$	l_2 Sobolev space of u and $u^{(p)}$ weighted by function w
y^+	non-dimensional wall normal distance

Greek Symbols

α	interface upwinding coefficient, $\alpha = 1$ implies upwinded, $\alpha = 0.5$ implies central differenced
γ	geometric expansion ratio
ϵ_1	global averaged kinetic energy decay rate
ϵ_2	global averaged enstrophy based decay rate
ζ	3 rd coordinate in reference domain
η	2 nd coordinate in reference domain
ι	correction function parameter, typically coefficient of p^{th} derivative in Sobolev norm
$\kappa(\mathbf{A})$	condition number of matrix \mathbf{A}
μ	dynamic shear viscosity
μ_b	dynamic bulk viscosity
ν	rate of linear diffusion
ξ	1 st coordinate in reference domain
$\rho(\mathbf{A})$	spectral radius of matrix \mathbf{A}
ψ_i	i^{th} basis polynomial, typically Legendre polynomial of the first kind
$\boldsymbol{\omega}$	vorticity, $\nabla \times \mathbf{V}$
Ω	spatial domain
Ω_n	spatial domain partition
$\hat{\Omega}$	computational spatial domain

Superscripts

$\bar{\bullet}$	interpolated primitive transformed to physical domain
$y^{(i)}$	i^{th} derivative of y
$\hat{\bullet}$	value in computational domain



$\tilde{\bullet}$	variables projected into polynomial space
\bullet^δ	globally-continuous local polynomial approximation of value
$\bullet^{\delta C}$	correction to discontinuous values
$\bullet^{\delta D}$	local discontinuous polynomial approximation of value
$\bullet^{\delta Di}$	local discontinuous polynomial approximation of inviscid value
$\bullet^{\delta Dv}$	local discontinuous polynomial approximation of viscous value
$\bullet^{\delta I}$	common interface value

Subscripts

\bullet_B	property of bottom interface
\bullet_L	property of left interface
\bullet_R	property of right interface
\bullet_T	property of top interface
\bullet_x	differentiation with respect to x

Other Symbols

${}_nF_m(\mathbf{N}, \mathbf{M}; z)$	the n-m generalised hypergeometric function at z [13, 18]
\mathcal{L}_p	p^{th} order interpolation operator
\mathbb{N}	set of natural numbers, i.e. positive integers
$\hat{\nabla}$	gradient operator in computational space
\mathcal{O}	big O notation showing limiting behaviour of function
$(x)_i$	rising Pochhammer function of x with i steps
$\overline{(x)}_i$	falling Pochhammer function of x with i steps
\mathbb{R}	set of real numbers
\mathcal{R}_p	p^{th} order interpolation remainder operator
\mathbb{R}_+	set of positive real numbers

$[\bullet]$	ceiling function
$[\bullet]$	floor function
\bullet^T	vector or matrix transpose

Acronyms / Abbreviations

CFL	Courant–Friedrichs–Lewy number
CPR	Correction Procedure via Reconstruction
DFR	Direct Flux Reconstruction
DG	Discontinuous Galerkin
DNS	Direct Numerical Simulation
DRP	Dispersion Relation Preserving
ENO	Essentially Non-Oscillatory
ESFR	Extended range Stable Flux Reconstruction
FD	Finite Difference
FE	Finite Element
FLOP	FLoating point OPeration
FR	Flux Reconstruction
FV	Finite Volume
GJFR	Original Jacobi stable Flux Reconstruction
GLSFR	Generalised Lebesgue Stable Flux Reconstruction
GPU	Graphics Processing Unit
GSFR	Generalised Sobolev stable Flux Reconstruction
LCL	Lumped Chebyshev–Lobatto
LCP	Lifting Collocation Penalty
LES	Large Eddy Simulation



LSD	Legendre Spectral Difference
NDG	Nodal Discontinuous Galerkin
NSE	Navier–Stokes Equations
OSFR	Original Stable Flux Reconstruction
PDE	Partial Differential Equation
qDG	quasi Discontinuous Galerkin
RANS	Reynolds Averaged Navier–Stokes
RK	Runge–Kutta
SD	Spectral Difference
SG	Staggered Grid
SV	Spectral Volume
TGV	Taylor–Green Vortex
WENO	Weighted Essentially Non-Oscillatory

Chapter 1

Introduction

1.1 Motivation for High-Order Methods

For a considerable time, engineers have been reliant on computational methods for simulating fluid flow. They use Computational Fluid Dynamics (CFD) to aid or improve design or advance knowledge about the behaviour and nature of fluid flow. This shift to computational methods has been necessary due to the immense cost of producing scale models or testing full-size rigs and fundamental to CFD is reducing the overhead of the design and testing process.

When undertaking a simulation within CFD, there are two key questions. First, is what equation or set of equations are going to be attempted to be approximately solved? The second is what method is going to be used to solve them? For the latter, this has long meant using first or second order methods, but these questions are strongly coupled.

Considering why second order was widely used early in the development of CFD, from a mathematical point of view these methods are more straightforwardly derived and naturally came first. However, early in the use of numerical methods for solving PDEs the computer environment was dominated by a lack of FLOPs available for computation. For example, the CRAY-1, from circa 1975, had a FLOPs to bandwidth ratio of 0.0625. Hence, for algorithms to be feasible they had to have low operation counts and high operation efficiency. Therefore, early methods were typically second order and used a structured grid where a point's location numbering determined its neighbours. As an example of an early method, take a simple central finite difference method for solving a 1D linear advection equation. When using forward Euler temporal integration, each update requires two additions and one multiplication. Compared to four additions and one multiplication for fourth order central difference.

Moving back to the question of what system of equations is going to be solved. It was common for Reynolds-Averaged Navier–Stokes (RANS) to be employed, where it is



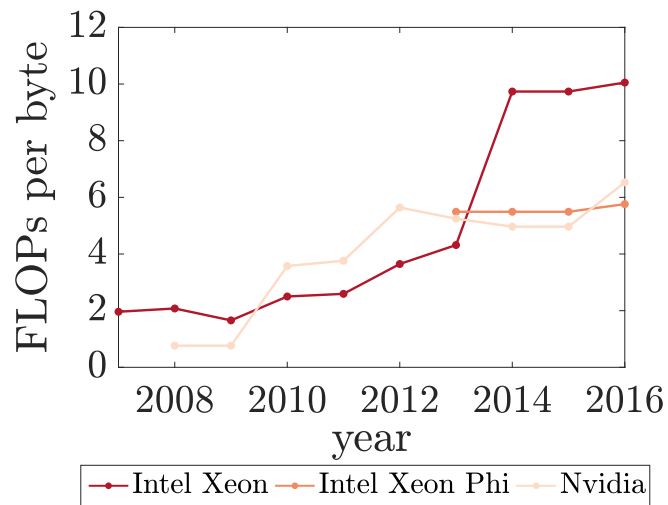


Fig. 1.1 Ratio of theoretical double precision FLOPs to memory bandwidth for several CPUs and GPUs. Data courtesy of Karl Rupp under CC BY 4.0 license.

generally assumed that the solution is steady and a closure model is applied. The results of this method are generally highly smooth solutions that, due to the use of a model, require calibration. Consequently, RANS is strictly a postdictive tool. This inability to accurately predict flow physics was problematic, a notable application where this was unacceptable was in weather prediction [133, 134] and meant a change was required.

In response to the inadequacies of RANS, Large Eddy Simulation (LES) has been coming to the forefront of CFD in the last few decades, along with hybrids of these two approaches [136]. NASA's CFD Vision 2030 [132] reflects this, while also highlighting the biggest barrier to ubiquity, which is that LES aims to resolve a large proportion of the energy contained in vortical structures directly on the grid (80-90%). This is a problem, because it gives rise to high grid requirements, however high-order has been found to be useful in reducing these requirements. One of the many works that demonstrated this is that of Trojak et al. [151], where it was shown that the number of points required to resolve a wave could be reduced through increasing order. Which in turn could reduce the grid requirements, for example from 25 points per wave for second order FD to six at sixth order for 1D linear advection. A further point explored by Chow & Moin [36] and Ghosal [54] showed that the need to keep the truncation error small to enable the accurate use of sub-grid scale models meant the grid requirements were high. Yet a move to higher order would mean that the scaling of the truncation error was to a higher power of grid spacing, thus lowering the grid requirements by decoupling the aliasing and truncation error. Hence, the sub-grid scale model was able to more accurately model the under-resolved scales.

What has allowed these benefits of high order, when applied as LES, to become feasible is that over the last several decades the computing environment has changed substantially from the days of the CRAY-1. This change is highlighted in Fig. 1.1 and shows how the FLOP to bandwidth ratio has changed with time. Computer hardware has moved to a position to where there is now a growing abundance of FLOPs and where efficient applications are more likely to become bandwidth limited. Hence, by reducing the overall memory overhead through high-order methods, the effect of memory bandwidth can be reduced. However, this point has several caveats.

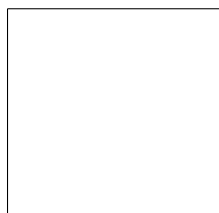
First is that the increase in the available FLOPs has largely been due to developments such as the use of highly parallel graphic processing units (GPUs) and readopting vector processing. Therefore, for methods to actually utilise those FLOPs a high degree of vectorisation or parallelisation is required within the algorithm. Secondly, high order methods have higher operation counts which in turn increase the number of memory accesses. Resultantly, not only are more FLOPs required per update, but more data has to be moved from memory. Hence, to maintain efficiency high-order methods will also need to incorporate some degree of memory locality. These two method can sometimes be linked for example in finite element methods and is to be discussed in Section 1.3.1.

So far it has been implicit that the discussion of high order was referring to the method for calculating the spatial component of the system. However, in the move to high order careful consideration of the coupling between the spatial scheme and the temporal integration has to be given. A key result for finite element methods is the that time step limit scales with element size, hence the increase in element size caused by higher resolution can help increase the time step size. However, the step limit will also scale either linearly or quadratically as the spatial order is increased [59]. Hence, there is a balance to be struck between order and time scheme if long time integrations are to be efficiently and accurately handled. This point will be discussed further in Section 1.3.1

The aim here has been to show that, through the changing needs of physics resolving methods, and through the change in computer hardware, high-order methods have become a feasible means of simulating physics. However, whether a particular high order method is suitable will be dependent on the case to be considered, but generally they allow for better utilisation of the available compute resources while reducing the required number of degrees of freedom.

1.2 Motivation For The Current Study

The motivation for using higher order methods is clear — they can allow for more accurate results and solutions to problems that previously could not be considered due



to computational limitations. Hence, the current work is to investigate one of these high order schemes. Yet, before schemes can be considered of industrial relevance two things need to be in place. Firstly, the scheme needs to have matured to a point such that there is sufficient understanding to design algorithms and data structures for it to be efficiently implemented. Secondly, the behaviour of a numerical scheme should be well enough understood that a practitioner can apply them in ways which take advantage of their abilities, whilst reducing the influence of their deficiencies. This second point is the area of interest in the current work.

Typically, in industrial calculations, two effects are combined: a set of stiff equations which have been discretised on a reduced quality mesh; and equations which exhibit a mix of advection, diffusion, and source terms — both linear and non-linear. In an industrial or engineering application the grid quality tends to suffer as the domains of interest are highly complex and far from canonical. Hence, it is firstly important that grids can be easily generated for complex geometries and then once a grid is produced, that the numerical scheme is not heavily degraded on non-ideal grids. This motivated the present study into how to characterise numerical methods to gain insight. The focus here is being placed on the characteristics on stretched grids for linear advection and diffusion. These categories will define the work going forward, as well as providing subdivision of topics in literature.

The key characteristics of a scheme that should be understood are its ability to resolve key features and its temporal stability. These metrics can then be passed down into ‘rules of thumb’ and subsequently used to inform the meshing process as well as further research. For example, if the temporal stability in some case is found to be too restrictive when using explicit methods it may be necessary to move to implicit time integration. This is a non-trivial matter and to ensure stability and efficient implementation further research would be needed. The evaluation of resolution can be broken down into wave resolution, energy decay rate, aliasing, and temporal stability. Wave resolving can be informative for first and higher derivatives as potential solutions can be thought of as a superposition of waves. Furthermore, once wave transmission properties are known, deconvolution of the filter kernel can then be implemented to re-energise under-resolved wavenumbers. This links to the energy decay rate that can be utilised for finding new schemes as will be described later. More detail concerning existing evaluation techniques will be presented in Section 1.3.

So far, the justification for both the use of higher order methods and the present study has been kept general. Becoming more specific, the family of schemes whose characteristics are explored in this work are based on Flux Reconstruction (FR) [65, 160]. Details of the development of the field that led to FR, the techniques currently used in analysis, and the state of the art will be laid out in Section 1.3. The overall structure will

be: in Chapter 2 the numerical method of FR will be defined; in Chapter 3 the topic of aliasing at high order will be investigated; Chapter 4 will investigate the effect of mesh deformation in FR; Chapter 5 will look to define new types of FR; and in Chapter 6 conclusions will be made. Several appendices are included to aid the reader. These are: a brief introduction to orthogonal polynomials, additional analysis of some theoretical work present, a description of extended range FR, and pseudo code for some work included in Chapter 5. The remainder of this chapter is devoted to a review of the literature contributing to the development of ideas in this work.

1.3 Literature Review

We now present some key ideas and supporting literature that lead up to the present study. We will begin by introducing some contemporary numerical methods for conservation equations and how they went on to be extended to higher orders.

1.3.1 Development of High-Order Methods

Finite Difference Approaches

Much of the early work on the use of high-order methods was developed around a class of methods called Finite Difference (FD). This is owing to them being conceptually intuitive in their simplest form. FD can broadly take 2 forms: simple finite difference, the likes of which can be calculated from Taylor series; and compact difference or Padé schemes (so-called due to the use of the Padé approximation).

We will focus first on simple FD schemes. A significant historical account of techniques is available in Harlow's memoirs [56]. Initially, these methods were applied to form first and later second-order approximations of first and second derivatives [87, 88]. However, the first move towards high order was Roberts and Weiss [118] with a fourth order central difference scheme in space that was primarily developed for solving Maxwell's equations, but which was generalised for hyperbolic equations. This scheme's primary disadvantage was its mildly prohibitive CFL limit of 0.25. The restrictive CFL limits of high-order FD methods can be ameliorated in several ways, such as high order temporal integration, multi-grid [22], or implicit temporal methods, these will be discussed in more detail in Section 1.3.1.

Commonly these simple FD schemes make use of their consistent stencil by having a structured grid. Indeed, all the original methods had structured grids, unstructured methods only being developed later. Structured grids represent something of a compromise; due to knowing in advance the communication required, implementation can be highly



optimised. For example, with tools such as GPU optimisation [23], they make porting to heterogeneous architecture simpler. However, the other side of the compromise is that structured grids do mean that complex geometries are difficult to mesh and, in some cases, meshes may be impossible to produce.

Finally, these FD schemes can be taken beyond what can formally be defined from Taylor series expansion via Dispersion Relation Preserving (DRP) schemes [97, 142]. DRP schemes modify the coefficients of an FD scheme of formal accuracy order, with the aim of improving the numerical properties of the method. For example, this could include reducing the dissipation rate of acoustic waves. The cost of this improvement is the loss of formal order of accuracy, but if the coefficients are chosen well this effect can be minimised, whilst still improving performance. For example, DRP schemes have been employed to provide high fidelity simulation of high-pressure turbine blades [170], something which has previously been challenging.

Next, we move on to what are commonly called compact finite difference schemes or compact schemes, which were introduced in a number of papers. Of note is Orszag et al. [111], in which a fourth order compact scheme is proposed and Lele [89], in which a more generalised set of compact schemes were introduced that could be adjusted for different wave propagation characteristics. Compact schemes make use of the interconnection of neighbouring points to give a wider stencil of differencing whilst maintaining a locally compact stencil. An example is shown in Fig. 1.2. This has the benefit of physically reducing the stencil required by each point in the implementation, whilst retaining a high-order spatial discretisation. Practically this is achieved by framing each block as a sparse banded matrix — for which there are highly optimised algorithms. Therefore, each block acts as a highly parallelisable region with a high degree of coupling that can propagate information quickly. Resultantly, compact schemes are best suited to large structured blocks. When applied to complex geometries, it becomes necessary to use many blocks. The problem this poses is that it has been traditional for large overlap regions to be used at the interface of blocks, increasing inter-block communication and hence harming parallelism. More recently, methods of characteristics have come to be used together with one-sided differencing to remove the need for block overlaps [79], however characteristic based methods typically introduce excess diffusion at the interface. Other developments aimed at solving the problems caused by complex geometries have led to the use of other schemes to form an interface between blocks and between boundaries [50]. However, as problem size increases, hybrid approaches becomes less favourable due to the potential communication bottlenecks this could pose — as well as the load balancing issues introduced. The further issue of all these methods of block interfacing is that they can cause degradation to the solution quality.

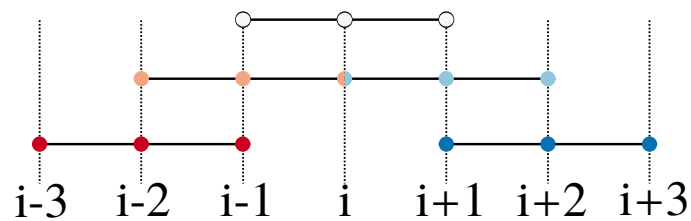


Fig. 1.2 An example stencil of a Compact FD scheme, showing the interconnection between node and how this can be leveraged to give a far wider stencil.

Having introduced the two main branches of the FD method, it should have become clear that FD approaches lack any formal enforcement of conservation. This is common to many methods that work with the strong conservation form of equations. Instead, these methods rely on the accurate approximation of gradients to keep solution approximately conservative. This point links to later discussion of how other techniques differ.

The final point for consideration on FD methods is their susceptibility to Gibbs' phenomenon [55]. Gibbs' phenomena is the inaccuracy caused by the approximation of discontinuous functions with a continuous basis, and, even in the limit as the order goes to infinity, the solution does not converge. An interesting point that Lax [85] explored was that for any finite difference scheme of second order or higher, spurious oscillations due to Gibbs' cannot be removed by any adjustments of the differencing coefficients. One aspect that makes FD particularly susceptible is the use of a moving stencil, as tuned point layouts can reduce the local effect. Coupled to this is that central FD schemes have zero dissipation [89] and are susceptible to instabilities caused by the growth of high frequency modes. For example, Gibbs' or through the boundary treatment [28]. A common approach to reduce the effects of these oscillations is then to apply a filter [78, 164], but this needs careful tuning and has an added computational cost.

Finite Volume Approaches

The Finite Volume (FV) class of methods has been extremely popular for a considerable time and with good reason. If the derivation of the Navier–Stokes equations are considered, a common approach is to consider conservation of mass, momentum, and energy on a small control volume of fluid. FV approaches use this idea as the basis of the method. We begin by introducing the approach as taken for a second order accurate method, of which there are many techniques that have developed. We will focus on what is typically called a cell vertex centred method [152].

A typical set up of such a method is shown in Fig. 1.3. Here data is stored at the grid vertices (shown in red/orange) and a control volume is formed by linking the cell centroids. Simply put, to advance the solution at i, j in time, the flux through the control



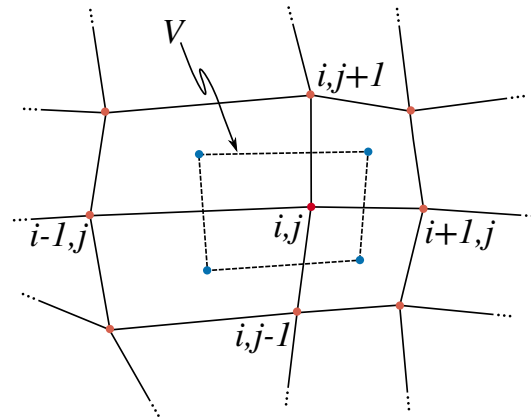


Fig. 1.3 Schematic of cell vertex finite volume grid, with dual generated via connecting centroids.

volume, V , has to be calculated. This in turn is done by evaluating the flux at the control volume face associated with each edge. The method for evaluating the face flux is the primary component of an FV method and is where considerable effort has been focused, for example, the popular MUSCL scheme of Van Leer [155, 156]. However, we are concerned here with the development of high-order techniques so will go on to discuss how FV can be adapted to give higher order estimates of the face flux.

A key subset of high-order approaches we will focus on is the family of Essentially Non-Oscillatory schemes (ENO) [4, 57, 58]. These schemes are relatively representative of FV high order methods in their technique of achieving order, in that they use an extended stencil to form a polynomial that can be interpolated or integrated. Where the ENO family of schemes differs is in their approach to reducing spurious oscillation in the solution. As was mentioned earlier, around discontinuous features or features that have large amounts of high wavenumber content there is a problem that fitting causes spurious oscillations. ENO attempts to counter this by downgrading the order of the solution or moving the stencil in the presence of oscillations based on some criterion. This was taken further by Weighted ENO (WENO) [95, 130], where the various solutions from different stencils are blended together using a weighting function. We mention ENO and WENO as they marked an important change: polynomial fitting and extension of the technique to arbitrary orders.

Finite Volume methods have been found to be a useful and robust set of methods, consequently being used widely and applied to problems beyond the research environment. This is in part due to their simple nature and the fact that second-order methods lend themselves to unstructured grids and to a certain level of parallelism. However, as the approximation of face fluxes are moved to higher orders, the stencil increases. If then an unstructured method is also needed, forming stencils can become a complex task. For

example, one extension of WENO to unstructured grids — that of Pringuey and Cant [27] — is highly complex. Furthermore, the extra communication and bespoke interpolation this requires can greatly reduce the efficiency of the method. This is also true of other high-order FV methodologies.

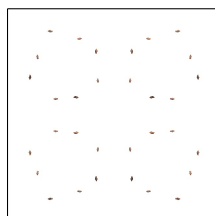
Element Based Approaches

Beyond FD and FV are a class of schemes that are commonly thought of as either Finite Element (FE) or Galerkin approaches. This class of schemes take the domain and subdivide it into elements. The FE approach [24], commonly called continuous Galerkin, uses these subdomains, a basis, and a weight function to find a global minimum to a variational form of the conservation equation that is to be solved. Weight functions form a necessary part of the method due to the inherent discretisation of numerical methods.

By contrast, Discontinuous Galerkin (DG), introduced by Reed and Hill in their seminal paper [117], aims to similarly find a global minimum to the variational form of a conservation equation. However, the difference is that DG only looks for a solution that is C^0 continuous. Since the inception of DG, the method has developed enormously and a comprehensive review can be found in Cockburn et al. [37]. The key development that these methods introduced was localised polynomial fitting. This was initially as a post-processing step to increase the accuracy of the solution [38], but was extended to each time step by Dumbser & Munz [49]. This extension was for the purpose of Lax-Wendroff temporal integration, but led to the general use of polynomial reconstruction for the solution and flux [46]. A development that occurred at a similar time was Nodal DG [60], that used a simplified method of polynomial fitting based on nodal values.

Consequently, DG can be split into nodal and modal methods. Nodal methods use nodal values to form polynomial fits and a Lagrange basis, whereas modal methods use the coefficients of the basis. Modal approaches are typically advantageous when the stiffness matrix is sparse which occurs on linear problems. While nodal methods are comparatively more computationally straightforward for non-linear problems, but in their original form do not guarantee the interpolation is the Galerkin projection. So hence can experience larger polynomial aliasing errors than their modal counterparts.

Early DG methods also inspired another series of schemes based on subdivision. These schemes broadly fall into the category of spectral collocation methods [114]. The popularity of subdivision was due to eliminating the burden of large stencils, that is common to other high-order approaches, although in some instances meant a large number of equations had to be solved due to the number of polynomial bases. As a consequence of the localised fitting that developed, unstructured DG methods [14] can be implemented in ways that are more typically efficient than other high-order techniques.



Temporal Integration Schemes

It was common before the 1980s for the space and time schemes to be bundled together as one unified scheme, take for example the Lax–Wendroff scheme [87]. However, a key development came in the work of Jameson et al. [74], where the space and time scheme were separated it what is called the method of lines. This development allowed for ideas to grow separately and for the machinery developed for ODEs to be employed for the temporal integration. This branch of methods can then be split into two classes, explicit and implicit.

Explicit methods are the most straightforwardly implemented, where only the information at the current or previous time is needed to move the solution forwards. There are many explicit integration method, but most noteworthy are explicit Runge–Kutta (ERK) methods. This set of schemes has the ability to be modified such that various properties are possible, such as low storage [29, 77]. A somewhat fundamental issue with ERK schemes is that for temporal order greater than four, the number of steps needed increases beyond the order [26]. For example, a fifth order ERK scheme requires a minimum of six steps. The importance of this is that to truly see the benefits of a high-order spatial scheme the temporal integration method also needs to be high order, or encure small time steps. For example by considering the consistency and rate of convergence, it can be found that, as may have been expected, the truncation error order is dominated by the lowest order in space and time [5]. However, the extra operations of increasing the temporal order does cause an increase in the temporal stability [161]. A further side effect of high-order coupled to explicit time schemes is that as spatial order is increased, the limits on time step inversely scale with order either linearly or quadratically [60].

The second class of methods are implicit methods, where the next time step is expressed as function of both the current/previous steps and as well as future steps. For implicit RK methods this results in a set of equations which couple the substeps [69]. The advantage of implicit methods is that it is possible to find an A-stable methods, where all time step sizes are stable. Comparing this situation to explicit methods, where it is provable that explicit A-stable methods do not exist [107]. Hence, implicit methods can be very useful for stiff problems where a large range of time scales make simulations computationally expensive. The disadvantage of these methods is that this large coupled set of equation has to be solved. For some methods this can be framed as a matrix problem, which has a high memory overhead associated with it, especially as order increases as memory scales with order to the sixth power when 3-dimensional [17, 167]. Other methods frame the problem as non-linear root finding, typically this means using Newton iterations or modified Newton iterations. The problem this encounters is that the flux Jacobian has to be calculated, which is computational expensive and still requires a

large amount of memory. Therefore, high order implicit temporal methods have largely been avoided when high spatial order is to be used.

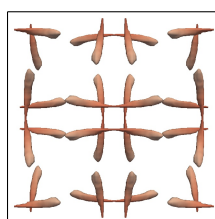
A further method, that has proved useful when applying artificial compressibility [98, 35], is dual time stepping [71]. This poses each implicit real time step as a steady problem when considered in a pseudo times. This method comes with significant computational overhead but the rate of convergence in pseudo-time can be increased using some of the standard methods, such as multigrid [99].

1.3.2 Computational Considerations

Until now the discussion has largely been about numerical methods and their numerical characterisation. However, in all but the most trivial of cases, the method has to operate in hardware. This is the point at which the best numerical schemes can fail as there are four things that become important. These are the availability of FLOPs; memory availability; memory bandwidth; and memory latency. In early methods, such as FD, and to some extent continuing to the present time, the problems of computation were typically associated with FLOPs and memory availability. The solution to this was to increase the number of processors. However, the returns of this are diminishing, see Amdahl's Law [9], due to most calculations having a serial element of computation at a fundamental level.

The development that has significantly changed scientific computing in the past decade has been the development and ubiquitous availability of multi-core CPUs and the utilisation of GPUs. Both of these developments have made more cores readily available for computing. Now GPUs are available with many thousands of single and double precision cores (see Nvidia's Volta architecture [110]) and CPUs are available with hundreds of threads (see Intel's Knights Landing architecture [135]). Hence, with careful crafting, a numerical method can be created with high levels of parallelism to utilise this hardware. Consequently, when designing a scheme, this has to be kept in mind. The end result is then that modern schemes can suffer from being memory bound, i.e insufficient memory bandwidth to feed the available FLOPs or slowing due to latency. In the case of Intel's KNL, latency can be a large problem with the onboard memory having high bandwidth but at the cost of high latency. Therefore, to produce a numerical scheme that is computationally efficient, parallelism needs to be considered together with how memory can be kept contiguous and how the number of cache misses can be reduced.

This, then, is the current climate of high performance computing hardware, within which contemporary numerical methods in computational physics must reside.



1.3.3 Flux Reconstruction

The method under investigation in the current study is Energy-Stable Flux Reconstruction (shortened to FR) proposed by Huynh [65–67]. The energy stability of this method was proved initially by Vincent et al. [160] for linear advection via a modified Sobolev norm analysis. Further details of the use of Sobolev spaces in this context can be found in Kuskina and Lax [84, 90].

The development of FR in 1D, and later on quadrilateral and hexahedral geometries, was largely influenced by the Staggered Grid (SG) approach of Kopriva & Kollias [81] and Kopriva [80]. This approach sought to solve some issues surrounding spectral element methods at the time and proposed using two grids within a sub-domain together with polynomial interpolation. This method had the advantage of being naturally extended, via a tensor product, to hypercube geometries, but was also developed into the Spectral Difference (SD) [96, 140] method for simplex elements. The application to simplex elements made use of the work of Raviart and Thomas [116], which was also used earlier to form a similar method called Spectral Volume (SV) [166]. Spectral volume took the staggered grid approach and used a further subdivision which allowed for stricter enforcement of conservation, similar to locally applying a FV method.

These methods became of increasing interest as they offered high-order in such a way that made meshing more straight forward. But further to this, the domain-subdivision that improved mesh generation, also increased the computational efficiency. This computational efficiency was investigated for large scale FR calculations [163], where it was found that FR could achieve 58% of peak LINPACK performance when run on a large cluster. This indicates that FR, through its formulation, has inherited the computational efficiency of these other methods.

Common to FR and the staggered grid and spectral element methods which inspired it, is the need to form a continuous flux polynomial. In the FV method, the same problem is encountered but is experienced purely as conservation. A simplistic method that is used in FV to form a continuous flux is central differencing. However, as is well-known, central differencing causes no dissipation but significant dispersion in the linear case, and hence some form of stabilisation has to be used. Instead, it has been common in FR to use a method that has some degree of upwinding, as this causes dissipation most notably at the high wavenumbers. Typical methods that have been applied to the first derivative component of the calculation are approximate Riemann solvers — such as Roe [120] — or flux-vector splitting [93, 94, 139]. A method that is favoured is the Rusanov flux [124] as it is computationally cheap to calculate. For the continuity of the second order flux components, it has been typical to use methods such as BR1/BR2 [14, 16] or Local

Discontinuous Galerkin (LDG) [39]. A paper of note to aid in the choice of Riemann solver is [115], which gives exhaustive detail of the pitfalls of various techniques.

The major component that differentiates FR from SG, SD, or SV methods is the means by which the common interface values are applied. In FR this manifests as a correction function that applies small changes to the element interior points while ensuring the boundary value is that set by the common interface values. Correction functions will be discussed in more detail in a later section.

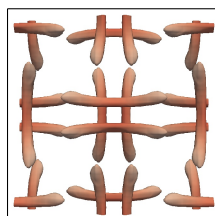
Successive extensions have been made to FR to allow for the handling of simplex geometries, such as by Castonguay et al. [32] and Williams et al. [172]. These made use of the same triangular space [116] and basis functions [45] that were applied in SD and SV approaches. Most recently the FR method has been adapted to ensure flow conservation [1–3], i.e that the scheme is conservative, which was previously not strictly the case. Some recent further developments to FR, that are beyond the scope of this work, are Direct Flux Reconstruction (DFR) methods [122, 123]. These use interpolation together with thoughtful solution point placement to reduce the operation count of FR and may be of interest if they can be cast in such a way to give the same numerical character.

1.3.4 PDEs Characteristic of Industry

Advection Equations

The PDE to which FR was first applied was the advection equation [65], with the majority of analytical results being for linear advection, for example, Asthana et al. [10] and Vincent et al. [161]. The first major work in forming a more general approach to FR was, as has already been mentioned, that of Vincent et al. [160]. A generalised form was found as a result of imposing some assumptions on the stability analysis. The resulting stability analysis proved that for 1D linear advection the energy of the conserved variable is bounded and decreases with time, this is sufficient to say that the scheme is energy stable. If the underlying assumption made to find the generalised energy stable FR scheme is modified, as was done by Vincent et al. [162], then yet another, extended, range of stable correction functions can be found for linear advection. An extension of these stability analyses was performed by Sheshadri et al. [127], where the energy stability of quadrilaterals was explored. As a result of these efforts, there is now a large family of energy stable schemes that is broadly referred to as Flux Reconstruction.

To broaden the knowledge about how FR transmits waves — and therefore arbitrary solutions — von Neumann analysis is a useful tool. This was first performed in the early paper by Huynh [65] in line with the earlier work on high-order methods by Lele [89] and Isaacson [68], with Vincent et al. [161] repeating this analysis for the previously discovered family of schemes. From this, they were able to show that the general form



of FR linked together SD, Huynh, and DG methods. This work was two-fold, as it also explored the temporal stability of the fully discretised scheme, giving analytical CFL limits. Previously, Huynh [65] had only examined the semi-discrete form *i.e* exact temporal integration was used. From this spatio-temporal analysis correction functions were found that displayed super-convergence when temporal discretisation with carried out with a family of Runge-Kutta schemes. This property of super-convergence was found to be realised by DG methods by Cockburn et al. [38] when semi-discretised and therefore, what had been found was a series of correction functions that could counter the dissipation and dispersion error of the temporal integration, restoring the super-convergence characteristic of DG methods. The von Neumann analysis of linear advection was repeated by Asthana et al. [10] and yet another series of correction functions was found that gave minimal dispersion and dissipation errors. Moving to higher dimensionality problems Williams et al. [172] showed the beginnings of a 2D von Neumann analysis for linear advection. However, the scope of this investigation was severely limited as the focus of the work was properties of FR on triangular elements, with solution point placement later optimised for advection on tetrahedra in the connected work by Witherden et al. [175]. It should be noted at this point that Huynh [65] proved for linear advection the stability of FR with a hypercube reference domain is not affected by solution point placement.

For industrially relevant problems, mesh quality is typically worse than for the idealised analytical problems that have up until now been considered, with typical domains being highly complex systems leveraging the unstructured nature of the scheme to mesh all manner of geometries. Some recent work [11] has begun to perform a more generalised von Neumann/Fourier analysis. With Mengaldo et al. [104] even purporting to have performed wavenumber free eigensolution analysis of DG for under-resolved LES. Here, they were focusing on the band of scheme performance in which insufficient resolution causes dramatic changes to the solution. Based on this there is still much to be discovered about the wave propagating behaviour in higher dimensions as well as the spatio-temporal stability on lower quality grids.

Diffusion Equations

Another important equation set to engineers are diffusion equations, which have parabolic behaviour. Flux Reconstruction of the diffusion equation was presented in Huynh [66] and was generalised and found to be energy stable in Williams and Jameson [172]. This analysis again used the modified Sobolev norm approach and found that diffusion terms add a stabilising effect proportional to the viscosity as expected. An extension was made to tetrahedral cells by Williams & Jameson [172]. An adapted von Neumann analysis can be performed on the linear advection-diffusion equation as was shown by

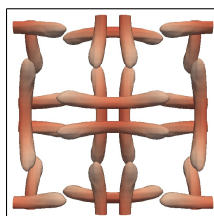
Watkins et al. [168]. A similar procedure was followed to fully discretise the scheme in order to find the CFL limits. The limitation of this paper is that this was solely performed for nodal DG via FR, hence the scope of the insight gained was limited. Castonguay [30] did briefly show some results from von Neumann analysis however these are again narrow in scope. The more general von Neumann analysis of the linear diffusion and linear advection-diffusion in higher dimensions and on stretched grids is yet to be explored.

A more recent further development in the algorithms for solving fluid flows equations is hyperbolic diffusion [102, 108, 109]. This method aims to decrease the computational time of advection-diffusion equation by rewriting the governing equation such that only a first-order derivative is used, therefore transforming the diffusion equation from being a parabolic equation to hyperbolic. This is done by introducing another equation for each diffusion term and associating a diffusion timescale with each. The motivation for this in the present work is that, as will become clear once the numerical method is presented, when diffusion is incorporated within the FR scheme, a greater proportion of time is spent performing interface calculations. As the interface calculation cannot be vectorised the potential for parallelisation is not as great as the other steps in the algorithm. Hence, hyperbolic diffusion offers the possibility of optimisation, and if it can be incorporated into a full NSE solver, potential speed up.

A further advantage of hyperbolic diffusion is that when hyperbolised the diffusion equation is given a characteristic speed and direction of propagation. When applied to a parabolic equation, such as the diffusion of heat, this means that the solution has a front. This property that can be particularly useful when solving the Eikonal equation for wall distance, see Tucker et al. [153], although the Eikonal is already hyperbolic typical methods employ an adapted Hamilton-Jacobi form that contains diffusive terms. The advantage of hyperbolic diffusion being that the calculation can potentially be stopped once a sufficient wall distance is calculated, typically out to $y^+ = 60 \sim$ to ~ 100 .

1.3.5 Correction Functions

Underpinning the methodology of FR and CPR is a procedure in which the discontinuous local approximations of the flux are made to be globally continuous. It was through a generalisation of the procedure in which correction functions are calculated that unified stable FR schemes. As was described in the previous section, this was first performed by Vincent et al. [160], giving the family of FR that we will refer to as Original Stable FR (OSFR). This original approach to generalising correction function search for function that ensured that the functional space contracted in time. An interesting result that this family led to is that OSFR on linear problems could be defined as top mode filtered NDG [8, 178].



Later, this family was extended using ideas from the spectral element community [162] giving rise to what we will call Extended Stable FR (ESFR). In this work it is shown that ESFR is equivalent to different filter, that effects more than just the top mode, instead around half of the modes.

These two works and subsequent investigations [7, 161, 163, 168, 171] have shown the importance of correction functions in defining the numerical characteristics of the method. For example, in an investigation of OSFR, varying the correction function could raise the CFL limit by $\sim 110\%$ compared to NDG methods [161]. However, NDG methods can give rise to super-convergence [6, 11, 38, 65, 174] and SD methods are somewhere between the two with slower convergence but higher CFL limits and more favourable dispersion and dissipation characteristics.

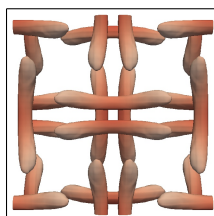
The exact conditions in which super-convergence may occur can be difficult to realise however. Super-convergence, and the higher than p^{th} order convergence that can be seen in several FR schemes, is dependent on the nature of the solution that is initialised in the element. In particular, the use of a nodal presentation can lead to error due to the solution not being a least squared projection of the true solution. This can give rise to spurious modes in the solution with an associated increase to the error. However, often these modes have short half-lives and so decay leaving a constant error. Consequently, super-convergence of the solution in flow simulations primarily occurs when flow structures form and remain in the flow field for a long time, hence allowing the spurious features to decay.

This brief discussion of corrections functions aims to show that work has so far has shown that through the manipulation of the correction function, the character of FR can vastly change. This character of the scheme can then be tuned to the specific application that is required. In terms of implementation these changes are subsequently easy to implement as it merely requires the entry of a matrix to be changed. Hence, any development in this area is important in further unifying FR with other methods and could lead to the discovery of further performance improvements.

1.4 Conclusions

High order methods generally have increased resolution and subsequently can reduce the number of degrees of freedom required. The cost of this increased resolution is an increase to the number of operation required per update. However, higher order structured methods or finite element based methods allow for far higher computational efficiency, which may offset the extra cost. In the context of PDEs, higher order methods also typically result in lower CFL limits, which can be balanced by larger element size due to higher resolution.

These compromises are key to designing a numerical method, the specific weighting in the compromises are determined by the application and computing environment. In the current climate there is an abundance of FLOPs, but comparatively limiting memory bandwidth. This means that higher resolution and more efficient schemes are more favoured. Due to this, high order Flux Reconstruction is a promising numerical method, and hence further developing the understanding and finding performance increases is of particular importance.



Chapter 2

Flux Reconstruction Methodology

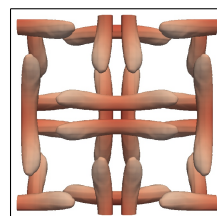
2.1 Preliminaries

As has already been stated the Flux Reconstruction (FR) approach to be investigated is that of Huynh [65] and Vincent et al. [160]. An overview of the method is given here for the benefit of the reader. However, the exact implementation used follows that of Castonguay [30]. A cautionary note must be given that although the work of Castonguay [30] has many useful notes on efficient implementation there are also several typographical errors, and other peer reviewed sources should be consulted on implementation. Any of those already cited are of use, particularly Sheshadri et al. [128]. Over the next two sections, FR applied to the one dimensional linear advection equation and two-dimensional second order PDEs on quadrilateral elements is presented.

Throughout the sections that follow domain subdivision, as is common to DG methods, will be utilised. Therefore, this subdivision is presented here with the specifics of the domains to be subdivided given later where appropriate. If the domain of the calculation is Ω then the subdivision is:

$$\Omega = \bigcup_{n=1}^N \Omega_n \quad \text{and} \quad \bigcap_{n=1}^N \Omega_n = \emptyset \quad (2.1)$$

where $\Omega \in \mathbb{R}^d$, d is the dimensionality and N is the number of elements. The standardised sub-domain $\hat{\Omega}$ is used and will be called the computational space. In the case where the geometry is based on hypercubes, the computational space is taken as $\hat{\Omega} = [-1, 1]^d$. To



transform from $\Omega_n \rightarrow \hat{\Omega}$ a Jacobian is defined as:

$$\mathbf{G}_n = \begin{bmatrix} \frac{\partial x_1}{\partial \xi_1} & \frac{\partial x_2}{\partial \xi_1} & \cdots & \frac{\partial x_d}{\partial \xi_1} \\ \frac{\partial x_1}{\partial \xi_2} & \frac{\partial x_2}{\partial \xi_2} & \cdots & \frac{\partial x_d}{\partial \xi_2} \\ \vdots & \vdots & \ddots & \vdots \\ \frac{\partial x_1}{\partial \xi_d} & \frac{\partial x_2}{\partial \xi_d} & \cdots & \frac{\partial x_d}{\partial \xi_d} \end{bmatrix} \quad \text{and} \quad J_n = |\mathbf{G}_n| \quad (2.2)$$

where x_i is the i^{th} spatial variable in the physical domain, Ω_n , and ξ_i is the i^{th} spatial variable in the computational domain, $\hat{\Omega}$. In lower dimensional problems, the spatial variables will typically be described as ξ , η , and ζ . Having set up the computational domain, for brevity, the computational gradient operator is defined as:

$$\hat{\nabla} = \begin{bmatrix} \frac{\partial}{\partial \xi_1} \\ \frac{\partial}{\partial \xi_2} \\ \vdots \end{bmatrix} \quad (2.3)$$

With these conventions in place the numerical method may now be defined.

2.2 One-Dimensional Approach for First-Order PDEs

We will begin by presenting the Flux Reconstruction (FR) methodology when applied to a first order conservative PDE. The precise manner in which we reconstruct the solution follows the work of Huynh [65] and Vincent et al. [160], where a more detailed view of the technique is presented. We set out to solve a 1D conservative equation of the form:

$$\frac{\partial u}{\partial t} + \frac{\partial f}{\partial x} = 0 \quad (2.4)$$

where u is the primitive and f is the flux variable. The aim of FR then is to take a polynomial approximation of the solution defined in each sub-domain, Ω_j , and form a continuous approximation of the flux. Therefore, if we define a set of broken polynomials over the sub-domains we can then form a global solution as:

$$u^\delta = \bigcup_{n=1}^N u_n^\delta \approx u \quad \text{and} \quad f^\delta = \bigcup_{n=1}^N f_n^\delta \approx f. \quad (2.5)$$

Here we have defined u_j^δ and f_j^δ as being the approximate solution and flux in the j^{th} element. The work comes from ensuring that these represent a series of continuous polynomials. The stages in ensuring this are: first we transform Eq.(2.4) into reference

domain:

$$\frac{\partial \hat{u}^\delta}{\partial t} + \frac{\partial \hat{f}^\delta}{\partial \xi} = 0 \quad (2.6)$$

defining

$$\hat{u}^\delta = J_n u^\delta \quad \text{and} \quad \hat{f}^\delta = J_n f^\delta \quad (2.7)$$

The next stage is then to actually form the polynomial for \hat{u}^δ in Eq.(2.7). To do this we define it as a sum over a basis:

$$\hat{u}^\delta = \sum_{i=0}^p \hat{u}_i^\delta(\xi) l_i(\xi) \quad (2.8)$$

where here we use the Lagrange basis defined as:

$$l_i = \prod_{\substack{j=0 \\ j \neq i}}^p \left(\frac{\xi - \xi_j}{\xi_i - \xi_j} \right). \quad (2.9)$$

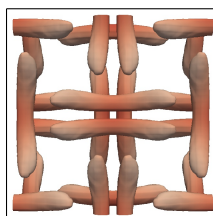
Any basis could be used in place of l_i , however the advantage of the Lagrange basis is its natural application to nodal methods.

The third stage is to form a discontinuous flux polynomial in the reference domain – this is different from \hat{f}^δ , which is piecewise continuous. We will symbolise the discontinuous flux as $\hat{f}^{\delta D}$. The polynomial is then defined as:

$$\hat{f}^{\delta D} = \sum_{i=0}^p \hat{f}_i^{\delta D} l_i(\xi) \quad (2.10)$$

the advantage of this technique is that it is straightforward to calculate $\hat{f}_i^{\delta D}$ from \hat{u}^δ , and it is this that is the source of the inter-element discontinuities.

Step four begins the process of making a continuous flux polynomial. We initially interpolate the solution polynomial to the edges of the element as $\hat{u}_L^\delta = \hat{u}^\delta(-1)$ and $\hat{u}_R^\delta = \hat{u}^\delta(1)$. These interpolated values can then be used to calculate discontinuous interface values, $\hat{f}_L^{\delta D}$ and $\hat{f}_R^{\delta D}$. At every interface there are now pairs of collocated points that store the discontinuous flux on either side of the interface, e.g. we have $\hat{f}_{j-1,R}^{\delta D}$ and $\hat{f}_{j,L}^{\delta D}$. Once the discontinuous collocated flux values are obtained they can then be used to calculate a common interface value for each pair of values. This can be done using many methods, however for hyperbolic equation sets it is often advantageous to use an upwinding methods via an appropriate approximate Riemann solver [145]. This is advantageous as the upwinding introduces diffusion that will act to stabilise the scheme, whereas if central differencing is used some smoothing/diffusion must be applied to



ensure stability. For each element in 1D we then have a left and right common interface value, namely $\hat{f}_L^{\delta I}$ and $\hat{f}_R^{\delta I}$.

Step five is then the application of common interface value to build a correction to the discontinuous flux to form a continuous polynomial. At this stage we introduce the correction function, which is the means by which we propagate the common interface value into the element. In 1D we have a left and right correction function, corresponding to the left and right element edge. The correction functions will be defined as $h_L(\xi)$ and $h_R(\xi)$ respectively, with the boundary conditions:

$$h_L(-1) = 1 \quad \text{and} \quad h_L(1) = 0; \quad (2.11)$$

$$h_R(-1) = 0 \quad \text{and} \quad h_R(1) = 1. \quad (2.12)$$

then forming the correction as:

$$\hat{f}^{\delta C} = (\hat{f}_L^{\delta I} - \hat{f}_L^{\delta D})h_L(\xi) + (\hat{f}_R^{\delta I} - \hat{f}_R^{\delta D})h_R(\xi) \quad (2.13)$$

Hence the continuous flux function is then:

$$\hat{f}^{\delta} = \hat{f}^{\delta D} + \hat{f}^{\delta C} = \hat{f}^{\delta D}(\xi) + (\hat{f}_L^{\delta I} - \hat{f}_L^{\delta D})h_L(\xi) + (\hat{f}_R^{\delta I} - \hat{f}_R^{\delta D})h_R(\xi) \quad (2.14)$$

Finally, to calculate the continuous gradient of the flux we differentiate Eq.(2.14). First let us rewrite Eq.(2.14) to use the interpolation step of Eq.(2.10):

$$\hat{f}^{\delta} = \hat{f}^{\delta D} + \hat{f}^{\delta C} = \sum_{i=0}^p \hat{f}_i^{\delta D} l_i(\xi) + (\hat{f}_L^{\delta I} - \hat{f}_L^{\delta D})h_L(\xi) + (\hat{f}_R^{\delta I} - \hat{f}_R^{\delta D})h_R(\xi) \quad (2.15)$$

Upon differentiation this then becomes:

$$\frac{\partial \hat{f}^{\delta}}{\partial \xi} = \sum_{i=0}^p \hat{f}_i^{\delta D} \frac{dl_i(\xi)}{d\xi} + (\hat{f}_L^{\delta I} - \hat{f}_L^{\delta D}) \frac{dh_L(\xi)}{d\xi} + (\hat{f}_R^{\delta I} - \hat{f}_R^{\delta D}) \frac{dh_R(\xi)}{d\xi} \quad (2.16)$$

At this stage we can discuss further the correction function and its order. Previously when defining $\hat{f}^{\delta D}$ because of the availability of data we could only fit an order p polynomial for $\hat{f}^{\delta D}$. However, as we now have taken the gradient of the correction and it is required that it lie fully in the polynomial space of FR. Hence, h_L and h_R may be set to be polynomials of order $p + 1$. Consequently, $\hat{f}^{\delta C}$ may be order $p + 1$ and, from a polynomial fitting view, this reflects the extra information that the correction function is offering to the fit.

The last stage in the FR methodology is the use of Eq.(2.16), in conjunction with a temporal integration method, to advance the solution \hat{u}^{δ} in time. The simplest method for advancing Eq.(2.4) in time would be explicit temporal integration, commonly via explicit

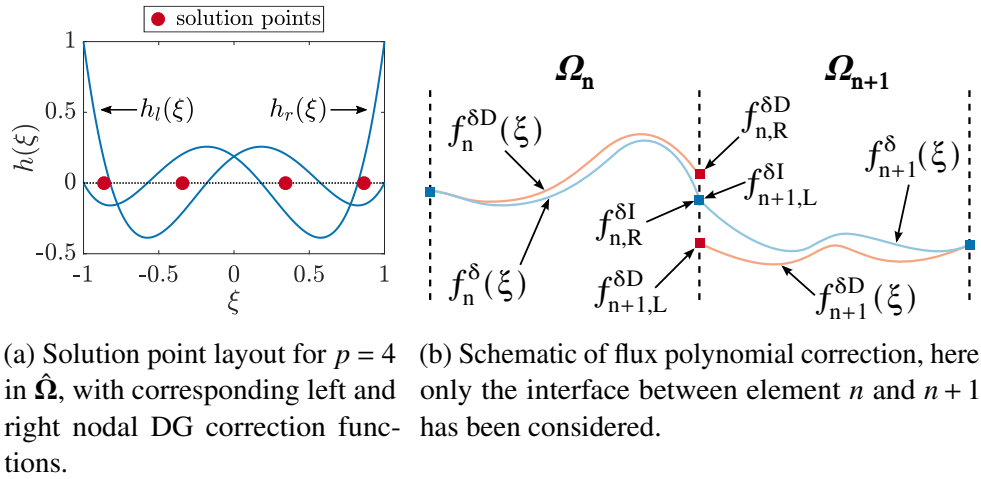


Fig. 2.1 Point layout in $\hat{\Omega}$ for $p = 4$ and example of flux correction.

Runge-Kutta methods. Kennedy [77] gives a comprehensive derivation and overview of explicit Runge-Kutta method when applied to the Navier-Stokes equation.

2.3 Two-Dimensional Approach for Second-Order PDEs

Extension of the method to two dimensions is straightforward for quadrilateral elements [65], therefore the extension will be presented alongside an introduction to the procedure for second order PDEs. The method for generalised FR on second order PDEs is taken from Castonguay et al. [33] and Sheshadri et al. [128]. Here the second order PDE being solved is advection with linear diffusion, which can be written as:

$$\frac{\partial u}{\partial t} + \nabla \cdot \mathbf{F} = 0 \quad (2.17)$$

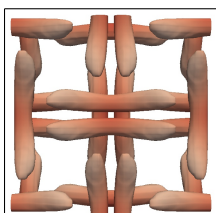
$$\mathbf{F} = \begin{bmatrix} f \\ g \end{bmatrix} = \begin{bmatrix} u - \nu q_x \\ u - \nu q_y \end{bmatrix} \quad (2.18)$$

where ν are the convective velocity and rate of diffusion respectively. q_x and q_y are then defined as:

$$q_x = \frac{\partial u}{\partial x} \quad , \quad q_y = \frac{\partial u}{\partial y} \quad (2.19)$$

where $f = f(q_x, u)$ and $g = g(q_y, u)$.

The flux reconstruction process for an advection-diffusion problem will then differ from the purely advection case in that we have to also ensure that q_x and q_y are the gradient of a continuous solution. This is done using the same correction methodology as



in Eq.(2.15):

$$\hat{u}^\delta = \hat{u}^{\delta D} + \sum_{i=0}^p \left[(\hat{u}_{L,i}^{\delta I} - \hat{u}_{L,i}^{\delta D})h_{L,i} + (\hat{u}_{R,i}^{\delta I} - \hat{u}_{R,i}^{\delta D})h_{R,i} + (\hat{u}_{T,i}^{\delta I} - \hat{u}_{T,i}^{\delta D})h_{T,i} + (\hat{u}_{B,i}^{\delta I} - \hat{u}_{B,i}^{\delta D})h_{B,i} \right] \quad (2.20)$$

where L, R, T and B subscripts are used to indicate the left, right, top and bottom interface values respectively. The common interface values, for example $u_{L,i}$, can simply be taken as the average across the interface, as the diffusion from the approximate Riemann solver is sufficient to prevent any instabilities here. The transformed values of q_x and q_y can simply be calculated then via differentiation of Eq.(2.20):

$$\hat{\nabla} \cdot \hat{u}^\delta = \begin{bmatrix} \hat{q}_x^\delta \\ \hat{q}_y^\delta \end{bmatrix} = \begin{bmatrix} \frac{\partial \hat{u}^{\delta D}}{\partial \xi} + \sum_{i=0}^p \left((\hat{u}_{L,i}^{\delta I} - \hat{u}_{L,i}^{\delta D}) \frac{\partial h_{L,i}}{\partial \xi} + (\hat{u}_{R,i}^{\delta I} - \hat{u}_{R,i}^{\delta D}) \frac{\partial h_{R,i}}{\partial \xi} \right) \\ \frac{\partial \hat{u}^{\delta D}}{\partial \eta} + \sum_{i=0}^p \left((\hat{u}_{T,i}^{\delta I} - \hat{u}_{T,i}^{\delta D}) \frac{\partial h_{T,i}}{\partial \eta} + (\hat{u}_{B,i}^{\delta I} - \hat{u}_{B,i}^{\delta D}) \frac{\partial h_{B,i}}{\partial \eta} \right) \end{bmatrix} \quad (2.21)$$

Once the transformed discontinuous gradient is calculated the discontinuous flux at the solution points can be calculated, and hence the discontinuous flux function can be formed as:

$$\hat{f}^{\delta D}(\xi, \eta) = \sum_{i=0}^{n_s} \hat{f}_i^{\delta D} l_i(\xi, \eta) \quad (2.22)$$

and in the case of a maximal order basis l_i then becomes the product of two 1D Lagrange polynomials.

The next stage is to extrapolate the solution to the flux points and calculate the inviscid and viscous interface fluxes, e.g. $\hat{f}_{L,i}^{\delta Di}$ and $\hat{g}_{L,i}^{\delta Dv}$ for the left inviscid and viscous flux terms respectively. An appropriate method must then be used to calculate the common interface value for the inviscid/hyperbolic and viscous/parabolic terms separately. The method for the inviscid/hyperbolic term was discussed in Section 2.2. As for the viscous/parabolic term, methods such as BR1, BR2, LDG, could be used, with a more complete list of possibilities found in [33]. Finally, the terms can be added together to find the common interface flux, e.g. $\hat{f}_{L,i}^{\delta I}$.

Now we can construct the divergence of the discontinuous flux and flux correction as:

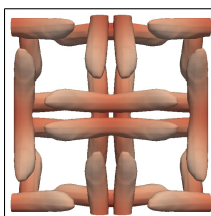
$$\hat{\nabla} \cdot \hat{\mathbf{F}}^{\delta D} = \sum_{i=0}^{n_s} \left(\hat{f}_i^{\delta D} \frac{\partial l_i(\xi, \eta)}{\partial \xi} + \hat{g}_i^{\delta D} \frac{\partial l_i(\xi, \eta)}{\partial \eta} \right) \quad (2.23)$$

$$\hat{\nabla} \cdot \hat{\mathbf{F}}^{\delta C} = \sum_{i=0}^p \left((\hat{f}_{L,i}^{\delta I} - \hat{f}_{L,i}^{\delta D}) \frac{\partial h_{L,i}}{\partial \xi} + (\hat{f}_{R,i}^{\delta I} - \hat{f}_{R,i}^{\delta D}) \frac{\partial h_{R,i}}{\partial \xi} + \right. \\ \left. (\hat{g}_{B,i}^{\delta I} - \hat{g}_{B,i}^{\delta D}) \frac{\partial h_{B,i}}{\partial \eta} + (\hat{g}_{T,i}^{\delta I} - \hat{g}_{T,i}^{\delta D}) \frac{\partial h_{T,i}}{\partial \eta} \right) \quad (2.24)$$

With the discontinuous and corrected transformed flux gradient calculated the solution can then be advanced forwards in time via:

$$\frac{\partial \hat{u}^{\delta}}{\partial t} = -\hat{\nabla} \cdot \hat{\mathbf{F}}^{\delta D} - \hat{\nabla} \cdot \hat{\mathbf{F}}^{\delta C} \quad (2.25)$$

To conclude, the key difference when considering an equation with second order derivatives is that the gradient terms must be constructed from a continuous solution and hence the reconstruction step must first be applied to u before being applied to f . The introduction in the last two sections is of course quite terse, but does highlight the key features of FR, as well as the general paradigm being followed. For a more exhaustive explanation the reader is advised to consider the cited material. If any further detail is required beyond the overview given here, it will be presented in a later section as necessary.



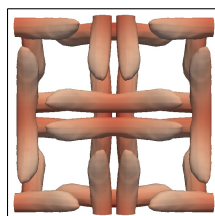
Chapter 3

Effect of Flux Function Order and Working Precision

3.1 Introduction

Over the course of the last three decades Large Eddy Simulation (LES) has become increasingly used for the exploration of flow physics. Looking forward to how CFD will be used tomorrow, NASA CFD Vision 2030 [132] predicts that hybrid RANS/LES and wall-modelled LES will become increasingly used in aerospace design. These methods are likely to prevail until sufficient technological developments allow for wall-resolved LES to become a feasible part of the design process. One effect of this continuing shift from low fidelity modelling to high fidelity simulation is that the gap is bridged, in part, by adapting existing RANS tools for LES. For example, ANSYS Fluent began as a tool for solving the RANS equations, but has increasingly developed LES capability [165]. While, more recently, some tools have been developed from the outset to be spectral or capable of high orders, for example Nektar++[76], PyFR [174], etc.

Through this journey from predominantly low order RANS to LES and then onto high-order, several dogmas have developed that have continued into recent methods. Chief among which is the form of the variables stored when solving a conservation equation. In the context of fluid mechanics, this commonly comes down to whether the primitive or conservative variables are stored. To the knowledge of the author, the only justification given for this choice one way or the other comes from Fluent's documentation, where the given arguments are 'it is a natural choice when solving incompressible flows' and 'to obtain more accurate velocity and temperature gradients in viscous fluxes, and pressure gradients in inviscid fluxes'. Yet, which variables are stored is an important feature of a scheme as it will impact how the flux terms are constructed and their relative order. This dogma forms the primary question to be answered. In particular: is the error introduced



through the construction of the terms required in fluids dynamics sufficient for one storage method to be favourable?

In fluid dynamics, it is common to require second derivatives to simulate viscous effect. In turn this requires gradients of the primitives. Several methods are actively used to calculate these terms, the Senga2 code [27] uses the product rule on the gradient of the conserved variables, whereas several industrial codes directly calculate the gradient of the primitive. Due to the differences in the two methods, the viscous fluxes will have different orders. We wish to understand if these differences are significant and secondly if one method is more efficient.

A related topic that has seen much work is relating to spectral aliasing in LES and the mechanisms by which it is brought about. For example Moser et al. [106], Blaisdell et al. [20], and Kravchenko et al. [82]. These works focus on the aliasing brought about in spectral methods by the differentiation stage of a non-linear flux. It was broadly concluded that the skew-symmetric form can reduce the effect of aliasing, without active de-aliasing techniques. But, depending on the flow conditions, occasionally the skew-symmetric aliasing error can be large. A more recent study by Winters et al. [173], compared two splitting techniques when applied to the DG method. These investigations are mentioned as this work was found to be the most similar in nature to the problem confronted here. However, throughout the work on the skew-symmetric form, little attention has been paid to which variable are stored, yet the same spectral analysis would indicate it could have a noticeable impact.

The second dogma that we wish to investigate whether it is valid that variables should be stored in double precision, or if single precision is adequate. This links to the question of which variables are stored, as different operation counts will cause the effect of working precision to be different.

In most typical calculations the norm is to use double precision throughout, however, as the size of problems to be tackled grows so too does the memory usage. Therefore, it would be beneficial for both reducing memory overhead and increasing computational speed if single precision were used. Further to this, some hardware — notably many GPUs — include only comparatively few double precision arithmetic units, and therefore the increase in computational speed can be as much as 32 times by moving from 32 to 64-bit precision. Some investigation into this question has been performed, notably by Homann et al. [62] on the DNS of incompressible homogeneous turbulence using a variable precision incompressible pseudo-spectral scheme. However, they saw little to no difference when the precision was changed, but this may have been due to the explicit enforcing of incompressibility. Another investigation into precision was presented in the review paper by Bailey [12], which spanned several physics regimes. This investigation, however, was in the opposite direction, looking at the effect of using 128-bit precision.

It was found that it could be important and concluded that better support of adaptive precision should be made by software and hardware. Therefore, we wish to investigate if the same insensitivity to working precision is true for high order polynomial based methods, or as Bailey [12] found it could, in fact, be important.

3.2 Discrete Error Mechanism

In this section we wish to study the mechanism for which errors can enter approximate solutions. In particular, we do this from a polynomial point of view which is most applicable to an approximation in a finite element framework. Let us start by studying a simple generalised conservative equation:

$$\frac{\partial u}{\partial t} + \frac{\partial f}{\partial x} = 0 \quad (3.1)$$

In this case, we will solve on the periodic domain $[-1, 1]$, for simplicity. Then the effect of solving this numerically is that we have some finite basis. Let us then set that the solution, u , may be constructed as some p^{th} order polynomial. In this case, we will use the Legendre basis:

$$u = \sum_{i=0}^p \tilde{u}_i \psi_i(x) \quad (3.2)$$

where ψ_m is the m^{th} order Legendre polynomial of the first kind. If the flux function is then $f = f(u^n)$ for $n \in \mathbb{N}$, then for the flux we get:

$$f = \sum_{i=0}^{np} \tilde{f}_i^P \psi_i(x) \quad (3.3)$$

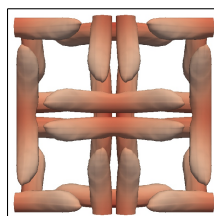
However, as previously stated, the functional space of the numerical solver is limited to be p^{th} order. We wish to then project the high order flux on to this space using an ℓ_2 projection, which is commonly used in Galerkin methods [60]. Starting by defining the projected flux as:

$$f^P = \sum_{i=0}^p \tilde{f}_i^P \psi_i(x) \quad (3.4)$$

then we wish to minimise:

$$\int_{-1}^1 (f - f^P)^2 dx \quad (3.5)$$

By using the modal presentation and the orthogonality of Legendre polynomial the optimal projection is then just the truncation of Eq. (3.3) to p^{th} order. We can then define



the truncation error as:

$$e_T = f - f^P = \sum_{i=p+1}^{np} \tilde{f}_i \psi_i(x) \quad (3.6)$$

This is not the complete picture however, as in nodal methods such as FR, a Galerkin projection is not employed. Instead, Lagrange polynomials are used to form a polynomial approximation from point values. This may be presented in 1D as:

$$f^\delta = \sum_{i=0}^p f(x_i) l_i(x) \quad (3.7a)$$

$$l_i(x) = \prod_{\substack{j=0 \\ j \neq i}}^p \frac{x - x_j}{x_i - x_j} \quad (3.7b)$$

Due to this representation f^δ and f^P are not strictly equal. We may then define a projection error as:

$$e_P = f^P - f^\delta = \sum_{i=0}^p \tilde{f}_i \psi_i - \sum_{i=0}^p f(x_i) l_i(x) \quad (3.8)$$

and hence

$$f^\delta = f - e_T - e_P \quad (3.9)$$

Of the two components of the error, the truncation error is often unavoidable due having a finite basis. The projection error term on the other hand is more problematic as it is this term that introduces polynomial aliasing into the solution. Furthermore, due to the dependence of e_P on the point location it is difficult to gain insight into general trends. Through Taylor's theorem though we can look at the effect of both e_T and e_P . Let us begin by defining the interpolation remainder as:

$$\mathcal{R}_p f = f - \mathcal{L}_p f = f - f^\delta \quad (3.10)$$

where \mathcal{L}_p is a p^{th} order linear interpolation operator. Using Taylor's theorem it can then be stated that [83]:

$$\mathcal{R}_p f(\xi) = \frac{f^{(p+1)}(\epsilon)}{(p+1)!} \prod_{i=0}^p (\xi - \xi_i) \quad (3.11)$$

where we restrict $\xi \in [-1, 1]$, ξ_i are the interpolation points, and $\epsilon \in [-1, 1]$ is dependent on ξ .

As an example let us modify the Burger's equation by squaring the conserved variable, which leads to:

$$\frac{\partial u^2}{\partial t} + \frac{\partial u^4}{\partial \xi} = 0 \quad (3.12)$$

This gives the opportunity for information to be stored in two ways comparable to methods used for Euler's equations — namely, storing u or u^2 and forming the flux term by either squaring u^2 or raising u to the power of four. This gives two possible flux polynomials when transformed into the computational domain:

$$\hat{v}^2(\xi) = (\hat{u}^2)^2 = \hat{f}_2 = \sum_{i=0}^{2p} \tilde{f}_{2,i} \psi_i \quad (3.13)$$

$$\hat{v}^4(\xi) = \hat{u}^4 = \hat{f}_4 = \sum_{i=0}^{4p} \tilde{f}_{4,i} \psi_i \quad (3.14)$$

where we have defined v to be the variable that is stored. To understand how errors may then enter the solution we wish to understand the scaling of the remainder of the flux interpolation to a finite polynomial space of order p . The maximal norm can then be used to give an estimate as:

$$\|\mathcal{R}_p f\|_\infty \leq \frac{1}{(p+1)!} \|q_{p+1}\|_\infty \|f^{(p+1)}\|_\infty. \quad (3.15)$$

Here q_{p+1} is defined as:

$$q_{p+1} = (\xi - \xi_0)(\xi - \xi_1) \dots (\xi - \xi_p) \quad (3.16)$$

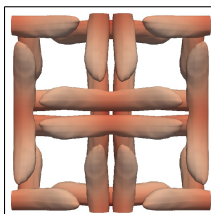
with ξ_i being the points at which the value of f is stored. Taking the domain to be $[-1, 1]$ therefore $\|q_{p+1}\|_\infty \leq 2$. We now use Eqs. (3.13 & 3.14) to refine the remainder estimates, which requires a bounding value of $\|f^{(p+1)}\|_\infty$. Firstly, it is known that the maximum absolute value of a Legendre polynomial is at $\xi = \pm 1$ ($\xi \in [-1, 1]$) and, due to the recursive definition of Legendre polynomials, the maximum value of the derivative is at $\xi = \pm 1$. If the value of a differentiated Legendre polynomial at ± 1 is:

$$\frac{d^m \psi_n(\pm 1)}{d\xi^m} = \frac{(\pm 1)^{n-m} (n+m)!}{2^m m! (n-m)!} \quad (3.17)$$

A consequence is that, for a given set of differentiated Legendre polynomials, $\{\psi'_n, \psi''_n, \dots, \psi_n^{(m)}\}$, the maximum value in this set is the edge value of the m^{th} derivative. Hence, a bound can be placed on $\|f^{(p+1)}\|_\infty$ using Eq. (3.17) and the maximum Legendre mode coefficient as:

$$\|f_2^{(p+1)}\|_\infty \leq \left[\frac{2(3p+1)!}{2^{p+1}(p+1)!(p-1)!} \right] \max_{i \in \{0 \dots 2p\}} |\tilde{f}_{2,i}| \quad (3.18)$$

$$\|f_4^{(p+1)}\|_\infty \leq \left[\frac{2(5p+1)!}{2^{p+1}(p+1)!(3p-1)!} \right] \max_{i \in \{0 \dots 4p\}} |\tilde{f}_{4,i}| \quad (3.19)$$



Hence, the interpolation remainder may be bounded as:

$$\|\mathcal{R}_p f_2\|_\infty \leq 4 \left[\frac{(3p+1)!}{2^{p+1}(p-1)![(p+1)!]^2} \right] \max_{i \in \{0 \dots 2p\}} |\tilde{f}_{2,i}| \quad (3.20)$$

$$\|\mathcal{R}_p f_4\|_\infty \leq 4 \left[\frac{(5p+1)!}{2^{p+1}(3p-1)![(p+1)!]^2} \right] \max_{i \in \{0 \dots 4p\}} |\tilde{f}_{4,i}| \quad (3.21)$$

It can be seen by inspection that:

$$\frac{(3p+1)!}{(p-1)!} \leq \frac{(5p+1)!}{(3p-1)!}, \quad \forall p \in \mathbb{N} \quad (3.22)$$

From this, there are two conclusions that can be drawn. Firstly, the interpolation remainder of f_4 will always be bigger than f_2 . Secondly, the difference between the remainders will grow factorially fast as the order is increased. Therefore, higher order methods will be far more affected by this mechanism of error introduction.

By reconsidering Eq. (3.12) it is apparent that we are actually concerned with approximating the derivative of the flux. To calculate this the remainder may be differentiated to:

$$\mathcal{R}'_p f = \frac{df}{dx} - \frac{d}{dx} \mathcal{L}_p f = \frac{d}{dx} \mathcal{R}_p f \quad (3.23)$$

Following this through to differentiate the Taylor theorem result of Eq. (3.11) we get:

$$\mathcal{R}'_p f(\xi) = \frac{f^{(p+1)}(\epsilon)}{(p+1)!} \frac{d}{d\xi} \prod_{i=0}^p (\xi - \xi_i), \quad \xi \in [-1, 1] \quad (3.24)$$

Again finding the maximal norm:

$$\|\mathcal{R}'_p f\|_\infty = \frac{P}{(p+1)!} \max_{i \in \{0 \dots p\}} (\|q_p^i\|_\infty) \|f^{(p+1)}\|_\infty \quad (3.25)$$

defining q_p^i as:

$$q_p^i = \prod_{j=0, j \neq i}^p (\xi - \xi_j) \quad (3.26)$$

If we then apply the results of Eqs. (3.20 & 3.21), it is demonstrated that the primary difference in the gradient remainder is a factor of p .

Also, within the FR algorithm, we require the interpolated values of the flux at the interfaces. This can be more straightforwardly calculated, *i.e.* $\mathcal{R}_p f(\pm 1)$.

$$\mathcal{R}_p f(\pm 1) = \frac{f^{(p+1)}(\epsilon)}{(p+1)!} \prod_{i=0}^p (\pm 1 - \xi_i) \quad (3.27)$$

We will not consider the infinity norm in this case, as Eq. (3.27) gives sufficient details. The main feature of note is that the behaviour of this remainder is primarily influenced by the interpolation point locations. For example, if $\xi_0 = -1$ and $\xi_p = 1$, as in a Gauss–Lobatto quadrature, the aliasing error introduced through interpolation to the edges would be zero. However, for other reasons explored by Castonguay [31] and Roe [121] this is problematic in higher dimensions. By comparing the remainder due to differentiation and interface interpolation, it can be seen that the differentiation gives a remainder that is approximately p times bigger. This indicates that the error that will dominate is due to the differentiation of polynomials experiencing aliasing.

3.3 Primitive and Conserved Variables

3.3.1 Euler’s Equations

We will begin by considering the 1D Euler’s equations in the conservative form.

$$\frac{\partial \mathbf{Q}_c}{\partial t} + \frac{\partial \mathbf{f}(\mathbf{Q}_c)}{\partial x} = 0 \quad (3.28)$$

for

$$\mathbf{Q}_c = \begin{bmatrix} \rho \\ \rho u \\ E \end{bmatrix}, \quad \text{and} \quad \mathbf{f}(\mathbf{Q}_c) = \begin{bmatrix} \rho u \\ \rho u^2 + p \\ u(E + p) \end{bmatrix}. \quad (3.29)$$

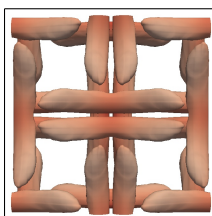
The concern is what information should be stored between time steps, while still solving this equation, and considering the previous section what will the effect be on the flux function order.

Conserved Variable Computation

In an implementation where the conserved variables are not stored directly, if the conserved form of Euler’s equations is to be solved, then the conserved variables must be computed at some stage.

$$\mathbf{Q}_p \rightarrow \mathbf{Q}_c \quad (3.30a)$$

$$\begin{bmatrix} \rho \\ u \\ p \end{bmatrix} \rightarrow \begin{bmatrix} \rho \\ \rho u \\ \frac{p}{\gamma-1} + \frac{1}{2}\rho(u^2) \end{bmatrix} = O \begin{bmatrix} \xi^p \\ \xi^{2p} \\ \xi^{3p} \end{bmatrix} \quad (3.30b)$$



This transformation is shown in Eq. (3.30). It should be clear that if \mathbf{Q}_p is represented by a polynomial of order p , then the terms ρu , ρv , and ρw will be polynomials of order $2p$, while $u(E + p)$ will be of order $3p$. Therefore, the energy equation will be most impacted by truncation and aliasing and, furthermore, the spatial variation in \mathbf{Q}_p will not have to be significant before truncation and aliasing occurs due to the high degree of the energy equation here.

Inviscid Flux Computation

In most implementations seen by the author, when the primitives are stored they are also subsequently used to form the flux, as opposed to using \mathbf{Q}_c . Therefore, the order of the flux formed from the primitives is:

$$\mathbf{Q}_p \rightarrow \mathbf{f} \quad (3.31a)$$

$$\begin{bmatrix} \rho \\ u \\ p \end{bmatrix} \rightarrow \begin{bmatrix} \rho u \\ \rho u^2 + p \\ u\left(\frac{\gamma p}{\gamma-1} + \frac{1}{2}\rho(u^2)\right) \end{bmatrix} = O \begin{bmatrix} \xi^{2p} \\ \xi^{3p} \\ \xi^{4p} \end{bmatrix} \quad (3.31b)$$

If instead the conserved variables are used we obtain:

$$\mathbf{Q}_c \rightarrow \mathbf{f} \quad (3.32a)$$

$$\begin{bmatrix} \rho \\ \rho u \\ E \end{bmatrix} \rightarrow \begin{bmatrix} (\rho u) \\ \frac{(3-\gamma)(\rho u)^2}{2\rho} + (\gamma-1)E \\ \frac{(\rho u)}{\rho}\left(\gamma E - \frac{1}{2}(\gamma-1)\frac{(\rho u)^2}{\rho}\right) \end{bmatrix} = O \begin{bmatrix} \xi^p \\ \xi^{2p}/\xi^p \\ \xi^{3p}/\xi^{2p} \end{bmatrix} \quad (3.32b)$$

Here we have been somewhat careless with notation. It is intended for $O(\xi^{2p}/\xi^p)$ to mean a $2p^{\text{th}}$ order polynomial divided by a p^{th} order polynomial. If the polynomial $1/O(\xi^p)$ is then expanded about zero to form a series of monomials, the series is $O(\xi^\infty)$. From this, we can see that in Eq. (3.32) we have avoided the ξ^{4p} term, but at the expense of dividing by ρ . This raises whether this formulation is more accurate — specifically, is the convergence of the $1/\rho$ series sufficiently fast to reduce aliasing? It may be possible to extend the analysis of section 3.2 to include reciprocals using the work of Leslie [91], however so far it has not been possible to provide a bound. Therefore, this effect will be investigated numerically. Importantly though, this storage method avoids the error introduced through the conversion in Eq. (3.30).

Another option that will be explored is storing the conserved variables but with energy substituted for pressure, \mathbf{Q}_{c+p} . The reason being that in industrial codes pressure

is used frequently and this option would reduce the work involved in converting an implementation. Hence, the conversion from \mathbf{Q}_{c+p} to the flux, \mathbf{f} , is:

$$\mathbf{Q}_{c+p} \rightarrow \mathbf{f} \quad (3.33a)$$

$$\begin{bmatrix} \rho \\ \rho u \\ p \end{bmatrix} \rightarrow \begin{bmatrix} (\rho u) \\ \frac{(\rho u)^2}{\rho} + p \\ \frac{(\rho u)}{\rho} \left(\frac{\gamma p}{\gamma-1} + \frac{1}{2} \frac{(\rho u)^2}{\rho} \right) \end{bmatrix} = \mathcal{O} \begin{bmatrix} \xi^p \\ \xi^{2p}/\xi^p \\ \xi^{3p}/\xi^{2p} \end{bmatrix} \quad (3.33b)$$

This method will also require a conversion step to retrieve the conserved variables if Eq. (3.28 & 3.29) are to be solved. This will then introduce aliasing of order:

$$\mathbf{Q}_{c+p} \rightarrow \mathbf{Q}_c \quad (3.34a)$$

$$\begin{bmatrix} \rho \\ \rho u \\ p \end{bmatrix} \rightarrow \begin{bmatrix} (\rho) \\ (\rho u) \\ \frac{p}{\gamma-1} + \frac{1}{2} \frac{(\rho u)^2}{\rho} \end{bmatrix} = \mathcal{O} \begin{bmatrix} \xi^p \\ \xi^p \\ \xi^{2p}/\xi^p \end{bmatrix} \quad (3.34b)$$

This method has the potential to reduce the aliasing in forming the conserved variables and flux, as there is no longer the ξ^{4p} that is present in Eq. (3.31). However, this is again dependent on the nature of $1/\rho$.

3.3.2 Navier–Stokes Equations

To confront more complex problems of fluid dynamical relevance, it is essential to consider the Navier–Stokes equations, written in the 3D conservative form as:

$$\frac{\partial \mathbf{Q}_c}{\partial t} + \nabla \cdot \mathbf{F}(\mathbf{Q}_c, \nabla \mathbf{Q}_p) = 0 \quad (3.35)$$

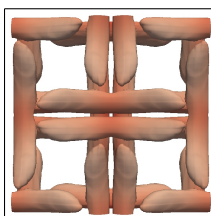
where

$$\nabla \cdot \mathbf{F} = (\mathbf{f}^{\text{inv}} - \mathbf{f}^{\text{vis}})_x + (\mathbf{g}^{\text{inv}} - \mathbf{g}^{\text{vis}})_y + (\mathbf{h}^{\text{inv}} - \mathbf{h}^{\text{vis}})_z \quad (3.36)$$

If we take the bulk viscosity, μ_b , to be zero, then \mathbf{f}^{vis} can be defined as:

$$\mu \begin{bmatrix} 0 \\ \tau_{xx} \\ \tau_{xy} \\ \tau_{xz} \\ u\tau_{xx} + v\tau_{xy} + w\tau_{xz} + \frac{\kappa}{\mu} T_x \end{bmatrix} = \mu \begin{bmatrix} 0 \\ \frac{4}{3}u_x - \frac{2}{3}(v_y + w_z) \\ u_y + v_x \\ w_x + u_z \\ u(\frac{4}{3}u_x - \frac{2}{3}(v_y + w_z)) + v(u_y + v_x) + w(w_x + u_z) + \frac{\kappa}{\mu} T_x \end{bmatrix} \quad (3.37)$$

with \mathbf{g}^{vis} and \mathbf{h}^{vis} similarly defined.



The importance of considering this equation is that — due to phenomena such as the energy cascade — in a method which does not suffer from polynomial aliasing, aliasing will arise in LES anyway, due to the partial resolution of vortical motions. Hence, for turbulent flows, any difference is likely to be more marked as truncation and polynomial aliasing tends to amplify the numerical aliasing.

Clearly for the case when primitive variables are stored, the gradients of the primitive can be directly calculated and used to form the viscous flux. However, when the conserved variables are stored there are two options available to form the gradients needed here: convert the conserved variables to the primitives and calculate the gradients needed directly:

$$\begin{bmatrix} \rho \\ \rho u \\ \rho v \\ \rho w \\ E \end{bmatrix} \rightarrow \begin{bmatrix} \rho \\ u \\ v \\ w \\ p \end{bmatrix} \rightarrow \begin{bmatrix} \rho_x & \dots \\ u_x & \dots \\ v_x & \dots \\ w_x & \dots \\ \frac{c_v}{\gamma-1}(\rho^{-1}p_x - \rho^{-2}p\rho_x) & \dots \end{bmatrix}; \quad (3.38)$$

Or calculate the gradient of the conserved variables and use the product rule to convert them to what is needed:

$$\begin{bmatrix} \rho_x & \rho_y & \rho_z \\ (\rho u)_x & (\rho u)_y & (\rho u)_z \\ (\rho v)_x & (\rho v)_y & (\rho v)_z \\ (\rho w)_x & (\rho w)_y & (\rho w)_z \\ E_x & E_y & E_z \end{bmatrix} \rightarrow \begin{bmatrix} \rho_x & \rho_y & \rho_z \\ u_x & u_y & u_z \\ v_x & v_y & v_z \\ w_x & w_y & w_z \\ T_x & T_y & T_z \end{bmatrix}. \quad (3.39)$$

These two options can be more simply written as:

$$\mathbf{Q}_c \rightarrow \mathbf{Q}_p \rightarrow \nabla \mathbf{Q}_p \quad (3.40)$$

$$\mathbf{Q}_c \rightarrow \nabla \mathbf{Q}_c \rightarrow \nabla \mathbf{Q}_p \quad (3.41)$$

where $\nabla \mathbf{Q}$ is the gradient of \mathbf{Q} . Here the final row of $\nabla \mathbf{Q}$ is the gradient of temperature, ∇T , for convenience in the calculation of the viscous flux.

The method for calculating the required gradients from the product rule applied to the conserved variable gradient formulation is:

$$\frac{1}{\rho} \begin{bmatrix} \rho \rho_x & \dots \\ ((\rho u)_x - \rho^{-1}(\rho u)\rho_x) & \dots \\ ((\rho v)_x - \rho^{-1}(\rho v)\rho_x) & \dots \\ ((\rho w)_x - \rho^{-1}(\rho w)\rho_x) & \dots \\ (E_x - \rho^{-1}E\rho_x) - ((\rho u)u_x + (\rho v)v_x + (\rho w)w_x) & \dots \end{bmatrix} = \begin{bmatrix} \rho_x & \rho_y & \rho_z \\ u_x & u_y & u_z \\ v_x & v_y & v_z \\ w_x & w_y & w_z \\ T_x & T_y & T_z \end{bmatrix} \quad (3.42)$$

The polynomial orders of this step are then:

$$\begin{aligned}
 & \frac{1}{\rho} \begin{bmatrix} \rho\rho_x \\ ((\rho u)_x - \rho^{-1}(\rho u)\rho_x) \\ ((\rho v)_x - \rho^{-1}(\rho v)\rho_x) \\ ((\rho w)_x - \rho^{-1}(\rho w)\rho_x) \\ [(E_x - \rho^{-1}E\rho_x) - ((\rho u)u_x + (\rho v)v_x + (\rho w)w_x)] \end{bmatrix} = \\
 O & \begin{bmatrix} \xi^{p-1}(\eta\zeta)^p \\ \xi^{p-1}(\eta\zeta)^p / (\xi\eta\zeta)^p + \xi^{2p-1}(\eta\zeta)^{2p} / (\xi\eta\zeta)^{2p} \\ \xi^{p-1}(\eta\zeta)^p / (\xi\eta\zeta)^p + \xi^{2p-1}(\eta\zeta)^{2p} / (\xi\eta\zeta)^{2p} \\ \xi^{p-1}(\eta\zeta)^p / (\xi\eta\zeta)^p + \xi^{2p-1}(\eta\zeta)^{2p} / (\xi\eta\zeta)^{2p} \\ \xi^{p-1}(\eta\zeta)^p / (\xi\eta\zeta)^p + \xi^{2p-1}(\eta\zeta)^{2p} / (\xi\eta\zeta)^{2p} + \xi^{2p-1}(\eta\zeta)^{2p} / (\xi\eta\zeta)^{2p} \end{bmatrix} \quad (3.43)
 \end{aligned}$$

Again, it should be clear that the momentum and energy (rows 2-5) terms experience the most aliasing, although it is not clear what effect that the division will have on aliasing. However, it is likely that the decay rate of the infinite quotient series will be fast in most cases. This will be dependent though on the nature of the function ρ , and most notably when higher Mach number flows are considered and the density field more spatially varying.

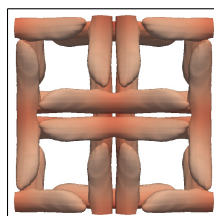
Table 3.1 Variable storage schemes to be compared

Type	Primary Storage	Stress Tensor Calculation
A	\mathbf{Q}_p	$\mathbf{Q}_p \rightarrow \nabla\mathbf{Q}_p$
B	\mathbf{Q}_c	$\mathbf{Q}_c \rightarrow \mathbf{Q}_p \rightarrow \nabla\mathbf{Q}_p$
C	\mathbf{Q}_c	$\mathbf{Q}_p \rightarrow \nabla\mathbf{Q}_c \rightarrow \nabla\mathbf{Q}_p$
D	\mathbf{Q}_{c+p}	$\mathbf{Q}_{c+p} \rightarrow \mathbf{Q}_p \rightarrow \nabla\mathbf{Q}_p$

Table 3.1 summaries the methods of variable storage and gradient calculation that will be investigated for the Navier–Stokes equations and Euler’s equations (where applicable).

At this point, we wish to link the ideas presented in Section 3.2 with the methods of this section. It should be clear that in order for this form of error to be incorporated into the solution, then at some stage interpolation or polynomial fitting has to be used within the calculation. For FR, this comes when the gradient is calculated or the edge points are interpolated from the points inside the element. However, if only the nodal values are used, as is the case in second-order Finite Volume (FV) methods, then there is no mechanism by which this error mechanism can affect the solution. Take the example of converting primitive variables to conservative variables, and back again:

$$\mathbf{Q}_p \rightarrow \mathbf{Q}_c \rightarrow \mathbf{Q}'_p. \quad (3.44)$$



It should be apparent that beyond any rounding error introduced in the floating-point arithmetic, $\mathbf{Q}_p = \mathbf{Q}'_p$. Therefore, the means of variable storage will not affect FV but will affect any method that in some way interpolates or fits a polynomial. To test this claim a second order FV method was subjected to some investigations presented later and the difference was found to be of the order of machine accuracy.

3.4 Isentropic Convecting Vortex

To evaluate the impact of the changes suggested in Section 3.3 we will begin by studying the effect on the error and total kinetic energy on the isentropic convecting vortex (ICV) [129]. The ICV is of interest as it is an analytical solution to Euler's equations and hence allows for the error at a given time to be calculated. One problem that we are confronted with when using high order, the ICV, and a periodic domain, is that the solution is only guaranteed to be C^0 continuous. This can be understood by considering the initial condition:

$$\rho = \left(1 - \frac{(\gamma - 1)\beta^2}{8\gamma\pi^2} \exp(1 - r^2)\right)^{\frac{1}{\gamma-1}} \quad (3.45a)$$

$$u = u_0 + \frac{\beta}{2\pi}(y_0 - y) \exp\left(\frac{1 - r^2}{2}\right) \quad (3.45b)$$

$$v = v_0 + \frac{\beta}{2\pi}(x - x_0) \exp\left(\frac{1 - r^2}{2}\right) \quad (3.45c)$$

$$w = 0 \quad (3.45d)$$

$$p = \left(1 - \frac{(\gamma - 1)\beta^2}{8\gamma\pi^2} \exp(1 - r^2)\right)^{\frac{\gamma}{\gamma-1}} \quad (3.45e)$$

$$r^2 = (x - x_0)^2 + (y - y_0)^2 \quad (3.45f)$$

where u_0 and v_0 are the advective velocities and β is the vortex strength (typically $\beta = 5$ is used). To set the initial values for \mathbf{Q}_p etc. the nodal values of the initial condition are used, as opposed to a Galerkin projection. From Eq. (3.45), it can be seen that as the distance r is increased the vortex slowly decays and, on a finite but periodic domain, this will lead to discontinuities in the gradient. This is a point that will be of importance later when reviewing results and was explored by Spiegel et al. [137] where some interesting plots of shear near the boundaries are presented.

The metrics that we will use to review the accuracy are the point averaged absolute error in the density:

$$e(t) = \frac{1}{N_p} \sum_{i=1}^{N_p} |\rho_i - \rho(\mathbf{x}_i, t)|_2 \quad (3.46)$$

and the total kinetic energy:

$$E_k(t) = \frac{1}{2|\Omega|} \int_{\Omega} \rho \mathbf{V} \cdot \mathbf{V} dx \quad (3.47)$$

where $|\Omega|$ is the domain volume.

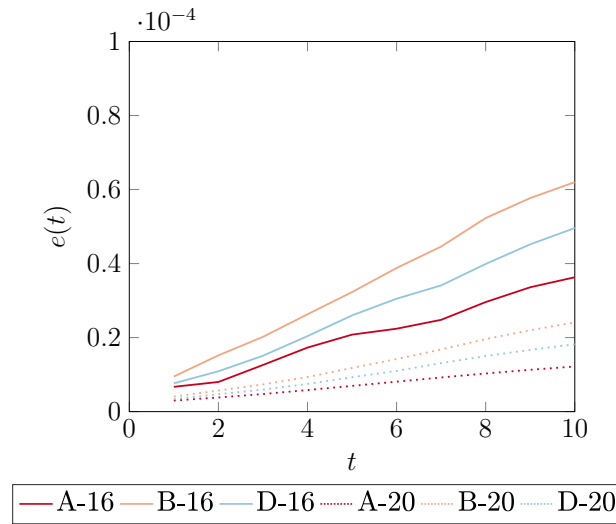
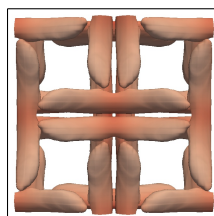


Fig. 3.1 Variation of error in ICV density with time for FR, $p = 4$, using methods A, B and D on $16 \times 16 \times 2$ and $20 \times 20 \times 2$ element grids.

We begin by investigating the effect of storing the primitive variables (A), conservative variables (B), and conservative variables with energy substituted for pressure (D) on the error. This is shown in Fig. 3.1. Clearly, method A has the lowest levels of error followed by D then B and this ordering does not change as the grid is refined. This result makes clear that storing the pressure instead of energy can make a marked difference to the scheme. In schemes (B) and (D), as the stored variable-to-flux conversation is the same, the origin of the difference can be found to be from the conversion from stored variable to conserved variable that occurs, Eq. (3.34).

The result of the error increasing for (B) and (D) compared to (A) may be thought to be contrary to the expected outcome. However, to understand what is going on let us now consider how the kinetic energy changes with time.

Figure 3.2 shows how the kinetic energy in the domain changes with time. For both grid resolutions, the rate of kinetic energy dissipation of A is higher than B and D, while B and D are similar. B and D show far less dissipation with the dissipation of method B being less than D in the higher resolution case, Fig. 3.2b. The mechanism responsible for this behaviour is that the reduction in the flux function order and the change to the stored to conservative conversions, reduces to the error introduced via truncation and projection. This in turn increases the resolution of the schemes (B) and (D) as higher wavenumbers



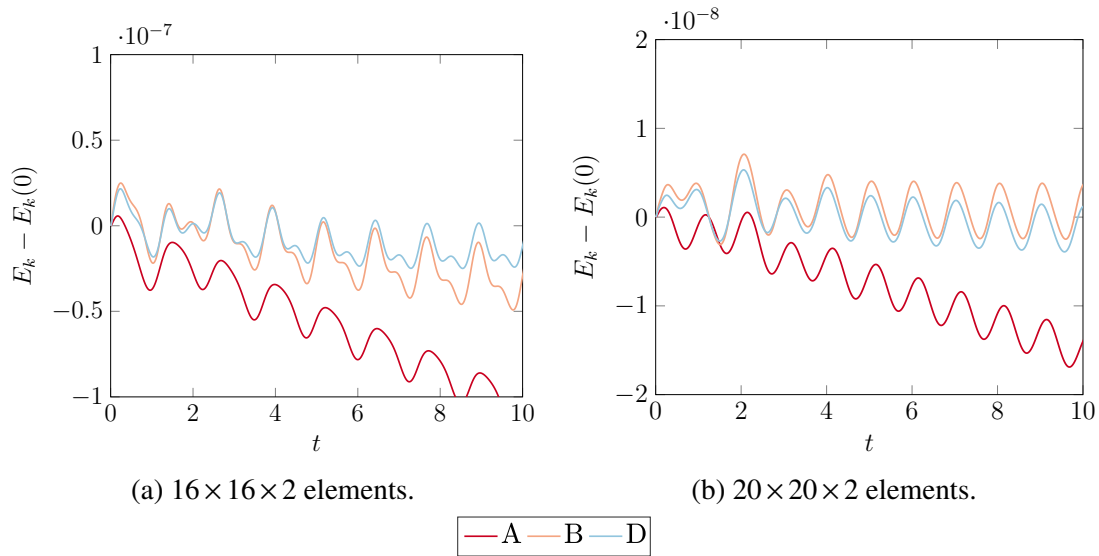


Fig. 3.2 Variation in total kinetic energy of the ICV, FR $p = 4$, for two grid resolutions, using methods A, B, and D.

can be resolved without causing excess error. To understand how this is reconciled with the somewhat contradictory results of Fig. 3.1 consider the ICV definition. The initial conditions defined earlier are formally C^0 continuous on a finite domain. Therefore, the lower dissipation exhibited by methods B and D leads to the errors introduced via the discontinuities in the gradient not being as damped as in the case of A. Hence, the error grows faster while also showing less dissipation.

3.5 Taylor–Green Vortex

3.5.1 Effect of Flux Function Order

If the various forms of variable storage are now applied to the full Navier–Stokes equations for a flow with turbulence, we can investigate in a more practical sense what the effect may be. The flow of choice for this is the canonical Taylor–Green vortex [143, 21], where the exact flow field used is defined in [42, 34, 131]. This case is chosen as not only is it a case for the Navier–Stokes equations, but it exhibits transition from a laminar regime to a fully turbulent flow, via the mechanism of vortex stretching and shearing. This is key, as not only is it more representative of real engineering flows, but transition to turbulence will introduce the energy cascade to the flow and hence induce aliasing. We will go onto use this particular flow throughout this work and therefore some time will be devoted here to an explanation of its set up and behaviour.

The initial condition is taken to be:

$$u = U_0 \sin\left(\frac{x}{L}\right) \cos\left(\frac{y}{L}\right) \cos\left(\frac{z}{L}\right) \quad (3.48a)$$

$$v = -U_0 \cos\left(\frac{x}{L}\right) \sin\left(\frac{y}{L}\right) \cos\left(\frac{z}{L}\right) \quad (3.48b)$$

$$w = 0 \quad (3.48c)$$

$$p = p_0 + \frac{\rho_0 U_0^2}{16} \left(\cos\left(\frac{2x}{L}\right) + \cos\left(\frac{2y}{L}\right) \right) \left(\cos\left(\frac{2z}{L}\right) + 2 \right) \quad (3.48d)$$

$$\rho = \frac{P}{RT_0} \quad (3.48e)$$

where we define the case by the non-dimensional parameters as:

$$R_e = \frac{\rho_0 U_0 L}{\mu}, \quad P_r = 0.71 = \frac{\mu \gamma R}{\kappa(\gamma - 1)}, \quad M_a = \frac{U_0}{\sqrt{\gamma R T_0}} \quad (3.49)$$

with the free variables set as:

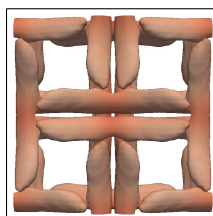
$$U_0 = 1, \quad \rho_0 = 1, \quad p_0 = 100, \quad R = 1, \quad \gamma = 1.4, \quad L = 1 \quad (3.50)$$

This is then solved on a domain $\Omega \in [-\pi, \pi]^3$ with periodic boundary conditions. Again the initial condition is set using the nodal values. From the above definitions, varying R_e and M_a allow for a series of different flow regimes can be explored, however first and foremost this case intended as an incompressible case. Hence, if we wish to explore that, it is typical for compressible schemes to use a Mach number, M_a , of approximately 0.08. To give an appreciation of the flow field we have plotted iso-surfaces of q -criterion through time for $q = 0.5$, $R_e = 1600$, and $M_a = 0.08$ in the right corner as a flip-book. This shows the rapid decay of the vortex cores then the build up of vorticity through shear and then the transition to turbulence. If the simulation is continued, it is known that for $R_e > \sim 500$ the turbulence exhibited is isotropic [21].

The metrics that we will use to study the behaviour of the numerical method applied to the TGV are the rate of kinetic energy dissipation and enstrophy dissipation:

$$\epsilon_1 = -\frac{dE_k}{dt} = -\frac{d}{dt} \left(\frac{1}{2\rho_0 U_0^2 |\Omega|} \int_{\Omega} \rho \mathbf{V} \cdot \mathbf{V} dx \right) \quad (3.51)$$

$$\epsilon_2 = \frac{\mu}{\rho_0^2 U_0^2 |\Omega|} \int_{\Omega} \rho (\boldsymbol{\omega} \cdot \boldsymbol{\omega}) dx \quad (3.52)$$



where $\boldsymbol{\omega}$ is the vector is vorticity, μ is the shear viscosity, and where ϵ_1 & ϵ_2 have been normalised. We will also make use of the enstrophy error term:

$$\mathcal{E} = \frac{\epsilon_2 - \epsilon_{2,\text{ref}}}{\epsilon_{2,\text{ref}}} \quad (3.53)$$

Flux function order is the primary focus of this chapter, and, as such, we want to investigate if the different methods of variable storage impact the accuracy of the solution. As a result, there are two things which will be varied, the first of which is the Reynolds number. Three cases are investigated, with $R_e = 400, 1600,$ and 3000 , with DNS data (ref) available from Brachet [21]. This is because varying the Reynolds numbers triggers a variety of different physics, as will be discussed later. The second variable we propose changing is the Mach number, where values of $M_a = 0.08$ and 0.3 will be tested. The effect of compressibility on the TGV was investigated by [113] at various Mach numbers between 0.5 and 2 , with 0.5 not being found to exhibit shocklets. Therefore, testing at $M_a = 0.3$ will test the introduction of errors due to larger spatial variations in ρ , but without introducing issues relating to shock capturing.

For the majority of the investigation, a 3D Navier–Stokes FR scheme will be used. The grid topology used will be hexahedral, constructed using a tensor product of the 1D FR scheme. More details on this construction of FR can be found in [174, 31, 172] including the extension to diffusion equations. The method of calculating the inviscid common interface flux chosen is Rusanov flux with Davis wave speeds [124, 41]. The viscous common interface flux is found using Bassi and Rebay’s BR1 scheme [14, 15]. At the present we are not concerned with the associated effects of correction functions choice and, because of this, an FR correction function that recovers Nodal DG will be used [65, 60].

Let us first consider the TGV case when $R_e = 1600$ at Mach numbers 0.08 and 0.31 . We will look to compare the four methods presented in Section 3.3 for FR with $p = 4$ on a mesh with 80^3 degrees of freedom, the results of which are shown in Fig. 3.3. It is seen that when $M_a = 0.08$, Fig. 3.3a, there is a small improvement when storing data as conserved variables over primitive variables. The results of the conservative variables with pressure instead of energy can be seen to be almost identical to the primitive variable results. It can also be noted that the largest difference is seen around the time of peak dissipation and not in the region $4 < t < 7$. This seems to indicate that the effect of changing the method of variable storage is to reduce the dissipation at the smallest scales, as the low flux order again increases resolution. It is apparent that it does not introduce extra sources of dispersion which would cause over dissipation around $4 < t < 7$ when small scales begin to enter the flow.

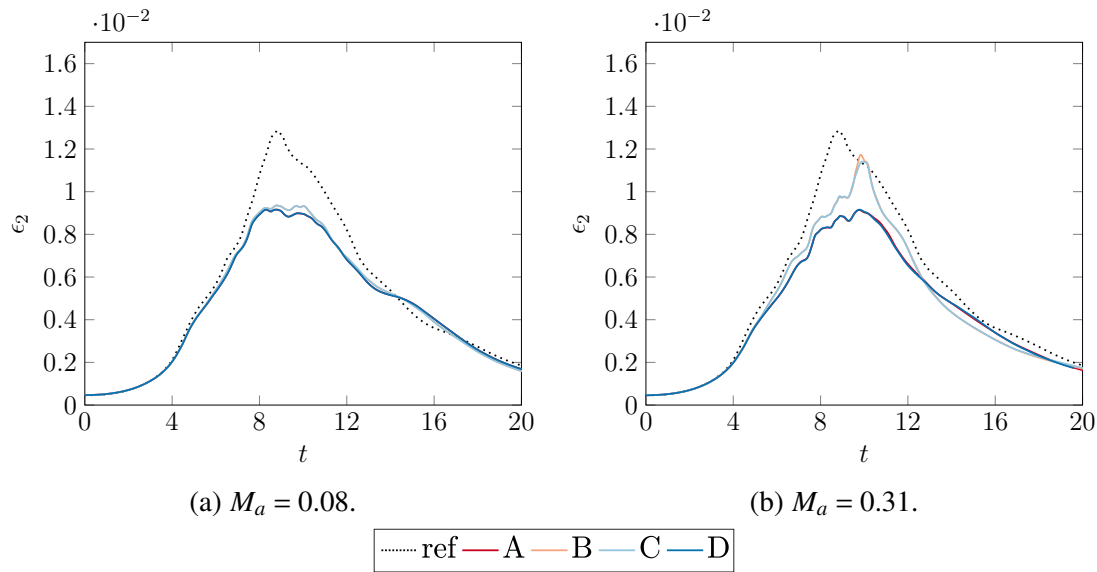
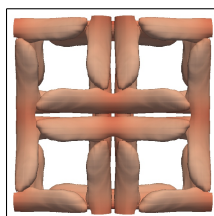


Fig. 3.3 Enstrophy of the Taylor–Green Vortex with $R_e = 1600$, $p = 4$ and 80^3 degrees of freedom for storage methods A-D.

Moving onto the case when $M_a = 0.31$, as is indicated by this higher Mach number, the solution will exhibit larger spatial variations in the density, due to increased compressibility. From the analysis in Section 3.3 it is clear that the division by density with large spatial variations could lead to higher levels of error, predominantly through the truncation mechanism. However, at lower Mach numbers, this will lead to faster convergence of the division terms.

The enstrophy for the $M_a = 0.31$ case is shown in Fig. 3.3b and clearly shows a far larger change between the full conservative and the primitive methods. Again the cases of primitive and partial conservative with pressure are similar — this suggests that the improvement is largely originating from the change in the handling of the energy equation. Clearly the largest difference between the method happens for $8 < t < 12$. From DeBonis [42], we see that around this time energy has moved to the higher frequencies, but the $-5/3$ power law has not yet been established. This means that at this time the spatial variation of the variables is large, and the density due to initially being approximately uniform. Therefore, at higher Mach numbers the error in schemes B and C has two competing components. The reduction due to the use of the momentum terms in the flux, and a potential increase due to spatial variation in the density.

At the higher Mach number, there is a noticeable difference in Fig. 3.3b between the fully conservative with the gradient calculated from the converted primitives and the gradient calculated from the application of the product rule. It is hard to attribute this difference to a particular aspect, this will be explored further at lower Reynolds numbers.



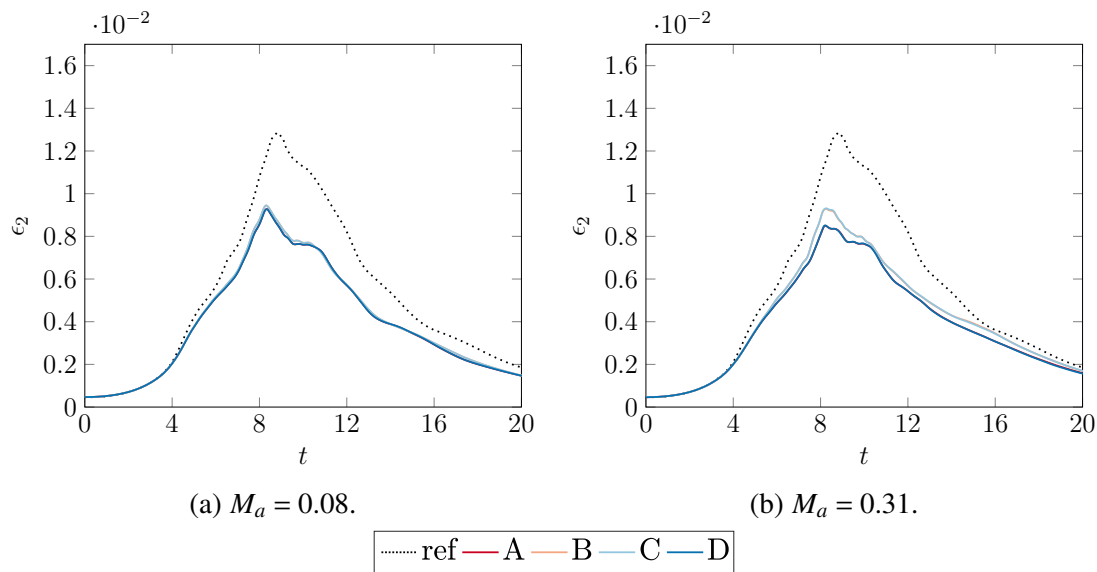


Fig. 3.4 Enstrophy of the Taylor–Green Vortex with $R_e = 1600$, $p = 3$ and 80^3 degrees of freedom.

In Section 3.2 we showed analytically the dependency of interpolation rounding error on order and that it increases factorially as the polynomial order is increased. To investigate the effect of order we consider the case of $R_e = 1600$ run at $p = 3$ for the same number of degrees of freedom. The results of this are shown in Fig. 3.4. By comparison of Fig. 3.4a & 3.4b, we can see that there is still a larger difference between the methods in the high Mach number case than at low Mach number. However, when comparing Fig. 3.4 & 3.3, the difference between methods is markedly smaller at lower order. This evidence is in agreement with the earlier analytical predictions: as we move to a higher order, this mechanism of error becomes increasingly important.

We will now explore the effect of increasing the Reynolds numbers for the same grid resolution. In particular, we choose $R_e = 3000$, which was explored with DNS by Brachet et al. [21] and with DG by Chapelier et al. [34]. The results of the application of $p = 4$ FR with the various methods of storage are presented in Fig. 3.5. Firstly studying the $M_a = 0.08$ case, there is again a noticeable difference between the conservative and primitive enstrophy, which we can attribute to the decrease in numerical/aliasing based dissipation, due to the absence of over-dissipation when small scales begin to be generated and the increase in dissipation at the expected peak. This suggests that the small scales are being preserved for longer thus enabling their increased contribution to physical dissipation.

When the Mach number is increased to $M_a = 0.31$ we initially see a larger difference between the formulations, followed by the solution diverging. A similar divergence was observed by Chapelier et al. [34] when using DG on an under-resolved mesh, although

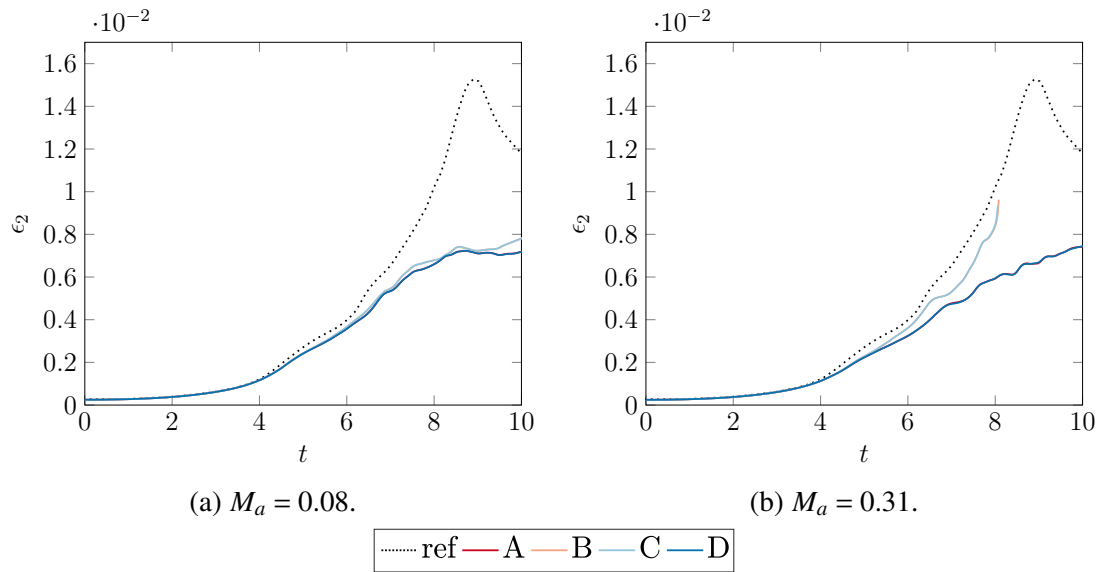
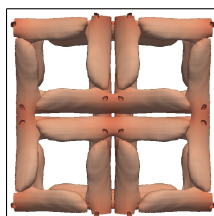


Fig. 3.5 Enstrophy of the Taylor–Green Vortex with $R_e = 3000$, $p = 4$ and 80^3 degrees of freedom.

they were solving the explicitly filtered LES equations. They attributed the divergence to insufficient numerical dissipation to stabilise the under-resolved grid. From the other results presented here, it has been shown that storing the conserved variables leads to reduction in dissipation at high wavenumbers due to the lower order of the flux function. Also, it is well-known that DG, particularly for non-linear problems, will require stabilisation through a de-aliasing method [60]. This appears to be the problem now confronted by methods B and C, and mitigations for FR have been investigated by Spiegel et al. [138] and for NDG by Hesthaven et al. [60].

Finally for the storage methods, differences will be compared between methods B and C when applied to a case with larger magnitude viscous terms. For this we will consider a case at $R_e = 400$. Initially a grid with 80^3 degrees of freedom was used, however this resolution was found to give approximately DNS results. Because of this there was little to no content in the flow that was effected by truncation of polynomial aliasing and hence the degrees of freedom was reduced to 40^3 . This give a cell Reynolds number of $R_{e,\text{cell}} = 50$ at $p = 4$, which is more indicative of LES. The results of which are shown in Fig. 3.6, indicate only a small change between the methods B and C, and due to overshoot at both Mach numbers, it is hard to discern if one method is better than another. However, as we are about to explore, there may be a computation saving of one method over another.

The different methods outlined in Section 3.3 will obviously require differing numbers of floating-point operations as some conversion steps are required or different numbers of multiplications to build things like the flux terms. Therefore, we wish to understand what the impact on computational performance is, to this end we will profile the implementation.



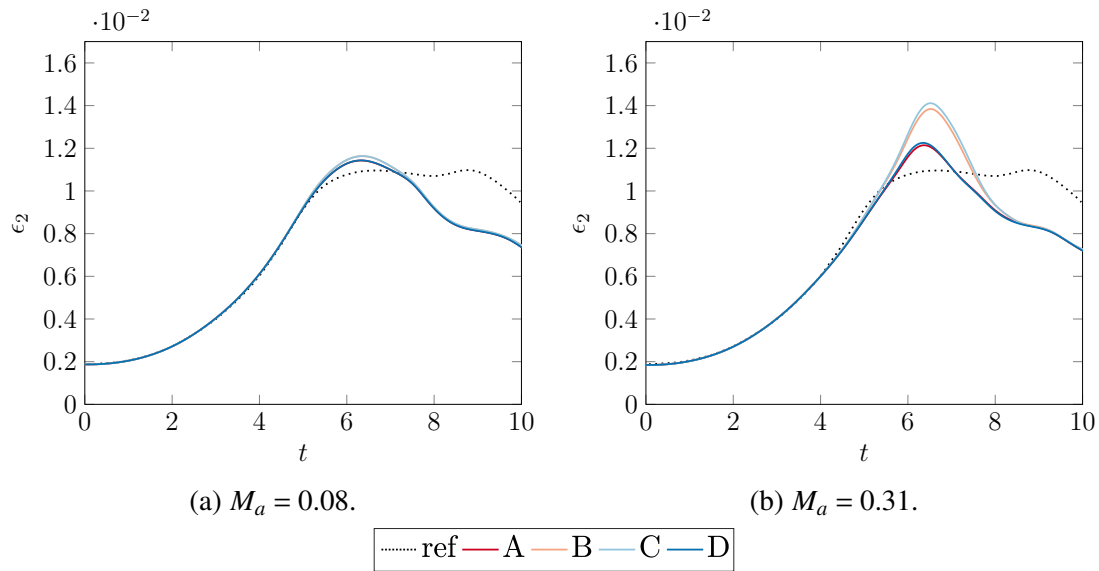


Fig. 3.6 Enstrophy of the Taylor–Green Vortex with $R_e = 400$, $p = 4$ and 40^3 degrees of freedom.

Table 3.2 Computation time comparison for one full RK44 explicit time step on a 8^3 , $p=4$, mesh.

Type	Computation time (ms)	Speed-Up relative to A
A	6.423	1.000
B	5.832	1.101
C	5.634	1.140
D	6.757	0.951

The implementation of FR used is an in house FR solver called Forflux, written in Fortran with CUDA Fortran and cuBLAS — both version 9.1 — for GPU acceleration. The implementation has been constructed such that all the data required for the FR algorithm is resident in the on-board GPU memory, hence the CPU plays little to no role in the computation. However, the CPU is required for inter-block communication, but the current implementation does not have support for MPI and so is only suitable for small cases.

The case profiled is a TGV, $p = 4$, with 8^3 elements run on a Titan Xp. Using the profiler, `pgprof`, the runtime for one complete explicit time step was found and is shown in Table 3.2.

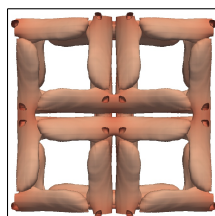
It is clear that the continual conversion to or from the primitive variables has a noticeable impact on the computational time. In this case, the method that required the fewest number of conversions, method C (conservative variables using the product rule to calculate the gradient of the primitives), was the fastest. Method C gave a 12.3% reduction in computational time, which, all other things being equal, makes this a reasonable optimisation strategy to consider. Method D on the other hand, (conservative variables with E swapped for p), was slower as there are even more conversions required than in the base primitive method.

3.5.2 Effect of Working Precision

Finally, a brief numerical investigation on the impact of varying the working precision of the calculation when applied to turbulent and transitional flows. For this, we will limit our comparison to methods A and B, as it has previously been shown that the largest difference was between these two methods. The results of tests are shown in Fig. 3.7, where 32-bit floating-point (fp32) and 64-bit floating-point (fp64) precisions were used. Initially, the preprocessor ran to the same arithmetic accuracy as the solver, but inaccuracies caused a loss of preservation. This will be explored further in a later chapters.

The difference between precisions is made clearer in Fig. 3.8. It is apparent that the difference is most visible for $t > 10$. By this time the flow field has transitioned and is dominated by small scale vortex interaction. However, it is not solely due to high frequencies in the solution that the effect is more pronounced, but also due to the decay. As time proceeds, the range of solution reduces. For example the absolute velocity range goes from $[0, 1]$ to $[0, 0.52]$ from $t = 0$ to $t = 20$. Therefore, as the error in terms like the Jacobian remain constant, the precision error will have a greater impact when the solution range is smaller.

Figure 3.8 goes on to show that larger differences due to precision are experienced at lower Mach number. It is believed that this is because at lower Mach number the



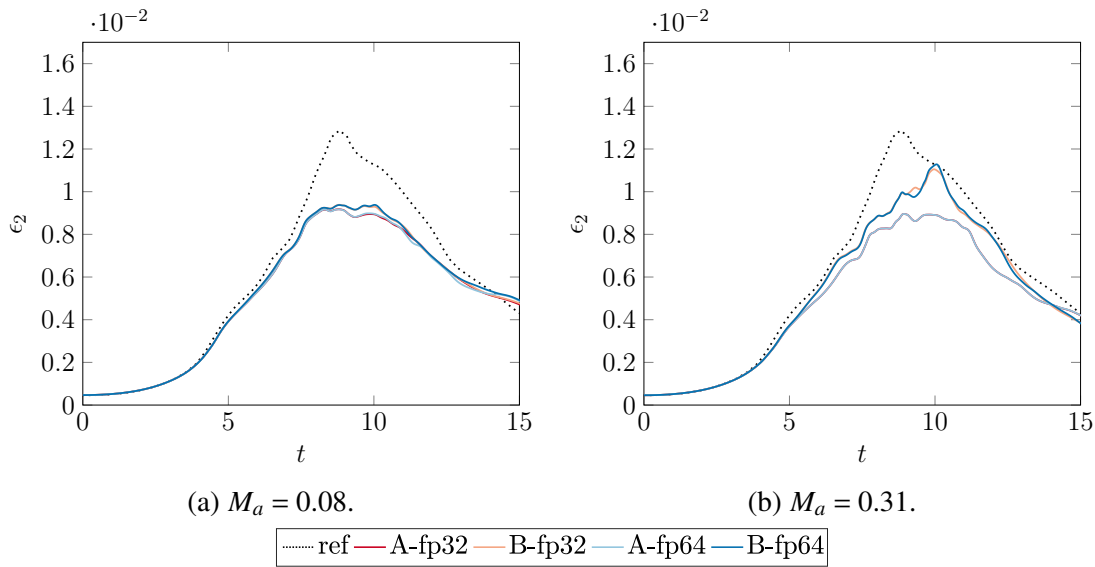


Fig. 3.7 Enstrophy of the Taylor–Green Vortex with $R_e = 1600$, $p = 4$ and 80^3 degrees of freedom for storage methods A and B in 32 (fp32) and 64 (fp64) bit precision.

scheme is more sensitive to numerical aliasing occurring in the interpolation. As the Mach number is increased and the physics begins to exhibit non-constant ρ , the small floating-point errors in variables are more compatible with the physics and hence its effect appears to be lessened.

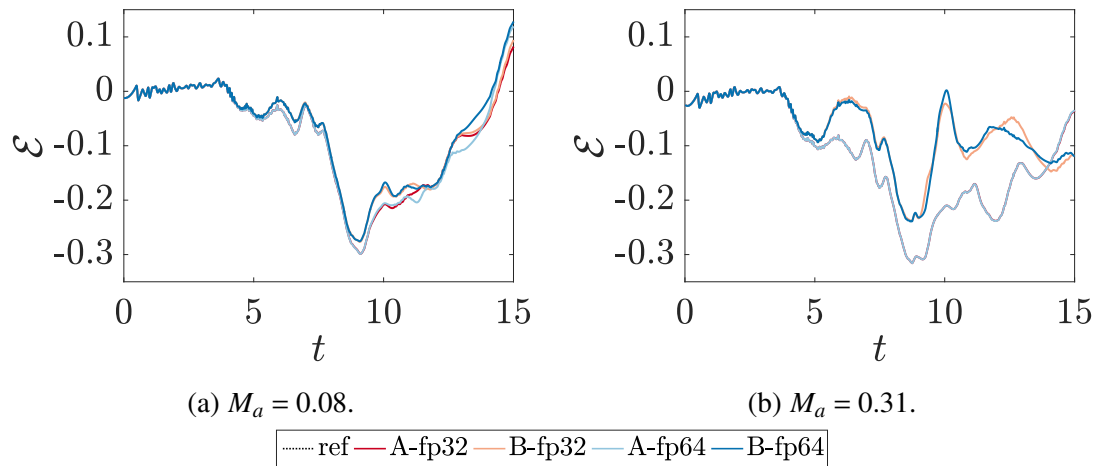


Fig. 3.8 Enstrophy error of the Taylor–Green Vortex with $R_e = 1600$, $p = 4$ and 80^3 degrees of freedom for storage methods A and B in 32 (fp32) and 64 (fp64) bit precision.

These results show that low Mach compressible flow are only negligibly affected by working precision when considering 32 and 64 bit precisions. However, in the calculation of global statistic care must be taken to the relative error of single precision compared to double. For example single precision has an epsilon of order 10^{-7} compared to 10^{-16} . This is the largest value where $(1 \pm \epsilon) = 1$ is true. Therefore, in calculating globally

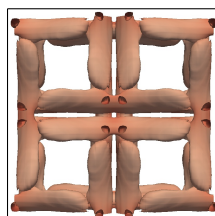
averaged properties care has to be taken as the accumulator can saturate. To mitigate this here, it was sufficient to have an accumulator over solution points in each cell and then a final accumulator over all cells in the domain.

3.6 Conclusions

Through this work, we sought to challenge two dogmas in CFD. The first was the use of primitive variables to construct flux functions. We compared the use of primitives with conserved variables and showed numerically that a noticeable difference can be seen in methods that use reconstruction. Analysis using Taylor's theorem showed that this is primarily due to the flux function order and as order increases, the difference found will become increasingly important.

An investigation into the effects of these choices on the method for constructing the viscous flux was also performed. When reconstructing from the conserved variables there are two potential methods, where either primitives are used as an intermediary or the product rule is used. Analysis showed a clear difference between the approaches, however in numerical investigations, these were limited due to the typically small magnitude of viscous terms. However, a larger impact will likely be present in flows with large gradients, such as in two-phase flow.

A final investigation was performed that aimed to challenge the dogma that double precision is important in CFD calculations. Numerical investigations on transitional flows showed that differences between single and double precision were negligible. However, differences become more noticeable over long-time integration, which can be attributed to two things. First, that in single-precision error accumulation will become apparent more quickly under explicit temporal integration due to larger relative error. Secondly, in this case, the range of the variable fields reduces with time due to dissipation, and so as time proceeds the absolute error from early on will get relatively larger. These points also highlight some key considerations when reducing the precision, due to the increased relative error of lower precision care has to be taken in accumulation. For example, when calculating globally averaged statistics or in statistics calculated through many operations.



Chapter 4

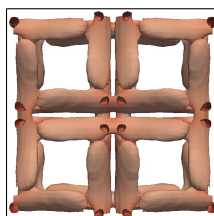
Flux Reconstruction for First-Order PDEs on Stretched Grids

4.1 Introduction

First order PDEs are ubiquitous in the physical sciences, with first order spatial terms occurring in Euler's equations, Maxwell's equations, and the Cauchy momentum equation. Commonly, these terms represent the spatial movement of information through the system, and therefore the accuracy of their computation is key, as the error introduced by these terms will propagate throughout the domain. Furthermore, it is common that the scale of the contribution of these terms in engineering equations dominates the solution.

The main advantage of high-order FR is its unstructured nature that makes parallelism straightforward owing to relatively few points in the algorithm that require inter-element communication. Solving real engineering problems tends to result in poorer quality meshes than canonical cases, for example Fig. 4.1 shows the trailing edge of a turbine blade. In this case, high levels of cell stretching, expansion, and skewness can be seen. It is also likely to have some cells around the tip of the trailing edge with flow incident at large angles. Hence, the performance characterisation of FR on poorer grids for first order PDEs is important, as knowledge of FR's behaviour can help to inform meshing requirements.

The analytical understanding of Flux Reconstruction has been explored to a large extent in the work of Vincent et al. [161], Jameson et al. [75], and Castonguay et al. [33], where the stability of linear advection, advection-diffusion, and non-linear problems were presented. The key findings were the energy stability of FR on linear problems, and the condition for energy stability on non-linear problems. In addition, by investigating the dispersion and dissipation characteristics of FR, the existence of superconvergence after temporal integration and the corresponding CFL limits were found. This work



was limited to one dimension — although still applicable, the investigation of the exact behaviour of FR in higher dimensions has been limited, such as that of Williams and Jameson [172] and Sheshadri and Jameson [127]. This work focused primarily on the proof of the Sobolev type energy stability in 2D in a manner similar to that of Hesthaven and Warburton [60], alongside some numerical studies performed for validation. In the original work of Huynh [65], the dispersion and dissipation was rudimentarily investigated in 2D, but without clear insight gained.

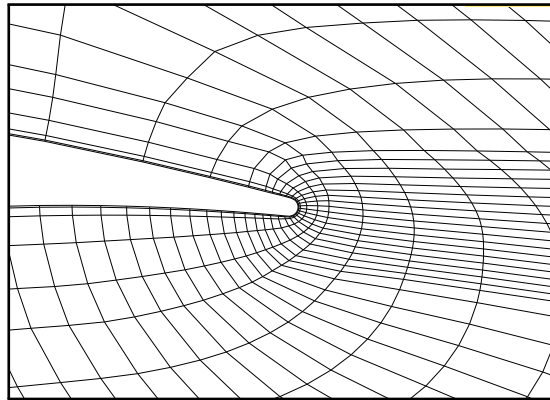


Fig. 4.1 Two-dimensional mesh slice of the trailing edge of a turbine blade, showing how the grid in real calculations can undergo large expansion and skewing, where every tenth node is shown. (Mesh kindly reproduced with the permission of Bryn Ubald).

Therefore, the objective here is to extend the theoretical understanding of FR with an extension to the one-dimensional analytical work of Vincent et al. [161] and Trojak et al. [149]. This extension will be shown for a two-dimensional case on quadrilaterals with rectilinear mesh stretching, but could also be performed on higher dimensional hypercubes. From the basis of this more general von Neumann analysis, the behaviour of FR on linearly mapped meshes can be explored. The investigation has been restricted to linear transformation as these are of key importance for complex industrial simulations due to their fundamental nature. For example, they occur in meshes where mesh generators have simply tessellated elements to fill the domain. Therefore, understanding their character is key, however, attention should be drawn to some recent work that has numerically investigated curved meshes [103, 176].

4.2 Two-Dimensional Von Neumann Analysis

The procedure for investigating the dispersion and dissipation properties of finite element methods has been laid out in some detail by Huynh [65], Hesthaven and Warburton [60], and Vincent et al. [161]. It is broadly classified as a von Neumann analysis. The procedure was, however, mainly performed in 1D, with critical insight into the analytical

performance of FR when applied to more realistic problems not considered. Extension of the analysis to higher dimension domains was performed by Lele [89] for various finite difference schemes. This did, however, avoid the increased complexity of finite element von Neumann analysis. To begin the extension we introduce the 2D linear advection equation:

$$\frac{\partial u}{\partial t} + \nabla \cdot \mathbf{F} = 0 \quad (4.1)$$

$$\mathbf{F} = \begin{bmatrix} f \\ g \end{bmatrix} = u\mathbf{a} = \begin{bmatrix} au \\ bu \end{bmatrix} \quad (4.2)$$

Flux Reconstruction then uses the superposition of the discontinuous and corrected flux divergence, meaning Eq. (4.2) can be rewritten as:

$$\frac{\partial \mathbf{u}_{i,j}}{\partial t} = -\nabla \cdot \mathbf{F}_{i,j}^{\delta D} - \nabla \cdot \mathbf{F}_{i,j}^{\delta C} \quad (4.3)$$

Taking the following definition of the Jacobian, the computational-physical domain transformation can be defined:

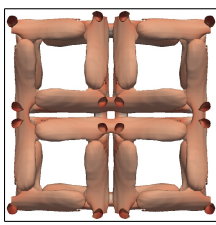
$$\mathbf{G} = \begin{bmatrix} \frac{\partial x}{\partial \xi} & \frac{\partial y}{\partial \xi} \\ \frac{\partial x}{\partial \eta} & \frac{\partial y}{\partial \eta} \end{bmatrix} = \begin{bmatrix} G_1 & G_2 \\ G_3 & G_4 \end{bmatrix} \quad \text{and} \quad J = |\mathbf{G}| \quad (4.4)$$

$$u = J^{-1} \hat{u}, \quad \mathbf{F} = J^{-1} \mathbf{G} \hat{\mathbf{F}}, \quad \nabla \cdot \mathbf{F} = J^{-1} \hat{\nabla} \cdot \hat{\mathbf{F}} \quad (4.5)$$

where $\hat{\nabla}$ is used to mean $[\frac{\partial}{\partial \xi}, \frac{\partial}{\partial \eta}]^T$ in 2D. A further restriction will be made that grid transformations are purely rectilinear, *i.e.* $G_2 = G_3 = 0$. This is to reduce the number of dependent variables, while still allowing an important form of grid deformation to be investigated. From the work of Huynh [65], Castonguay [30], and Sheshadri et al. [128], Eq. (4.2) is written in two dimensions as:

$$\hat{\nabla} \cdot \hat{\mathbf{F}}^{\delta D} = \sum_{i=0}^p \sum_{j=0}^p \hat{f}_{i,j}^{\delta D} \frac{dl_i(\xi)}{d\xi} l_j(\eta) + \sum_{i=0}^p \sum_{j=0}^p \hat{g}_{i,j}^{\delta D} \frac{dl_j(\eta)}{d\eta} l_i(\xi) \quad (4.6)$$

$$\begin{aligned} \hat{\nabla} \cdot \hat{\mathbf{F}}^{\delta C} = \sum_{i=0}^p \left((\hat{J}_{L,i}^{\delta I} - \hat{J}_{L,i}^{\delta D}) \frac{dh_{L,i}}{d\xi} + (\hat{J}_{R,i}^{\delta I} - \hat{J}_{R,i}^{\delta D}) \frac{dh_{R,i}}{d\xi} + \right. \\ \left. (\hat{g}_{B,i}^{\delta I} - \hat{g}_{B,i}^{\delta D}) \frac{dh_{B,i}}{d\eta} + (\hat{g}_{T,i}^{\delta I} - \hat{g}_{T,i}^{\delta D}) \frac{dh_{T,i}}{d\eta} \right) \end{aligned} \quad (4.7)$$



where L , R , B , and T subscripts mean left, right, bottom, and top respectively. Equation (4.6) may then be converted into a matrix form, such that:

$$\hat{\nabla} \cdot \hat{\mathbf{F}}^{\delta D} = \mathbf{D}_\xi \hat{\mathbf{f}}_{i,j}^\delta + \mathbf{D}_\eta \hat{\mathbf{g}}_{i,j}^\delta \quad (4.8)$$

$$\nabla \cdot \mathbf{F}^{\delta D} = G_{1,i,j}^{-1} \mathbf{D}_\xi \mathbf{f}_{i,j}^\delta + G_{4,i,j}^{-1} \mathbf{D}_\eta \mathbf{g}_{i,j}^\delta \quad (4.9)$$

To apply the correction function, we need to calculate the interface values around the element. For the case of generalised central/upwinding with upwinding ratio α , the common interface fluxes may be written as:

$$G_{4,i,j}^{-1} \hat{f}_L^{\delta I} = a(\alpha G_{4,i-1,j}^{-1} \hat{u}_{i-1,j,R}^\delta + (1-\alpha) G_{4,i,j}^{-1} \hat{u}_{i,j,L}^\delta) \quad (4.10)$$

$$G_{4,i,j}^{-1} \hat{f}_R^{\delta I} = a(\alpha G_{4,i,j}^{-1} \hat{u}_{i,j,R}^\delta + (1-\alpha) G_{4,i+1,j}^{-1} \hat{u}_{i+1,j,L}^\delta) \quad (4.11)$$

$$G_{1,i,j}^{-1} \hat{g}_B^{\delta I} = b(\alpha G_{1,i,j-1}^{-1} \hat{u}_{i,j-1,T}^\delta + (1-\alpha) G_{1,i,j}^{-1} \hat{u}_{i,j,B}^\delta) \quad (4.12)$$

$$G_{1,i,j}^{-1} \hat{g}_T^{\delta I} = b(\alpha G_{1,i,j}^{-1} \hat{u}_{i,j,T}^\delta + (1-\alpha) G_{1,i,j+1}^{-1} \hat{u}_{i,j+1,B}^\delta) \quad (4.13)$$

where $\alpha = 1$ gives rise to upwinding and $\alpha = 0.5$ produces central difference. Hence, the divergence correction can be written as:

$$\begin{aligned} \hat{\nabla} \cdot \hat{\mathbf{F}}_{i,j}^{\delta C} = & \frac{a\alpha}{G_{4,i,j}^{-1}} \left(G_{4,i-1,j}^{-1} \mathbf{h}_L \mathbf{l}_R^T \hat{\mathbf{u}}_{i-1,j}^\delta - G_{4,i,j}^{-1} \mathbf{h}_L \mathbf{l}_L^T \hat{\mathbf{u}}_{i,j}^\delta \right) + \\ & \frac{a(1-\alpha)}{G_{4,i,j}^{-1}} \left(G_{4,i+1,j}^{-1} \mathbf{h}_R \mathbf{l}_L^T \hat{\mathbf{u}}_{i+1,j}^\delta - G_{4,i,j}^{-1} \mathbf{h}_R \mathbf{l}_R^T \hat{\mathbf{u}}_{i,j}^\delta \right) + \\ & \frac{b\alpha}{G_{1,i,j}^{-1}} \left(G_{1,i,j-1}^{-1} \mathbf{h}_B \mathbf{l}_T^T \hat{\mathbf{u}}_{i,j-1}^\delta - G_{1,i,j}^{-1} \mathbf{h}_B \mathbf{l}_B^T \hat{\mathbf{u}}_{i,j}^\delta \right) + \\ & \frac{b(1-\alpha)}{G_{1,i,j}^{-1}} \left(G_{1,i,j+1}^{-1} \mathbf{h}_T \mathbf{l}_B^T \hat{\mathbf{u}}_{i,j+1}^\delta - G_{1,i,j}^{-1} \mathbf{h}_T \mathbf{l}_T^T \hat{\mathbf{u}}_{i,j}^\delta \right) \end{aligned} \quad (4.14)$$

where \mathbf{h}_L is the *gradient* of the left correction function at the solution points and again \mathbf{l}_L are the values of the polynomial basis at the left interface and so on for R , T , and B . Therefore, by grouping terms by their cell indexing and transforming each term into the physical domain:

$$\begin{aligned} \frac{\partial \mathbf{u}_{i,j}}{\partial t} = & -a G_{1,i,j}^{-1} (\mathbf{C}_L \mathbf{u}_{i-1,j}^\delta + \mathbf{C}_{0\xi} \mathbf{u}_{i,j}^\delta + \mathbf{C}_R \mathbf{u}_{i+1,j}^\delta) \\ & -b G_{4,i,j}^{-1} (\mathbf{C}_B \mathbf{u}_{i,j-1}^\delta + \mathbf{C}_{0\eta} \mathbf{u}_{i,j}^\delta + \mathbf{C}_T \mathbf{u}_{i,j+1}^\delta) \end{aligned} \quad (4.15)$$

where

$$\mathbf{C}_L = \alpha \mathbf{h}_L \mathbf{l}_R^T \quad \mathbf{C}_R = (1 - \alpha) \mathbf{h}_R \mathbf{l}_L^T \quad \mathbf{C}_{0\xi} = \mathbf{D}_\xi - \alpha \mathbf{h}_L \mathbf{l}_L^T - (1 - \alpha) \mathbf{h}_R \mathbf{l}_R^T \quad (4.16)$$

$$\mathbf{C}_B = \alpha \mathbf{h}_B \mathbf{l}_T^T \quad \mathbf{C}_T = (1 - \alpha) \mathbf{h}_T \mathbf{l}_B^T \quad \mathbf{C}_{0\eta} = \mathbf{D}_\eta - \alpha \mathbf{h}_B \mathbf{l}_B^T - (1 - \alpha) \mathbf{h}_T \mathbf{l}_T^T \quad (4.17)$$

Finally, the frequency response of the system is the key property of interest, and, importantly to engineers and technicians, how the cell's orientation relative to an oncoming wave affects performance. Therefore, we impose a trial solution of the form:

$$u(x, y; t) = \exp(ik(x \cos \theta + y \sin \theta - ct)) \quad (4.18)$$

and by substitution into Eq. (4.2), the advection velocity, \mathbf{a} , can be found, which is shown schematically in Fig. 4.2a.

$$\mathbf{a} = \begin{bmatrix} a \\ b \end{bmatrix} = \begin{bmatrix} \cos \theta \\ \sin \theta \end{bmatrix} \quad (4.19)$$

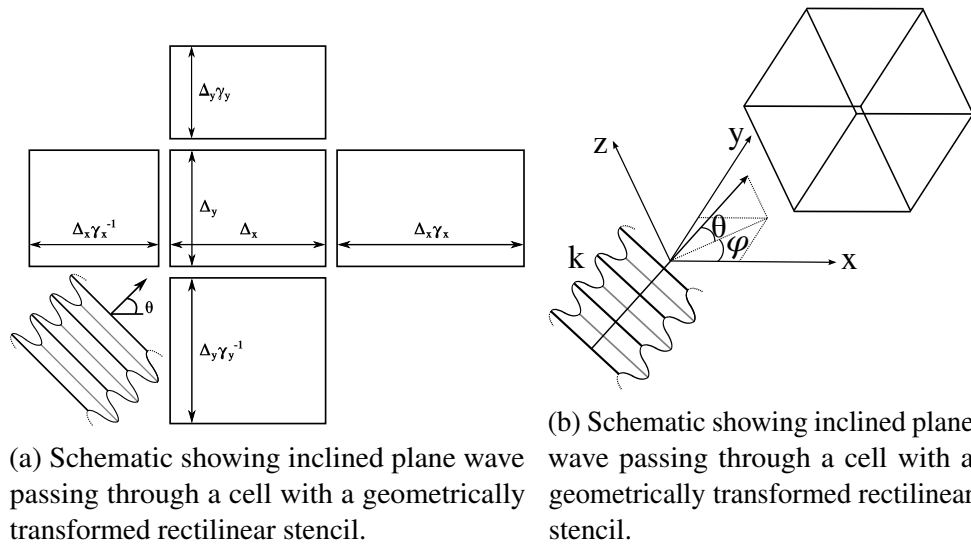
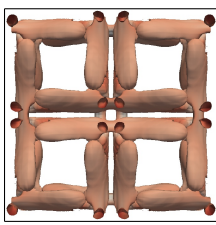


Fig. 4.2 Linear advection schematic for two and three dimensions.

The plane wave can then be projected into the computational domain and discretised as:

$$\mathbf{u}_{i,j} = \mathbf{v} \exp\left(ik\left((0.5(\xi + 1)\delta_i + x_i) \cos \theta + (0.5(\eta + 1)\delta_j + y_j) \sin \theta - ct\right)\right) \quad (4.20)$$



where, for brevity, $\delta_i = x_i - x_{i-1}$ and $\delta_j = y_j - y_{j-1}$ are defined. Inserting Eq. (4.20) into Eq. (4.15), an eigenvalue problem can be obtained as:

$$\begin{aligned} -ikc(k)\mathbf{v} = & -G_{1,i,j}^{-1} \cos \theta \left(\mathbf{C}_L \exp(-ik\delta_{i-1} \cos \theta) + \mathbf{C}_{0\xi} + \mathbf{C}_R \exp(ik\delta_i \cos \theta) \right) \mathbf{v} \\ & - G_{4,i,j}^{-1} \sin \theta \left(\mathbf{C}_B \exp(-ik\delta_{j-1} \sin \theta) + \mathbf{C}_{0\eta} + \mathbf{C}_T \exp(ik\delta_j \sin \theta) \right) \mathbf{v} \end{aligned} \quad (4.21)$$

where $\Re k(c(k)) = \Re(\omega)$ and $\Im(kc(k)) = \Im(\omega)$ are the dispersion and dissipation, respectively, and ω is the modified angular frequency response of the system. By studying the trial solution of Eq. (4.18) it can be understood that if $\Im(\omega) > 0$ then the amplitude of the wave will increase and vice versa. Furthermore, if $\Re(\omega) \neq k$ then a wave will move at a different speed compared to the other waves inside the packet, causing the quality of the interpolation to be affected as the solution is advanced in time as the components that make it up move at different speeds. An important point is the difference between phase velocity ω/k and group velocity $d\omega/dk$. Phase velocity is the speed of a wave in a packet of waves. Group velocity is the speed of the packet. Therefore, changes to $d\omega/dk$ can be thought of as a change to the physics due to the numerical method.

Equation (4.21) can alternatively be cast in the form of an update equation. If initially Eq. (4.15) is combined with Eq. (4.20), then a new matrix, $\mathbf{Q}_{i,j}$, can be defined:

$$\frac{\partial \mathbf{u}_{i,j}}{\partial t} = \mathbf{Q}_{i,j} \mathbf{u}_{i,j} \quad (4.22)$$

$$\begin{aligned} \mathbf{Q}_{i,j} = & -G_{1,i,j}^{-1} \cos \theta \left(\mathbf{C}_L \exp(-ik\delta_{i-1} \cos \theta) + \mathbf{C}_{0\xi} + \mathbf{C}_R \exp(ik\delta_i \cos \theta) \right) \\ & - G_{4,i,j}^{-1} \sin \theta \left(\mathbf{C}_B \exp(-ik\delta_{j-1} \sin \theta) + \mathbf{C}_{0\eta} + \mathbf{C}_T \exp(ik\delta_j \sin \theta) \right) \end{aligned} \quad (4.23)$$

This definition of the semi-discrete FR operator, \mathbf{Q} , can then be used to form what is called the update equation by imposing some temporal discretisation. As such, it can be written that:

$$\mathbf{u}_{i,j}^{n+1} = \mathbf{R}(\mathbf{Q}_{i,j}) \mathbf{u}_{i,j}^n \quad (4.24)$$

$$\mathbf{R}_{33} = \mathbf{I} + \frac{\tau \mathbf{Q}_{i,j}}{1!} + \frac{(\tau \mathbf{Q}_{i,j})^2}{2!} + \frac{(\tau \mathbf{Q}_{i,j})^3}{3!} \quad (4.25)$$

where the superscript denotes the time level, and the update matrix is \mathbf{R} . Shown here is also an example definition for \mathbf{R} for a 3-step 3rd-order Runge-Kutta time integration scheme. Finally, in keeping with von Neumann's theorems [68, 86] and Banach's fixed point theorem [83], the spectral radius of \mathbf{R} has to be less than or equal to 1 for stability. $\rho(\mathbf{R}) \leq 1 \forall k \in \mathbb{R}$.

In recent works by Vermeire et al. [159] and Trojak et al. [150], the Fourier analysis was extended by fully discretising the equation. This is performed by taking Eq. (4.24) and again applying Eq. (4.18). This results in:

$$\exp(-ik(c-1)\tau)\mathbf{v} = \lambda\mathbf{v} = \exp(ik\tau)\mathbf{R}(k, \tau)\mathbf{v} \quad (4.26)$$

where the time step from n to $n+1$ is τ . Hence, rearranging for the modified wave speed:

$$c = \frac{i\log(\lambda)}{k\tau} + 1 \quad (4.27)$$

where λ are the eigenvalues of $\exp(ik\tau)\mathbf{R}$. The advantage of this further analysis is that it gives the dispersion and dissipation relations of the full scheme as would be experienced when applied as implicit LES.

The results of this section can then be extended to n -dimensions. The analysis can broadly be repeated but is beyond the scope of this work. But, importantly, the prescribed solution could be taken as:

$$u = \exp(ik(x\cos\phi\cos\theta + y\cos\phi\sin\theta + z\sin\phi - ct)) \quad (4.28)$$

where the angles are as shown in Fig. 4.2b, and hence the 3D convective velocities for linear advection are:

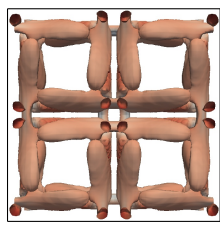
$$\mathbf{a} = \begin{bmatrix} \cos\phi\cos\theta \\ \cos\phi\sin\theta \\ \sin\phi \end{bmatrix} \quad (4.29)$$

4.3 Two-Dimensional Convergence Analysis

The techniques applied to the linear advection equation of Section 4.2 can be further extended to examine the effects of the grid and wave angle upon the error convergence. This method was initially presented for 1D uniform grids in FR by Astana et al. [11], and for fully-discrete equations by Trojak et al. [150]. Here we will extend the analysis to include stretched grids in two dimensions. To begin, we will diagonalise the semi-discrete FR operator matrix as:

$$\mathbf{Q} = \mathbf{W}\mathbf{T}\mathbf{W}^{-1} = \mathbf{W}i\mathbf{k}\mathbf{\Lambda}\mathbf{W}^{-1} \quad (4.30)$$

Here \mathbf{W} is an eigenvector matrix and $\mathbf{\Gamma}$ is diagonal eigenvalue matrix. The matrix $\mathbf{\Lambda}$ is then a normalised form of the eigenvalue matrix, used to simplify later notation. This diagonalisation may then be exponentially integrated in order to advance the solution



continuously in time such that:

$$\mathbf{u}_{i,j}^\delta(t) = \exp(ct\mathbf{Q})\mathbf{u}(0) = \mathbf{W}\exp(ikct\mathbf{\Lambda})\mathbf{W}^{-1}\mathbf{u}_j(0) \quad (4.31)$$

Here the definition of a matrix exponential has been used with $\mathbf{W}^{-1}\mathbf{W} = \mathbf{I}$ to simplify the form. The initial condition is then required and is defined as:

$$\mathbf{u}_{i,j}(0) = \exp(ik(x_j \cos(\theta) + y_j \sin(\theta)))\mathbf{W}\boldsymbol{\beta} \quad (4.32)$$

For convenience we will define the solution shift based on the cell location as:

$$u_{c,i,j} = \exp(ik(x_i \cos(\theta) + y_j \sin(\theta))) \quad (4.33)$$

The initial condition may then be substituted into Eq. (4.31), leading to:

$$\mathbf{u}_{i,j}^\delta(t) = u_{c,i,j}\mathbf{W}\exp(-ikct\mathbf{\Lambda})\boldsymbol{\beta} = u_{c,i,j}\sum_{n=0}^{p^2}\exp(-ikct\lambda_n)\beta_n\mathbf{w}_n \quad (4.34)$$

Here \mathbf{w}_n is the n^{th} eigenvector taken from \mathbf{W} and β_n is the n^{th} coefficient taken from $\boldsymbol{\beta}$. The semi-discrete error may then be calculated by analytically evolving the discrete solution using exponential integration. Hence, the analytical solution in time is:

$$\mathbf{u}_{i,j}(t) = u_{c,i,j}\exp(-ikct)\mathbf{u}_{i,j}(0) = u_{c,i,j}\exp(-ikct)\sum_{n=0}^{p^2}\beta_n\mathbf{w}_{Q,n} \quad (4.35)$$

Therefore, the semi-discrete error can be formed by subtracting Eq. (4.35) from Eq. (4.34) as:

$$\begin{aligned} \mathbf{e}_{i,j}(t,k) &= \mathbf{u}_{i,j}^\delta(t,k) - \mathbf{u}_{i,j}(t,k) \\ &= u_{c,i,j}\exp(-ikct)\sum_{n=0}^{p^2}\left(\exp(ikct(\lambda_n + 1)) - 1\right)\beta_n\mathbf{w}_{Q,n} \end{aligned} \quad (4.36)$$

This measure of the semi-discrete error can then inform the error changing with grid and wavenumber, both of which were analytically investigated for 1D NDG via FR by Astana et al. [11]. Subsequently, the error may form a rate of convergence, which for grid spacing is then:

$$r_h(t,k) = \frac{\log(\|\mathbf{e}_{i,j}(t,k,J_1)\|_2) - \log(\|\mathbf{e}_{i,j}(t,k,J_2)\|_2)}{\log(J_1) - \log(J_2)} \quad (4.37)$$

Here J_1 and J_2 are the Jacobians for two difference grid spacings. The rate of convergence with wavenumber is similarly defined as:

$$r_k(t, J) = \frac{\log(\|\mathbf{e}_{i,j}(t, k_1, J)\|_2) - \log(\|\mathbf{e}_{i,j}(t, k_2, J)\|_2)}{\log(k_1) - \log(k_2)}. \quad (4.38)$$

4.4 Analytical Findings

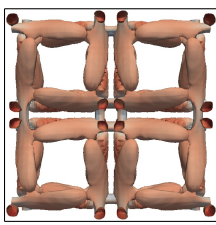
The analytical methods presented in Sections 4.2 & 4.3 allow us to investigate many properties of FR, however from Eq. (4.23-4.25) it can be seen that the functional space of \mathbf{Q} is 8 dimensional, leading to the functional space of $\rho(\mathbf{R})$ being 9 dimensional $(\tau, \gamma_x, \gamma_y, \Delta_x, \Delta_y, k, \theta, \iota, p)$. Therefore, we need to restrict our investigation to some key results relating to grid deformation. Firstly, understanding the dispersion and dissipation ($\Re(\omega)$ & $\Im(\omega)$) in 2D for both uniform and stretched grids will be important. Secondly, we wish to briefly understand how higher dimensionality and grid deformations affect the temporal stability of FR through evaluation of the CFL limits [40]. Then we will go on to study the effect of grid deformation and incident angle on the rate of convergence. We will finish with the analytic study with the evaluation of the fully-discrete dispersion and dissipation relations. Throughout this investigation we will also look to understand the effect of the correction function on these properties.

4.4.1 Review of 1D Grid Expansion

Before commencing with the Fourier/von Neumann analysis in 2D, a brief review of the behaviour exhibited in one dimension is given. Figure 4.3 shows the results for upwinded NDG correction functions at various orders of accuracy.

The results are separated into the real and imaginary parts of $\hat{\omega}$, where they represent dispersion and dissipation respectively. Ideally $\Re(\hat{\omega}) = 1$ and $\Im(\hat{\omega}) = 0$. However, the numerical discretisation will cause deviation from the ideal dispersion, while the interface upwinding here will cause dissipation. In [151] a non-conservative Jacobian definition was used that resulted in variation of the numerical characteristics as the grid is deformed. However, if a conservative Jacobian is properly applied, then grid stretching has no impact upon dispersion and dissipation of FR other than a change in the Nyquist wavenumber. For a geometrically deformed grid the Nyquist wavenumber will be:

$$k_{\text{nyq}} = \frac{1}{2\gamma(p+1)} \quad (4.39)$$



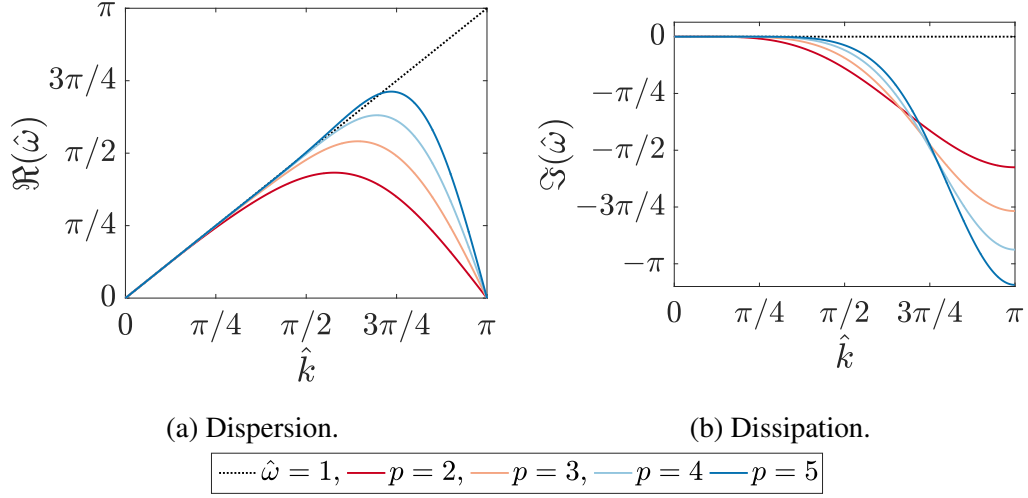


Fig. 4.3 Upwinded 1D FR, for various orders with NDG correction functions.

This raises a question for linear systems in 2D, as the grid is stretched in x and y , what is the impact? And what implications will any effects have on the practical application of the scheme?

4.4.2 Effect of Grid on Semi-Discrete Dispersion and Dissipation

For the higher dimensional case, we begin by considering the dispersion and dissipation on a uniform grid in two dimensions as order is varied. We are concerned here with the primary mode — as FR has multiple modes, this is the one that physically represents the wave. Although, as was found by Asthana et al. [11], this may not be how the energy distributes itself. We identify the physical mode as that which has the largest contribution to the energy at very low, well resolved, wavenumbers.

For this investigation into the dispersion and dissipation characteristics of FR, we wish to make a note of the Nyquist frequency of the elements. The Nyquist frequency has a dependency on the expansion ratio. This is found from the harmonic mean of the 1D Nyquist frequencies, then normalised by the adjacent element size at that angle. Hence, the normalised wavenumber is then:

$$\hat{k} = k/k_{\text{ng}} = \frac{1}{2}k \max\{\cos(\theta), \sin(\theta)\} \left(\frac{1}{p+1}\right) \sqrt{\left(\frac{\cos(\theta)}{\gamma_x}\right)^2 + \left(\frac{\sin(\theta)}{\gamma_y}\right)^2} \quad (4.40)$$

The dispersion and dissipation relations are then shown in Figs. 4.4 and 4.5. It is clear that for all orders FR becomes dispersive as the incidence angle is increased to $\theta = 45^\circ$, but then returns to a dispersion similar to that of $\theta = 0^\circ$ close to $\theta = 45^\circ$. This can be seen by the bowing out of the contour as the angle approaches 45° before receding at

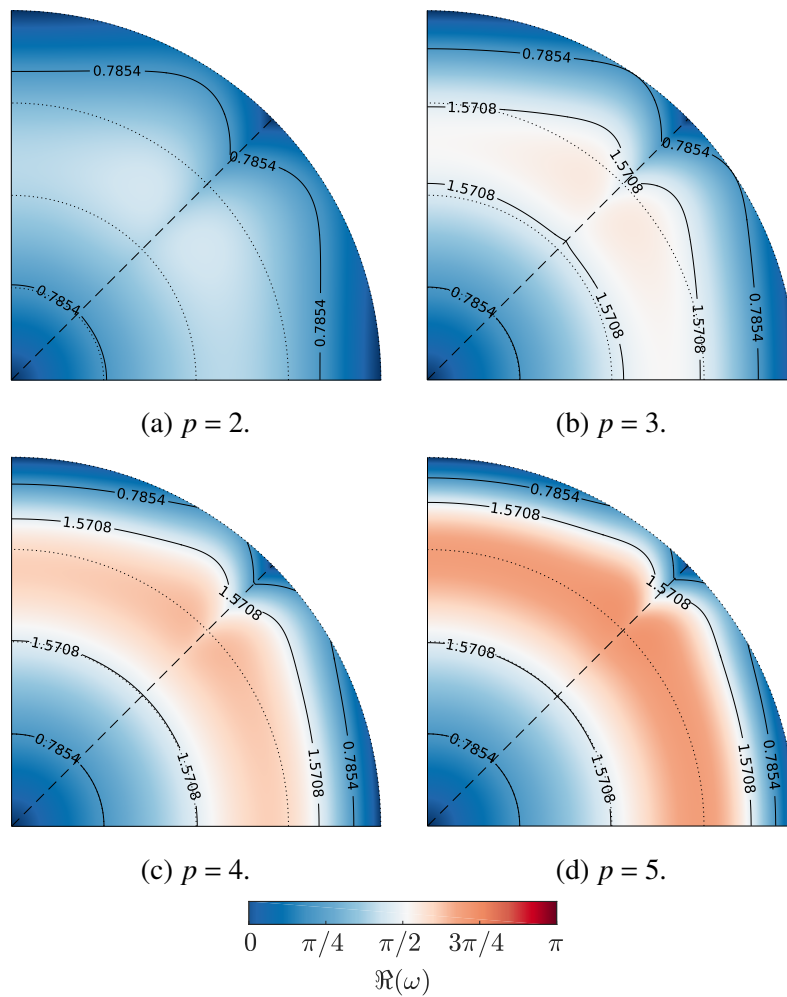
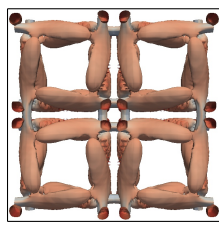


Fig. 4.4 Primary mode dispersion for 2D upwinded FR, with Huynh g_2 corrections, at various orders. Normalised wavenumber as radial distance (markers at $\pi/4$ intervals), and element angle of incidence as azimuthal distance.



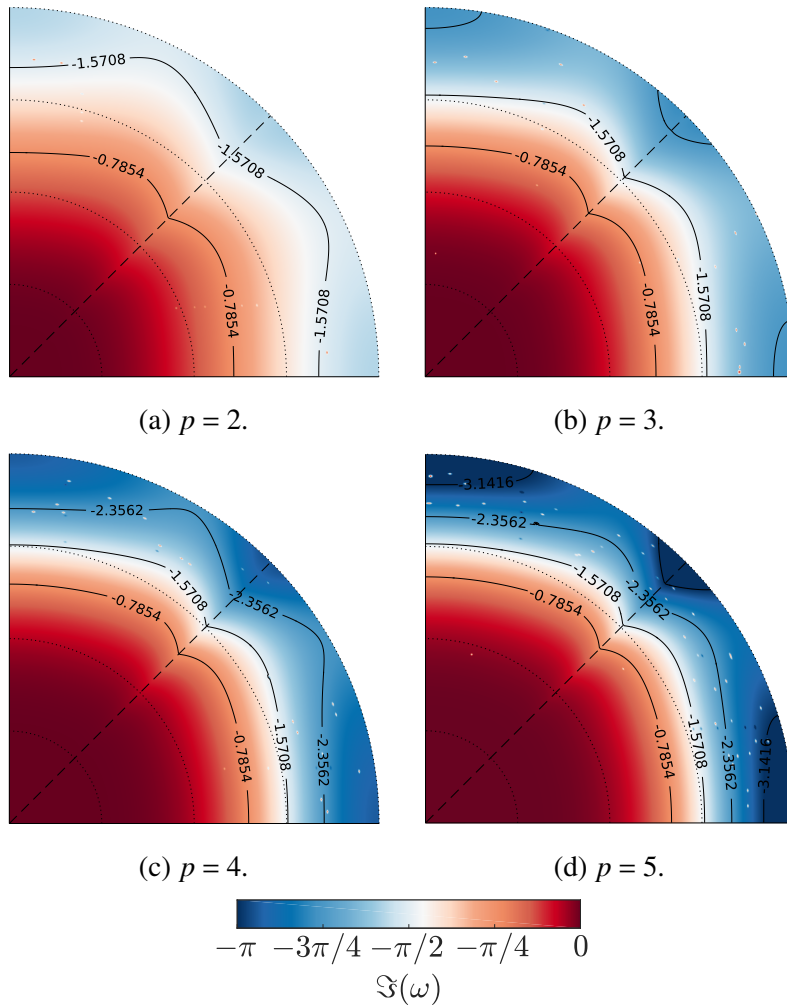


Fig. 4.5 Primary mode dissipation for 2D upwinded FR, with Huynh g_2 corrections, at various orders. Normalised wavenumber as radial distance (markers at $\pi/4$ intervals), and element angle of incidence as azimuthal distance.

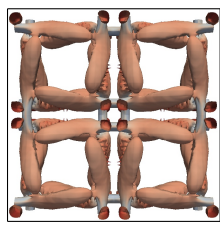
$\theta = 45^\circ$. In the case of dissipation for uniform grids, the dissipation decreases as the angle increases towards a minimum at $\theta \approx 30^\circ$. Once again at $\theta = 45^\circ$, the dissipation returns to the that of a wave at 0° . This behaviour, where both the dispersion and dissipation at $\theta = 0^\circ$ and 45° are the same, is due to the projection of the wave in y being zero in the $\theta = 0^\circ$ case and the projections in x and y being the same in the $\theta = 45^\circ$ case.

Looking at the trends seen as order is varied, order seems to only have a minor impact on the angular spread over which the dispersion and dissipation changes. By comparison with the results of Lele [89], where a similar test is performed for finite and compact difference schemes, FR shows a comparatively smaller change in performance as the angle is varied. It is thought that this is due to the method of polynomial fitting used by FR, namely that this implementation of FR used a tensor grid of monomials *i.e.*, the number of solution points is $(p + 1)^d$ and hence the monomials in the interpolation go from $(\xi^0 \eta^0, \xi^1 \eta^0 \dots \xi^p \eta^p)$. By contrast, finite differences do not include the mixed terms, which will become increasingly dominant as the angle is increased.

Moving on, we then consider the impact of non-uniform grids on the character of the dispersion and dissipation. In particular, we explore the effect of grid expansion and contraction and how they interact if there is expansion orthogonal to contraction. Initially we will focus on Huynh's g_2 correction function, the results of which are summarised in Fig. 4.6.

Let us first focus on the case of $\gamma_x = 1$ and $\gamma_y = 1.1$, as is presented in Figs. 4.6a & 4.6b. In the region of $0^\circ < \theta < 45^\circ$, the impact of the perpendicular grid expansion has been to reduce $\Re(\hat{\omega})$ — most notably near $\theta = 45^\circ$ — as is exemplified in Fig. 4.7a. Conversely, in the range $45^\circ < \theta < 90^\circ$ the grid expansion has caused an increase in dispersion. For the case of $p = 3$ explored here, this action is beneficial, however, as order is increased further this may cause a detrimental dispersion overshoot to develop. Studying the impact on dissipation for the $\gamma_x = 1, \gamma_y = 1.1$ case, associated with the increase in dispersion, there is additional dissipation over the central wavenumbers. This is preceded by a reduction in dissipation near the Nyquist wavenumber. This behaviour is reversed for dissipation in $45^\circ < \theta < 90^\circ$.

We may now apply a contraction perpendicular to an expansion, shown in Figs. 4.6c & 4.6d. The trends that were discussed for the $\gamma_x = 1, \gamma_y = 1.1$ seem to continue when an additional contraction is applied. However, the contraction has served to amplify the effect, which is more clearly visible in Fig. 4.7. It should also be remarked that the dispersion and dissipation at $\theta = 45^\circ$ is no longer the same as in the $\theta = 0^\circ$ case. This is due to the projection into x and y no longer being the same, which can be understood from Eq. 4.40. This equation also indicates the origin of the differences with angle and deformation. That, after projection into x and y , the wave components will have different



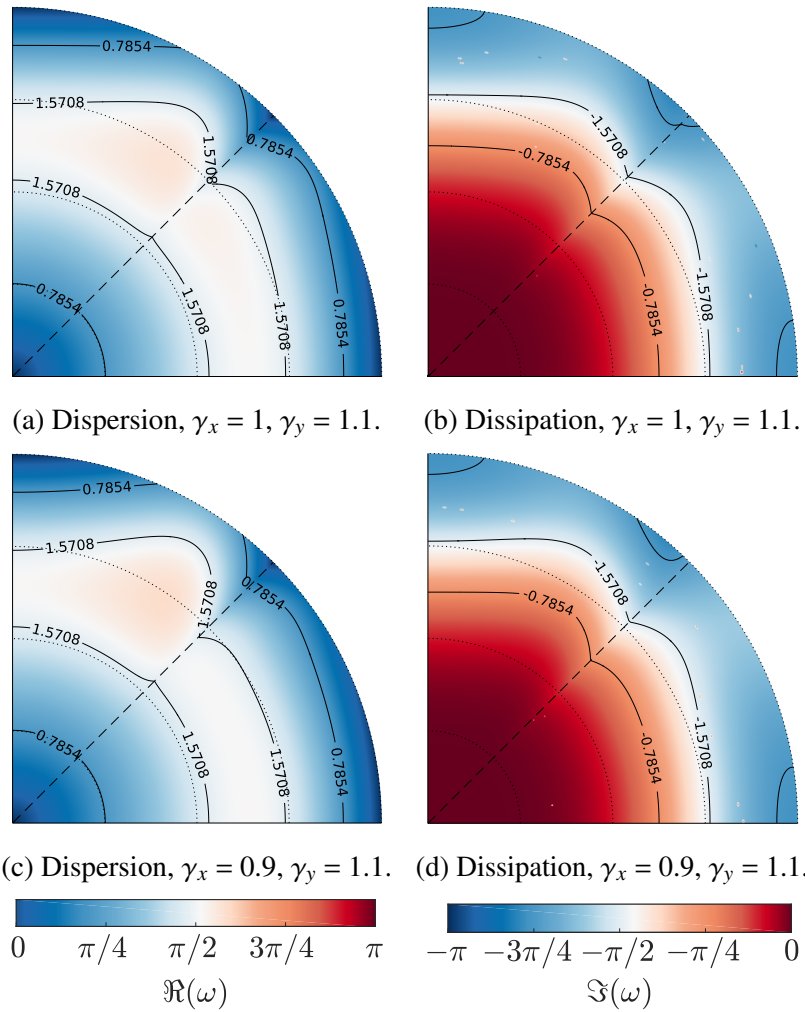


Fig. 4.6 Two dimensional upwinded FR, $p = 3$ with Huynh g_2 corrections, for different grid expansion factors. Normalised wavenumber as radial distance (markers at $\pi/4$ intervals), and element angle of incidence as azimuthal distance.

normalised wavenumbers in the element they are advecting from, and hence different properties.

To understand this further we can think about a given wave decomposed into x and y components initially at $\theta = 45^\circ$. For $\gamma_x = 1$ and $\gamma_y = 1.1$ we may calculate the normalised wavenumber of the projections in the adjacent upwind element, this will aid in understanding how the incoming solution is affected. The y component will be smaller due to the smaller size of the element from which it is advecting. At low wavenumbers this difference will have a small impact on the 2D result as in both x and y we have $\omega \approx 1$. However, at higher wavenumbers the effect will become more pronounced. Larger variations are then seen at other angles due to the projections, even for a uniform grid, having different wavenumbers and hence properties. This also explains why, in Fig. 4.7, we see the effect of grid deformation being approximately symmetric about the uniform case. Furthermore, why an expansion and contraction causes further deviation of the properties.

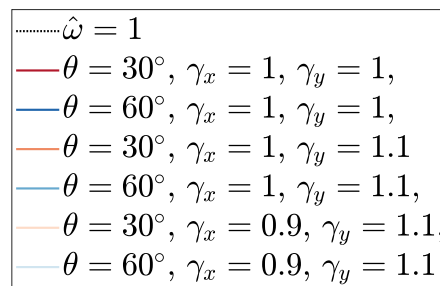
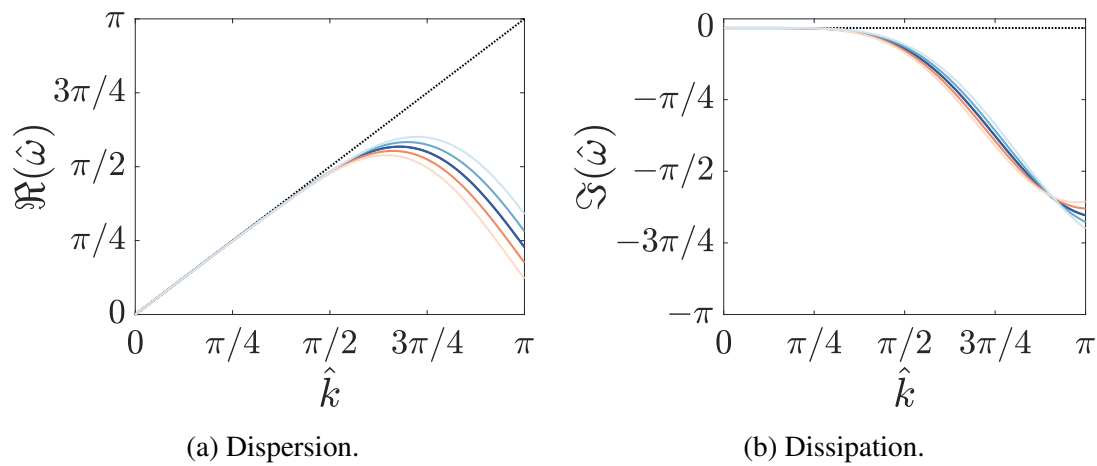
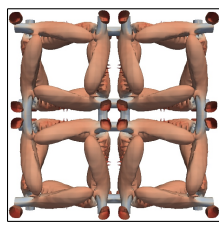


Fig. 4.7 Two dimensional upwinded FR, $p = 3$, with Huynh g_2 corrections at selected incident angles and stretching.

We now vary the correction function and investigate the effect of grid stretching. Here we will apply NDG correction functions, the results of which are presented in Fig. 4.8. When applied to a uniform grid, it is evident that NDG exhibits similar behaviour to Huynh's g_2 as the incidence angle is varied. Nonetheless, the variation of dispersion



and dissipation with θ appears to be smaller for NDG. As the grid is then deformed, the same changes in the properties take place. Yet, due to NDG's dispersion over shoot in the uniform case, stretching has led to the changes in dispersion becoming more significant. The result of the higher dissipation of NDG in the fully discrete form is consistent with the result of the semi-discrete form. However, at high wavenumbers larger variations in dispersion is observed to accompany this high dissipation in the fully discrete form. Hence, it may be expected that NDG will perform better numerically on non-uniform meshes as dispersion errors will undergo more dissipation. This is somewhat contrary to what may have predicted from the semi-discrete form and is an important finding.

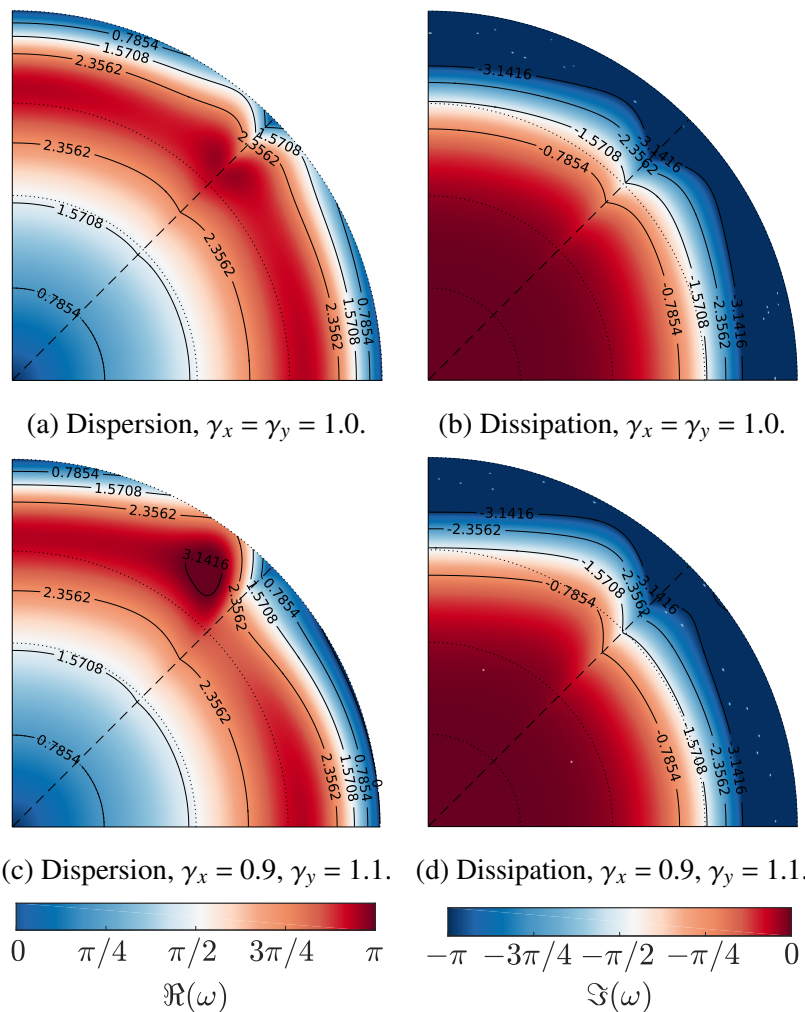


Fig. 4.8 Two dimensional upwinded FR, $p = 3$ with NDG corrections, for different grid expansion factors. Normalised wavenumber as radial distance (markers at $\pi/4$ intervals), and element angle of incidence as azimuthal distance.

4.4.3 Effect of Grid on Error and Convergence

The dispersion and dissipation relations explored show that grid expansion, contraction and incidence angle can have an appreciable impact on the numerical characteristics of FR. A means of measuring the impact of these variations is through calculating analytically the error of the method, Section 4.3.

Beginning with a uniform grid, the error with wavenumber for a uniform grid can be seen in Fig. 4.9. Here, time has been normalised by the time period of the wave. Fig. 4.9a shows that we may group the error into three regions. At low wavenumbers, the well resolved waves have low error. At high wavenumbers, where the lower dissipation of Huynh g_2 correction functions leads to some high amplitude oscillations. In previous work [11, 150], these oscillations were found to be due to the solution be formed from secondary, erroneous, modes. Lastly, there is a central range of wavenumbers where the solution is still mainly composed of the primary mode, however, the primary mode's dissipation is increasing. Therefore, waves quickly become damped and the error grows.

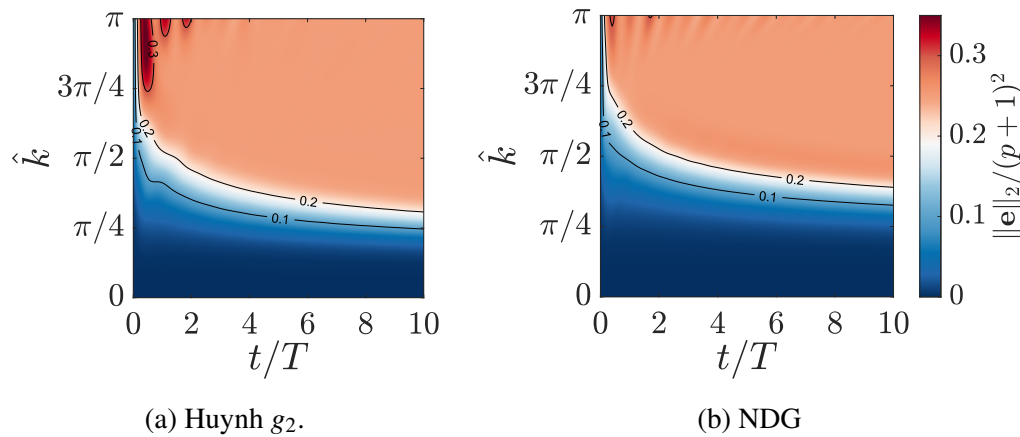
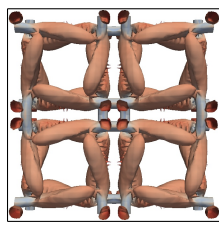


Fig. 4.9 Semi-discrete error of FR, $p = 3$, with upwinded interfaces on a uniform grid for $\theta = 45^\circ$.

Comparison may be made to the error evolution for NDG, shown in Fig. 4.9b. It is evident that NDG has lower error and a wider range of wavenumbers over which waves are well resolved. At higher wavenumbers NDG also produces lower amplitude spurious waves. This is due to the higher dissipation of NDG compared to g_2 . In the intermediate range of wavenumbers, transients in the error early on are visible for both NDG and g_2 . However, they appear smaller for NDG, again associated with the higher dissipation and reduced half-life of the spurious modes.

The error results presented here were for a wave at 45° . We now wish to understand how the error and resolution at various wavenumbers effects the rate of convergence with grid spacing. The rate of convergence with grid spacing is calculated via Eq. (4.37)



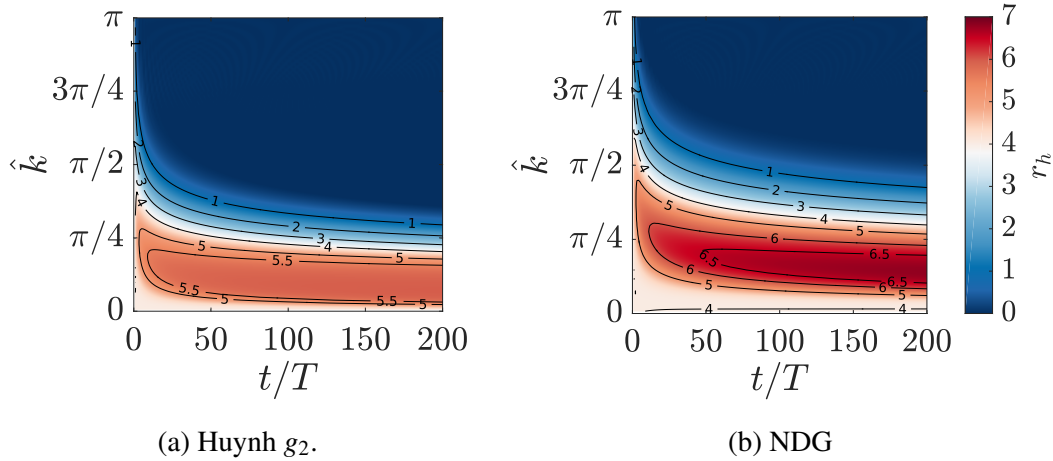


Fig. 4.10 Grid spacing rate of convergence of FR, $p = 3$, with upwinded interfaces on a uniform grid for $\theta = 0^\circ$.

and a value of $J_1/J_2 = 2$ will be used. The results of which are presented in Fig. 4.10. These results are interesting as they also show three distinct regions, let us begin by examining the behaviour for wavenumbers $\hat{k} > \pi/2$. In this range, the rate of convergence has dropped to approximately zero, which implies the error at the two grids levels is the same. This is due to the wavenumbers being high and a ratio of $J_1/J_2 = 2$ being insufficient for these wave to be sufficiently resolved on the finer grid, which can be understood from studying Fig. 4.9. The second region is for $\hat{k} \approx \pi/6$. In this region the change in the grid spacing can provide a marked improvement in the amount of error. As the Jacobian ratio is increased this region enlarges as the resolution improves for higher frequency waves on the finer grid. At very low wavenumbers the rate of convergence is approximately constant at ≈ 4 . At these wavenumbers the waves are very well resolved. This includes the small components of the wave which are projected into the spurious modes. As these spurious modes are also well resolved here, the decay of these modes is slow compared to there decay at higher frequencies and so the rate in this time range is approximately constant.

By choosing a wave that falls in the well resolved region, in this case $k = 2$, we may then sweep through angles and study the effect on rate of convergence as angle is varied. For NDG, Fig. 4.11a, the initial rate of convergence is 4 and, after the dissipation of spurious modes, the rate can be seen to be increasing towards 7. This is the expected behaviour explored by Asthana et al. [11]. As the angle is varied, however, the time for the scheme to reach the convergence-rate-limit increases. This indicates that as the incidence angle is increased, the half-life of the secondary modes increases. This is rooted in the use of an anisotropic quadrature to form the polynomial approximation. In particular, we use a tensor grid, which has higher resolution on the diagonal. Hence,

although the primary mode is unaffected, we have shown here that the resolution of the secondary mode as increased. Consequently, this could mean that when the method is applied practically, grid alignment could impact results.

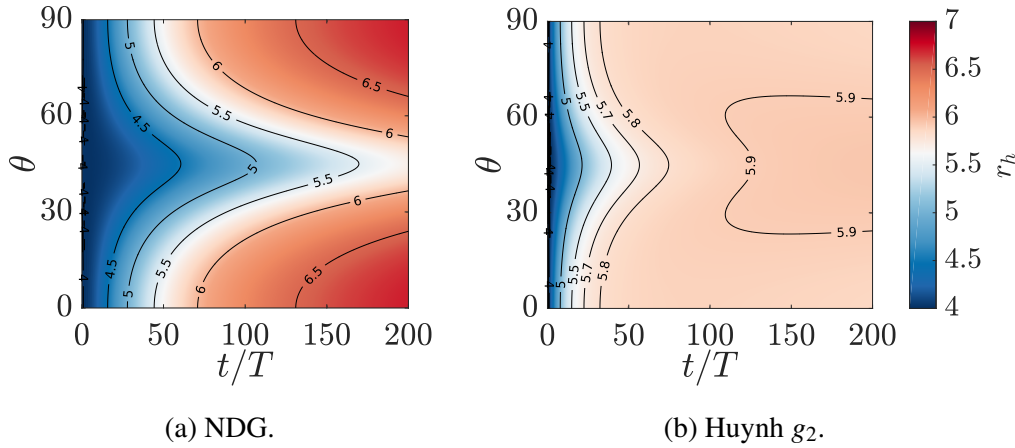


Fig. 4.11 Grid spacing rate of convergence of FR, $p = 3$, with upwinded interfaces on a uniform grid.

Again, investigating the effect of changing to Huynh’s g_2 correction function (Fig. 4.11b) we see that the initial rate is the expected value of 4, which asymptotes to a value of 6. The decrease relative to NDG is due to the well know super-convergence of DG [6, 38], and in FR is rooted in the g_2 correction function having lower order, $p - 1$, terms. For g_2 correction functions, the reduction in the dissipation for $\theta \approx 30^\circ$ and $\theta \approx 60^\circ$ coincides with an increase in the time to reach the convergence limit, similar to that observed for NDG. However, the g_2 correction functions goes on to have a slight increase in the convergence limit around $\theta = 45^\circ$. In a more general sense, it may be remarked that g_2 correction functions may be more resilient in higher dimensions due to smaller variation in properties that this rate investigation has shown.

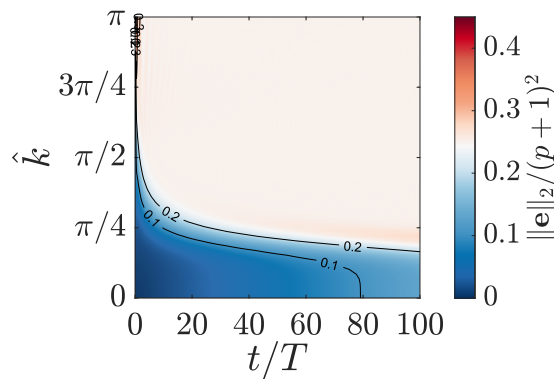
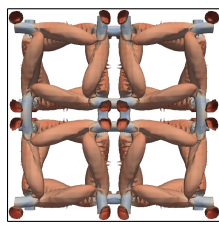


Fig. 4.12 Semi-discrete error of FR, $p = 3$, upwinded interfaces with: $\gamma_x = 1$, $\gamma_y = 1.1$, and $\theta = 30^\circ$. Here Huynh’s g_2 correction function has been applied.



Now applying a grid expansion in the y direction, we obtain the error results presented in Fig. 4.12. Here we have extended the time window of the analysis to demonstrate a key result. For the range of wavenumbers that would be expected to be well resolved, the error steadily increases with time. This is not due to excess dissipation. It is clear from Fig. 4.6b that the change in dissipation in this range is negligible, and is in fact reduced. Inspection of the values of Λ instead show there is a small reduction in the phase velocity (ω/k), which will have an associated reduction in the group velocity ($\partial\omega/\partial k$). Therefore, the speed at which the wave is propagating is incorrect and manifests itself as a gradually oscillating error. Due to this behaviour of the error, it has not been possible to calculate the rate of convergence on stretched grids.

4.4.4 Effect of Grid on CFL Limit

We add here a brief note on the temporal stability limits on non-uniform grids. The definition of CFL limit, extended to higher dimension, that we will apply is:

$$\text{CFL}_d = \tau \sum_{i=1}^d \frac{a_i}{\Delta_i} \quad (4.41)$$

where d is the dimensionality, τ is the time step and, a_i and Δ_i are the characteristic velocity and grid spacing in the i^{th} dimension, respectively. The CFL limit is then the maximum value of CFL at which the scheme is stable in a von Neumann sense.

We undertook analysis of where the angle, x to y ratio ($\Delta x/\Delta y$), and stretching factors (γ_x and γ_y) were varied. It was found that there is no dependence between these factors and the CFL limit when the CFL number is defined as in Eq. (4.41). This means that when applied to a 2D plane wave the CFL number based on τ is:

$$\text{CFL} = \tau \left(\frac{\cos(\theta)}{\Delta x} + \frac{\sin(\theta)}{\Delta y} \right) \quad (4.42)$$

This is clearly an implication of solving a linear equation that could be decomposed into an x and y directions. Moreover, as the correction function was varied the CFL limit in 2D was found to be the same as those presented for 1D by Vincent et al. [161].

4.4.5 Effect of Grid on Fully Discrete Dispersion and Dissipation

Following on from the exploration of grid expansion on temporal stability limits, we will present the fully discretised Fourier analysis in 2D. In this investigation, we again focus on the Huynh g_2 and NDG correction functions, and the effect of angle and grid on the

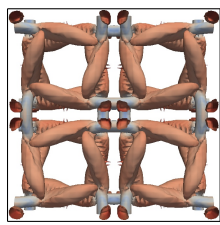
dispersion and dissipation relations. Throughout this investigation as the angle is swept through $0 - 90^\circ$, the CFL number will be held constant.

Figure 4.13 shows the results when using the Huynh g_2 correction function, with RK44 explicit temporal integration and $\text{CFL} = 0.8\text{CFL}_{\text{max}}$. As the angle and wavelength are swept there are some clear anomalous regions, most notably in the dissipation. This is due to difficulties in selecting the primary mode due to large gradients in these regions.

Focusing initially on the $\theta = 0^\circ$, a large amount of error in the dispersion relation is encountered. Notably, at the high wavenumbers, the rapid changes in $\Re(\hat{\omega})$ mean a large group velocity ($\partial\omega/\partial k$). This result was also encountered in the work of Vermeire et al. [159], and can result in spurious waves travelling rapidly through the solution, particularly when the method is applied as implicit LES (ILES). What the 2D analysis shows is that as the angle of incidence is increased there is an angle at which the group velocity switches from positive to negative. This occurs here at $\theta \approx 10^\circ$ and then back again at $\theta \approx 35^\circ$. This could have a significant impact on the solution when the method is applied as multidimensional ILES. As shown here, spurious high frequency waves will propagate rapidly in different directions depending on the angle of incidence.

Figures 4.13c-4.13f show that grid stretching causes similar changes in behaviour as was observed in the semi-discrete case. The added impact here is that the angle at which the sign of the group velocity changes has been impacted by the grid deformation.

Changing the correction function to use NDG and again maintaining $\text{CFL} = 0.8\text{CFL}_{\text{max}}$, we obtain the results shown in Fig. 4.14. When $\theta = 0^\circ$, we again see large variations in the dispersion. However, for NDG at high wavenumbers, there is initially an increase in $\Re(\hat{\omega})$ followed by a sharp decrease. This will bring about very high values of group velocity. Sweeping the incidence angle shows somewhat different behaviour to g_2 correction functions. There is still a form of change that occurs at $\theta \approx 10^\circ$ and $\theta \approx 35^\circ$, but it has a different character. Now after the switch, the initial increase in dispersion is reduced and by inspection the group velocity at the extreme end of the frequency range seems to have reduced. Throughout the range of wavenumbers with high group velocities, Fig. 4.14b shows that there is a large amount of dissipation that may reduce the effect of the dispersion. Therefore, it seems that DG for ILES with explicit temporal integration may cause smaller dispersion errors for waves that are not grid aligned. Figures 4.14c-4.14f display the effect of grid deformation, which can again be seen to cause a similar change as to that of the semi-discrete case.



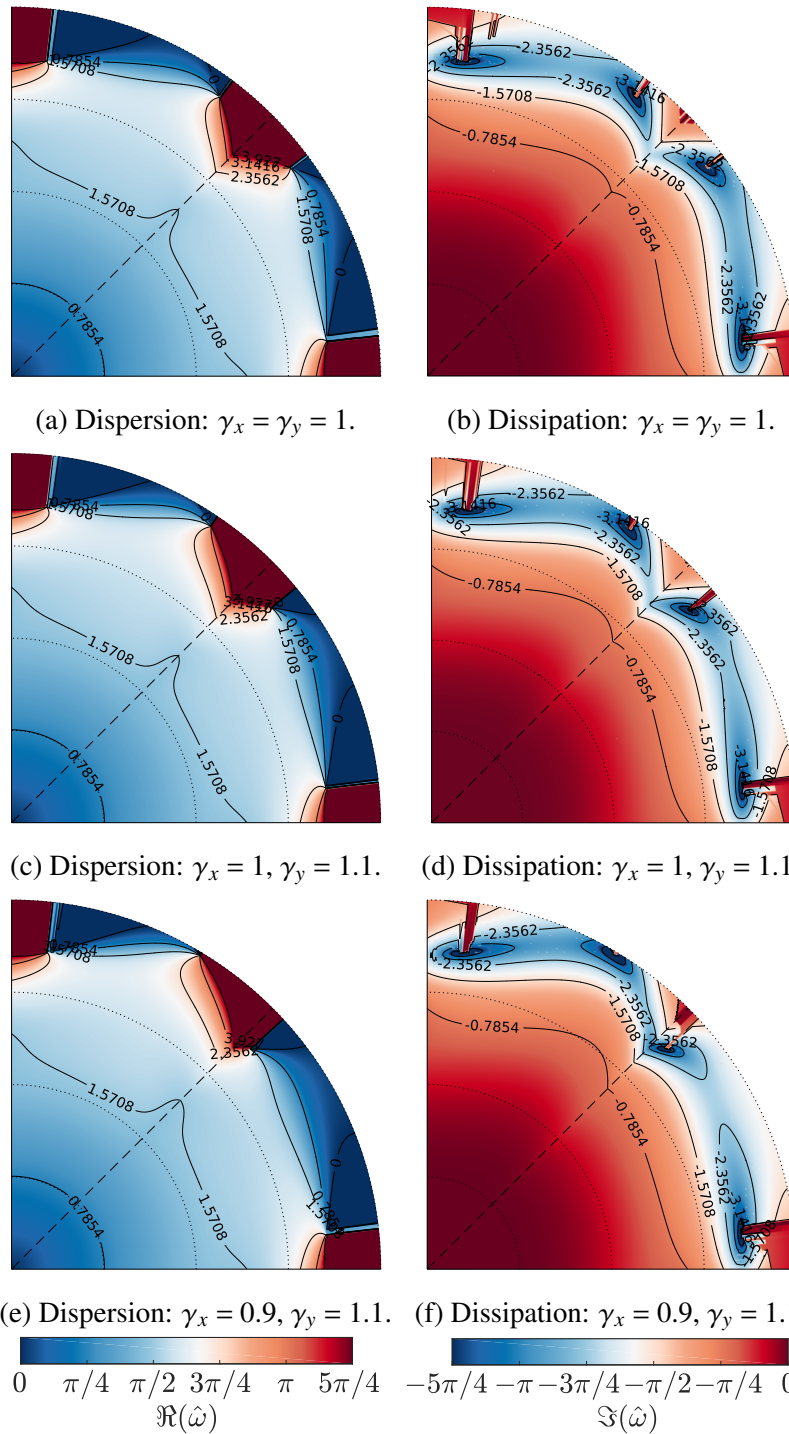


Fig. 4.13 Dispersion and dissipation of upwinded FR, $p = 3$, with Huynh g_2 corrections, explicit RK44 temporal integration, and $\text{CFL} = 0.8\text{CFL}_{\max}$. The radial distance is the normalised wavenumber (including the effect of angle), and the azimuthal distance is the angle of incidence to the element.

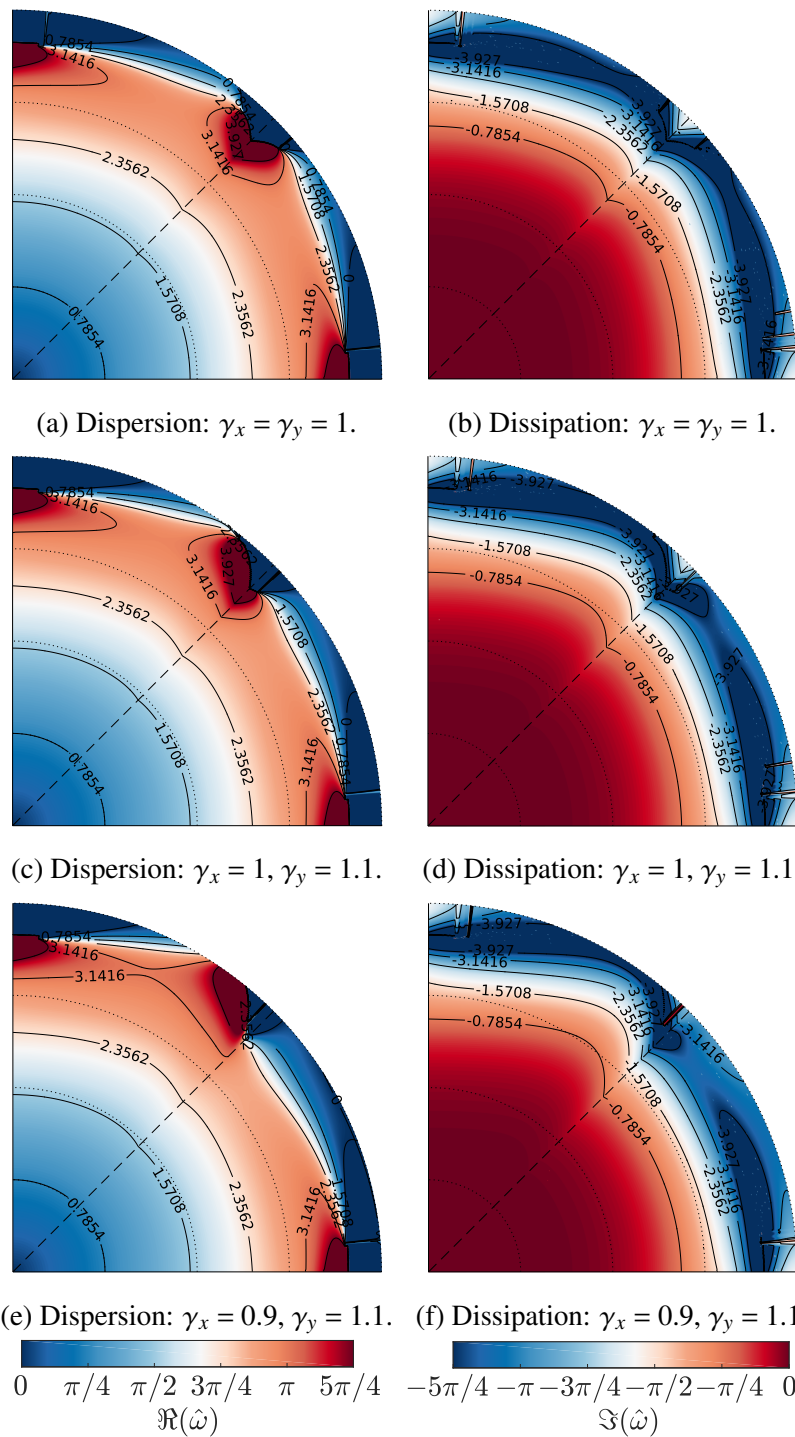
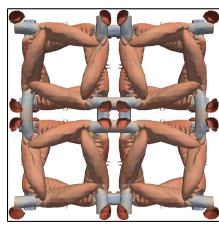


Fig. 4.14 Dispersion and dissipation of upwinded FR, $p = 3$, with NDG corrections, explicit RK44 temporal integration, and $CFL = 0.8CFL_{\max}$. The radial distance is the normalised wavenumber (including the effect of angle), and the azimuthal distance is the angle of incidence to the element.



4.5 Non-linear Navier–Stokes Equations with Deformed Grids

It is common within the CFD community to use the canonical Taylor–Green Vortex (TGV) [143] test case to assess the numerics of a solver applied to the Navier–Stokes equations with turbulence — and to that end, there is a plethora of DNS data available for comparison [21, 42]. However, this case is quite contrived and ultimately will favour spectral or structured methods due to the Cartesian and periodic domain, whilst also being unrepresentative of engineering flows that are often wall bounded and/or have complex geometries. Hence, we propose deforming the elements, initially linearly by jittering the corner nodes to be more representative of real mesh conditions. Importantly, these deformations will introduce cross multiplication into the Jacobian, as well as local regions of expansion and contraction.

The initial conditions of the TGV applied here are those of DeBonis [42], where the character of the flow is controlled by the non-dimensional parameters defined as:

$$Re = \frac{\rho_0 U_0 L}{\mu}, \quad Pr = 0.71 = \frac{\mu \gamma R}{\kappa(\gamma - 1)}, \quad Ma = 0.08 = \frac{U_0}{\sqrt{\gamma R T_0}} \quad (4.43)$$

where we will use the standard set of free-variables for the velocity, density, pressure, and gas characteristics:

$$U_0 = 1, \quad \rho_0 = 1, \quad p_0 = 100, \quad R = 1, \quad \gamma = 1.4, \quad L = 1 \quad (4.44)$$

Here, due to the solver implementation, we use a specific gas constant of unity and hence, to achieve the required Reynold and Prandtl numbers, the dynamic viscosity and thermal conductivity can be set appropriately. The statistics that will be studied here are the decay of the kinetic energy and the enstrophy decay rate, which are defined respectively as:

$$-\frac{dE_k}{dt} = -\frac{1}{2\rho_0|\Omega|} \frac{d}{dt} \int_{\Omega} \rho(u^2 + v^2 + w^2) d\mathbf{x} \quad (4.45)$$

$$\epsilon = \frac{\mu}{\rho_0^2|\Omega|} \int_{\Omega} \rho(\boldsymbol{\omega} \cdot \boldsymbol{\omega}) d\mathbf{x} \quad (4.46)$$

where $\boldsymbol{\omega} = \nabla \times [u, v, w]^T$ is vorticity and $|\Omega|$ is the domain volume. Throughout, a reference DNS solution — ref — is provided from Brachet et al. [21]. Further information on the initial condition of the TGV is given in Section 3.5.

The FR method is extended to 3D hexahedrals — from 2D quadrilaterals — by the same tensor product formulation of Huynh [65]. The inviscid common interface

calculation was performed using a Rusanov flux [124] with a Davis [41] wave speed. The viscous common interface calculation was the BR1 method of Bass & Rebay [14, 15].

4.5.1 Randomised Grids

As has been stated, we begin by taking a uniform periodic mesh on the domain $\Omega \in [-\pi, \pi]^3$, and jittering corner nodes of the elements that are interior to the domain. The degree of jitter is calculated using a time seeded random number shifted to be centred about zero and scaled by a global factor, j_f , between zero and unity. The scaling factor is such that zero gives a uniform mesh and unity could lead to edges of zero length. This transformation is defined as:

$$x' = x + j_f \frac{l(\hat{x} - 0.5)}{n_x} \quad (4.47a)$$

$$y' = y + j_f \frac{l(\hat{y} - 0.5)}{n_y} \quad (4.47b)$$

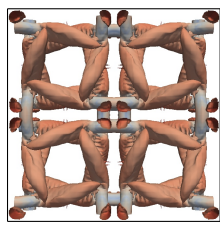
$$z' = z + j_f \frac{l(\hat{z} - 0.5)}{n_z} \quad (4.47c)$$

where x' etc. are the new points, x etc. are a uniform base grid, and $\hat{x}_j \in (0, 1]$ etc. are random numbers. To assess the grid quality, we seek a single a metric to describe the relative quality of the meshes produced. We opted for a volume ratio shape factor, slightly redefined as:

$$q_h = \frac{6\sqrt{\pi}V_h}{S_h^{3/2}} \quad (4.48)$$

where S_h is the surface area of the hexahedral element and V_h is the volume of the hexahedral elements. The quality metric, q_h , is then defined as the ratio of the volume of the element to the volume of a sphere with the same surface area, with $q_h = \sqrt{\pi/6}$ for a perfect cube. To put this parameter into context, some example meshes are shown in Fig. 4.15.

After jittering, the solution and flux points are to be positioned. We begin by investigating the use of positioning these points by using the thin plate spline radial basis function (RBF) together with the mapping from the uniform to jittered corner nodes. The reason for the use of this method is that, for more complex element transformations, it is a robust method for defining the transformation. Initially, the Jacobian will be defined using the non-conservative ($\xi_x = y_\eta z_\zeta - y_\zeta z_\eta$) formulation, and combining the solution and flux points a sufficiently high order polynomial may be fitted through the point data such that the mapping is completely captured. This might be expected to be sufficient for the linear transformation used here.



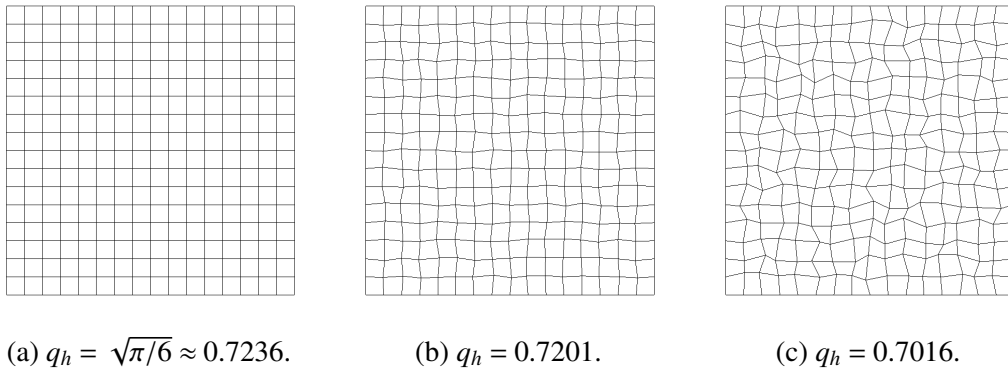


Fig. 4.15 Example slices through a 3D hexahedral mesh to illustrate the mesh quality metric.

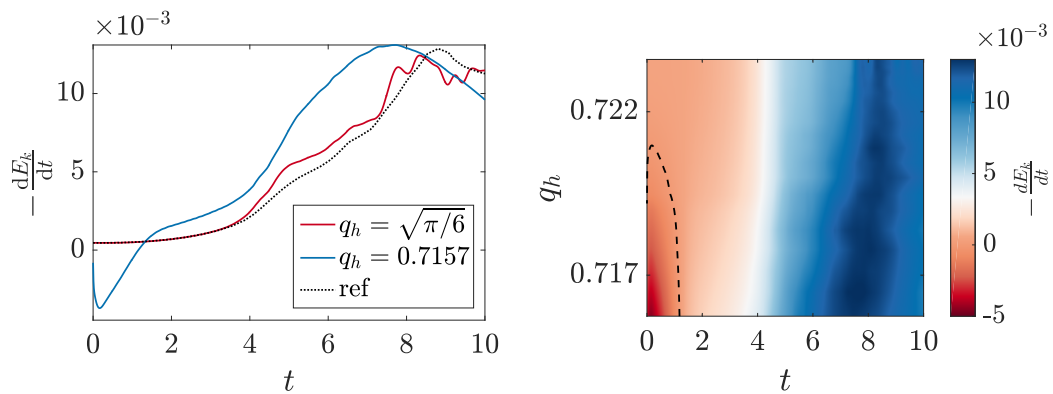
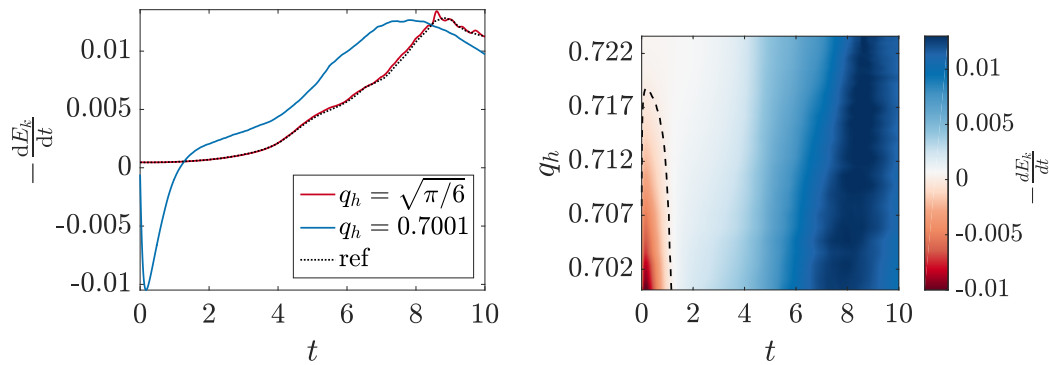


Fig. 4.16 Effect of jitter on turbulent kinetic energy dissipation of the TGV ($R_e = 1600$) for FR, $p = 2$, with Huynh g_2 correction functions on a 120^3 DoF mesh. Explicit time step size is $\Delta t = 1 \times 10^{-3}$.



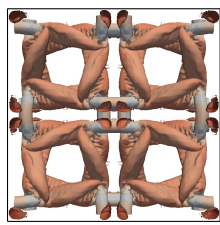
(a) Selected turbulent kinetic energy dissipation. (b) Variation of turbulent kinetic energy dissipation with jitter. Dashed contour at zero dissipation.

Fig. 4.17 Effect of jitter on turbulent kinetic energy dissipation of the TGV ($R_e = 1600$) for FR, $p = 4$, with Huynh g_2 correction functions on a 120^3 DoF mesh. Explicit time step is $\Delta t = 1 \times 10^{-3}$.

Figure 4.16 & 4.17 shows the first of these results. First looking at Fig. 4.16a & 4.17a we see two specific dissipation curves for a uniform and jittered mesh. At the beginning of the simulation, there is a clear time at which the global energy increases. Extending these runs to cover multiple grid qualities, Fig. 4.16b & 4.17b, it is observed that as the grid quality decreases a region where turbulent kinetic energy increases soon emerges. As time progress, energy dissipation is again seen and the point of peak dissipation arrives early, moving from $t \approx 8.5$ to $t \approx 7.5$. The same behaviour is seen for both $p = 2$ and $p = 4$. From comparison of $p = 2$ and $p = 4$, it seems that $p = 4$ is slightly more robust to grid deformation, as $p = 4$ was able to run at $q_h \approx 0.7$, whereas for $p = 2$, q_h could not be reduced much below 0.717 for 120^3 DoF without completely diverging.

The explanation of this is believed to be due to two interacting components. The first is that, although the randomised grid transformation applied here is linear, the thin plate spline RBF method will not recover an exactly linear model of the transformation. Hence, the second factor is that the non-conservative method for defining the Jacobian is no longer sufficient to accurately define what is now essentially a non-linear transformation. Remedial actions will be presented shortly.

Studying the effect of jittered grids on enstrophy, shown in Fig. 4.18, it is clear that as the grid is stretched the enstrophy increases. This is indicative of an increase in the vorticity, with the rise occurring within $t = 0 - 1$. This is consistent with energy being added at the large scales, as at this time there are only large scales present. After the initial increase, the enstrophy returns to following the trend of uniform case. However, in the case of $p = 2$, Fig. 4.18a, a larger initial increase is seen followed by a wider peak. The wider peak is similar in character to that of the uniform case and is due to the grid



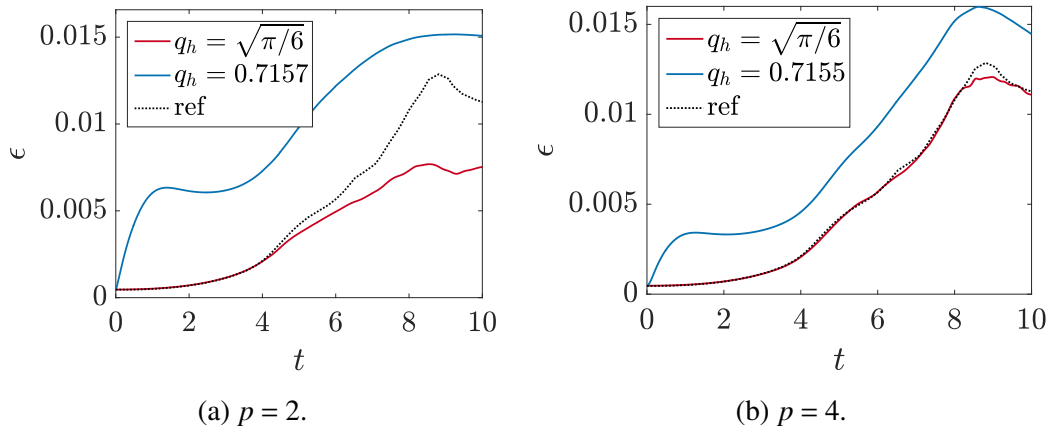


Fig. 4.18 Comparison of TGV ($R_e = 1600$) entrophy for 120^3 degree of freedom grid with similar q_h .

being mildly under-resolved in the $p = 2$ case relative to the DNS. This aims to show that RBF grid transformation can result in non-linearities in the grid and, when coupled to a non-conservative Jacobian, this manifests itself as the energy of the largest scales increasing.

We will investigate further the effect of mesh jittering by instead using the symmetric conservative method similar to that of Thomas et al. [144] ($\xi_x = [(y_\eta z - z_\eta y)_\zeta - (y_\zeta z - z_\zeta y)_\eta]/2$). Further to this we will also use the grid interpolation methodology of Abe [1].

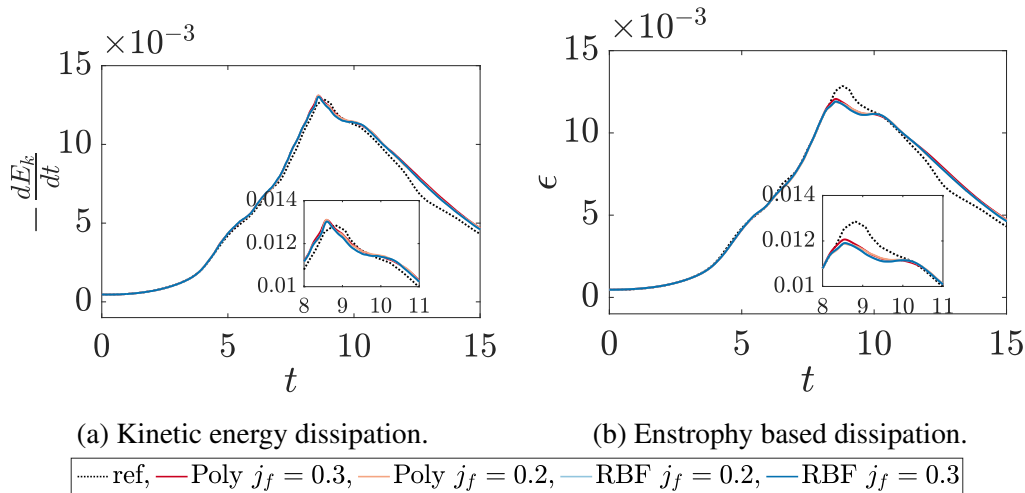


Fig. 4.19 Comparison of polynomial and RBF methods for point placement on jittered meshes. This is for a TGV, $R_e = 1600$, $p = 4$, 120^3 DoF, RK44, and $\Delta t = 10^{-3}$. A jitter factor of $j_f = 0.3$ and 0.2 gives $q_h = 0.7157$ and 0.7199 respectively.

The results comparing the RBF to a polynomial interpolation methods of point placement are shown in Fig. 4.19 for Huynh g_2 correction functions. Foremost is that in both cases the issue of non-conservation appear to have been removed. Secondly, the

methods of point placement appear to give wholly similar results. The most notable difference is shown in the enstrophy based dissipation of the polynomial method at $j_f = 0.3$, see Fig. 4.19b, where the peak value is slightly increased. Coupled to the slight over dissipation in the kinetic energy measure that is unchanged between methods, this may indicate that the polynomial method introduces additional dispersion. However, this difference is mostly negligible.

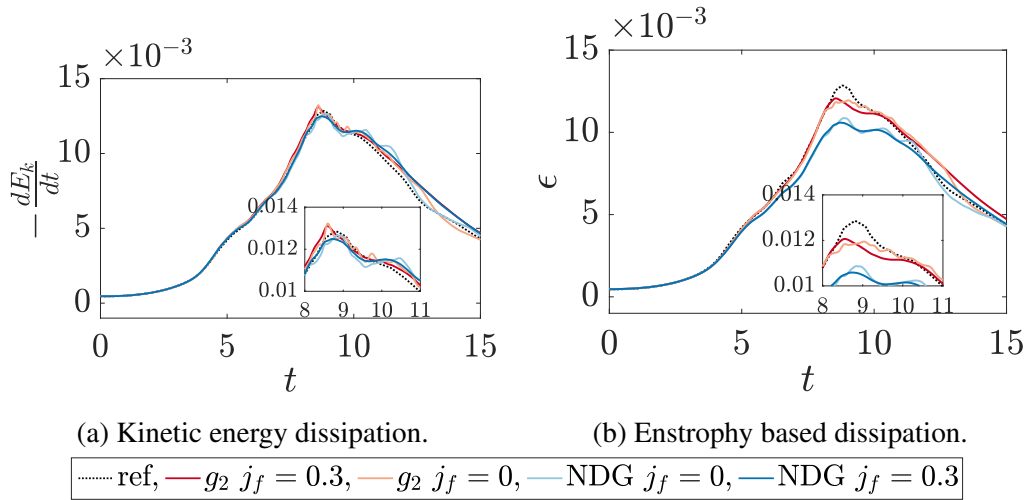
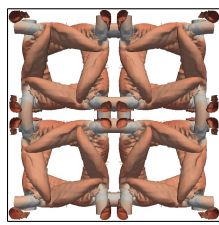


Fig. 4.20 Comparison of Huynh g_2 correction functions with NDG for jittered meshes. This is for a TGV, $Re = 1600$, $p = 4$, 120^3 DoF, RK44, and $\Delta t = 10^{-3}$. A jitter factor of $j_f = 0.3$ gives $q_h = 0.7157$.

Now, varying the correction function, we will use polynomial point placement and the symmetric conservative Jacobian definition, Fig. 4.20. From Fig. 4.20a it is clear the lower dissipation of g_2 corrections over NDG has led to a more accurate approximation. We may infer this is due to increased dissipation, particularly at the smallest scales. This will cause the vorticity to be reduced and hence the enstrophy will be reduced. This somewhat confirms the prediction of the convergence rate study of Section 4.3.

As the mesh is then randomised, g_2 corrections show an increased enstrophy peak, likely as a result of dispersion. This is then followed by a dissipation deficit due to the energy deficit. The additional dispersion error is in accordance with the predictions of Section 4.4.5. Here, the fully discrete analysis showed that on both uniform grids and to a greater extent on non-uniform grids, the scheme suffered from dispersion error without accompanying dissipation to reduce them. When looking at the NDG results, the opposite is true. Although analytically large dispersion error was found, the scheme also has a large amount of accompanying dissipation. This is reflected in the TGV results, where peak enstrophy is reduced. For both correction functions there are additional errors in the dissipation after the peak for the jittered grids, as the solution tend towards homogeneous decaying turbulence. Initially, the TGV is anisotropic, however for $Re < \sim 500$, the flow



will become isotropic with time [21]. Therefore, as time goes on, waves will go from largely grid aligned to range over all angles. These waves will then be affected by the anisotropic properties shown in Section 4.4. As could also be predicted from the results of Section 4.4, these inaccuracies are made worse by a randomised grid.

To provide some reference as to how FR performs relative to an established method we will use an edge-based Finite Volume (FV) method for comparison. The FV method is a standard central second order method with L2 Roe smoothing [112] for stabilisation, which has been validated previously [126]. The particular FR scheme used in this comparison is $p = 1$, giving second order, the same as the FV scheme. However, this puts FR at a significant disadvantage as its numeric characteristics at low order are particularly poor. For example, consider the dispersion and dissipation relations in Fig. 4.21, which, by comparison to the result of Lele [89], show that FR has noticeably lower resolving abilities when compared against a second order FD scheme.

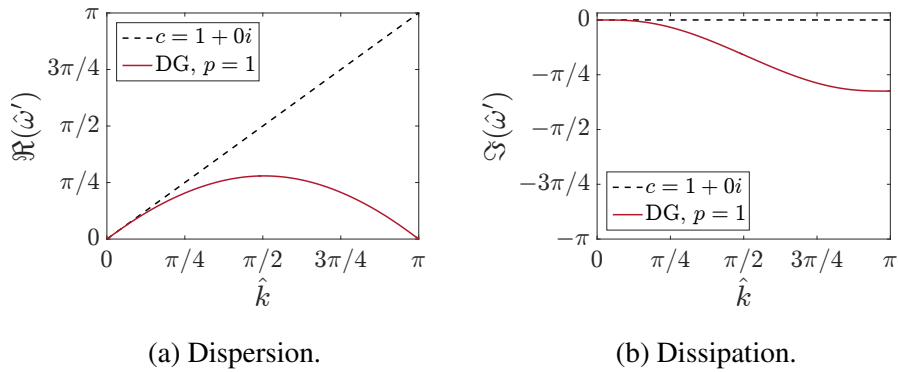


Fig. 4.21 Dispersion and Dissipation relation for 1D upwinded FR, $p = 1$, with DG correction function.

With this in mind, we present the results of tests on various jittered grids with a total of 170^3 degrees of freedom in Fig. 4.22. For the uniform case, the enstrophy clearly shows that FR is under-resolved compared to FV, which is also shown by a slightly increased rate of dissipation earlier — indicating that the implicit filter is too narrow. If we now consider the effect of jittering, several things may be concluded.

For $-dE_k/dt$ it seems that the peak value is less sensitive with FR than with FV, with central FV seeing some large amplitude oscillations in $-dE_k/dt$. This is likely to be rooted in the central differencing at the interfaces. If we change to a kinetic energy preserving formulation [72, 169], as is displayed in Fig. 4.23, these oscillations are removed. The sensitivity to jitter is then reduced to a similar level as FR. The enstrophy (Fig. 4.23b) seems to indicate that a large amount of what seemed to be resolved energy may have in fact been dispersion induced fluctuations. However, in both cases FV was able to run with grids up to $j_f = 0.9$ and $q_h = 0.6382$ — not shown. It appears that in these cases

the added stability of the smoothing has greatly helped FV. This is especially so in the central difference case where running without smoothing caused the case to fail even at low levels of jitter. For comparison, FR was only able to run with $j_f \approx 0.6$, before becoming unstable.

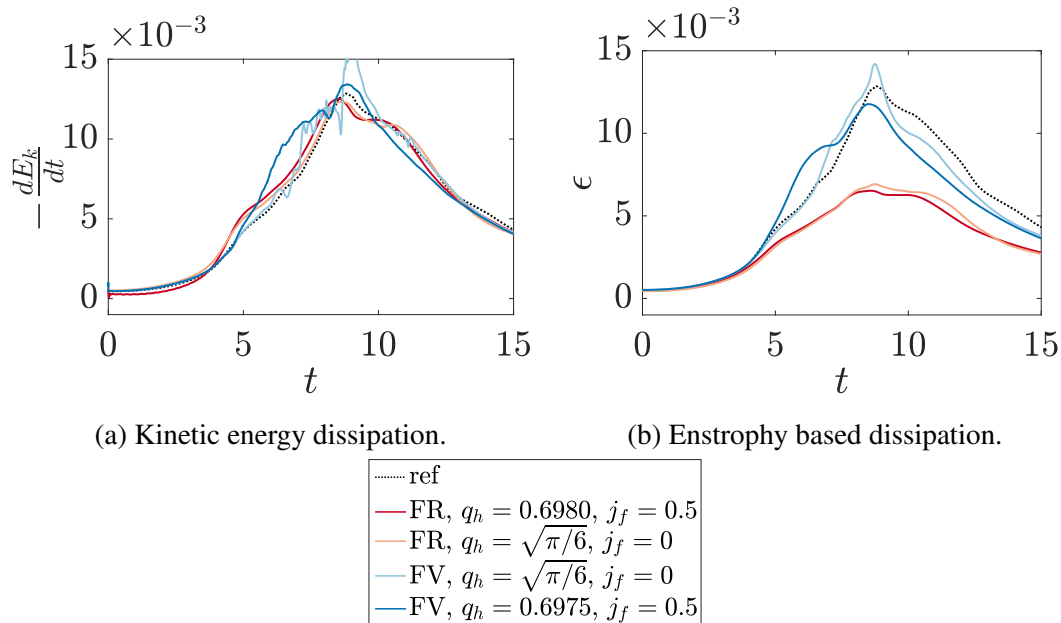
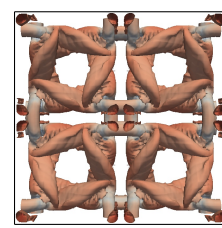


Fig. 4.22 Comparison of FR, $p = 1$ with DG correction functions with a second order central FV scheme with L2 Roe smoothing both with 170^3 degrees of freedom and $\Delta t \approx 5 \times 10^{-4}$. A reference DNS solution is provided by Brachet et al. [21].

Before moving on, it must be noted that for both FR and FV we see a dip in dE_k/dt . This is only present in the kinetic energy dissipation and no change in the enstrophy is observed. Therefore, the decrease must be due to an energy increase in the zeroth mode. The reason for this is not currently known. The results presented here show that, even for second order, FR is more resilient to mesh deformation than FV with traditional smoothing. A similar result was reported in [151], but for solely the Euler equations. Hence, this resilience seems to carry over to the Navier–Stokes equations. However, when FV with KEP is used the mesh sensitivity is greatly reduced and so this should be considered as important for FV solvers. This confirms the application specific results of Watson et al. [169]. FR and KEP together may also improve further the mesh resilience of FR.

4.5.2 Curved Grids

To end, we will briefly present some results on curved grids. A more complete numerical study was presented by Mengaldo et al. [103]. However, we seek to understand if the



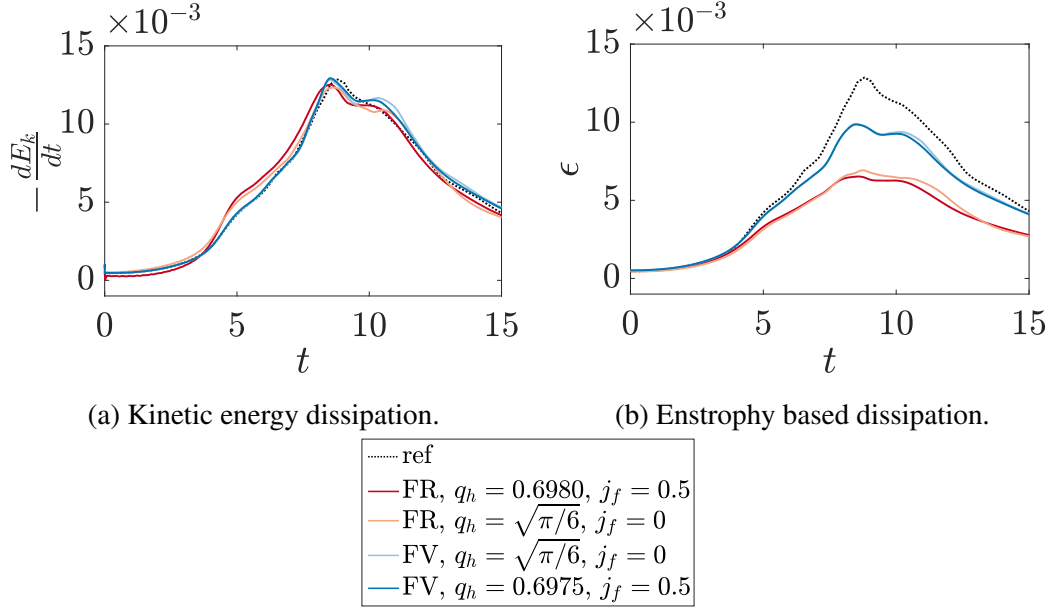


Fig. 4.23 Comparison of FR, $p = 1$ with DG correction functions with a second order KEP FV scheme with L2 Roe smoothing both with 170^3 degrees of freedom and $\Delta t \approx 5 \times 10^{-4}$. A reference DNS solution is provided by Brachet et al. [21].

behaviour of the stretched and jittered grids carries over. We will employ a similar curved grid transformation to that used by Abe et al. [1]. To remove some issues of point placement we will initially form a uniform grid and then deform the solution and flux points by the following:

$$x' = x + \frac{l}{n_x} A \sin\left(\frac{k_g \pi y}{l}\right) \sin\left(\frac{k_g \pi z}{l}\right) \quad (4.49a)$$

$$y' = y + \frac{l}{n_y} A \sin\left(\frac{k_g \pi x}{l}\right) \sin\left(\frac{k_g \pi z}{l}\right) \quad (4.49b)$$

$$z' = z + \frac{l}{n_z} A \sin\left(\frac{k_g \pi x}{l}\right) \sin\left(\frac{k_g \pi y}{l}\right) \quad (4.49c)$$

Symbols take the same meaning as before, with the added definition of k_g — the grid wavenumber, and A , the grid wave amplitude. In keeping with Abe et al. [1] we will use $k_g = 4$ and $A = 0.4$.

Using this definition for a 120^3 DoF $p = 4$ mesh, results in $q_h = 0.7128$ and $\Delta \mathbf{x}_{\max} / \Delta \mathbf{x}_{\min} = 1.5$ — see Fig. 4.24. The result of applying a TGV to this grid are displayed in Fig. 4.25. This shows that for both NDG and g_2 the curved grid causes a larger variation in the enstrophy, mostly manifesting as over dissipation — and hence dispersion — at $t \approx 10$. This error is less for NDG but due to its presence with both correction functions, it may be concluded that this grid deformation results in the increase of high frequency dispersion with FR.

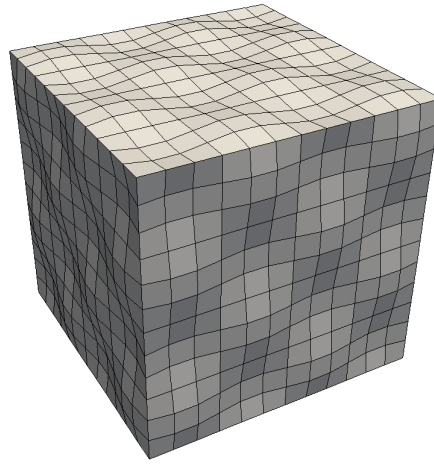


Fig. 4.24 Example 120^3 DoF curved grid for $p = 4$, $A = 0.4$, and $k_g = 4$. Here a sub-sample of every 10^{th} point is shown.

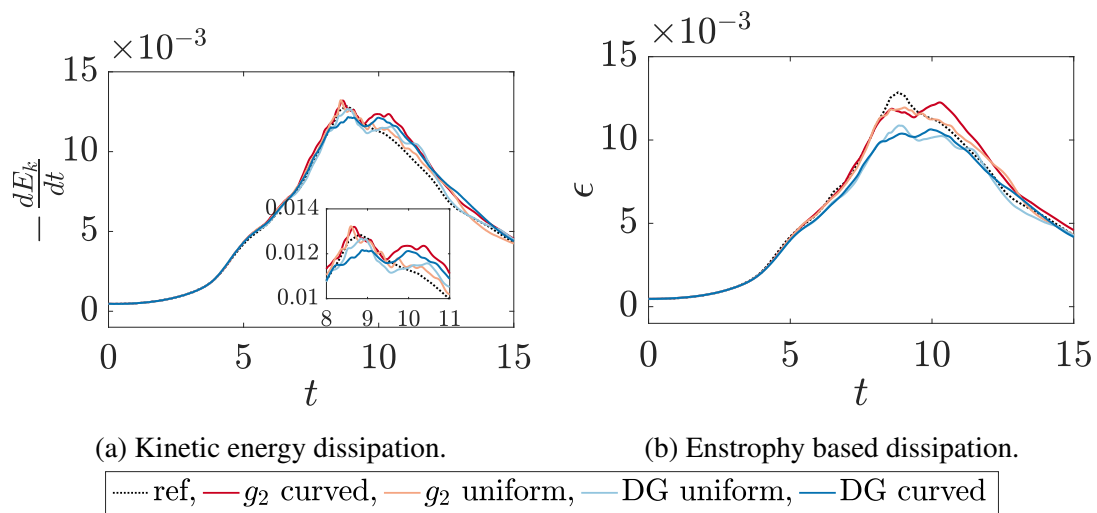
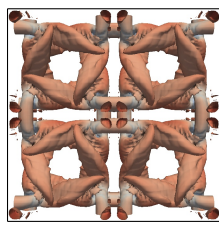


Fig. 4.25 TGV results for FR, $p = 4$, on a curved grid with 120^3 DoF. RK44 explicit time stepping is used with $\Delta t = 10^{-3}$.



4.6 Conclusions

Through this work, a theoretical extension of the FR von Neumann analysis to higher dimensions has been presented. This allowed us to understand the character of the dispersion and dissipation relations of FR as the incident angle of a wave was varied. Differences were noted between the behaviours of FR and finite differencing methods, primarily that FR saw a lower variation in character with the angle of incidence.

Investigations were then performed on deformed meshes. The same mechanism that caused the variation of properties with angle on a uniform grid meant that deformed grids saw a greater variation. For expanding grids this led to dispersion overshoot for waves more aligned with the expansion. Associated with the increase in dispersion was a decrease in dissipation. Application of an expansion and contraction led to this variation being amplified. Investigation of the fully discretised system found large angular variations in the dispersion and dissipation. In some instances, a small perturbation of the angle could cause a complete reversal of the group velocity. Here it was found that for CFL numbers close to the CFL limit, DG may be more resilient due to large levels of dissipation that would reduce the effect of high group velocity induced dispersion errors. The last theoretical investigation into the semi-discrete error and convergence found that Huynh's g_2 correction function suffered less from anisotropy with wave angle, suggesting it may be more suitable for ILES at a lower percentage of the CFL limit.

Numerical experiments were then undertaken to explore the link and impact of the theoretical findings. Some remarks were made about the effect of using RBF projection for grid definition, which highlighted the importance of a symmetric conservative Jacobian definition. Then, by using the Taylor–Green vortex case on randomised grids, it was observed that Huynh's g_2 correction function did indeed show signs of increased dispersion on randomised grids. However, they were better able to resolve the flow thanks, in part, to lower dissipation at high wavenumbers. Conversely, NDG correction functions showed signs of increased dissipation on randomised grids. Finally, some comparison was made between second order FR and an industrial second order finite volume method. It was found if more traditional L2Roe smoothing was used, FV was less resilient to mesh deformation than FR. However, if KEP was employed for the FV method, then both methods were comparably robust. Yet, in both cases FV was better able to resolve the flow. Hence, if a second order method is sought for practical applications, then FV with KEP is recommended. The use of KEP form of FR remains an open question, and an avenue which may lead to further improvements in FR.

Chapter 5

Novel Correction Functions

5.1 Introduction

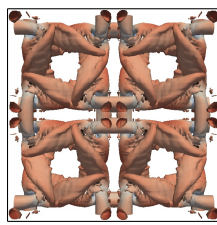
The numerical method of Flux Reconstruction (FR) was introduced in Chapter 2. What should have been apparent is that within the FR methodology, the correction function plays an important role in the solution and has a large impact on the exact character of the scheme. To reiterate this, consider FR applied to a 1D conservation law to give:

$$\frac{d\hat{u}^\delta}{dt} = - \sum_{j=0}^p \hat{f}_j^{\delta D} \frac{dl_j}{d\xi}(\xi) - (\hat{f}_L^{\delta I} - \hat{f}_L^{\delta D}) \frac{dh_L}{d\xi}(\xi) - (\hat{f}_R^{\delta I} - \hat{f}_R^{\delta D}) \frac{dh_R}{d\xi}(\xi) \quad (5.1)$$

These values can then be used to advance \hat{u}^δ in time via a suitable temporal discretisation of this semi-discrete expression.

In 2011, Vincent et al. [161] discovered a one-parameter family of correction functions, herein referred to as original stable FR (OSFR) schemes, that led to stable FR schemes for linear advection problems. This work was subsequently extended to linear advection-diffusion problems by Castonguay et al. [33]. More recently, Vincent et al. [162] identified a multi-parameter family of linearly stable FR correction functions which are herein referred to as the extended stable FR (ESFR) schemes. In a series of numerical experiments, Vermeire and Vincent [158] observed that several of these schemes are more stable for ILES simulations than NDG. However, despite this progress, several questions around what exactly a correction function is – and, more practically, how one should be chosen – remain. To this end, we aim to extend the theoretical understanding of FR correction functions.

The aim of this work is to enable correction functions to be found that can increase the accuracy, temporal stability, or both, for FR. The advantage that this possesses is that,



in the framework of FR, changing the correction function is straightforward – resulting in only limited work in the implementation for the end user to see benefits.

5.2 Stability Definition

5.2.1 Preliminaries

In order to form a numerical scheme that is energy stable, we need to find a functional space whose energy does not increase with time when the method is applied to a linear problem. This condition is similar to treating FR as a linear operator and imposing that the operator is a contraction in the sense of Banach’s fixed point theorem [83]. This condition is dependent on us being able to define a functional space. A necessary and sufficient condition for this is that we must be able to find a valid norm, $\|x\|$, that meets the following conditions [83]:

- $\|x\| \geq 0$ (positivity)
- $\|x\| = 0 \iff x = 0$ (definiteness)
- $\|ax\| = |a|\|x\|$ (homogeneity)
- $\|x + y\| \leq \|x\| + \|y\|$ (triangle inequality)

Having found a norm that satisfies these conditions, a sufficient condition for energy stability can be defined as:

$$\frac{d}{dt}\|u\|^2 \leq 0 \quad (5.2)$$

From the work of Hesthaven & Warbuton [60], we may formulate a similar necessary and sufficient condition, however, this will be dependent on the norm. For clarity, we will define what is meant by necessary and sufficient. If we have two statements A and B, then if B is necessary for A then A cannot be true unless B is also true. But if A is sufficient for B, then A being true implies B is true, but B being true does not imply A is true.

Returning to the discussion of norms, the question then becomes, how to create the norm, and when is the condition of Eq. (5.2) met? There are several candidates that will be presented and then explored for FR in the remainder of this chapter. It should be noted that this was not the technique used by Vincent et al. [162], who employed arguments based around the finite element nature of the FR method to produce a multi-parameter family of FR correction functions. *A posteriori*, the effective norms that this method implied were then found. The exact formulation of these functions is contained in appendix B.

At this stage it will be useful to define the form of the solution, \hat{u}^δ , as one of two polynomial interpolations:

$$\hat{u}^\delta = \sum_{i=0}^p \tilde{u}_i \psi_i(\xi) \quad (5.3)$$

or

$$\hat{u}^\delta = \sum_{i=0}^p \tilde{u}_i J_i^{(\alpha,\beta)}(\xi) \quad (5.4)$$

where ψ_n is the n^{th} order Legendre polynomial of the first kind and $J_n^{(\alpha,\beta)}$ is the n^{th} order Jacobi polynomial, with (α,β) as control variables. Both forms of the interpolation will be used throughout this chapter, depending on the circumstances.

5.2.2 Sobolev Norm

The original norm — cast into the reference domain — that was used to define a set of FR correction functions [160] was a modified finite Sobolev norm:

$$\|\hat{u}^\delta\|_{W_2} = \sqrt{\int_{-1}^1 (\hat{u}^\delta)^2 + \iota \left(\frac{\partial^p \hat{u}^\delta}{\partial \xi^p} \right)^2 d\xi} \quad (5.5)$$

The key step that was taken in defining a set of FR schemes was the modification of multiplying the p^{th} derivative by a free parameter. This gave an adjustable variable that would alter the numerical method. The associated condition on stability, when cast into the reference domain [60], was then:

$$\frac{d}{dt} \|\hat{u}^\delta\|_{W_2}^2 = \frac{d}{dt} \int_{-1}^1 (\hat{u}^\delta)^2 + \iota \left(\frac{\partial^p \hat{u}^\delta}{\partial \xi^p} \right)^2 d\xi \leq (\hat{u}_L^\delta)^2 - (\hat{u}_R^\delta)^2 \quad (5.6)$$

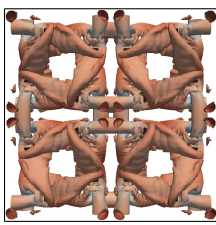
However, for this to be a valid norm it must satisfy the conditions of Section 5.2.1. As differentiation is linear, the satisfaction of these criteria will follow naturally if positivity is proven, namely if:

$$0 < \|\hat{u}^\delta\|_{W_2} < \infty \quad \forall \hat{u}^\delta \neq 0 \quad (5.7)$$

Then by making use of Eq. (5.3) it was then shown that:

$$\frac{-1}{(2p+1)(a_p p!)^2} < \iota < \infty. \quad (5.8)$$

where $a_p = (2p)! / (2^p (p!)^2)$.



5.2.3 Weighted Sobolev Norm

Following on from the definition of OSFR, we may define a weighted Sobolev norm [177] in the reference domain. Here we will use the Jacobi weight function, giving:

$$\|\hat{u}^\delta\|_{W_2^{t,w}} = \sqrt{\int_{-1}^1 \left((\hat{u}^\delta)^2 + \iota \left(\frac{\partial^p \hat{u}^\delta}{\partial \xi^p} \right)^2 \right) (1-\xi)^\alpha (1+\xi)^\beta d\xi} \quad (5.9)$$

Thus, the criterion on energy stability in time for a finite polynomial solution, when cast into the reference domain, is that:

$$\frac{d}{dt} \|\hat{u}^\delta\|_{W_2^{t,w}}^2 = \frac{d}{dt} \int_{-1}^1 \left((\hat{u}^\delta)^2 + \iota \left(\frac{\partial^p \hat{u}^\delta}{\partial \xi^p} \right)^2 \right) w_{\alpha,\beta}(\xi) d\xi \leq - \int_{-1}^1 \frac{\partial (\hat{u}^\delta)^2}{\partial \xi} w_{\alpha,\beta}(\xi) d\xi \quad (5.10)$$

where

$$w_{\alpha,\beta}(\xi) = (1-\xi)^\alpha (1+\xi)^\beta \quad (5.11)$$

and for brevity we will define the average as:

$$\frac{1}{2} \int_{-1}^1 w_{\alpha,\beta}(\xi) d\xi = \bar{w}_{\alpha,\beta} \quad (5.12)$$

This weight function is that used for the orthogonality definition of Jacobi polynomials and, before proceeding, we will lay out some results for Jacobi polynomials that will be used throughout. Firstly, the orthogonality condition:

$$\int_{-1}^1 J_m^{(\alpha,\beta)} J_n^{(\alpha,\beta)} w_{\alpha,\beta} d\xi = \underbrace{\frac{2^{\alpha+\beta+1}}{2n+\alpha+\beta+1} \frac{\Gamma(n+\alpha+1)\Gamma(n+\beta+1)}{n!\Gamma(n+\alpha+\beta+1)}}_{q_n^{(\alpha,\beta)}} \delta_{mn} \quad (5.13)$$

where $\Gamma(x)$ is the gamma function and δ_{mn} is the Kronecker delta function. Secondly, it will be useful to differentiate a Jacobi polynomial and express the result as a series of Jacobi polynomials over the same basis. From Doha [43] we find:

$$\frac{d^m J_n^{(\alpha,\beta)}}{d\xi^m} = 2^{-m} (n+\alpha+\beta+1)_m \sum_{i=0}^{n-m} D_{n-m,i}(\alpha+m, \beta+m, \alpha, \beta) J_i^{(\alpha,\beta)} \quad (5.14)$$

where

$$D_{j,i}(\gamma, \delta, \alpha, \beta) = \frac{(j+\gamma+\delta+1)_i (i+\gamma+1)_{j-i} \Gamma(i+\alpha+\beta+1)}{(j-i)! \Gamma(2i+\alpha+\beta+1)} \times {}_3F_2 \left(\begin{matrix} i-j, & j+i+\gamma+\delta+1, & i+\alpha+1 \\ i+\gamma+1, & 2i+\alpha+\beta+2 \end{matrix}; 1 \right) \quad (5.15)$$

We define here that $(x)_i$ is the rising Pochhammer function and ${}_3F_2(\dots; z)$ is the 3-2 generalised hypergeometric function [13, 18]. In the interest of brevity in later sections we will also define the constant:

$$b_p^{(\alpha, \beta)} = \frac{\partial^p J_p^{(\alpha, \beta)}}{\partial \xi^p} = 2^{-p}(p + \alpha + \beta + 1)_p \quad (5.16)$$

Proceeding without describing a specific numerical method, the norm described by Eq. (5.9) must then indeed be a norm; *i.e.* it must be positive, definite, homogeneous, and obey the triangle inequality. Of particular concern to us is the positivity condition, for the remaining conditions, again, follow immediately due to the linear nature of differentiation. Hence, it is required that:

$$0 < \|\hat{u}^\delta\|_{W_2^{t,w}}^2 = \int_{-1}^1 \left((\hat{u}^\delta)^2 + \iota \left(\frac{\partial^p \hat{u}^\delta}{\partial \xi^p} \right)^2 \right) (1 - \xi)^\alpha (1 + \xi)^\beta d\xi < \infty \quad (5.17)$$

for $\hat{u}^\delta \neq 0$. Therefore, following the method of Vincent et al. [160] we can substitute Eq. (5.4) into Eq. (5.17) as:

$$0 < \sum_{i=0}^p \tilde{u}_i^2 q_i^{(\alpha, \beta)} + \iota (b_p^{(\alpha, \beta)})^2 q_0^{(\alpha, \beta)} < \infty \quad (5.18)$$

Then grouping terms of the same order:

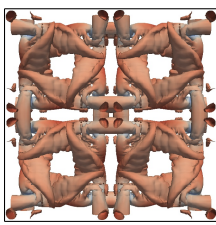
$$0 < \sum_{i=0}^{p-1} \tilde{u}_i^2 q_i^{(\alpha, \beta)} + \left(q_p^{(\alpha, \beta)} + \iota (b_p^{(\alpha, \beta)})^2 q_0^{(\alpha, \beta)} \right) \tilde{u}_p^2 < \infty \quad (5.19)$$

As \tilde{u}_i^2 is always positive, the limit on the value of ι is:

$$-\iota_{\text{crit}} = -\frac{q_p^{(\alpha, \beta)}}{(b_p^{(\alpha, \beta)})^2 q_0^{(\alpha, \beta)}} \leq \iota < \infty \quad (5.20)$$

The value of ι_{crit} can be evaluated in a closed form that shows it is always positive, and hence quasi-DG (qDG) schemes ($\iota = 0$) will always have a positive norm, leading us to expect a large region of stability.

$$\iota_{\text{crit}} = \frac{q_p^{(\alpha, \beta)}}{(b_p^{(\alpha, \beta)})^2 q_0^{(\alpha, \beta)}} = \left(\frac{\alpha + \beta + 1}{2p + \alpha + \beta + 1} \right) \left(\frac{(\alpha + 1)_p (\beta + 1)_p}{(\alpha + \beta + 1)_p} \right) \times \left(\frac{2^p}{(p + \alpha + \beta + 1)_p} \right)^2 \quad (5.21)$$



To show this is compatible with previous work, let us suggest $(\alpha, \beta) = (0, 0)$. Remembering that $(1)_p = p!$, we get:

$$\frac{q_p^{(0,0)}}{(b_p^{(0,0)})^2 q_0^{(0,0)}} = \frac{(p!)^3}{(2p+1)} \left(\frac{2^p}{(2p)!} \right)^2 \quad (5.22)$$

Which is identical to the result of section 5.2.2.

5.2.4 Generalised Sobolev Norm

In sections 5.2.2 & 5.2.3 the norm was defined with the zeroth and p^{th} order derivatives. This defined a metric and is sufficient to define the topology of the functional space. However, this metric can be generalised further by including all derivatives in the norm, and consequently more fully defining the functional space. First defining the general modified Sobolev norm as:

$$\|u\|_{n, W_2^p} = \sqrt{\int_{-1}^1 \sum_{i=0}^p (u^{(i)})^2 d\xi} \quad (5.23)$$

where $u^{(i)}$ is the i^{th} spatial derivative of u and $W^{p,2}$ is the p^{th} order l_2 Sobolev space. (In this case $W^{p,2} = H^p$, where H is a Hilbert space). This can then be modified to form:

$$\|u\|_{n, W_2^{p,\iota}} = \sqrt{\int_{-1}^1 \sum_{i=0}^p \iota_i (u^{(i)})^2 d\xi} \quad (5.24)$$

The modified stability condition is then:

$$\frac{d}{dt} \|u\|_{n, W_2^{p,\iota}}^2 \leq - \sum_{i=0}^{p-1} \iota_i \left[(\hat{u}_R^{\delta(i)})^2 - (\hat{u}_L^{\delta(i)})^2 \right] \quad (5.25)$$

after being cast into the reference domain. Before applying a particular numerical scheme, we can constrain the values of ι_i such that positivity is ensured, *i.e.* $0 < \|\hat{u}^\delta\|_{n, W_2^{p,\iota}}^2 < \infty$. From the definition of the norm:

$$0 < \int_{-1}^1 \sum_{i=0}^p \iota_i (\hat{u}^{\delta(i)})^2 d\xi < \infty \quad (5.26)$$

If we then apply Eq. (5.3):

$$0 < \int_{-1}^1 \sum_{i=0}^p \iota_i \left(\sum_{j=0}^p \tilde{u}_j \frac{d^i \psi_j}{d\xi^i} \right)^2 d\xi < \infty \quad (5.27)$$

which can then be simplified to:

$$0 < \sum_{j=0}^p \iota_0 \left(\frac{2}{2j+1} \right) \tilde{u}_j^2 + \int_{-1}^1 \sum_{i=1}^{p-1} \iota_i \left(\sum_{j=0}^p \tilde{u}_j \frac{d^i \psi_j}{d\xi^i} \right)^2 d\xi + \iota_p \left(\frac{(2p)!}{2^p p!} \right)^2 v_p^2 < \infty \quad (5.28)$$

A closed form for the integration of the product of two arbitrary Legendre polynomial derivatives does exist and will be presented later. However, the exact evaluation will be dependent on the order, p , as well as on the solution, \hat{u}^δ . The effect the solution has on stability originates from the cross multiplication of \tilde{u}_i terms, the origin of which can be understood by formulating the derivative of a Legendre polynomial as a Legendre series [13, 44]. For example, there may be a $\tilde{u}_1 \tilde{u}_3$ term that arises in Eq. (5.28). As will be presented later, these terms can be easily zeroed by setting ι_i . But consequently, although Eq. (5.28) does constitute a necessary and sufficient condition for stability, due to this feature, we will only be able, *a priori*, to form numeric limits on \mathbf{I}_p that are *sufficient* conditions for stability, i.e. there may be other stable correction functions in the set.

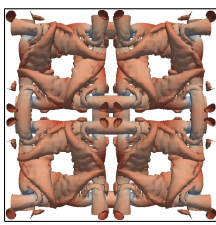
In the case $\iota_i = 0$ for $0 < i < p$, i.e. when the scheme becomes OSFR, these cross multiplication terms vanish and the stability condition becomes that presented by Vincent et al. [160]. In this case the condition is formally necessary and sufficient for stability.

5.2.5 Lebesgue Norm

Finally, for both the generalised Sobolev norm and the standard Sobolev norm there is a special case that may be considered degenerate. This is the Lebesgue norm, which is formed when taking $\iota_i = 0 \forall i \neq 0$ and $\iota_0 = 1$:

$$\|u\|_{n,L^2} = \sqrt{\int_{-1}^1 u^2 d\xi} \quad (5.29)$$

We say this is a ‘degenerate’ norm as when exploring it and the generalised Sobolev norm later, it will be shown to be a degenerate solution to a linear problem.



5.3 Finding Stable Correction Functions

5.3.1 Sobolev Norm — Original Stable FR

In chapter 2, we introduced the FR approach, how correction functions are used to form a piecewise continuous solution, and how FR's stability can be defined through norms. We now wish to take these ideas and apply them to fulfil the primary aim of discovering new correction functions. Before presenting our extensions to the OSFR schemes, it is useful to review the key results from the original OSFR paper of Vincent et al. [160] — specifically, that OSFR corrections functions are obtained by setting:

$$h_L = \frac{(-1)^p}{2} \left(\psi_p - \frac{\eta_p \psi_{p-1} + \psi_{p+1}}{1 + \eta_p} \right), \quad (5.30)$$

and

$$h_R = \frac{1}{2} \left(\psi_p + \frac{\eta_p \psi_{p-1} + \psi_{p+1}}{1 + \eta_p} \right), \quad (5.31)$$

where $\psi_p = \psi_p(\xi)$ is a Legendre polynomial of order p and

$$\eta_p = \iota(2p + 1)(a_p p!)^2 \quad \text{and} \quad a_p = \frac{(2p)!}{2^p (p!)^2}, \quad (5.32)$$

where the range of values taken by ι is limited by Eq. (5.8).

5.3.2 Weighted Sobolev Norm — Generalised Jacobi Stable FR

Moving onto the definition of the Jacobi stable FR correction functions, let us now consider applying FR to a linear advection problem. Without loss of generality we shall assume a unit convection velocity such that $f(u) = u$. It follows that:

$$\frac{d\hat{u}^\delta}{dt} = -\frac{\partial \hat{u}^\delta}{\partial \xi} - (\hat{u}_L^{\delta I} - \hat{u}_L^\delta) \frac{dh_L}{d\xi} - (\hat{u}_R^{\delta I} - \hat{u}_R^\delta) \frac{dh_R}{d\xi} \quad (5.33)$$

Previously, for the proof of OSFR [160], Eq. (5.33) would be multiplied by \hat{u}^δ and integrated over the reference domain. However, as we want to use a weight function, we shall defer this integration step, as this simplifies the use of the product rule. Multiplying Eq. (5.33) by \hat{u}^δ we obtain:

$$\hat{u}^\delta \frac{d\hat{u}^\delta}{dt} = -\hat{u}^\delta \frac{\partial \hat{u}^\delta}{\partial \xi} - (\hat{u}_L^{\delta I} - \hat{u}_L^\delta) \hat{u}^\delta \frac{dh_L}{d\xi} - (\hat{u}_R^{\delta I} - \hat{u}_R^\delta) \hat{u}^\delta \frac{dh_R}{d\xi} \quad (5.34)$$

and, applying the product rule, this can be written as:

$$\begin{aligned} \frac{1}{2} \frac{d(\hat{u}^\delta)^2}{dt} = & -\frac{1}{2} \frac{\partial(\hat{u}^\delta)^2}{\partial\xi} - (\hat{u}_L^{\delta I} - \hat{u}_L^\delta) \left(\frac{\partial h_L \hat{u}^\delta}{\partial\xi} - h_L \frac{\partial \hat{u}^\delta}{\partial\xi} \right) \\ & - (\hat{u}_R^{\delta I} - \hat{u}_R^\delta) \left(\frac{\partial h_R \hat{u}^\delta}{\partial\xi} - h_R \frac{\partial \hat{u}^\delta}{\partial\xi} \right) \end{aligned} \quad (5.35)$$

This step is important as it allows the formation of the conserved variable at the interface, as well ensuring that only derivatives of \hat{u}^δ are present. We may now proceed to multiply by the weight function and integrate over the reference domain:

$$\begin{aligned} \frac{1}{2} \frac{d}{dt} \int_{-1}^1 (\hat{u}^\delta)^2 w_{\alpha,\beta} d\xi = & -\frac{1}{2} \int_{-1}^1 \frac{\partial(\hat{u}^\delta)^2}{\partial\xi} w_{\alpha,\beta} d\xi \\ & - (\hat{u}_L^{\delta I} - \hat{u}_L^\delta) \int_{-1}^1 \left(\frac{\partial h_L \hat{u}^\delta}{\partial\xi} - h_L \frac{\partial \hat{u}^\delta}{\partial\xi} \right) w_{\alpha,\beta} d\xi \\ & - (\hat{u}_R^{\delta I} - \hat{u}_R^\delta) \int_{-1}^1 \left(\frac{\partial h_R \hat{u}^\delta}{\partial\xi} - h_R \frac{\partial \hat{u}^\delta}{\partial\xi} \right) w_{\alpha,\beta} d\xi \end{aligned} \quad (5.36)$$

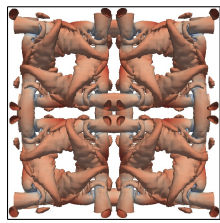
Now proceeding to form the second component of the weighted Sobolev norm, we first take the p^{th} spatial derivative of Eq. (5.33):

$$\frac{d}{dt} \frac{\partial^p \hat{u}^\delta}{\partial \xi^p} = -\frac{\partial^{p+1} \hat{u}^\delta}{\partial \xi^{p+1}} - (\hat{u}_L^{\delta I} - \hat{u}_L^\delta) \frac{d^{p+1} h_L}{d\xi^{p+1}} - (\hat{u}_R^{\delta I} - \hat{u}_R^\delta) \frac{d^{p+1} h_R}{d\xi^{p+1}}, \quad (5.37)$$

Given \hat{u}^δ is a p^{th} order polynomial, Eq. (5.37) may be multiplied by the p^{th} derivative of \hat{u}^δ and integrated over the reference domain with the weighting function to give:

$$\begin{aligned} \frac{1}{2} \frac{d}{dt} \int_{-1}^1 \left(\frac{\partial^p \hat{u}^\delta}{\partial \xi^p} \right)^2 w_{\alpha,\beta} d\xi = & -2(\hat{u}_L^{\delta I} - \hat{u}_L^\delta) \frac{\partial^p \hat{u}^\delta}{\partial \xi^p} \frac{d^{p+1} h_L}{d\xi^{p+1}} \bar{w}_{\alpha,\beta} \\ & -2(\hat{u}_R^{\delta I} - \hat{u}_R^\delta) \frac{\partial^p \hat{u}^\delta}{\partial \xi^p} \frac{d^{p+1} h_R}{d\xi^{p+1}} \bar{w}_{\alpha,\beta} \end{aligned} \quad (5.38)$$

This simplification can be made due to the respective orders of \hat{u}^δ , h_L , and h_R . To now form the complete weighted Sobolev norm, we take Eq. (5.36) and add ι times Eq. (5.38)



as:

$$\begin{aligned}
\frac{1}{2} \frac{d}{dt} \int_{-1}^1 \left((\hat{u}^\delta)^2 + \iota \left(\frac{\partial^p \hat{u}^\delta}{\partial \xi^p} \right)^2 \right) w_{\alpha, \beta} d\xi &= -\frac{1}{2} \int_{-1}^1 \frac{\partial (\hat{u}^\delta)^2}{\partial \xi} w_{\alpha, \beta} d\xi \\
&- (\hat{u}_L^{\delta I} - \hat{u}_L^\delta) \int_{-1}^1 \left(\frac{\partial h_L \hat{u}^\delta}{\partial \xi} - h_L \frac{\partial \hat{u}^\delta}{\partial \xi} \right) w_{\alpha, \beta} d\xi \\
&- (\hat{u}_R^{\delta I} - \hat{u}_R^\delta) \int_{-1}^1 \left(\frac{\partial h_R \hat{u}^\delta}{\partial \xi} - h_R \frac{\partial \hat{u}^\delta}{\partial \xi} \right) w_{\alpha, \beta} d\xi \quad (5.39) \\
&- 2(\hat{u}_L^{\delta I} - \hat{u}_L^\delta) \iota \frac{\partial^p \hat{u}^\delta}{\partial \xi^p} \frac{d^{p+1} h_L}{d\xi^{p+1}} w_{\alpha, \beta} \\
&- 2(\hat{u}_R^{\delta I} - \hat{u}_R^\delta) \iota \frac{\partial^p \hat{u}^\delta}{\partial \xi^p} \frac{d^{p+1} h_R}{d\xi^{p+1}} w_{\alpha, \beta}
\end{aligned}$$

Hence, by analogy to Vincent et al. [160] and Section 5.3.1, if the following conditions are imposed on the correction function:

$$\int_{-1}^1 \left(h_L \frac{\partial \hat{u}^\delta}{\partial \xi} \right) w_{\alpha, \beta} d\xi - \iota \frac{\partial^p \hat{u}^\delta}{\partial \xi^p} \frac{d^{p+1} h_L}{d\xi^{p+1}} \int_{-1}^1 w_{\alpha, \beta} d\xi = 0 \quad (5.40)$$

$$\int_{-1}^1 \left(h_R \frac{\partial \hat{u}^\delta}{\partial \xi} \right) w_{\alpha, \beta} d\xi - \iota \frac{\partial^p \hat{u}^\delta}{\partial \xi^p} \frac{d^{p+1} h_R}{d\xi^{p+1}} \int_{-1}^1 w_{\alpha, \beta} d\xi = 0 \quad (5.41)$$

then

$$\begin{aligned}
\frac{1}{2} \frac{d}{dt} \int_{-1}^1 \left((\hat{u}^\delta)^2 + \iota \left(\frac{\partial^p \hat{u}^\delta}{\partial \xi^p} \right)^2 \right) w_{\alpha, \beta} d\xi &= -\frac{1}{2} \int_{-1}^1 \frac{\partial (\hat{u}^\delta)^2}{\partial \xi} w_{\alpha, \beta}(\xi) d\xi \\
&- (\hat{u}_L^{\delta I} - \hat{u}_L^\delta) \int_{-1}^1 \left(\frac{\partial h_L \hat{u}^\delta}{\partial \xi} \right) w_{\alpha, \beta} d\xi \quad (5.42) \\
&- (\hat{u}_R^{\delta I} - \hat{u}_R^\delta) \int_{-1}^1 \left(\frac{\partial h_R \hat{u}^\delta}{\partial \xi} \right) w_{\alpha, \beta} d\xi
\end{aligned}$$

In order to find correction functions that can meet the conditions of Eq. (5.40 & 5.41) we need to define the projection of \hat{u}^δ , h_L , and h_R into the Jacobi polynomial basis. For this we will use Eq. (5.4) and:

$$h_L = \sum_{i=0}^{p+1} \tilde{h}_{L,i} J_i^{(\alpha, \beta)} \quad \text{and} \quad h_R = \sum_{i=0}^{p+1} \tilde{h}_{R,i} J_i^{(\alpha, \beta)} \quad (5.43)$$

With these definitions, we may now substitute Eq. (5.43) into Eq. (5.40) to get:

$$\int_{-1}^1 \left(\sum_{i=0}^{p+1} \sum_{j=0}^p \tilde{h}_{L,i} \tilde{u}_j J_i^{(\alpha, \beta)} \frac{dJ_j^{(\alpha, \beta)}}{d\xi} \right) w_{\alpha, \beta} d\xi - \tilde{u}_p \tilde{h}_{L,p+1} b_p^{(\alpha, \beta)} b_{p+1}^{(\alpha, \beta)} q_0^{(\alpha, \beta)} = 0 \quad (5.44)$$

To solve this integral condition we may constrain \tilde{h}_L , without loss of generality, to only have terms in $p-1$, p , and $p+1$. We then observe that the only contribution to the equality in Eq. (5.44) is from the $p-1$ th term of \tilde{h}_L . Therefore, if we can find a closed form of $D_{p-1,p-1}(\alpha+1,\beta+1,\alpha,\beta)$ we can relate $\tilde{h}_{L,p-1}$ to $\tilde{h}_{L,p+1}$ through ι . Hence, substituting the values into Eq. (5.15) we find that the hypergeometric function component becomes ${}_3F_2(0,\dots;1)$ and, from the definition of the rising Pochhammer function, this must have a value of unity. Hence, we may write:

$$D_{p-1,p-1}(\alpha+1,\beta+1,\alpha,\beta) = \frac{(2p+\alpha+\beta-1)(2p+\alpha+\beta)}{2(p+\alpha+\beta)} \quad (5.45)$$

which leads to:

$$\iota = \frac{\tilde{h}_{L,p-1}}{\tilde{h}_{L,p+1}} \underbrace{\left(\frac{(p+\alpha+\beta+1)(p+\alpha+\beta+2)_{p-1} q_{p-1}^{(\alpha,\beta)}}{2(p+\alpha+\beta)_{p-1} b_p^{(\alpha,\beta)} b_{p+1}^{(\alpha,\beta)} q_0^{(\alpha,\beta)}} \right)}_{A_p} \quad (5.46)$$

Using the fact that $h_L(-1) = 1$ and $h_L(1) = 0$ we find:

$$(-1)^p = \tilde{h}_{L,p} \underbrace{\left(\frac{(\beta+1)_p}{p!} \left[\left(\frac{p+\alpha}{p+\beta} \right) \frac{\iota p(p+1) + (p+\beta)(p+\beta+1)A_p}{\iota p(p+1) + (p+\alpha)(p+\alpha+1)A_p} + 1 \right] \right)}_{\kappa_p^{(\alpha,\beta)}} \quad (5.47)$$

$$\tilde{h}_{L,p+1} = -\frac{A_p J_p^{(\alpha,\beta)}(1) \tilde{h}_{L,p}}{\iota J_{p-1}^{(\alpha,\beta)}(1) + A_p J_{p+1}^{(\alpha,\beta)}(1)} = -\frac{A_p(p+1)(p+\alpha) \tilde{h}_{L,p}}{\iota p(p+1) + (p+\alpha+1)(p+\alpha)A_p} \quad (5.48)$$

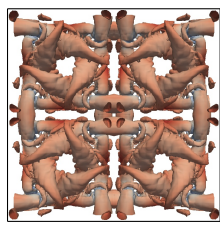
Repeating for the right and putting this all together we obtain:

$$h_L = \frac{(-1)^p}{\kappa_p^{(\alpha,\beta)}} \left(J_p^{(\alpha,\beta)} - \frac{\iota(p+1)(p+\alpha) J_{p-1}^{(\alpha,\beta)} + (p+1)(p+\alpha) A_p J_{p+1}^{(\alpha,\beta)}}{\iota p(p+1) + (p+\alpha+1)(p+\alpha) A_p} \right) \quad (5.49)$$

$$h_R = \frac{1}{\kappa_p^{(\beta,\alpha)}} \left(J_p^{(\alpha,\beta)} + \frac{\iota(p+1)(p+\beta) J_{p-1}^{(\alpha,\beta)} + (p+1)(p+\beta) A_p J_{p+1}^{(\alpha,\beta)}}{\iota p(p+1) + (p+\beta+1)(p+\beta) A_p} \right) \quad (5.50)$$

Spectral Difference Schemes

We will now use the results found in the preceding section to define a useful subset of correction functions. It has been shown [65, 73, 160] that FR is able to recover SD schemes [80, 96, 140] for equation sets with homogeneous linear flux functions. The implication being that the treatment of aliasing, introduced by non-linear or heterogeneous flux functions, is different in FR to a native SD scheme. To obtain an SD scheme within



FR the roots in the interior of the reference domain for the left and right correction functions must be the same, i.e. $h_L(\xi_z) = h_R(\xi_z) = 0$ for $\xi_z \in (-1, 1)$.

The simplest method of achieving this is by prescribing the interior zeros to be a set of quadrature points. In the first proof of energy stability of SD schemes the canonical Gauss–Legendre quadrature [73] was utilised, but other quadratures have been considered. For example, Lui et al. [96] saw the potential for a Gauss–Legendre–Lobatto quadrature, which is similar to the early spectral collocation methods [114]. As the choice of quadrature is arbitrary, it is proposed that this is extended to the full set of Gauss–Jacobi quadratures, where the p^{th} Gauss–Jacobi points are the roots of the p^{th} order Jacobi polynomial [83]. These gives rise to the correction functions:

$$h_{L,\text{SD}} = \frac{(1-\xi) J_p^{(\alpha,\beta)}(\xi)}{2 J_p^{(\alpha,\beta)}(-1)} \quad \text{and} \quad h_{R,\text{SD}} = \frac{(1+\xi) J_p^{(\alpha,\beta)}(\xi)}{2 J_p^{(\alpha,\beta)}(1)} \quad (5.51)$$

where the correction functions are normalised for the edge value, as Jacobi polynomials do not guarantee unit magnitude at ± 1 . The recurrence relation for Jacobi polynomials [19] leads us to the following form:

$$\begin{aligned} h_{L,\text{SD}} = & \left(-\frac{(p+\alpha)(p+\beta)}{(2p+\alpha+\beta+1)(2p+\alpha+\beta)} J_p^{(\alpha,\beta)} \right. \\ & + \frac{1}{2} \left(1 + \frac{\alpha^2 - \beta^2}{(2p+\alpha+\beta+2)(2p+\alpha+\beta)} \right) J_p^{(\alpha,\beta)} \\ & \left. - \frac{(p+1)(p+1+\alpha+\beta)}{(2p+\alpha+\beta+1)(2p+\alpha+\beta+2)} J_{p+1}^{(\alpha,\beta)} \right) \frac{(-1)^p \Gamma(p+1) \Gamma(\beta+1)}{\Gamma(p+\beta+1)} \end{aligned} \quad (5.52)$$

and

$$\begin{aligned} h_{R,\text{SD}} = & \left(\frac{(p+\alpha)(p+\beta)}{(2p+\alpha+\beta+1)(2p+\alpha+\beta)} J_p^{(\alpha,\beta)} \right. \\ & + \frac{1}{2} \left(1 - \frac{\alpha^2 - \beta^2}{(2p+\alpha+\beta+2)(2p+\alpha+\beta)} \right) J_p^{(\alpha,\beta)} \\ & \left. + \frac{(p+1)(p+1+\alpha+\beta)}{(2p+\alpha+\beta+1)(2p+\alpha+\beta+2)} J_{p+1}^{(\alpha,\beta)} \right) \frac{\Gamma(p+1) \Gamma(\alpha+1)}{\Gamma(p+\alpha+1)} \end{aligned} \quad (5.53)$$

This method's advantage in extending the set of SD correction functions is that we may use the work of the previous section in order to prove the theoretical energy stability. We therefore assert:

Lemma 5.3.1. *SD Energy Stability. A given SD correction function with $\alpha, \beta \in (-1, \infty)$ will always give $\|\hat{u}^\delta\|_{W_2^{t,w}}$ to be positive and hence is a valid norm.*

Proof. Using Eq.(5.46) to produce an expression of ι for SD schemes, which, after normalisation by ι_{crit} , gives:

$$\frac{\iota_{\text{SD}}}{\iota_{\text{crit}}} = \frac{p}{p+1} \quad (5.54)$$

As ι_{crit} is always positive, so must ι_{SD} always be positive. \square

Lastly, we will note that this definition of SD schemes may be extended to include all quadratures in $[-1, 1]$ by defining the correction function as:

$$h_L = \frac{(1-\xi)}{2} \frac{J_m^{(\alpha,\beta)}(\xi)}{J_m^{(\alpha,\beta)}(-1)} \quad \text{for } |m|_1 = p \quad (5.55)$$

where $m = (m_1, m_2 \dots)$ is a multi-index and (α, β) may vary with m_i . This is included for completeness, however the focus will be on the Jacobi SD function of Eq.(5.51).

To briefly touch on some characteristics of the Jacobi SD correction function, consider the Gauss–Jacobi quadratures that make up the interior zeros of the correction function. Figure 5.1 aims to demonstrate how the quadrature is affected by the variation of α and β , primarily that for $\alpha = \beta$ the quadrature is symmetric. Furthermore, in the limit as $\alpha, \beta \rightarrow -1$ the quadrature gets pinned to the edges and as $\alpha, \beta \rightarrow \infty$ the quadrature gets compressed to the middle. The effect this has for the case when $\alpha \neq \beta$ is that the left and right correction functions are asymmetric, this also a property of GJFR correction function in general.

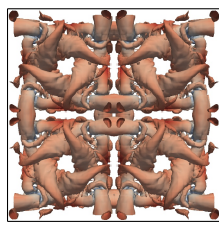
Previously, in the work by Huynh [65], symmetry of the correction function was dictated without explicit reason, similarly Vincent et al. [160] gave no explicit reason for symmetry. In reality the above definitions show that asymmetric correction function are possible and stable. Yet for some practical purposes it is common sense to use symmetric correction functions, as this will result in the same wave propagation properties in all directions. However, asymmetry may be a useful property for example in the implementation of non-reflecting boundary conditions. However, here we will generally only consider the symmetric case of $\alpha = \beta$.

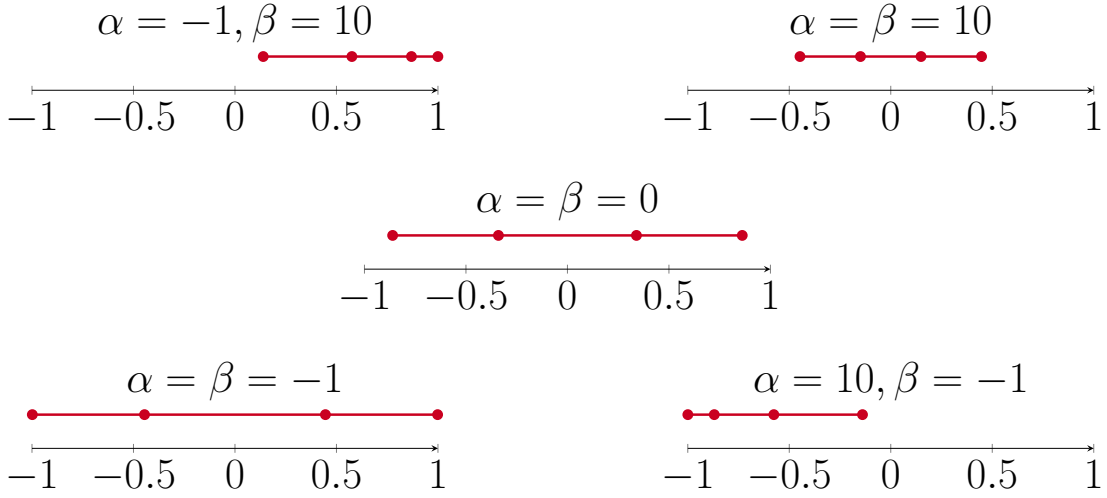
5.3.3 Generalised Sobolev Norm — Generalised Sobolev Stable FR

We now move onto defining GSFR correction functions, for which we again use the flux reconstructed form of the first order conservation law with unit convective velocity ($\hat{f}^\delta = \hat{u}^\delta$):

$$\frac{\partial \hat{u}^\delta}{\partial t} = -\frac{\partial \hat{u}^\delta}{\partial \xi} - (\hat{u}_L^{\delta I} - \hat{u}_L^\delta) \frac{dh_L}{d\xi} - (\hat{u}_R^{\delta I} - \hat{u}_R^\delta) \frac{dh_R}{d\xi} \quad (5.56)$$

Hence, we undertake defining the modified broken Sobolev norm from Eq. (5.56), which is performed via summation of recursive differentiation and multiplication of the variable



Fig. 5.1 Selected Gauss-Jacobi quadratures for $n = 4$.

with subsequent integration over the sub-domain to give:

$$\begin{aligned} \frac{1}{2} \frac{d}{dt} \int_{-1}^1 \sum_{i=0}^p \iota_i (\hat{u}^{\delta(i)})^2 d\xi &= - \underbrace{\frac{1}{2} \int_{-1}^1 \sum_{i=0}^p \iota_i \frac{\partial}{\partial \xi} \left(\frac{\partial^i \hat{u}^\delta}{\partial \xi^i} \right)^2 d\xi}_{I_D} - (\hat{u}_L^{\delta I} - \hat{u}_L^\delta) \underbrace{\int_{-1}^1 \sum_{i=0}^p \iota_i \frac{\partial^i \hat{u}^\delta}{\partial \xi^i} \frac{d^{i+1} h_L}{d\xi^{i+1}} d\xi}_{I_L} \\ &\quad - (\hat{u}_R^{\delta I} - \hat{u}_R^\delta) \underbrace{\int_{-1}^1 \sum_{i=0}^p \iota_i \frac{\partial^i \hat{u}^\delta}{\partial \xi^i} \frac{d^{i+1} h_R}{d\xi^{i+1}} d\xi}_{I_R} \quad (5.57) \end{aligned}$$

when I_D is combined with one round of integration by parts of I_L and I_R for $i = 0$ to form the conservation terms required for stability. Further details on this derivation can be found in Appendix C, but the result is that the following conditions are imposed on the correction functions:

$$\sum_{i=0}^p \iota_i \int_{-1}^1 \frac{d^i h_L}{d\xi^i} \frac{\partial^{i+1} \hat{u}^\delta}{\partial \xi^{i+1}} d\xi = \sum_{i=1}^p \iota_i \left| \frac{\partial^i \hat{u}^\delta}{\partial \xi^i} \frac{d^i h_L}{d\xi^i} \right|_{-1}^1 \quad (5.58)$$

$$\sum_{i=0}^p \iota_i \int_{-1}^1 \frac{d^i h_R}{d\xi^i} \frac{\partial^{i+1} \hat{u}^\delta}{\partial \xi^{i+1}} d\xi = \sum_{i=1}^p \iota_i \left| \frac{\partial^i \hat{u}^\delta}{\partial \xi^i} \frac{d^i h_R}{d\xi^i} \right|_{-1}^1 \quad (5.59)$$

If the correction functions and solution are taken as being a series of Legendre polynomials:

$$h_L(\xi) = \sum_{i=0}^{p+1} \tilde{h}_{L,i} \psi_i(\xi) \quad \text{and} \quad \hat{u}^\delta(\xi) = \sum_{i=0}^p \tilde{u}_i \psi_i(\xi) \quad (5.60)$$

then it is possible to find a closed set of equations that define $\tilde{h}_{L,i}$ in terms of ι_i . Legendre polynomials are chosen as their weighting function for the orthogonality condition is unity, greatly simplifying later derivations. Therefore, substitution of Eq. (5.60) into Eq. (5.58) gives:

$$\sum_{i=0}^p \iota_i \int_{-1}^1 \left[\sum_{n=0}^{p+1} \sum_{m=0}^p \tilde{h}_{L,n} \tilde{u}_m \frac{d^i \psi_n}{d\xi^i} \frac{d^{i+1} \psi_m}{d\xi^{i+1}} \right] d\xi - \sum_{i=1}^p \iota_i \left| \sum_{n=0}^{p+1} \sum_{m=0}^p \tilde{h}_{L,n} \tilde{u}_m \frac{d^i \psi_n}{d\xi^i} \frac{d^i \psi_m}{d\xi^i} \right|_{-1}^1 = 0 \quad (5.61)$$

To remove solution dependency from the correction function definition each \tilde{u}_m must be solved separately. Hence, this may be cast as a closed set of linear equations of the form:

$$\mathbf{L}_p \mathbf{h}_L = \begin{bmatrix} 0 & \dots & 0 & 1 \end{bmatrix}^T \quad (5.62)$$

where the penultimate entries of Eq. (5.62) are the enforcement of the boundary conditions on h_L , and, due to these boundary conditions, \mathbf{L}_p is a square matrix. The other rows are then the conditions for each \tilde{u}_m . The general form of the entries of \mathbf{L}_p can be written as:

$$\mathbf{L}_p[m-1][n] = \sum_{i=0}^p \iota_i \int_{-1}^1 \frac{d^i \psi_n}{d\xi^i} \frac{d^{i+1} \psi_m}{d\xi^{i+1}} d\xi - \sum_{i=1}^p \iota_i \left| \frac{d^i \psi_n}{d\xi^i} \frac{d^i \psi_m}{d\xi^i} \right|_{-1}^1 \quad (5.63)$$

where $m, n \in \mathbb{N}$ with $1 \leq m \leq p$ and $0 \leq n \leq p+1$. The $m=0$ case is removed as it is identically zero, and the final two rows will come from the boundary conditions on $h_L(\xi)$. To evaluate Eq. (5.63), it can be useful to consider the following result of Miller [105], which we modify to consider Legendre polynomials and the prescribed relationship of the derivatives.

$$\int_{-1}^1 \frac{d^m \psi_n}{d\xi^m} \frac{d^{m+1} \psi_k}{d\xi^{m+1}} d\xi = \sum_{i=0}^{\lfloor \frac{n-m}{2} \rfloor} \sum_{j=0}^{\lfloor \frac{k-m-1}{2} \rfloor} \frac{b_i(m,n) b_j(m+1,k)}{n+k-2(m+i+j)} [1 - (-1)^{n+k-2(m+i+j)}] \quad (5.64)$$

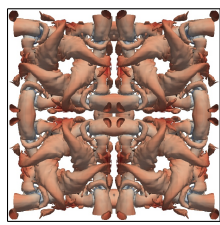
where we define:

$$b_i(m,n) = \frac{(-1)^i (2(n-i))!}{2^n (n-m-2i)! (n-i)! i!} \quad (5.65)$$

Then for the gradient of Legendre polynomials at the end point:

$$\frac{d^n \psi_j(-1)}{d\xi^n} = \frac{(-1)^{j-n} (j+n)!}{2^n n! (j-n)!} \quad \text{and} \quad \frac{d^n \psi_j(1)}{d\xi^n} = \frac{(1)^{j-n} (j+n)!}{2^n n! (j-n)!} \quad \text{for } j \geq n \quad (5.66)$$

which can be inferred from the work of Garfinkel [51] and Holdeman [61]. With these identities established specific examples may now be evaluated.



GSFR for $p = 2$

For the case of $p = 2$ the generalised correction function equation can be found to be:

$$\mathbf{L}_2 \tilde{\mathbf{h}}_L = \begin{bmatrix} -\iota_0 & 0 & 3\iota_1 & 0 \\ 0 & -\iota_0 & 0 & 15(\iota_1 + 3\iota_2) \\ 1 & 1 & 1 & 1 \\ 1 & -1 & 1 & -1 \end{bmatrix} \tilde{\mathbf{h}}_L = \begin{bmatrix} 0 \\ 0 \\ 0 \\ 1 \end{bmatrix} \quad (5.67)$$

And upon assessment of the limits presented by Eq. (5.28), the limits on \mathbf{I}_2 can be found to be:

$$\begin{bmatrix} 0 \\ -\frac{1}{2}\left(\frac{2}{3}\iota_0\right) \\ -\frac{1}{3}\left(\frac{2}{5}\iota_0 + 6\iota_1\right) \end{bmatrix} < \begin{bmatrix} \iota_0 \\ \iota_1 \\ \iota_2 \end{bmatrix} = \mathbf{I}_2 < \infty \quad (5.68)$$

GSFR for $p = 3$

$$\begin{bmatrix} -\iota_0 & 0 & 3\iota_1 & 0 & 10\iota_1 \\ 0 & -\iota_0 & 0 & 15(\iota_1 + 3\iota_2) & 0 \\ -\iota_0 & 0 & -(\iota_0 - 3\iota_1) & 0 & 15(3\iota_1 + 35\iota_2 + 105\iota_3) \\ 1 & 1 & 1 & 1 & 1 \\ 1 & -1 & 1 & -1 & 1 \end{bmatrix} \tilde{\mathbf{h}}_L = \begin{bmatrix} 0 \\ 0 \\ 0 \\ 0 \\ 1 \end{bmatrix} \quad (5.69)$$

Evaluating Eq. (5.28), the condition necessary for valid correction functions is:

$$0 < 2\iota_0 \tilde{u}_0^2 + \left(\frac{2}{3}\iota_0 + \iota_1\right) \tilde{u}_1^2 + \left(\frac{2}{5}\iota_0 + 6\iota_1 + 18\iota_2\right) \tilde{u}_2^2 + \left(\frac{2}{7}\iota_0 + 8\iota_1 + 150\iota_2 + 255\iota_3\right) \tilde{u}_3^2 + \iota_1 (\tilde{u}_1 + 2\tilde{u}_3)^2 < \infty \quad (5.70)$$

Due to the final term in Eq. (5.70), the transformation of this to a necessary condition on \mathbf{I}_3 is difficult. However, it can lead to a sufficient condition on the range of validity for \mathbf{I}_3 :

$$\begin{bmatrix} 0 \\ 0 \\ -\frac{1}{18}\left(\frac{2}{5}\iota_0 + 6\iota_1\right) \\ -\frac{1}{255}\left(\frac{2}{7}\iota_0 + 8\iota_1 + 150\iota_2\right) \end{bmatrix} < \mathbf{I}_3 < \infty \quad (5.71)$$

GSFR for $p = 4$

$$\begin{bmatrix}
\iota_0 & 0 & 3\iota_1 & 0 \\
0 & \iota_0 & 0 & 15(\iota_1 + 3\iota_2) \\
\iota_0 & 0 & (\iota_0 + 3\iota_1) & 0 \\
0 & \iota_0 & 0 & (-\iota_0 + 15\iota_1 + 150\iota_2) \\
1 & 1 & 1 & 1 \\
1 & -1 & 1 & -1
\end{bmatrix}
\begin{bmatrix}
10\iota_1 & 0 \\
0 & (42\iota_1 + 315\iota_2) \\
15(3\iota_1 + 35\iota_2 + 105\iota_3) & 0 \\
0 & 105(\iota_1 + 31\iota_2 - 63\iota_3 + 945\iota_4) \\
1 & 1 \\
1 & -1
\end{bmatrix}
\tilde{\mathbf{h}}_1 = \begin{bmatrix} 0 \\ 0 \\ 0 \\ 0 \\ 0 \\ 1 \end{bmatrix} \quad (5.72)$$

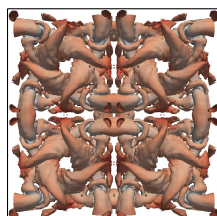
Evaluating Eq.(5.28) to find the necessary limits on validity:

$$\begin{aligned}
0 < 2\iota_0\tilde{u}_0^2 + \left(\frac{2}{3}\iota_0 + \iota_1\right)\tilde{u}_1^2 + \left(\frac{2}{5}\iota_0 + 2\iota_1 + 9\iota_2\right)\tilde{u}_2^2 + \left(\frac{2}{7}\iota_0 + 8\iota_1 + 150\iota_2 + 450\iota_3\right)\tilde{u}_3^2 \\
+ \left(\frac{2}{9}\iota_0 + 11\iota_1 + 290\iota_2 + 7350\iota_3 + 11025\iota_4\right)\tilde{u}_4^2 \\
+ \iota_1(2\tilde{u}_2 + 3\tilde{u}_4)^2 + \iota_1(\tilde{u}_1 + 2\tilde{u}_3)^2 + \iota_2(3\tilde{u}_2 + 20\tilde{u}_4)^2 < \infty \quad (5.73)
\end{aligned}$$

And hence, with the same reasoning as for $p = 3$, the sufficient conditions on \mathbf{I}_4 for valid correction functions are:

$$\begin{bmatrix}
0 \\
0 \\
0 \\
-\frac{1}{450}\left(\frac{2}{7}\iota_0 + 8\iota_1 + 150\iota_2\right) \\
-\frac{1}{105^2}\left(\frac{2}{9}\iota_0 + 11\iota_1 + 290\iota_2 + 7350\iota_3\right)
\end{bmatrix} < \mathbf{I}_4 < \infty \quad (5.74)$$

At this point it is worth noting the recursive nature of the matrix \mathbf{L}_p . Hence the set of correction functions at p is the union of the p^{th} order correction functions and the correction functions defined by \mathbf{L}_{p-1} and so on recursively down to the empty set. So if the p^{th} order correction function is defined by some eigenfunction \mathbf{c}_p then the space of correction functions is defined as $\oplus_{i=0}^p \mathbf{c}_i$, *i.e.* each time the order is increased, one extra eigenfunction is introduced. However, in the special case of $\mathbf{I}_p = [1, 0, \dots]^T$, the set of



correction functions collapse to a single value, unique for each p . This is an interesting property that is explored through the GLSFR correction function set.

To show that these correction functions are in fact unique by comparison to both the OSFR and the ESFR, an attempt must be made to reconstruct the GSFR correction functions in both the ESFR and the OSFR setting. Starting with OSFR, this method defines only the free parameter ι , as described in Eq. (5.30 & 5.32). Taking $p = 3$ and defining some arbitrary stable value of \mathbf{I}_3 , the equivalent value of ι can be found using the value of $\tilde{\mathbf{h}}_{p+1}$ found from Eq. (5.69). Hence:

$$\iota = \frac{1}{(2p+1)(a_p p!)^2} \left(\frac{(-1)^{p+1}}{2\tilde{\mathbf{h}}_{p+1}} - 1 \right) \quad (5.75)$$

To then compare to ESFR, it is easier to consider the gradient of h_L , defined in Eq. (B.1), and defining the Legendre polynomial weights of GSFR similarly as $\tilde{\mathbf{g}}_L$. Then for the case of $p = 3$ the corresponding ESFR weights can be found, using Eq. (B.11) from Vincent et al. [162], as:

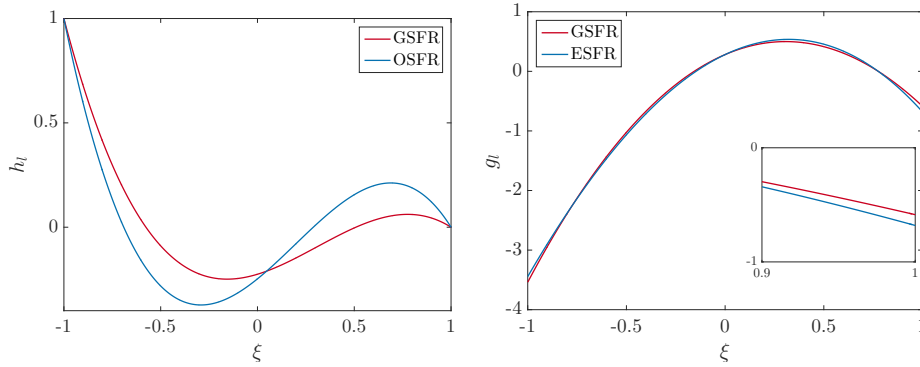
$$\kappa_1 = -\left(\frac{1}{\tilde{\mathbf{g}}_{L,2}} + \frac{2}{5} \right) \quad (5.76)$$

$$\kappa_0 = \frac{175\kappa_1^2 \tilde{\mathbf{g}}_{L,1} + 105\kappa_1 - 12\tilde{\mathbf{g}}_{L,1} + 18}{42\tilde{\mathbf{g}}_{L,1} - 63} \quad (5.77)$$

It can then be further shown that to be an ESFR correction function for $p = 3$, the following must be satisfied, together with Eq. (5.76):

$$\frac{175\kappa_1^2 \tilde{\mathbf{g}}_{L,3} + 105\kappa_1 + 42 - 12\tilde{\mathbf{g}}_{L,3}}{42\tilde{\mathbf{g}}_{L,3}} = \frac{175\kappa_1^2 \tilde{\mathbf{g}}_{L,1} + 105\kappa_1 - 12\tilde{\mathbf{g}}_{L,1} + 18}{42\tilde{\mathbf{g}}_{L,1} - 63} \quad (5.78)$$

where κ_1 is defined by Eq. (5.76). As is shown in Fig. 5.2, the correction functions found by satisfying Eq.(5.58 & 5.59) are in fact different from those defined by OSFR and ESFR. Furthermore, for OSFR it is trivial to show that it is a sub-set of GSFR — from their respective definitions, OSFR can be constructed when $\mathbf{I}_p = [1, \dots, 1]^T$. The ESFR norm definition detailed in [162] can be used to show ESFR is a subset of GSFR. This result could be expected as both OSFR and ESFR were found to be Sobolev stable. To find the corresponding values of \mathbf{I}_p for a given h_L , originating from either OSFR or ESFR, the subject of the equation defining the GSFR correction must be changed to \mathbf{I}_p . In the



(a) Left correction function comparison between OSFR and GSFR. (b) Left correction function gradient comparison between ESFR and GSFR.

Fig. 5.2 Comparison of OS, ES and GS correction functions. For $p = 3$ and taking $\mathbf{I}_3 = [1, 0.01, 0.01, 0.1]^T$.

case of $p = 3$ and setting $\iota_0 = 1$, this takes the form:

$$\underbrace{\begin{bmatrix} 3\tilde{\mathbf{h}}_{L,2} + 10\tilde{\mathbf{h}}_{L,4} & 0 & 0 \\ 15\tilde{\mathbf{h}}_{L,3} & 45\tilde{\mathbf{h}}_{L,3} & 0 \\ 3\tilde{\mathbf{h}}_{L,2} + 45\tilde{\mathbf{h}}_{L,4} & 525\tilde{\mathbf{h}}_{L,4} & 1575\tilde{\mathbf{h}}_{L,4} \end{bmatrix}}_{\mathbf{H}_3} \begin{bmatrix} \iota_1 \\ \iota_2 \\ \iota_3 \end{bmatrix} = \begin{bmatrix} \tilde{\mathbf{h}}_{L,0} \\ \tilde{\mathbf{h}}_{L,1} \\ \tilde{\mathbf{h}}_{L,0} + \tilde{\mathbf{h}}_{L,2} \end{bmatrix} \quad (5.79)$$

Hence, ESFR and OSFR are both recoverable from GSFR. The exception to the invertibility of \mathbf{H}_3 over the set of ESFR and OSFR is when either $\tilde{\mathbf{h}}_{L,3} = 0$ or $\tilde{\mathbf{h}}_{L,4} = 0$, as GSFR has multiple ways of constructing these lower order correction functions.

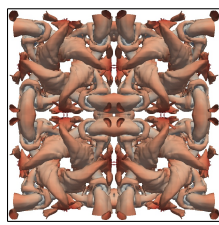
5.3.4 Lebesgue Norm — Generalised Lebesgue Stable FR

We will now look for corrections that satisfy the stability criterion, $d(\|u\|_{n,L^2})/dt \leq 0$, in this norm for the 1D FR conservation law:

$$\frac{\partial \hat{u}^\delta}{\partial t} = -\frac{\partial \hat{f}^\delta}{\partial \xi} - (\hat{f}_L^{\delta I} - \hat{f}_L^\delta) \frac{dh_L}{d\xi} - (\hat{f}_R^{\delta I} - \hat{f}_R^\delta) \frac{dh_R}{d\xi}$$

If the flux function is set such that linear advection is solved, then $\hat{f}^\delta = \hat{u}^\delta$. This then implies that:

$$\frac{\partial \hat{u}^\delta}{\partial t} = -\frac{\partial \hat{u}^\delta}{\partial \xi} - (\hat{u}_L^{\delta I} - \hat{u}_L^\delta) \frac{dh_L}{d\xi} - (\hat{u}_R^{\delta I} - \hat{u}_R^\delta) \frac{dh_R}{d\xi} \quad (5.80)$$



Multiplying Eq. (5.56) by the discontinuous conserved variable and integrating over the sub-domain:

$$\int_{-1}^1 \hat{u}^\delta \frac{\partial \hat{u}^\delta}{\partial t} d\xi = - \int_{-1}^1 \hat{u}^\delta \frac{\partial \hat{u}^\delta}{\partial \xi} d\xi - (\hat{u}_L^{\delta I} - \hat{u}_L^\delta) \int_{-1}^1 \hat{u}^\delta \frac{dh_L}{d\xi} d\xi - (\hat{u}_R^{\delta I} - \hat{u}_R^\delta) \int_{-1}^1 \hat{u}^\delta \frac{dh_R}{d\xi} d\xi \quad (5.81)$$

Applying the product rule and integration by parts to Eq. (5.81), the rate of energy decay of FR – which may also be recognised as the rate of change of the Lebesgue norm – is:

$$\begin{aligned} \frac{1}{2} \frac{d}{dt} \int_{-1}^1 (\hat{u}^\delta)^2 d\xi = & -\frac{1}{2} \int \frac{\partial (\hat{u}^\delta)^2}{\partial \xi} \xi + (\hat{u}_L^{\delta I} - \hat{u}_L^\delta) \hat{u}_L^\delta - (\hat{u}_R^{\delta I} - \hat{u}_R^\delta) \hat{u}_R^\delta \\ & + (\hat{u}_L^{\delta I} - \hat{u}_L^\delta) \underbrace{\int_{-1}^1 h_L \frac{\partial \hat{u}^\delta}{\partial \xi} d\xi}_{I_L} \\ & + (\hat{u}_R^{\delta I} - \hat{u}_R^\delta) \underbrace{\int_{-1}^1 h_R \frac{\partial \hat{u}^\delta}{\partial \xi} d\xi}_{I_R} \end{aligned} \quad (5.82)$$

If the integrals I_L and I_R are set equal to zero, then Eq. (5.82) may be reduced to:

$$\frac{1}{2} \frac{d}{dt} \int_{-1}^1 (\hat{u}^\delta)^2 d\xi = \frac{1}{2} ((\hat{u}_L^\delta)^2 - (\hat{u}_R^\delta)^2) + (\hat{u}_L^{\delta I} \hat{u}_L^\delta - \hat{u}_R^{\delta I} \hat{u}_R^\delta) \quad (5.83)$$

This can be further simplified into an expression for the transfer of energy across the boundary.

$$\frac{1}{2} \frac{d}{dt} \int_{-1}^1 (\hat{u}^\delta)^2 d\xi = \frac{1}{2} (2\hat{u}_L^{\delta I} - \hat{u}_L^\delta) \hat{u}_L^\delta - \frac{1}{2} (2\hat{u}_R^{\delta I} - \hat{u}_R^\delta) \hat{u}_R^\delta \quad (5.84)$$

and hence the energy stability after setting of the correction is controlled by the method used for interface calculation. In order to extract a condition in which $I_L = I_R = 0$, it is useful to consider the orthogonal polynomial basis, by using Eq. (5.3) and using the similar basis for the correction function as in Eq. (5.60). It may be useful at this point to be reminded of the result for Legendre polynomials [61], caused by their alternating odd-even nature:

$$\int_{-1}^1 \psi_l(\xi) \frac{d\psi_m(\xi)}{d\xi} d\xi = \begin{cases} 2, & \text{for } l/2 - \lfloor l/2 \rfloor \neq m/2 - \lfloor m/2 \rfloor, \quad l \leq m \\ 0, & \text{otherwise} \end{cases} \quad (5.85)$$

Initially focusing on the condition $I_L = 0$, the family of correction functions is found by satisfaction of the following:

$$\sum_{\substack{i=0 \\ i=\text{even}}}^{p-1} \tilde{h}_{L,i} = 0 \quad \text{and} \quad \sum_{\substack{i=0 \\ i=\text{odd}}}^{p-1} \tilde{h}_{L,i} = 0 \quad (5.86)$$

By enforcing the boundary conditions, namely: $h_L(-1) = 1$ and $h_L(1) = 0$, the final conditions on $\tilde{\mathbf{h}}_L$ may be found as:

$$\tilde{h}_{L,p+1} = \frac{(-1)^{p+1}}{2} \quad \text{and} \quad \tilde{h}_{L,p} = \frac{(-1)^p}{2} \quad (5.87)$$

By modifying the boundary conditions, conditions can be similarly defined for $I_R = 0$. The conditions $I_L = 0$ and $I_R = 0$ could be independently satisfied, however this can cause asymmetric correction functions. To enforce symmetry, if one condition is satisfied, and the following is applied:

$$\tilde{\mathbf{h}}_l = \text{diag}(-1, 1, -1 \dots) \tilde{\mathbf{h}}_r = \Lambda \tilde{\mathbf{h}}_r \quad (5.88)$$

Then symmetry is strictly enforced, and due to alternating positive-negative nature of Λ Eq. (5.86) is still enforced.

It can be seen by comparison to the OSFR scheme of Eq. (5.30) that this new set of correction functions are coincident with the previous family of corrections at only one point, $\eta_p = 0$, corresponding to Nodal DG or when the terms of Eq. (5.86) are all zero. Owing to the space this scheme inhabits and the method used to define it, this new set of corrections will henceforth be called Generalised Lebesgue Stable FR, GLSFR.

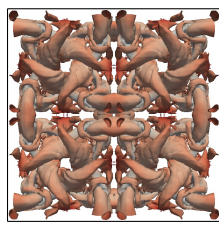
It may at this point be thought that the highly arbitrary family of correction functions that satisfy Eq. (5.86) may lead to the injection or sink of mass into the sub-elements. To placate this fear we consider the integration of Eq. (5.1) over the sub-domain, *i.e.* the rate of change of mass in the sub-domain:

$$\frac{d}{dt} \int_{-1}^1 \hat{u}^\delta d\xi = - \int_{-1}^1 \frac{\partial \hat{f}^\delta}{\partial \xi} d\xi - (\hat{f}_L^{\delta I} - \hat{f}_L^\delta) \int_{-1}^1 \frac{dh_L}{d\xi} d\xi - (\hat{f}_R^{\delta I} - \hat{f}_R^\delta) \int_{-1}^1 \frac{dh_R}{d\xi} d\xi \quad (5.89)$$

and considering the constraints on h_L and h_R , this becomes:

$$\frac{d}{dt} \int_{-1}^1 \hat{u}^\delta d\xi = (\hat{f}_L^\delta - \hat{f}_R^\delta) + (\hat{f}_L^{\delta I} - \hat{f}_L^\delta) - (\hat{f}_R^{\delta I} - \hat{f}_R^\delta) \quad (5.90)$$

$$= \hat{f}_L^{\delta I} - \hat{f}_R^{\delta I} \quad (5.91)$$



Hence, the rate of mass accumulation within an element is dependent on the interface calculation, the flux function, and, as was shown in Chapter 4, mesh deformation. But it is not dependent on the correction function, so long as the boundary conditions are fully enforced.

5.4 Analytical Findings

The investigation of correction functions has, so far, been focused on functional analysis, sitting at a high level, and ensuring an abstract form of stability. To give more meaningful insight into the behaviour of the sets of FR schemes defined, we wish to perform a Fourier and von Neumann analysis. Here we will inspect the spectral properties and ergodicity of FR applied to the linear advection and advection-diffusion equations for harmonic solutions. This form of analysis was outlined by Lele [89], for finite difference and applied to DG by Hu et al. [64] and Hesthaven & Warburton [60].

The analytical techniques were then adapted to FR by Huynh [65] and Vincent et al. [161], with the techniques extended to the fully discrete equations by Vermeire et al. [157] and Trojak et al. [150]. The formulation and structure of the analysis presented here follows that of Trojak et al. [149], which was also discussed in Chapter 4. We reiterate the outline of the analysis here for ease and to allow presentation of the extension to diffusion equations. It will be assumed here that a uniform grid is used. Starting with the semi-discrete matrixised form of FR applied to the linear advection equation:

$$\frac{\partial \mathbf{u}_j}{\partial t} = -J_j^{-1} (\mathbf{C}_+ \mathbf{u}_{j+1} - \mathbf{C}_0 \mathbf{u}_j - \mathbf{C}_- \mathbf{u}_{j-1}) \quad (5.92)$$

where the matrixised operators are defined as:

$$\mathbf{C}_+ = (1 - \alpha) \mathbf{g}_R \mathbf{l}_L^T \quad (5.93)$$

$$\mathbf{C}_0 = \mathbf{D} - \alpha \mathbf{g}_L \mathbf{l}_L^T - (1 - \alpha) \mathbf{g}_R \mathbf{l}_R^T \quad (5.94)$$

$$\mathbf{C}_- = \alpha \mathbf{g}_L \mathbf{l}_R^T \quad (5.95)$$

As before, \mathbf{D} is the discrete differentiation operator, \mathbf{g}_L and \mathbf{g}_R are respectively the left and right correction function gradients at the solution points, \mathbf{l}_L and \mathbf{l}_R are respectively the interpolation coefficients to the left and right flux points from the solution points. α is then defined to be the upwinding ratio, ($\alpha = 1$ meaning fully upwinded and $\alpha = 0.5$ meaning centrally differenced). A harmonic solution can then be imposed on this by using the Bloch wave:

$$u = v \exp(i(kx - \omega t)) \quad (5.96)$$

which, upon substitution into Eq. (5.92), gives the harmonic solution to linear advection via FR:

$$\frac{\partial \mathbf{u}_j}{\partial t} = -J_j^{-1} \left(\mathbf{C}_+ \exp(-ik\delta_j) + \mathbf{C}_0 + -\mathbf{C}_- \exp(-ik\delta_{j-1}) \right) \mathbf{u}_j = \mathbf{Q}_a \mathbf{u}_j \quad (5.97)$$

In the semi-discrete form this allows for the temporal derivative to be calculated, thus giving the eigenvalue problem:

$$c(k)\mathbf{v} = \frac{i}{k} \mathbf{Q}_a(k) \mathbf{u}_j \quad (5.98)$$

where the dispersion and dissipation can be found as $\Re(\hat{\omega}) = \Re(c)\hat{k}$ and $\Im(\hat{\omega}) = \Im(c)\hat{k}$ respectively.

Taking this analysis one step further, many problems of practical interest involve second order derivatives. Therefore, we wish to understand the behaviour and stability of this branch of correction functions when applied to diffusion and advection-diffusion problems. If we introduce the linear diffusion equation written as:

$$\frac{\partial u}{\partial t} = \nu \frac{\partial q}{\partial x} \quad (5.99)$$

$$q = \frac{\partial u}{\partial x} \quad (5.100)$$

where ν is viscosity. Thus, from Eq. (5.97), we may write:

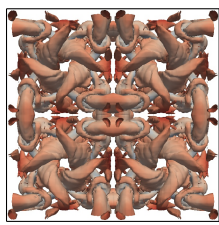
$$\frac{\partial \mathbf{u}_j}{\partial t} = J_j^{-1} \left(\mathbf{C}_{-1} \mathbf{q}_{j-1} + \mathbf{C}_0 \mathbf{q}_j + \mathbf{C}_{+1} \mathbf{q}_{j+1} \right) \quad (5.101)$$

By applying the same spatial discretisation to \mathbf{q} , \mathbf{q}_j can be written as:

$$\mathbf{q}_j = J_j^{-1} \left(\mathbf{C}_{-1} \mathbf{u}_{j-1} + \mathbf{C}_0 \mathbf{u}_j + \mathbf{C}_{+1} \mathbf{u}_{j+1} \right) \quad (5.102)$$

This implies that the same correction function is used for both the diffusion correction and the advection correction. This was found to give optimal performance [33, 30] and has the benefit of easier practical implementation. Proceeding, the semi-discretised linear diffusion equation for FR is then:

$$\frac{\partial \mathbf{u}_j}{\partial t} = (J_j^{-1})^2 \left[\underbrace{\mathbf{C}_{-1}^2}_{\mathbf{B}_{-2}} \mathbf{u}_{j-2} + \underbrace{(\mathbf{C}_{-1} \mathbf{C}_0 + \mathbf{C}_0 \mathbf{C}_{-1})}_{\mathbf{B}_{-1}} \mathbf{u}_{j-1} + \underbrace{(\mathbf{C}_{-1} \mathbf{C}_{+1} + \mathbf{C}_0^2 + \mathbf{C}_{+1} \mathbf{C}_{-1})}_{\mathbf{B}_0} \mathbf{u}_j + \underbrace{(\mathbf{C}_0 \mathbf{C}_{+1} + \mathbf{C}_{+1} \mathbf{C}_0)}_{\mathbf{B}_{+1}} \mathbf{u}_{j+1} + \underbrace{\mathbf{C}_{+1}^2}_{\mathbf{B}_{+2}} \mathbf{u}_{j+2} \right] \quad (5.103)$$



where the matrices \mathbf{C}_{-1} , \mathbf{C}_0 and \mathbf{C}_{+1} are defined as before. This form is similar to that presented by Watkins [168], although parts of their method are presented inaccurately. In this case, we will use BR1 for the calculation of the common interface flux, hence $\alpha = 0.5$. Applying a trial solution of $u = v \exp(ikx_j) \exp(-k^2 c_d t)$ to Eq. (5.103) and simplifying:

$$c_d \mathbf{v} = -a \left(\frac{J_j^{-1}}{k} \right)^2 \left(e^{ik(x_{j-2}-x_j)} \mathbf{B}_{-2} \mathbf{v} + e^{ik(x_{j-1}-x_j)} \mathbf{B}_{-1} \mathbf{v} + \mathbf{B}_0 \mathbf{v} + e^{ik(x_{j+1}-x_j)} \mathbf{B}_{+1} \mathbf{v} + e^{ik(x_{j+2}-x_j)} \mathbf{B}_{+2} \mathbf{v} \right) \quad (5.104)$$

If $\delta_j = x_j - x_{j-1}$, then this can be further simplified to:

$$c_d \mathbf{v} = - \left(\frac{J_j^{-1}}{k} \right)^2 \left(e^{-ik(\delta_{j-1}+\delta_j)} \mathbf{B}_{-2} + e^{-ik\delta_j} \mathbf{B}_{-1} + \mathbf{B}_0 + e^{ik\delta_{j+1}} \mathbf{B}_{+1} + e^{ik(\delta_{j+2}+\delta_{j+1})} \mathbf{B}_{+2} \right) \mathbf{v} \quad (5.105)$$

which also allows us to define the FR diffusion matrix as:

$$\mathbf{Q}_d = \left(J_j^{-1} \right)^2 \left(e^{-ik(\delta_{j-1}+\delta_j)} \mathbf{B}_{-2} + e^{-ik\delta_j} \mathbf{B}_{-1} + \mathbf{B}_0 + e^{ik\delta_{j+1}} \mathbf{B}_{+1} + e^{ik(\delta_{j+2}+\delta_{j+1})} \mathbf{B}_{+2} \right) \quad (5.106)$$

Equation (5.105) is again an eigenvalue problem, albeit a non-trivial one, where from [146, 168] the dissipation and dispersion are defined as $\Re(\hat{k}^2 c_d)$ and $\Im(\hat{k}^2 c_d)$ respectively, due to the presence of a second derivative. The physical mode is extracted from the $p + 1$ dimensional eigenproblem following the procedure of [168]. Finally, for the case of linear advection-diffusion, the fully discrete form may be written using the update matrix, which encompasses the temporal integration method.

$$\mathbf{Q}_{ad} = c \mathbf{Q}_a + \nu \mathbf{Q}_d \quad (5.107)$$

$$\mathbf{u}_j^{n+1} = \mathbf{R}(\mathbf{Q}_{ad}) \mathbf{u}_j^n \quad (5.108)$$

$$\mathbf{R}_{33}(\mathbf{Q}_{ad}) = \sum_{m=0}^3 \frac{(\tau \mathbf{Q}_{ad})^m}{m!} \quad (5.109)$$

where τ is the explicit time step. From the update matrix \mathbf{R} the fully discrete dispersion and dissipation can then be found by further substitution of the trial solution of Eq. (5.96) into Eq. (5.107).

$$\underbrace{e^{-ik(c-1)\tau}}_{\lambda} \mathbf{v} = e^{ik\tau} \mathbf{R} \mathbf{v} \quad (5.110)$$

$$c(k; \tau) = \frac{i \log(\lambda)}{k\tau} + 1 \quad (5.111)$$

Hence, from von Neumann's theorem [68], for temporal stability of the fully discrete scheme the spectral radius of the update matrix must be less than or equal to one, $\rho(\mathbf{R}) \leq 1$. For comparative purposes we then define the normalised time step for advection-diffusion as:

$$\hat{\tau} = \left(\frac{c}{h} + \frac{\nu}{h^2} \right) \tau \quad (5.112)$$

and this will be used to define the CFL limit.

The final analytic method that will be used is the rate of convergence of the solution error with grid spacing. In order to calculate the error with time we first define the diagonalisation of \mathbf{Q}_a as:

$$\mathbf{Q}_a = ik\mathbf{W}\mathbf{\Lambda}\mathbf{W}^{-1} \quad (5.113)$$

By diagonalising the semi-discrete operator in this manner, where \mathbf{W} is the eigenvector matrix and $\mathbf{\Lambda} = \text{diag}(\lambda_0 \dots \lambda_p)$, we may form the initial interpolation of the solution as:

$$\mathbf{u}_j^\delta(t=0) = \exp(ikx_j)\mathbf{W}\mathbf{v}_0 = \exp\left(ik(J_j(\zeta+1) + x_j)\right) \quad (5.114)$$

To calculate the rate of convergence, we need to monitor the semi-discrete error of the solution for different grid spacings. The derivation of the analytical semi-discrete and fully-discrete error can be found in [11, 150] and as the derivation is secondary to the aim, here we will jump to the end result for the semi-discrete error.

$$\mathbf{e}_j(t, J) = \mathbf{u}_j^\delta(t) - \mathbf{u}_j(t) = \exp(ik(x_j - t)) \sum_{n=0}^p \left(\exp(ikt(\lambda_n + 1)) - 1 \right) \mathbf{v}_{0,n} \mathbf{w}_n \quad (5.115)$$

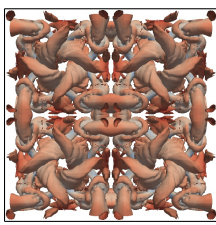
where \mathbf{w}_n is the n^{th} column vector of \mathbf{W} . If we define the l_2 norm of the error as $\|\mathbf{e}(t, J)\|_2 = E(t, J)_j$ then the grid convergence rate is:

$$r_h(t) = \frac{\log(E(t, J_1)_j) - \log(E(t, J_2)_j)}{\log J_1 - \log J_2} \quad (5.116)$$

where J_1 and J_2 are the Jacobians of the two grids over which the convergence rate is to be calculated. With the tools needed having been defined, we may now move on to presenting various findings for the classes of correction functions.

5.4.1 GJFR Results

We will begin the analysis of GJFR by studying qDG, which, for a given α & β , has the correction parameter set as $\iota = 0$. In the case of $\alpha = \beta = 0$ this is known to be equivalent to Nodal DG. Therefore, when the space of correction functions is extended using the



Jacobi weighting function, the set of schemes may be considered to be quasi-DG (qDG) due to the similarity of the norm to the NDG case.

The property that sets DG apart from other correction functions is that it achieves super-convergence [65, 11, 38, 6, 174], *i.e.* for sufficiently smooth and well resolved specific cases, the rate of error convergence can be of order $2p + 1$, whereas other FR schemes would normally be expected to obtain less. For FR observation of this property is reliant on either the initial smooth solution being set via a Galerkin projection, rather than nodally. Or, in the long time limit, the erroneous modes from the nodal projection decay more rapidly. Therefore, eventually then error from the primary mode will dominate the error and so super-convergence will be seen in the long time limit. Due to this it is difficult to see this convergence practically in initial-boundary problems as it requires statistically stationary features that persist for a long time.

Because of this feature we will initially look at the rate of convergence of the qDG, with a focus on the case when $\alpha = \beta$, *i.e.* symmetric weight functions. There are two rates of convergence that can be considered, the initial rate as $t \rightarrow 0$ and the long time rate as $t \rightarrow \infty$, with the initial rate being dictated by the secondary modes and the long time rate by the primary mode. Due to the secondary modes having short half-lives at well-resolved wavenumbers [150], we consider the most important convergence rate to be $t \rightarrow \infty$, and this is shown in Figure 5.3. It is evident then that for both the central difference and upwinded interface case, improvement may be made to the rate of convergence over standard DG schemes. It may be possible, then, to improve the practical performance of FR using a qDG scheme.

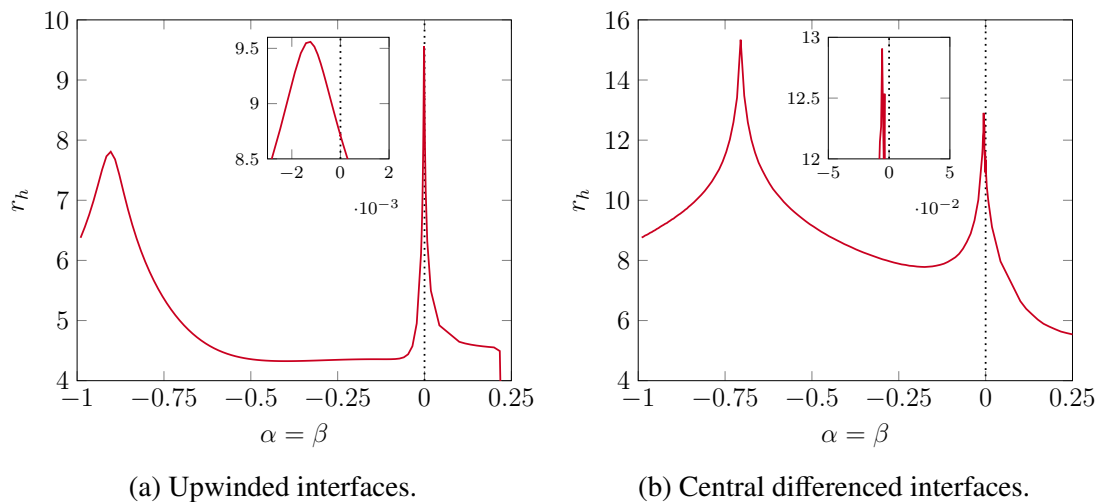


Fig. 5.3 Variation of the rate of error convergence with grid for quasi-DG correction functions, ($t = 0$) when, $p = 4$, $\alpha = \beta$, $J_2/J_1 = 0.5$, $k = 3\pi/4$ and, $t/T = 1000$. The dotted line is for $\alpha = \beta = 0$.

Second, we go on to study the stability of qDG once the temporal integration is discretised. For this we will make use of low storage RK schemes [77] as they can be simply and practically added to FR schemes and do not prohibitively increase memory usage, a major concern with the current cost of graphics RAM.

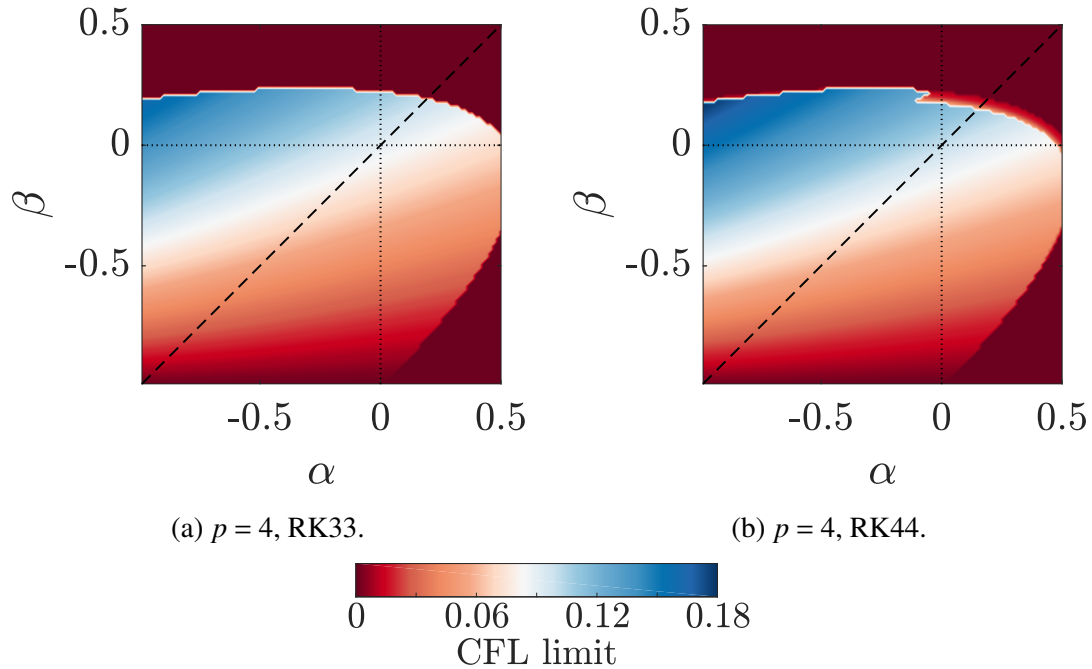
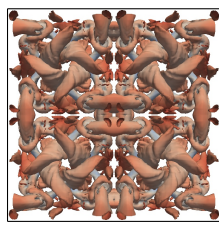


Fig. 5.4 CFL limit of various temporal integration methods for $\iota = 0$ with upwinded interfaces. The dashed line is for $\alpha = \beta$ and the dotted lines are $\alpha = 0$ and $\beta = 0$.

Figure 5.4 then shows that for both RK33 and RK44, as α or β is decreased the CFL limit is reduced. Furthermore, as $\beta \rightarrow -1$ temporal stability is lost, and in order to understand this it can be useful to consider the shape of the correction function as $\beta \rightarrow -1$ which is shown in Figure 5.5. From this it is evident that the maximum gradient increases, with significant changes occurring across the whole domain. This is the opposite of what Huynh [65] proposed as good characteristics for temporal stability, where most of the gradient was lumped at one end.

We now move on to study another subset of GJFR, SD. Spectral Difference via FR is often considered in some sense as being a canonical FR correction function [65, 160, 25, 158]. This is with good reason, as its dispersion and dissipation characteristics are quite favourable [161]. Yet the Jacobi generalisation allows us to extend the definition of the SD correction functions, allowing us to investigate whether yet more favourable characteristics can be achieved. To restrict the space of possible functions we will use a detail outlined in Section 5.3.2, that in the case of $\alpha \neq \beta$ the correction functions are not symmetric about $\zeta = 0$. This will bias convection due to directional variation in the



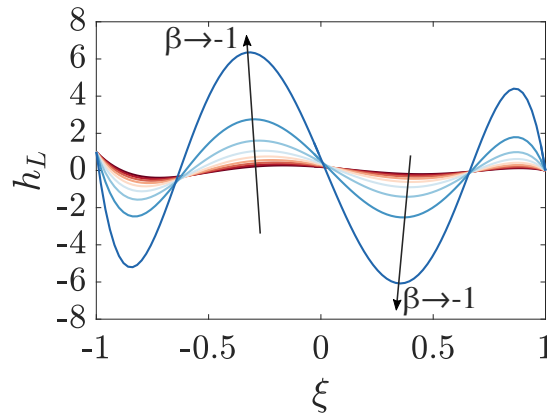
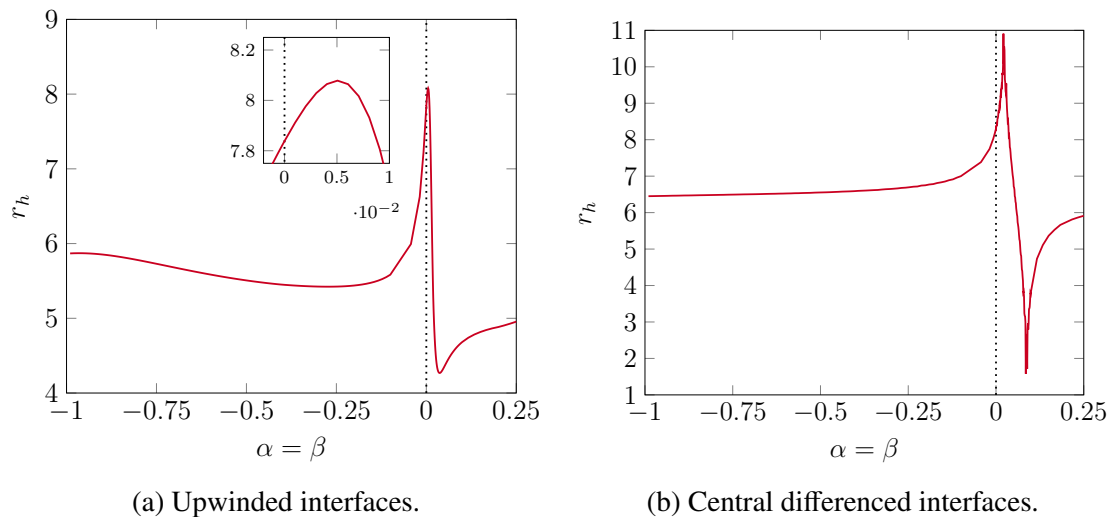


Fig. 5.5 qDG, $p = 4$, correction functions for $\alpha = 0$ as $\beta \rightarrow -1$ from $\beta = 0$.

phase and group velocities, which for most practical calculations would be unacceptable. Because of this, our study into the rate of convergence will focus on the case of $\alpha = \beta$.



(a) Upwinded interfaces.

(b) Central differenced interfaces.

Fig. 5.6 Variation of the rate of error convergence with grid for SD correction functions when, $p = 4$, $\alpha = \beta$, $J_2/J_1 = 0.5$, $k = \pi/2$ and, $t/T = 1000$. The dotted line is for $\alpha = \beta = 0$.

The long time rate of convergence is presented in Figure 5.6 for both upwinded and central differenced interfaces. In both cases, it is clear that improvements may be made. This improvement is only minor in the case of upwinded interfaces, however when the interface is centrally differenced, a three order increase in the rate of convergence can be seen for $\alpha = \beta \approx 2 \times 10^{-2}$. This is similar in size to the increase seen for qDG with central differencing.

After the peak rate of convergence, there is a sharp drop off in the rate of convergence towards unity order. A similar drop off in Figure 5.6a is also seen, albeit closer to the peak value. When implemented practically, an approximate Riemann solver is used across

the interface, which is likely to give a mix of upwinding and central flux — so the rate of convergence will vary somewhere between the Figure 5.3a & 5.3b. Because of this, to avoid hitting the penalty of the sharp decrease in order as the degree of upwinding changes, it may be more robust to use an $\alpha = \beta$ value closer to 5×10^{-3} (the upwind optimal) rather than the central optimal value.

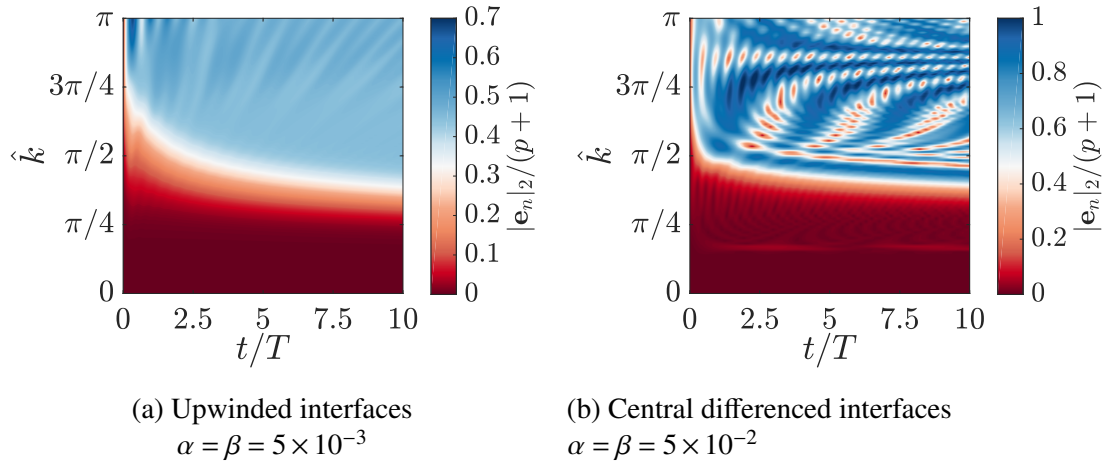
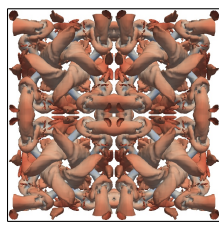


Fig. 5.7 Variation of error with time and normalised wavenumber ($\hat{k} = k/(p+1)$) for SD correction functions with optimal convergence from Figure 5.6, $p = 4$, $\Delta_x = 1$.

To ensure that the increased rates of convergence seen in Fig. 5.6 are not due to serendipitous interaction of errors, the development of the error with time is shown in Fig. 5.7. It is clear that the wavenumber used in the calculation of the rate of convergence is in the well resolved region, where the error is low. Therefore, it can be safely concluded that the increased rate of convergence is not due to chance cancellation of errors.

Again, when using these correction functions practically, a method of discrete time integration will be used. Figure 5.8 displays the CFL limit for $p = 4$ for two low storage RK explicit temporal integration schemes. Previously we showed that ι_{SD} would lead to the norm always being positive. This, together with the result for qDG, indicates that the critical value of ι is a necessary but not sufficient condition for stability and that additional contributions from Eq.(5.42) will further restrict the stability. This is not unexpected, as when $\alpha, \beta < 0$ it is clear that the weight function is ill-defined at the end-points; something which is not reflected in the value of ι_{crit} . However, ι_{crit} is not without merit and Figures 5.4 & 5.8 clearly show that there is a well-defined stable region of correction functions which contain the optimal points found in Figures 5.3 & 5.6. In the case of optimal SD, the CFL limit is approximately the same as for the original SD scheme ($\alpha = \beta = 0$) and the performance will be further explored in the next section.

For completeness, we include in Figure 5.9 the dispersion and dissipation relationships for the correction functions that give optimal rates of convergence. These relations can be



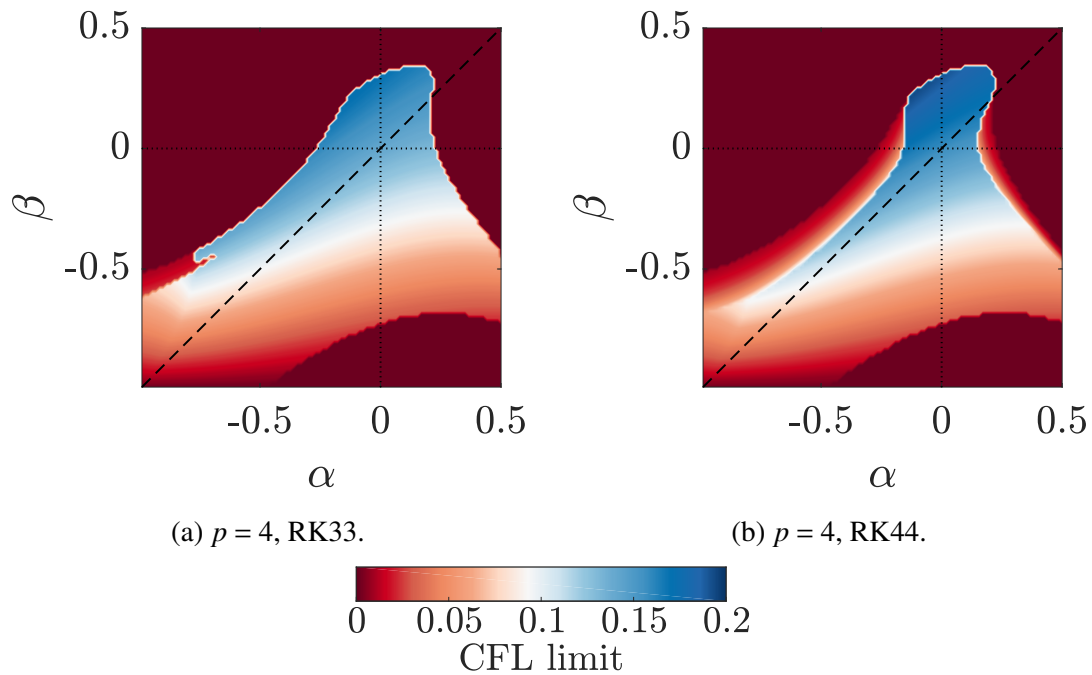


Fig. 5.8 CFL limit of various temporal integration methods for Jacobi SD with upwinded interfaces. The dashed line is for $\alpha = \beta$ and the dotted lines are $\alpha = 0$ and $\beta = 0$.

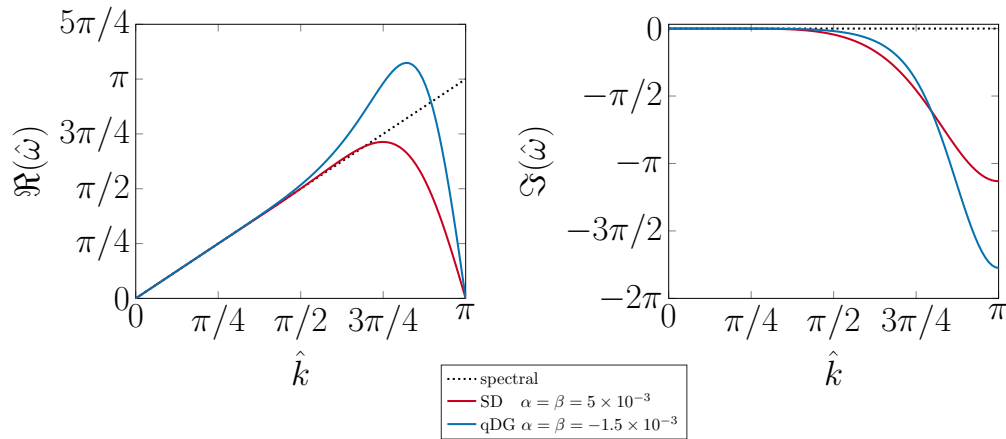
extracted from the diagonal matrix Λ and for the case of centrally differenced interfaces the dissipation is zero. The dispersion relations for centrally differenced interfaces are also split between two modes, one active at low frequencies, and the other active at high frequencies. Because of this we have included both modes. Comparison made between these relations and their OSFR counterparts found previously by Vincent et al. [161] show that the difference is only slight. This should give us confidence that the correction functions found will at least provide a reasonable answer in practical use.

5.4.2 GSFR Results

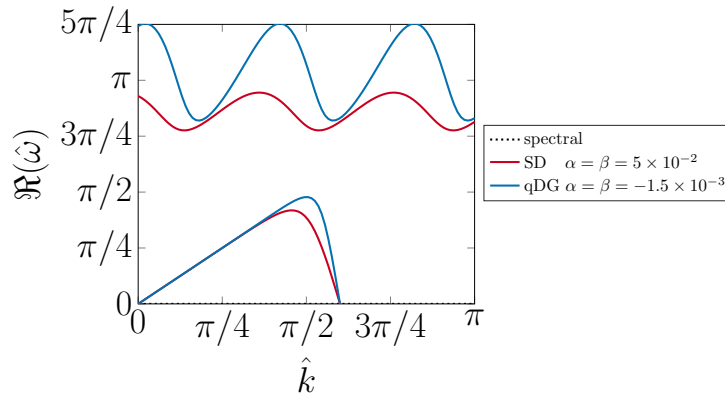
We will now present the analytic findings of GSFR, with the focus being on the temporal stability. This is due to the high dimensionality of the correction function space and the computational expense of calculating the convergence.

In section 5.2.4 and 5.3.3 sufficient conditions on \mathbf{I}_p were presented, however here we will allow \mathbf{I}_p to vary beyond these bounds to potentially aid understanding any underlying necessary and sufficient condition. Throughout this analysis ι_0 will also be taken as one; it should be understood that this is an arbitrary choice, but that choosing a different value will simply lead to a linear scaling of all other ι_i values shown here.

Beginning with the case of $p = 3$, Fig. 5.10 shows the variation of CFL number with \mathbf{I}_3 for low storage RK44 temporal integration. In this figure positive and negative log axes



(a) Dispersion and dissipation of upwinded interfaces.



(b) Dispersion of central interfaces.

Fig. 5.9 Dispersion ($\Re(\hat{\omega})$) and dissipation ($\Im(\hat{\omega})$) relations of the SD and qDG $p = 4$ correction functions found to give improved rates of convergence.

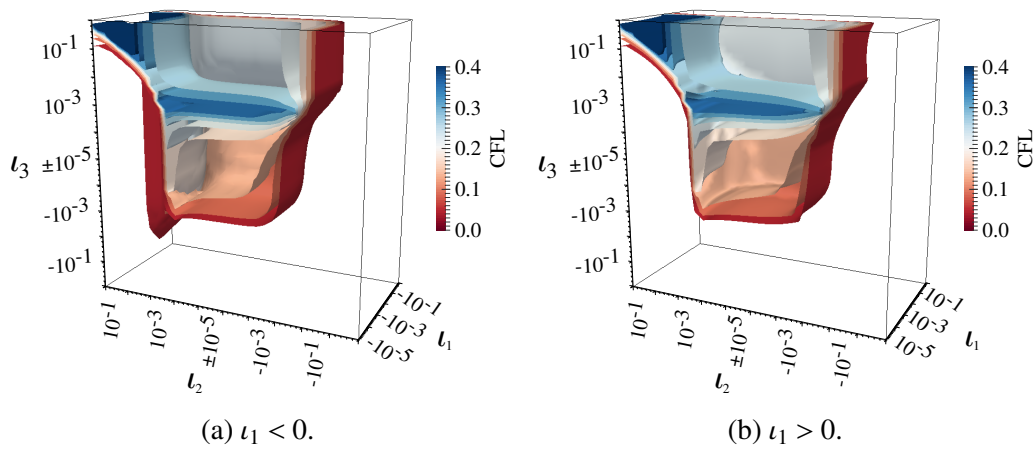
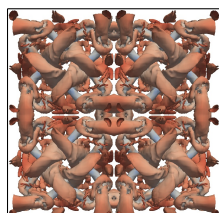


Fig. 5.10 CFL limit for upwinded FR with GSFR correction functions, $p = 3$, and RK44 temporal integration on a regular grid.



in ι_2 and ι_3 are used to clearly show the CFL manifold, the join is at $\pm 10^{-5}$. This chiefly shows the extent of the domain of \mathbf{I}_3 and also highlights some regions of interest. The first region to consider is that of $\iota_3, \iota_2 \rightarrow \infty$. In this case the correction function converges upon $p = 2$ correction functions. This is similar to the properties of the ESFR scheme. Secondly, consider the region of Fig. 5.10a at $\iota_1 = 5 \times 10^{-2}$ as $\iota_2 \rightarrow \infty$. Here an almost one dimensional region of high CFL is present, where the correction function order drops further to $p = 1$. Lastly consider the region where $\mathbf{I}_3 \approx [1, 0, 10^{-3}, 10^{-3}]^T$, here the CFL limit can be seen to have a local maximum. This region of local maximum is believed to give recovery of high-order due to the scale of the Legendre weights, which can be shown analytically through the position of the Nyquist wavenumber of the semi-discretised form, with degradation in the Nyquist limit indicating a drop in order of accuracy (OOA). To exactly find the OOA a numerical method will be introduced in Section 5.5.1.

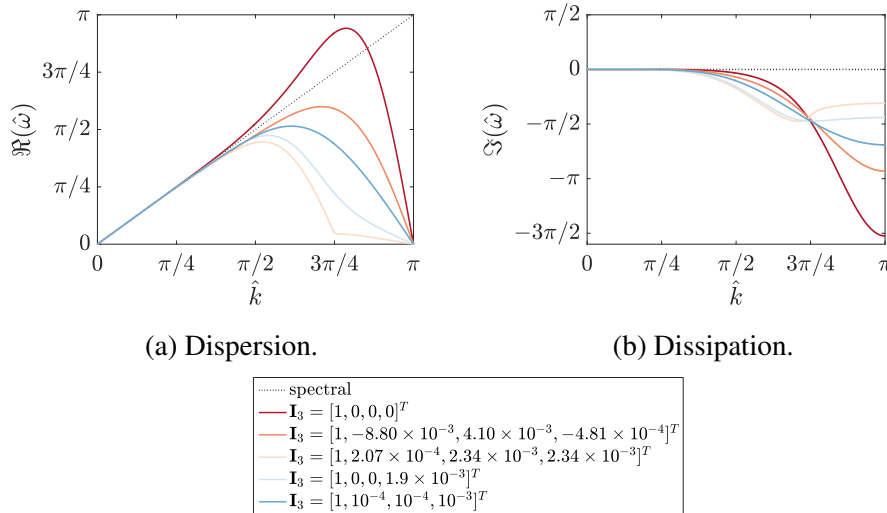


Fig. 5.11 Dispersion and dissipation for selected $p = 3$ GSFR correction functions with interface upwinding.

The dispersion and dissipation characteristics for some selected correction functions are presented in Fig. 5.11 for $p = 3$. The correction functions tested were: DG; the ESFR correction function that gives optimal temporal stability [157]; the GSFR optimal correction function; the OSFR correction function found to give optimal temporal stability with this combination of spatial-temporal scheme [161]; and lastly a stable GSFR correction function chosen arbitrarily.

For the third of these correction functions, the Nyquist wavenumber is maintained at that for an OOA of four as it was previously suspected it may. However, there is a significant region where the phase velocity is low, i.e $c_p = \hat{\omega}/\hat{k} \approx 0$, which may cause additional dispersion errors. Additionally, at high wavenumbers, there is a significant reduction in the dissipation exhibited. This combination of dispersion and dissipation

seems to have given rise to an increased CFL limit, but potentially at the cost of spectral performance and order of accuracy, both of which will be investigated later.

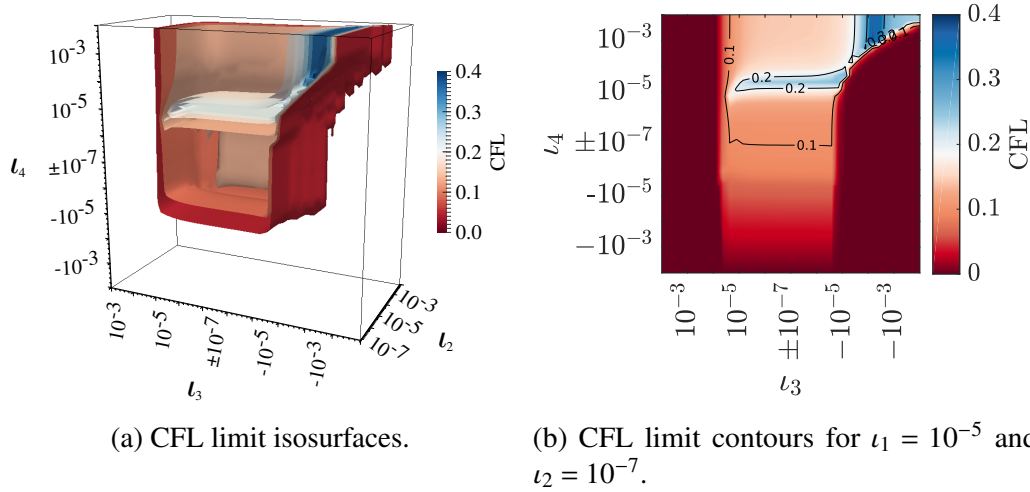


Fig. 5.12 CFL limit for upwinded FR with GSFR correction functions, $p = 4$, and RK44 temporal integration on a regular grid. ($l_1 = 1 \times 10^{-5}$).

Returning to the investigation of CFL limits, Fig. 5.12 shows two regions of interest for $p = 4$ which are similar to those shown for $p = 3$. However, now the first region is found in the $-l_3$ half plane, which may have been predicted by the interaction of the odd and even powers. Although a localised maximum CFL limit can be seen, the free parameter is four dimensional, and hence a search method will have to be used to find the global high-order recovering maximum CFL limit. This method will be explored fully in Section 5.5.1.

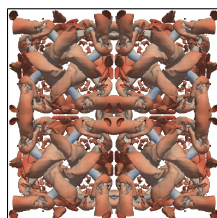
5.4.3 GLSFR Results

GLSFR presents us with a far broader scope of correction functions owing to the almost arbitrary nature of the variables defining them. As a result we will initially study the dispersion and dissipation of linear advection, with the primary aim of showing how, for what may be traditionally considered an inappropriate correction function, we are able to recover a stable scheme. Take the following example, when $p = 4$, and the correction weights are chosen arbitrarily to be:

$$\tilde{\mathbf{h}}_{10} = (5.22943203125 \times 10^4) \times 10^{-5} \quad (5.117)$$

$$\tilde{\mathbf{h}}_{11} = 0.1 \sqrt{2} \quad (5.118)$$

where Eq. (5.117) is 10^{-5} times the floating-point representation of the ASCII string ‘GLFR’. It is clearly apparent that this arbitrary correction function that satisfies Eq. (5.86)



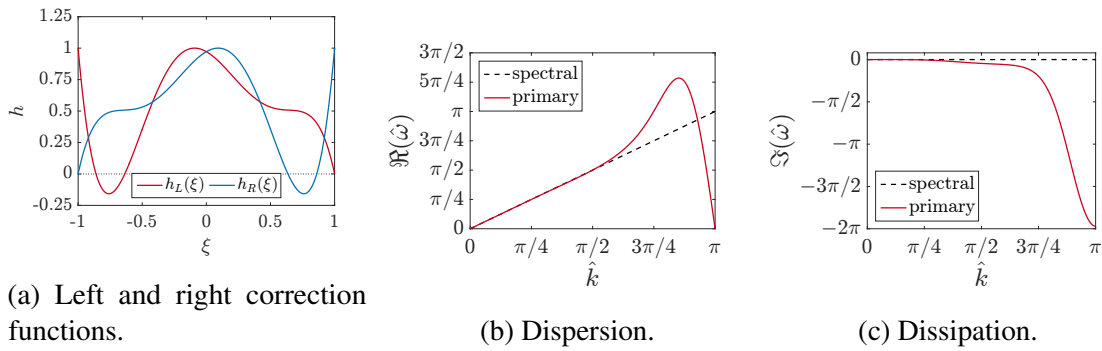


Fig. 5.13 Correction function and wave propagating characteristics for arbitrary correction weights as in Eq.(5.117 & 5.118), for $p = 4$ on a uniform grid with upwinded cell interfaces applied to linear advection.

is stable, although the wave propagating characteristics of this arbitrary example are not optimal. However, this aims to demonstrate initially that a correction function may be defined that was previously unproducible, leading to an incredibly general family of schemes.

In order to understand the space of temporally stable GLSFR correction functions, the 1D linear-advection von Neumann analysis is first investigated for various orders, correction functions, and interface calculations.

Figure 5.14 shows the region of stable correction functions when RK44 temporal integration is used, with a clear region of overlap between the upwinded and central cases. For previous correction function sets, the existence of the Sobolev norm was used to determine the region of stable correction functions, however due to the nature of the GLSFR Sobolev norm — in that it collapses onto the L^2 norm — this approach could not be taken. Instead, the results of Fig. 5.14 may be used to heuristically bound the correction function set. To demonstrate the wave propagation properties of GLSFR we perform both a semi-discrete and a fully discrete von Neumann analysis. We will take the case when $p = 4$ and compare the correction function that gives the highest CFL limit for both the upwinded and central case to DG. We choose DG as this is a commonly used scheme even within FR [163] due to the complexity currently with the simplex correction definition [32]. The CFL optimal case corresponds to $\mathbf{H}_4 = [\tilde{\mathbf{h}}_{10} = 0.77, \tilde{\mathbf{h}}_{11} = -0.52]$, with the DG comparison at $\mathbf{H}_4 = [0, 0]$.

It should be clear from Fig. 5.15 that GLSFR in the fully discrete case is able to greatly reduce the wave group velocity, however at the expense of dispersion overshoot. Furthermore, by comparison of the dispersion and dissipation it can be seen that this GLSFR correction function has a localised region of high dissipation around the wavenumber where the dispersion leads us to have a large negative group velocity. It might be

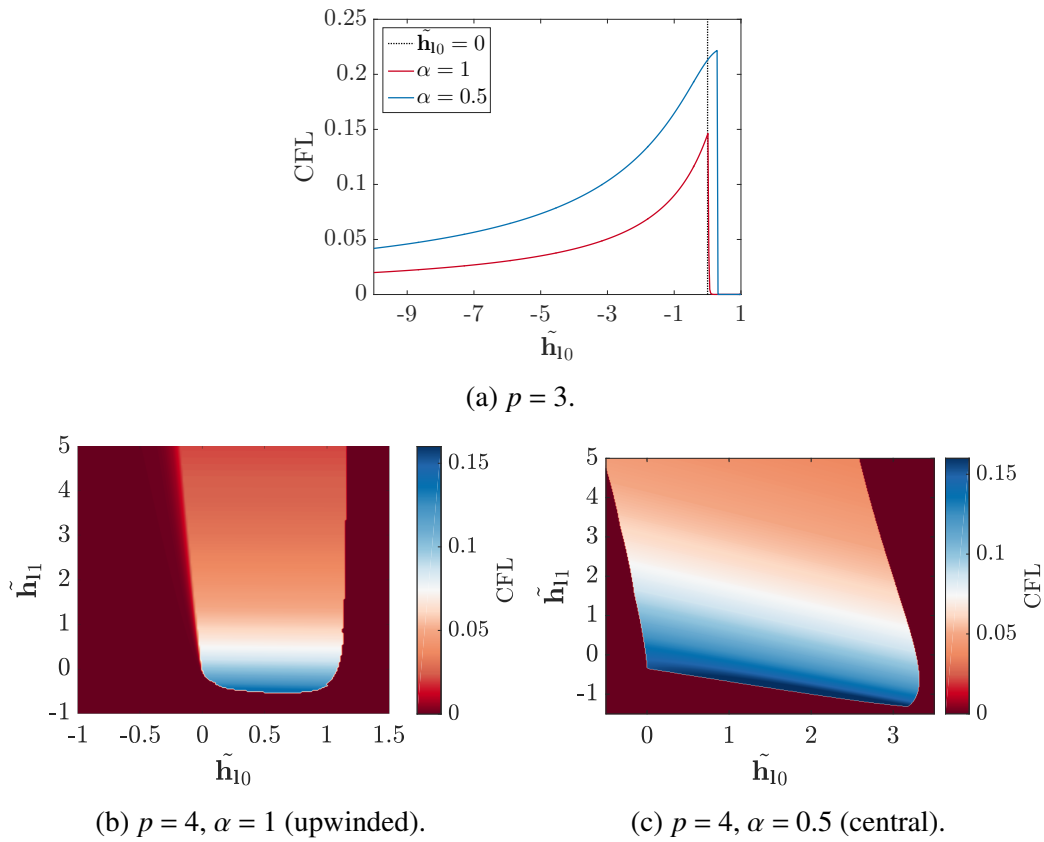


Fig. 5.14 Maximum stable CFL number for GLSFR [$c = 1, \nu = 0$], with RK44 temporal integration.

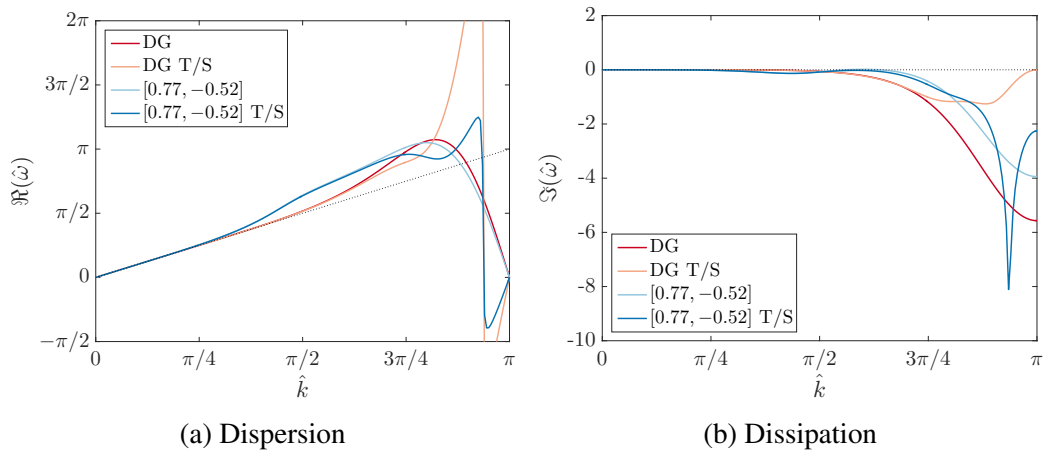
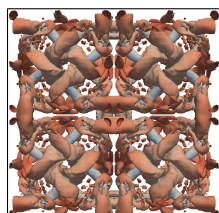


Fig. 5.15 Linear advection dispersion and dissipation comparison of spatial and temporal-spatial (T/S) analysis for upwinded FR, $p = 4$. This compares DG and with GLSFR with $\mathbf{H}_4 = [0.77, -0.52]$. The temporal-spatial analysis uses RK44 temporal integration at $\tau = 0.1$ in both cases.



concluded that such a scheme may give improved performance when applied to implicit LES.

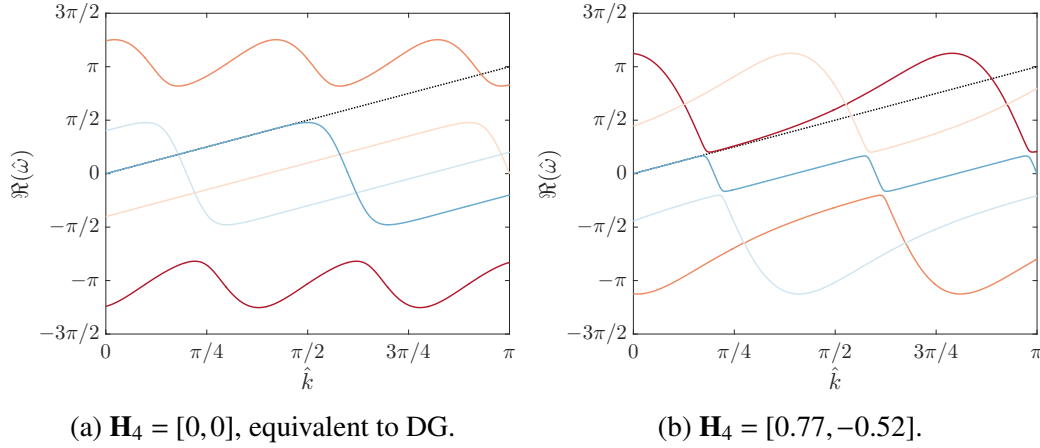


Fig. 5.16 Linear advection dispersion relations for central interface flux FR, $p = 4$, with the dispersion shown for all modes.

Lastly for the advection study, the semi-discrete dispersion relation for DG and $\mathbf{H}_4 = [0.77, -0.52]$ with central interfaces are included for completeness. It can be seen that the regions in DG where the dispersion relation is discontinuous have been greatly reduced, from [168, 11] and it can be understood that the smaller regions of discontinuity in the dispersion relation leads to less energy transfer to spurious modes.

To study the general trend in the CFL limit of the combined advection diffusion equation we use the case of $a = 10$ and $\nu = 1$, which was similarly used in the investigation by Watkins et al. [168].

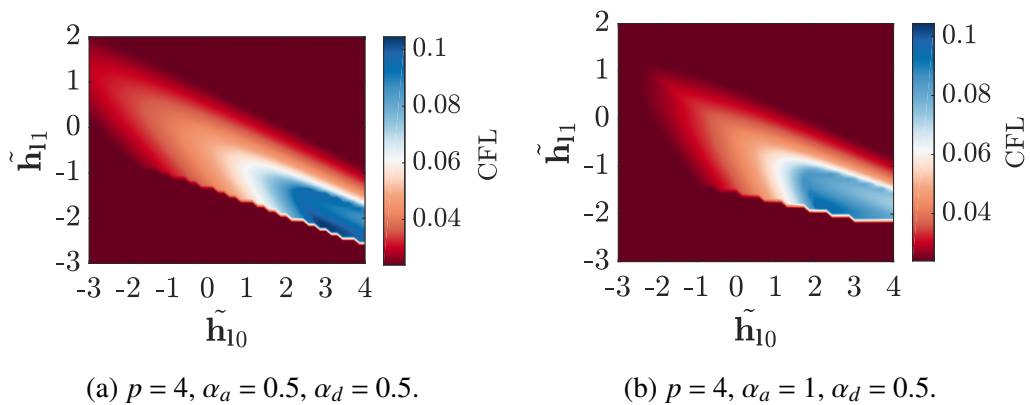


Fig. 5.17 Maximum stable CFL number for GLSFR [$c = 10, \nu = 1$], with RK44 temporal integration.

Figure 5.17 shows the CFL limits for $p = 4$ for various correction functions for the case when both the advection and diffusion interface calculation are centrally differenced

and the case when advection is upwinded and diffusion is centrally differenced. In both cases it can be seen that the stability profile is of a different character than pure advection, with higher values of $\hat{\mathbf{h}}_{10}$ being stable due to the additional stability introduced by the diffusion terms. The motivation of this test is the understanding it can bring to later studies. The main observation is the slant to the CFL profile, although this will be affected by the relative scale of the advection-diffusion terms.

5.5 Numerical Experiments

5.5.1 Linear Homogeneous Problems — GSFR

Generalised Sobolev stable correction functions have more variables that define their shape. Therefore, it is not as practical to explore the behaviour of the whole space of correction functions on a non-linear equation set. Hence, their behaviour will largely be examined on a set of linear cases. These tests were undertaken to validate analytical findings and provide useful further insight. The first such numerical test was contrived to calculate the lower bound of the order accuracy of the scheme while solving the linear advection equation with a wave speed of unity. As has been discussed earlier, it is possible in particular circumstances to achieve higher convergence like super-convergence. Yet, in the majority of cases the lower bound will be the realised order of the scheme.

The initial solution was taken to be a plane wave, with a wavenumber that would be expected to be well resolved on the grids from the relations in Chapter 4. To achieve the lower bound of the error, the initial condition will then be taken as the nodal values of:

$$u(x; t = 0) = u^e(x; t = 0) = \cos(kx), \quad k = \frac{1}{2\pi} \quad (5.119)$$

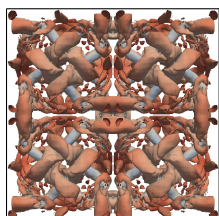
where $u^e(x, t)$ is the exact solution and $u(x, t)$ is the approximate solution from FR. Therefore, the initial condition is not a Galerkin projection of the exact solution, hence some energy will present in the spurious modes, resulting in the lower bound being found.

Taking the solution after some number of time integrations, the point averaged error can be calculated for several grid densities, with n_s points:

$$e_2 = \frac{1}{n_s} \sum_{i=1}^{n_s} |u^e(x_i, t) - u(x_i, t)| \quad (5.120)$$

$$e_2 = |u^e(x, t) - u(x, t)| = \mathcal{O}(n_s^{-k}) \quad (5.121)$$

where k is the numerically realised OOA, which can be found by taking logs. With this established, the correction functions can now be varied to show the effect of \mathbf{I}_p on OOA.



The domain set-up for this case was a periodic domain with $x \in [0, 2\pi]$, with the number of elements allowed to vary so that varying degrees of freedom could be tested. Element interfaces were fully upwinded and a time step was chosen such that the temporal integration was not the primary source of error.

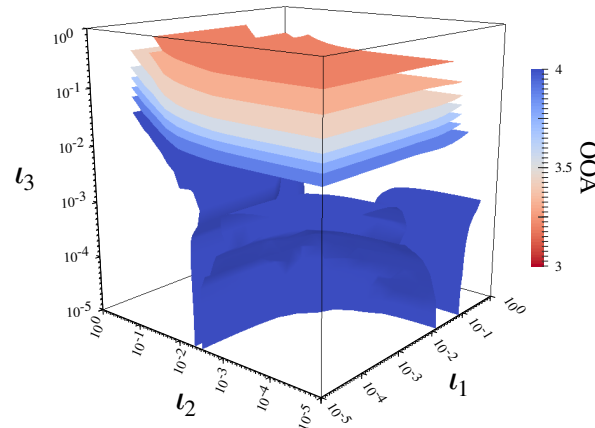


Fig. 5.18 Order of accuracy of GSFR, $p = 3$ for linear advection of a wave with $k = 1/2\pi$, at $t = \pi$.

Figure 5.18 shows the OOA as correction function is varied for $p = 3$, the region explored includes the peak CFL limit and the area where OOA is suspected to drop. What can be noted is that the analytically predicted decrease in order as $l_3 \rightarrow \infty$ is demonstrated numerically by $OOA \rightarrow p$. Reassuringly, the order accuracy in the region of $l_3 \approx 10^{-3}$, where peak temporal stability is believed to lie, is shown to have $OOA = p + 1$ and hence the maximum CFL limit may be increased without an apparent loss in order of accuracy. In particular, the GSFR correction function with peak temporal stability that was investigated in Fig. 5.11 is found to recover the expected $p + 1$ OOA.

The domain of \mathbf{I}_p is sufficiently small for $p = 3$ & 4, therefore permitting an exhaustive search that couples numerical OOA calculation and analytic CFL calculation to find the maximum CFL limit. The results of this search are shown in Table 5.1. In all cases the OOA recovered was $p + 1$, consistent with the expected order. It may be noted that in some cases a significant improvement upon the CFL limit may be made by comparison to Vincent et al. [161].

5.5.2 Linear Heterogeneous Problems — GSFR

Thus far, the investigation has focused exclusively on the linear advection equation. However, for practical applications, non-linear conservation equations will be encountered.

Table 5.1 Peak CFL of Order Recovering GSFR

p	RK Scheme	\mathbf{I}_p	τ
3	RK33	$[1, 1.274 \times 10^{-3}, 1.438 \times 10^{-2}, 7.848 \times 10^{-3}]^T$	0.385
	RK44	$[1, 2.069 \times 10^{-4}, 2.336 \times 10^{-3}, 2.336 \times 10^{-3}]^T$	0.390
	RK55	$[1, 6.952 \times 10^{-4}, -6.158 \times 10^{-5}, 2.336 \times 10^{-3}]^T$	0.443
4	RK33	$[1, 4.833 \times 10^{-4}, 2.336 \times 10^{-5}, -1.438 \times 10^{-4}, 2.637 \times 10^{-4}]^T$	0.431
	RK44	$[1, 1.624 \times 10^{-3}, 2.637 \times 10^{-4}, -2.637 \times 10^{-4}, 2.637 \times 10^{-4}]^T$	0.430
	RK55	$[1, 1.624 \times 10^{-3}, 1.274 \times 10^{-5}, -2.637 \times 10^{-4}, 8.859 \times 10^{-4}]^T$	0.354

Other than the introduction of shock-waves, the treatment of which is still an open question, non-linear equations also introduce aliasing error due to the multiplication of polynomials. This results in a solution that lies beyond the spectral resolution of the grid. Further insight into the origin and effect of order and aliasing was offered by Kravchenko and Moin [82]. Previously, to investigate this problem, a flux function used by Hesthaven and Warburton [60] and Vincent et al. [160] was defined as:

$$f(x; t) = \left((1 - x^2)^5 + 1 \right) u(x, t) \quad (5.122)$$

However, when applied to a periodic domain $\Omega = [-1, 1]$ the flux function of Eq. (5.122) is only C^0 continuous. Hence, it is proposed that it would be more suitable to use a flux function defined as:

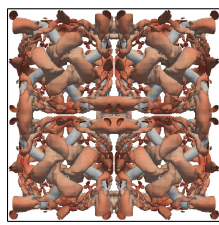
$$f(x; t) = (\sin(\pi x) + 2)u(x; t) \quad (5.123)$$

The advantage of this flux function is that, although strictly linear in u , the spatial dependence of the flux function introduces aliasing errors. Therefore, this gives useful insight into GSFR's application to fully non-linear problems, without the associated problems of shock formation. To understand the mechanism of production for aliasing error, consider the finite spatial Fourier series of an approximate solution $u(x, t)$:

$$u(x, t) = \sum_{n=-N/2}^{N/2-1} w_n(t) \exp\left(\frac{n\pi i x}{l}\right) \quad (5.124)$$

where $w_n(t)$ are time dependent Fourier weights, and l is the domain half-length. The half-length can be used to generalise Eq. (5.123), such that, together with application of the product rule, one has:

$$\frac{\partial(\sin(\frac{\pi x}{l}) + 2)u}{\partial x} = \left(\sin\left(\frac{\pi x}{l}\right) + 2 \right) \frac{\partial u}{\partial x} + \frac{\pi}{l} \cos\left(\frac{\pi x}{l}\right) u \quad (5.125)$$



By subsequent application of the Fourier series of Eq. (5.124):

$$\begin{aligned} \frac{\partial(\sin(\frac{\pi x}{l}) + 2)u}{\partial x} = \frac{\pi}{2l} \sum_{n=-N/2}^{N/2-1} w_n(t) & \left(4ni \exp\left(\frac{nx}{l}\right) \right. \\ & + \exp\left(\frac{(n-1)\pi ix}{l}\right)(1+ni) \\ & \left. + \exp\left(\frac{(n+1)\pi ix}{l}\right)(1-ni) \right) \end{aligned} \quad (5.126)$$

hence, aliasing is injected only by the highest frequency mode and will propagate down through the modes, as opposed to the flux function of Eq. (5.122), which would cause aliasing error injection at all modes. For the numerical experiment, the domain set up was $\Omega = [-1, 1]$ with periodic boundaries. The method of temporal integration used was low storage RK44, with τ set to be sufficiently small that the temporal integration had a negligible effect on the error. To illustrate the effect on the solution, the domain L^2 energy of the conserved variable is used, defined as:

$$E(t) = \int_{\Omega} u(x, t)^2 dx \quad (5.127)$$

and the initial condition will be taken as:

$$u(x; t = 0) = \sin(4\pi x) \quad (5.128)$$

The effect of having a flux function that is C^∞ continuous on Ω is that the periodic boundaries are analogous to solving the same equation on an infinite domain. Hence, the time period of the solution can be found analytically to be $T = 2/\sqrt{3}$. To evaluate the relative performance of correction functions, the L^2 energy error relative to some known value of the L^2 energy is compared for various correction functions. Due to the periodicity of the solution, the error at some time nT , $n \in \mathbb{N}$ may be straightforwardly calculated, i.e. analytical energy $E_a(nT) = 1$.

Figure 5.19 shows just such an error in the L^2 energy, for $p = 3$ with upwinded interfaces. Centrally differenced interfaces are not shown as, for all correction functions, the scheme had gone unstable within $t = 15T = 30/\sqrt{3}$. This is due to the coupling of the aliasing error to the zero dissipation associated with central difference. The result is that any error introduced into the solution does not become damped and hence instability arises. However, when considering the case of upwinded interfaces, the implicit dissipation in the scheme can be sufficient to stabilise the errors introduced through aliasing. It may also be noted that, from Fig. 5.10, the region of localised peak CFL number lies within a region

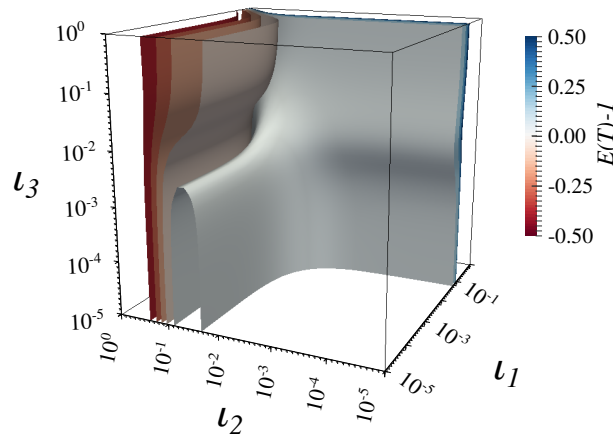


Fig. 5.19 L^2 energy error for FR, $p = 3$, using RK44 temporal integration with CFL = 0.06, for $\alpha = 1$ (upwinded) $t = T = 2/\sqrt{3}$.

of low aliasing error and hence correction functions in this region ($l_3 \approx 1 \times 10^{-3}, l_1 \approx 0$) may be good candidates for practical applications.

5.5.3 Isentropic Convecting Vortex — GSFR

We will conclude the investigation of GSFR with application to the 3D Euler’s equations, in particular the ICV case that was introduced earlier in Section 3.4. We will study the effect on the error of several specific GSFR correction functions that were found earlier to have favourable properties.

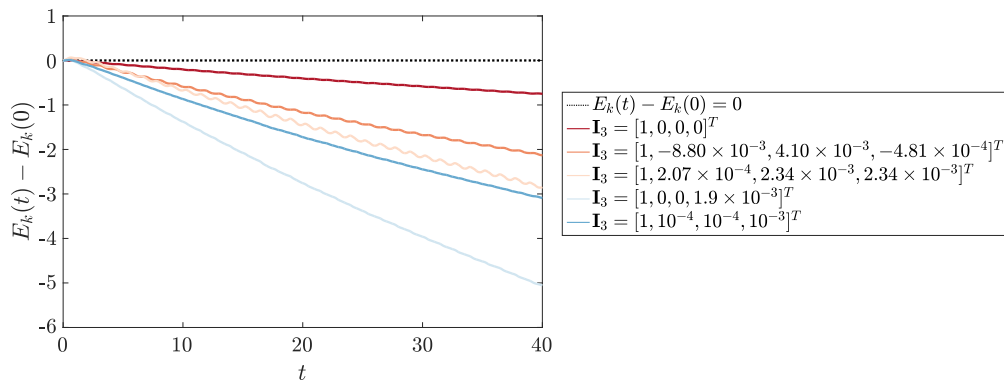
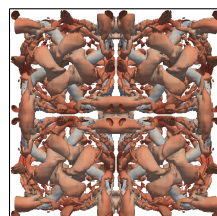


Fig. 5.20 Error in the domain integrated kinetic energy of the ICV for FR, $p = 3$, for various correction functions. Using RK44 temporal integration with $\tau = 10^{-3}$ on $\Omega = [-10, 10]^3$ with $16 \times 16 \times 1$ elements. For the error calculation, $E_k(0)$ was calculated on a $256 \times 256 \times 1$ grid. Finally the convective velocity was taken as $u_0 = v_0 = 1, w_0 = 0$.

Figure 5.20 shows the error in the domain integrated kinetic energy of the ICV for $p = 3$ using various correction functions. Here RK44 temporal integration with $\tau = 10^{-3}$ is used on $\Omega = [-10, 10]^3$ with $16 \times 16 \times 1$ elements. For the error calculation, $E_k(0)$



was calculated on a $256 \times 256 \times 1$ grid. Finally, the convective velocity was taken as $u_0 = v_0 = 1, w_0 = 0$.

The correction functions applied here are the same as those whose dispersion and dissipation characteristics are shown in Fig. 5.11. All the correction functions seem to be stable when applied to the ICV. In all cases tested there is a small region, $0 \leq t \leq 2$, where the kinetic energy increases above the initial value, this is likely due to the smoothing of the higher order discontinuities in the solution. These discontinuities arise because, although the domain is large, the solution is not strictly C^p continuous on a periodic domain. The effect of these discontinuities was seen to reduce as the domain is widened. This was investigated by Spiegel et al. [137], where it was furthermore shown that the periodic boundaries also introduced instability through shear. Also visible in Fig. 5.20, is that all the domain integrated error terms show a small degree of oscillation. This is due to the grid affecting integration accuracy, and the frequency reflects this.

Studying Fig. 5.20, it can be clearly seen that DG gives the best performance, although it may have been expected that the GSFR CFL optimal correction function would give the best performance, as Fig. 5.11 showed low dissipation at high wavenumbers. However, the grid used in this case is sufficient for the solution to be primarily formed of lower wavenumbers, where, as can be seen from the mid section of Fig. 5.11b, DG has the least dissipation. An interesting comparison can be made between the performance of the optimal CFL correction functions for OSFR, ESFR, and GSFR. The OSFR case is clearly far more dissipative, from which it could be postulated that the lower order Sobolev terms present in ESFR and GSFR can lead to the cancelling out of unwanted dissipation.

5.5.4 Taylor–Green Vortex

Lastly for GLSFR and GJFR we will build on the theoretical and linear work carried out in earlier sections by again using the Taylor–Green vortex test case [143, 21, 42]. Restating the reasoning for using this case, it is a well-known canonical case for the full incompressible Navier–Stokes equations, and is highly important as it exhibits laminar, transitional, and turbulent flow regimes. Therefore, if improvements can be made via correction function selection on such a case, this will translate well into an engineering CFD problem.

The physics of this case are controlled by the setting of three non-dimensional parameters, the Reynolds, Prandtl, and Mach numbers, with Reynold and Prandtl numbers controlled through setting the dynamic viscosity and thermal conductivity and Mach number controlled through setting the stagnation density relative to a reference velocity. The typical condition we will use, unless otherwise stated, is $Re = 1600$, $Pr = 0.71$ and $Ma = 0.081$. To give a qualitative understanding of the flow field of this case, the iso-

surfaces of the Q-criterion at $Q = 0.5$ are shown in the right-hand corner as a flip book. The time interval between frames is 0.1 normalised time units.

The aim of this case is to display the impact of changing the correction function by evaluating two metrics. The metrics to be evaluated were introduced earlier in Chapter 3, and are kinetic energy dissipation and enstrophy based dissipation:

$$\epsilon_1 = -\frac{dE_k}{dt} = -\frac{d}{dt} \left(\frac{1}{2\rho_0 U_0^2 |\Omega|} \int_{\Omega} \rho \mathbf{V} \cdot \mathbf{V} dx \right)$$

$$\epsilon_2 = \frac{\mu}{\rho_0^2 U_0^2 |\Omega|} \int_{\Omega} \rho (\boldsymbol{\omega} \cdot \boldsymbol{\omega}) dx$$

We will also evaluate the time averaged error in these terms, but will introduce the exact definition on a case by case basis.

GJFR Results

Some additional numerical investigations into the behaviour of GJFR are included in Appendix D, however for brevity we will proceed to the TGV results.

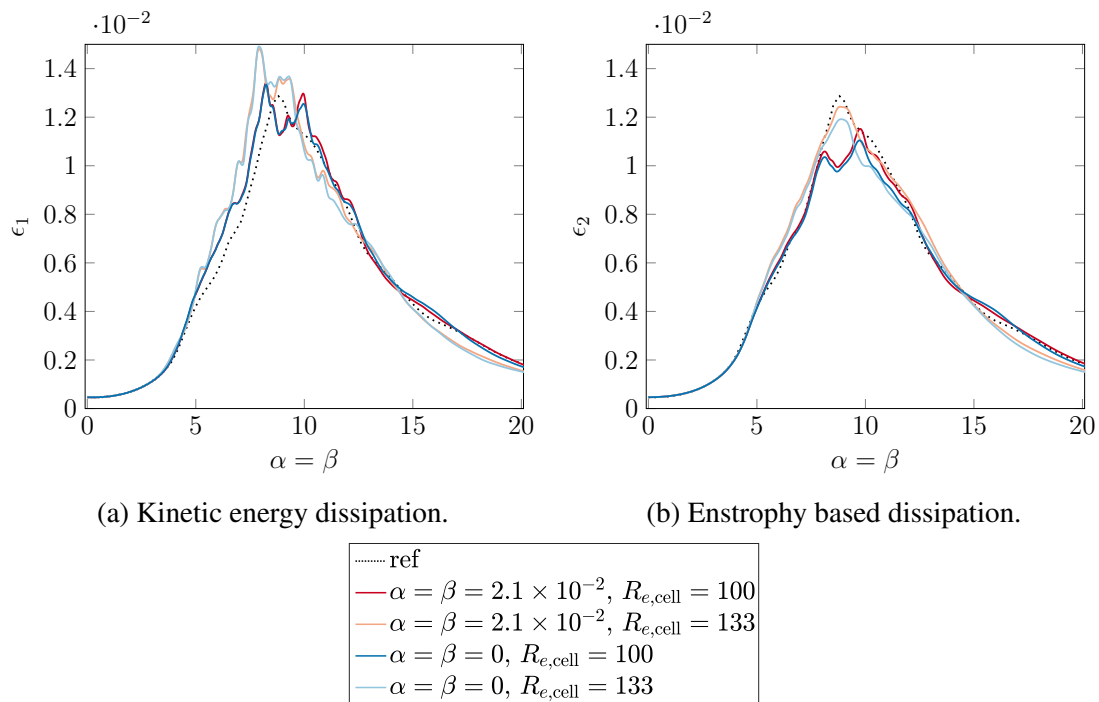
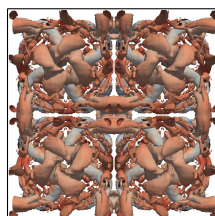


Fig. 5.21 Comparison of the Jacobi SD correction function ($\alpha = \beta = 2.1 \times 10^{-2}$) with the SD correction function recovered by OSFR for two under-resolved grids.

We will begin by evaluating the performance of the SD correction function found in Section 5.4.1. Again, we note here that SD via FR and native SD are only identical for



linear homogeneous equation sets. In Fig. 5.21, we compare two grids that are marginally under-resolved. For the TGV small scales are generated at times approximately in the range $3 < t < 7$. The moderate levels of over-dissipation around these times are indicative of dispersion due to under-resolution. Looking at ϵ_1 and comparing against the reference line we observe similar performance for both SD schemes. However, looking at ϵ_2 it is clear that on both grids the Jacobi SD correction function has an improved dissipation performance compared with the SD scheme recovered by OSFR. These results begin to suggest that this family of Jacobi correction functions may enable us to better tune the implicit filter of FR for ILES.

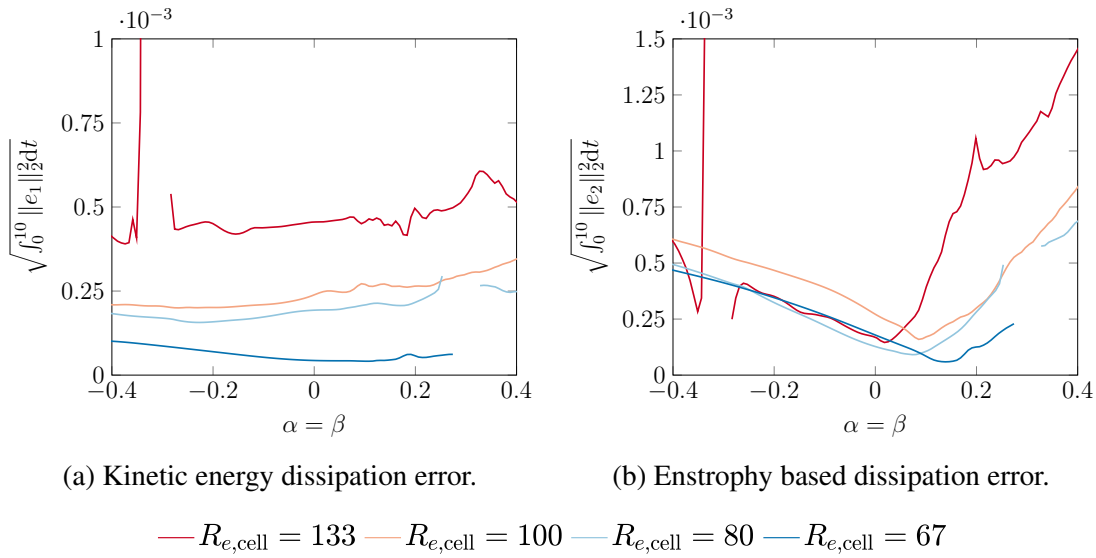


Fig. 5.22 Time averaged error in dissipation rates for the Taylor–Green Vortex, $p = 4$, with symmetric Jacobi SD correction functions.

In order to explore this further, we will investigate how the error in the dissipation varies with time over a range of Jacobi SD correction functions at different grid resolution levels. For this investigation we will use the l_2 error in ϵ_1 and ϵ_2 , which we will define as $\|e_1\|_2 = \|\epsilon_1 - \epsilon_{1,\text{ref}}\|_2$ and similarly for ϵ_2 , where $\epsilon_{1,\text{ref}}$ is the dissipation rate of the reference DNS solution [42, 21]. The resulting errors for several grid resolutions over the range of correction functions $-1 < \alpha = \beta \leq 0.5$ are shown in Fig. 5.22.

Before analysing the results further, we will remark on the temporal integration method. RK44 [77] explicit temporal integration was used with a time step at $R_{e,\text{cell}} = 100$ of $\Delta t = 10^{-3}$. This explicit time step was then linearly scaled as the grids were refined or coarsened, such that the acoustic CFL number remains approximately constant. A time step of $\Delta t = 10^{-3}$ has previously been used for high resolution DNS simulations and is understood to be more than sufficient to resolve the temporal dynamics of the TGV [42]. As such, we shall opt to discard any correction function which is found to be temporally

unstable with this time step — for such functions are unlikely to be of practical utility. Finally, we note that in the case of $R_{e,\text{cell}} = 133$, some schemes with particularly large errors were found to blow up at some time $t > 10$.

Looking at Fig 5.22a it is apparent that the integrated ϵ_1 error is less sensitive to variations in the correction function. As a result, this may be useful in giving more general information about grid resolution and order and will be discussed later. However, far higher sensitivity in the integrated ϵ_2 error is observed. There is clearly an optimal region around $0 < \alpha = \beta < 0.2$, which is similar to the region that was found theoretically to give optimal convergence for linear advection, as well as aligning with the region in Figure D.2 that was predicted to give improved performance.

Repeating this series of tests for qDG, we can see from comparison of Figs. 5.23 & 5.22 that for a range of α values the error of qDG is less than that of SD schemes. In some cases, with $\alpha \approx 0.25$, the error in the enstrophy is low and moderately invariant with $R_{e,\text{cell}}$. Referencing Section 5.4.1, there is no appreciable degradation in CFL limit at this point although it is near to the limit of theoretical stability. Thus, the Jacobi SD schemes trade a small amount of accuracy for an appreciable gain in the CFL limit.

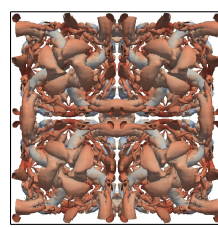
A key point to note about both the Jacobi SD and qDG tests is that in both cases correction functions were found that performed better when considering ϵ_2 than in ϵ_1 . This seems to indicate that the resolved turbulence and the implicit sub-grid model — which comes from the correction function — lead to physical vortical motions. However, the larger ϵ_1 means that there is still non-physical dissipation, but this must be in the larger bulk movement of the fluid, and hence not displayed in the gradients. As was mentioned previously, the variation ϵ_1 is smaller than ϵ_2 when considering changes in correction function. This indicates that ϵ_1 is controlled more by other factors such as the polynomial order, or, as this investigation shows, $R_{e,\text{cell}}$.

GLSFR Results

We now move on to briefly study the GLSFR correction function set applied to the TGV.

Figure 5.24 shows the approximate error for two different grid spacings as the correction function is varied with a constant time step of 1×10^{-3} . This time step was chosen as it should be sufficient to run with such a time step [101] and any reduction beyond this would symbolise that a correction function is not sufficiently temporally stable to be considered applicable for industrial problems.

Figure 5.14b & 5.14c showed that as the parameter $\tilde{\mathbf{h}}_{11}$ is increased the temporal stability is reduced, and this trend is also seen in the TGV results. The TGV error also exhibits a large asymmetry between the positive and negative values of $\tilde{\mathbf{h}}_{10}$, theoretical results also displayed a degree of asymmetry. However, from Fig. 5.17 the stability was



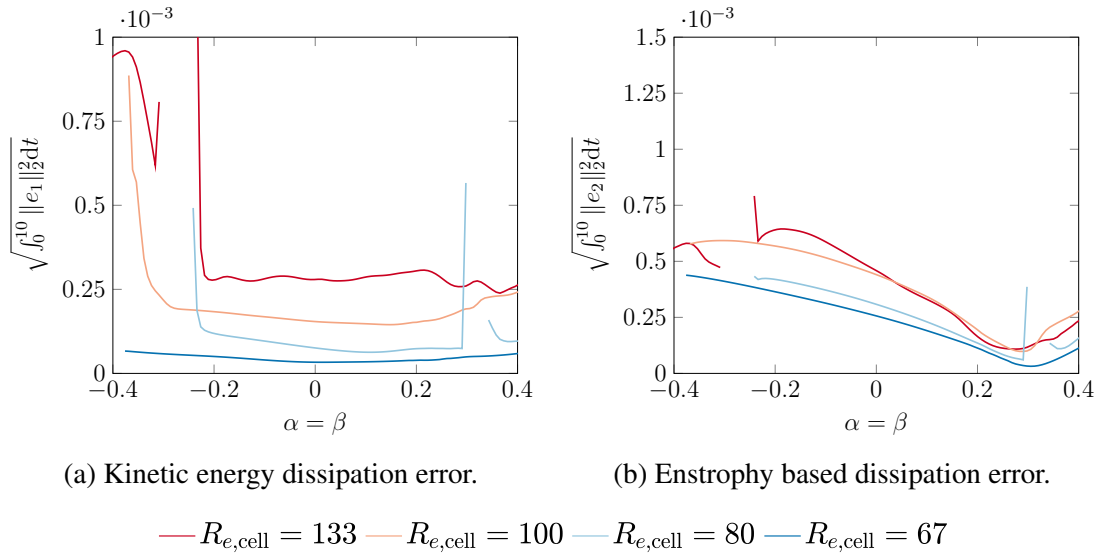


Fig. 5.23 Time averaged error in dissipation rates for the Taylor–Green Vortex, $p = 4$, with qDG correction functions for $\alpha = \beta$.

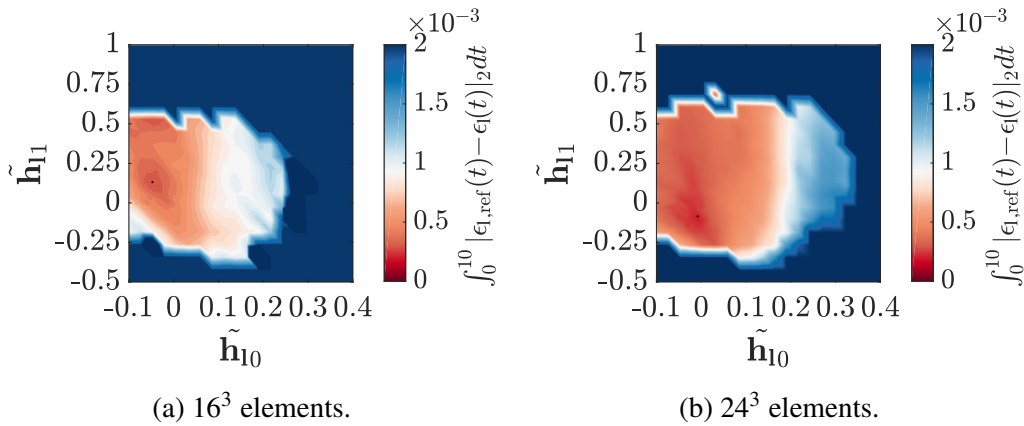


Fig. 5.24 Time integrated error in the kinetic energy dissipation of the Taylor-Green vortex, $R_e = 1600$ $P_r = 0.71$ $Ma = 0.08$, for FR, $p = 4$, with 800 GLSFR correction functions compared to DNS data for each grid resolution. RK44 temporal integration was used with a fixed time step of 1×10^{-3} . A point indicates the correction function tested with the lowest error.

improved for $\tilde{\mathbf{h}}_{10} > 0$, albeit this was for CFL limit. The implication of a higher CFL limit is a more dissipative scheme, whereas for reduced error a less dissipative scheme is necessary. Hence, the location of the error-optimal correction function is found to lie in the left-hand half plane.

A secondary point that may be made about GLSFR correction functions is that, for both grid resolutions, correction functions were found in broadly the same range of \mathbf{H}_4 that gave lower error than Nodal DG via FR. Hence, these correction functions are not merely a mathematical exercise but may provide improved performance for real fluid dynamical simulations.

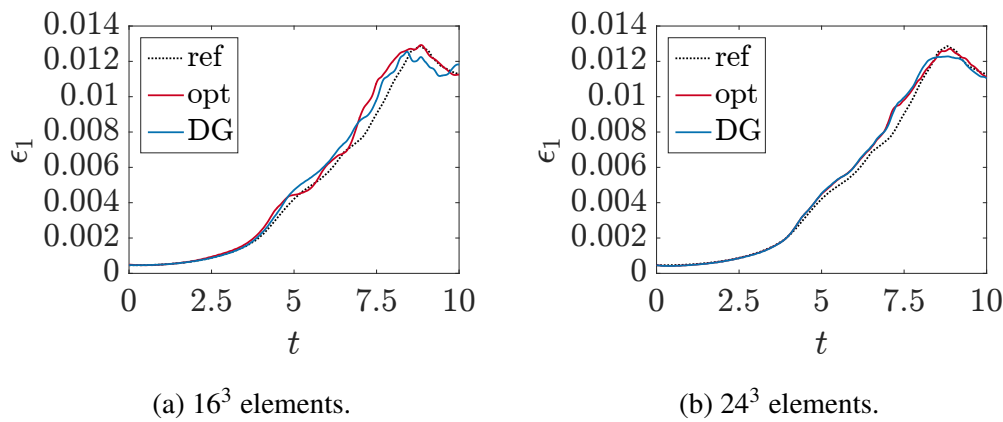
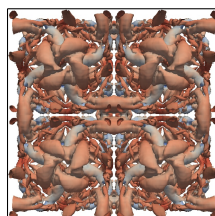


Fig. 5.25 Optimal GLSFR correction functions, $p = 4$, found in Fig.5.24 compared to Nodal DG via FR, with reference data taken from DeBonis [42]. RK44 temporal integration was used with a fixed time step of 1×10^{-3} .

Lastly, the kinetic energy dissipation of the optimal and DG correction function is compared for the two grid refinement levels in Fig. 5.25. In both cases the peak turbulent dissipation is better matched, but in both cases there is a region at $t \approx 7.5$ in which correction function tuning appears to make only modest or no improvement. In the case of Fig. 5.25a, tuning the correction function has resulted in extra dissipation at this time. The importance of $t \approx 7.5$ is due to the rate of change of dissipation being at its highest, the flow can be said to be transitioning to turbulence with turbulent structures forming. The factor that can be seen to have the greatest impact on improving the simulation of the physics at this time is increased grid resolution. For the mildly under-resolved case of 16^3 , extra dissipation seems to be important in producing extra shear to correctly form turbulence for the subsequent decay.



5.6 Conclusions

Several new energy stable families of correction functions have been found for FR. These were derived by a novel approach to generalising Sobolev energy stability. In some instances these sets were found to contain the previously defined OSFR [160] and ESFR [162] correction function sets. For a full picture of how these sets of correction functions intersect diagrammatically see Fig 5.26. Further work is needed to explore the full potential of the correction functions discovered, however some conclusions may be drawn from each of the sets defined.

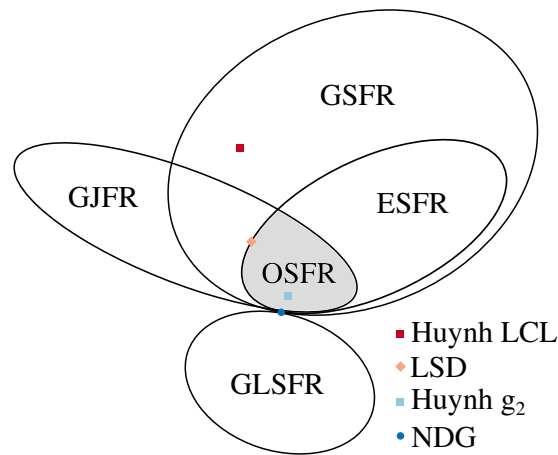


Fig. 5.26 Euler diagram to show the interconnection of the spaces of FR correction functions: Nodal DG (NDG) [65]; Original Stable FR (OSFR) [160]; Extended range Stable FR (ESFR) [162]; Generalised Sobolev stable FR (GSFR) [148]; Generalised Lebesgue Stable FR (GLSFR) [147] and, the Generalised Jacobi stable FR (GJFR) of the present work. Some specific examples of specific schemes are given, notably Huynh's Lumped Chebyshev-Lobatto (LCL) [65] scheme and the original Legendre spectral difference (LSD) scheme [80, 65, 73].

5.6.1 GJFR

Theoretical convergence studies and von Neumann analysis were then used to show that these new schemes can be used to increase accuracy without impacting temporal stability relative to previous FR schemes. Moreover, the newly derived schemes also enable the definition of quasi-DG schemes, where stability is found in a weighted L_2 norm. The same convergence study showed that these have the potential to increase the order of accuracy of DG, and in the case of $p = 4$ with central interfaces, an increase in the rate of convergence of two orders was found. Using the Generalised Jacobi approach it is possible to recover, at least for a linear flux function, a range of SD schemes. Numerical experiments were then performed to validate some findings, which showed that the

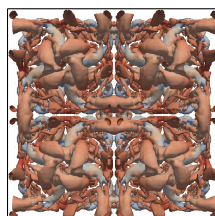
optimal correction function for the full Navier-Stokes equations lay in the same region predicted by theoretical linear investigations.

5.6.2 GSFR

Study of the linear advection equation, via a von Neumann analysis, was then used to show that for $p = 3$ a correction function could be found that led to an increase in the CFL number for RK44 temporal integration. It was also demonstrated that this correction function recovers numerically the expected OOA, with GSFR also enabling the recovery of functions from the lower order spaces. A one dimensional linear heterogeneous PDE was proposed to numerically investigate the performance of GSFR when applied to an equation that causes aliasing. The investigation showed that the region of high CFL limit for the case of $p = 3$ was within a stable area of low error. Finally, the solution of Euler's equations on the ICV test case was used to compare the relative performance when applied to fully non-linear PDEs. Of the correction functions tested all remained stable with reasonable performance, however it was found that DG gave the minimal decay in the kinetic energy for this test.

5.6.3 GLSFR

Von Neumann analysis for both the linear advection and linear advection-diffusion equations was then presented for this new set of corrections, and a region of temporally stable correction functions was found to exist for both upwinded and centrally differenced interfaces, when Runge-Kutta temporal integration was used. Through exploration of the dispersion and dissipation characteristics of some correction functions, it was shown that GLSFR may be able to provide improved performance for implicit LES calculations. Lastly, a series of Taylor–Green vortex tests was performed for two grid spacings, and it was found that in both cases a similar region of corrections gave good performance for minimising the error in the turbulent kinetic energy dissipation. In both cases correction functions were found that reduced the error when compared to DG. Therefore, it is concluded that GLSFR may be able improve the accuracy of FR when applied to real fluid-dynamical problems.



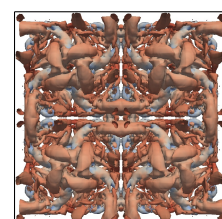
Chapter 6

Conclusions

Through this work I have aimed to challenge some dogmas existing in CFD, in particular when high order methods are applied. The first such dogma was storing the primitive variables and using these to construct the flux functions. It was found that in methods that utilise interpolation or fitting this can cause errors to be introduced. Ultimately it was found that storing the conserved variable was beneficial as the scale of the errors was reduced and the resolution mildly increased, in one case an increase in the TGV enstrophy of $\approx 30\%$ was found. This change is due to a reduction to the flux function order and was found to become increasingly important as order increases. The error that is introduced through storing the primitive does aid the stability of the scheme in some cases where typically aliasing driven instability cause divergence. Finally, storing the conserved variables was found to reduce the computation time compared to primitive by a factor of 1.14. This is due to removal of some conversion steps that are needed in methods using the primitives.

The dogma that double precision is essential in calculations was also confronted in this work. Comparison was made between single and double working precisions and it was found that the difference was negligible, of the order of 0.1% mostly and at worst 1% on globally averaged properties. The benefit of this change is that most modern architectures will have ratios of double to single precision arithmetic units of 1:2 or worse. This can lead to a speed up of 2 or more. Moreover, due to the reduced memory overhead larger cases can be run for the same memory and bandwidth or cases can be run more optimally through benefits such as reduction in cache misses.

The second series of investigations undertaken were to further understand FR when applied in higher dimensions and on non-uniform grids. The key results of this work were that FR experiences smaller changes to dispersion and dissipation properties as angle is varied compared to comparable order finite difference methods [89]. By then applying geometric expansions the variation in the dispersion and dissipation were tracked.



The primary effect observed was dispersion overshoot caused by grid expansion. This behaviour was explained by the misalignment of the wave propagation properties in the x and y directions caused by non-uniformities in mesh. An important result of this work is the comparison of Huynh's g_2 scheme with NDG via FR when fully discretised. This shows that DG, due to its increased dissipation at high wavenumbers, will damp out more of the spurious waves caused by large gradients in the dispersion. Further, that DG sees fewer large changes in the dispersion compared to g_2 . These results are contrary to what has been previously understood about FR in 1D [161], where DG was thought to have worse dispersion properties. Comparisons were then made through the rate of convergence as wave angle to the cell is varied. It was observed that DG saw larger variation to rate on convergence than g_2 .

Numerical tests were performed to understand the impact of these changes when applied to fluidmechanics. A TGV test case was used with a randomised hexahedral grid and it was found that DG was more dissipative at the finer scales than g_2 . However, g_2 was more effected by non-uniformity. This finding was in agreement with the earlier theoretical findings. Lastly for this study, comparison was made between second order FR and second order FV scheme, where FR was found to be more robust to non-uniformity, but had lower resolution at $p = 1$. The FV scheme's robustness could be improved to a level comparable to FR by utilising KEP [72].

The final series of investigation sought to increase the understanding and definition of correction functions. Through studying the norms used to define stability, three new families of correction function were defined, that vastly increased the number of permissible FR scheme. The properties of several specific examples where explored, an important family of correction functions that were defined was the Jacobi SD family that were defined via a Gauss–Jacobi quadrature. This family allows for a reduction in the dissipation and dispersion of classical SD schemes, while being able to be applied within existing FR frameworks. An important theoretical discovery was that the Generalised Sobolev correction definition also contained all the extended range correction functions of Vincent et al. [162]. The importance of this is that in this work and that of Vincent et al. [162] two separate norms where used to define the correction function, which shows that a stable correction function is uniquely defined by a norm.

6.2 Future Work

There are several opportunities for future work that have presented themselves throughout the research presented here. Foremost is the generalisation of correction functions to include any weight function. This then raises the question of using the weight function

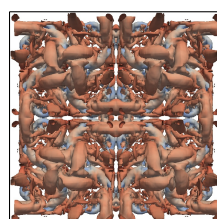
in the definition of lifting collocation penalty FR derivation to form a better solution approximation when applied to non-linear equations. A related area of future work is the use of adaptive Gauss–Christoffel quadrature to increase the accuracy of the solution with respect to some weight function. On application of this work is novel shock capturing schemes, for example the flow field can be used to create a weight function it may then be possible to generate a correction function with this that improves shock resolution.

A furthering of this work on generalising correction functions, is consideration of the stability of these methods in the summation-by-parts framework. The reason for this work is that there are some beliefs that only the L_2 norm is applicable for stability proofs. Although, such works as that included here show that stability can be defined in norms where the L_2 is a subset, a more formal analysis of this is needed to allow for these techniques to gain wider adoption in the community.

Some work that was outlined in my first year report that has not been included here was on Immersed boundary method in FR. The work demonstrated that IBM in FR is not stable, however the work did begin to analyse the stability of source terms in FR. This is work that can be continued. Notably for the application of two phase flows and in particular in the level set method in updating the boundary location. A problem that conventional level set methods have is that numerical dissipation in the boundary calculation require occasional reinitialisation. The problem is that this step will interrupt the parallelism of FR. Instead, using the source term stability understanding, we can add a correction source term that models the Eikonal equation, with the aim of removing the reinitialisation step.

The work on source terms can then be coupled to work on hyperbolic diffusion [108], this offers a way to more quickly compute the Eikonal source terms. However, the stability of this system of equations is unknown. These two components of work also link to some potential research in applying FR to the reaction-diffusion equation [154]. This is an important equation in ecology as well as combustion science, and provides interesting instabilities in 2 or more dimensions through the balancing of diffusion and non-linear source terms.

Some work for the long term is the application of FR to electro-dynamics, i.e Maxwell's equations. There has been some work on using DG as a method here, in particular some astounding work by Dumbser et al. [48] casting coupled Maxwell's and Navier–Stokes' equations in Einstein's field equations and then solving with ADER-DG [47]. However, it is still popular in electro-dynamics to use the Finite-Difference Time Domain method [141], a simple central difference method. FR could then be beneficial here for the same reasons as for using FR in fluid dynamics. There are several challenging problems this confronts us with though, one is that it is typical to require complex

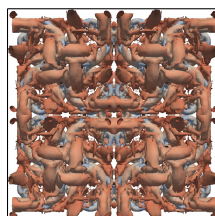


impedances, i.e. phase changes at interfaces. Linking to this is also that impedances of materials often change with frequency in many practical cases.

Finally, throughout this work a tensor product formulation was used to extend the method to higher dimensional hypercubes, however this is not the only option. Therefore, what is the effect of changing the basis? What is the associated cost in terms of solution error? Could an approximate Euclidean basis be used to reduce or remove the anisotropy? Some preliminary work using a modal FR method has shown that indeed different polynomial bases can be successfully used to reduce anisotropy. However, more work on this area is required.

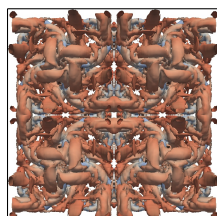
References

- [1] Y. ABE, T. HAGA, T. NONOMURA, AND K. FUJII, *On the Freestream Preservation of High-Order Conservative Flux-Reconstruction Schemes*, Journal of Computational Physics, 281 (2015), pp. 28–54.
- [2] ———, *Conservative High-Order Flux-Reconstruction Schemes on Moving and Deforming Grids*, Computers and Fluids, 139 (2016), pp. 2–16.
- [3] Y. ABE, I. MORINAKA, T. HAGA, T. NONOMURA, H. SHIBATA, AND K. MIYAJI, *Stable, Non-Dissipative, and Conservative Flux-Reconstruction Schemes in Split Forms*, Journal of Computational Physics, 353 (2018), pp. 193–227.
- [4] R. ABGRALL, *On Essentially Non-Oscillatory Schemes on Unstructured Meshes: Analysis and Implementation*, Journal of Computational Physics, 114 (1994), pp. 45–58.
- [5] R. ABGRALL AND M. RICCHIUTO, *High order methods for CFD*, in Encyclopedia of Computational Mechanics Second Edition, John Wiley & Sons, Ltd, 2017, pp. 1–54.
- [6] S. ADJERID, K. D. DEVINE, J. E. FLAHERTY, AND L. KRIVODONOVA, *A Posteriori Error Estimation for Discontinuous Galerkin Solutions of Hyperbolic Problems*, Computer Methods in Applied Mechanics and Engineering, 191 (2002), pp. 1097–1112.
- [7] M. ALHAWWARY AND Z. J. WANG, *Fourier Analysis and Evaluation of DG, FD and Compact Difference Methods for Conservation Laws*, Journal of Computational Physics, 373 (2018), pp. 835–862.
- [8] Y. ALLANEAU AND A. JAMESON, *Connections between the Filtered Discontinuous Galerkin Method and the Flux Reconstruction Approach to High Order Discretizations*, Computer Methods in Applied Mechanics and Engineering, 200 (2011), pp. 3628–3636.
- [9] G. M. AMDAHL, *Validity of the Single Processor Approach to Achieving Large Scale Computing Capabilities*, in AFIPS Spring Jopint Computer Conference, 1967, pp. 1–4.
- [10] K. ASTHANA AND A. JAMESON, *High-Order Flux Reconstruction Schemes with Minimal Dispersion and Dissipation*, Journal of Scientific Computing, 62 (2014), pp. 913–944.
- [11] K. ASTHANA, J. WATKINS, AND A. JAMESON, *On Consistency and Rate of Convergence of Flux Reconstruction For Time-Dependent Problems*, Journal of Computational Physics, 334 (2017), pp. 367–391.



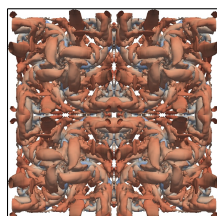
- [12] D. H. BAILEY, *High-Precision Floating-Point Arithmetic in Scientific Computing*, Computing in Science and Engineering, 7 (2005), pp. 54–61.
- [13] W. N. BAILEY, *On The Product of Two Legendre Polynomials*, Mathematical Proceedings of the Cambridge Philosophical Society, 29 (1933), pp. 173–176.
- [14] F. BASSI AND S. REBAY, *A High-Order Accurate Discontinuous Finite Element Method for the Numerical Solution of the Compressible Navier–Stokes Equations*, Journal of Computational Physics, 131 (1997), pp. 267–279.
- [15] ———, *An Implicit High-Order Discountinuous Galerkin Method for the Steady State Compressible Navier-Stokes Equations*, in Computational Fluid Dynamics '98, Athens, Greece, 1998, John Wilery & Sons Ltd., pp. 1226–1233.
- [16] F. BASSI, S. REBAY, G. MARIOTTI, S. PEDINOTTI, AND M. SAVINI, *A High Order Accurate Discontinuous Finite Element Method for Inviscid and Viscous Turbomachinery Flows*, in Turbomachinery - Fluid Dynamics and Thermodynamics, 2nd European Conference, Antwerpen, Mar 5-7, 1997, pp. 99–108.
- [17] F. BASSIL, *GMRES Discontinuous Galerkin Solution of the Compressible Navier–Stokes Equations*, in Discontinuous Galerkin Methods: Theory, Computations and Applications, M. Griebel, D. E. Keyes, R. M. Nieminen, D. Roose, and T. Schlick, eds., Springer-Verlag, Berlin Heidelberg, first ed., 2000, ch. 14, pp. 197–208.
- [18] H. BATEMEN, A. ERDELYI, W. MAGNUS, F. OBERHETTINGER, AND F. TRICOMI, *Higher Transcendental Functions, Volume 1*, McGraw-Hill Book Company, New York Toronto London, first ed., 1953.
- [19] R. BEALS AND R. WONG, *Special Functions and Orthogonal Polynomials*, Cambridge University Press, Cambridge, first ed., 2016.
- [20] G. A. BLAISDELL, E. T. SPYROPOULOS, AND J. H. QIN, *The Effect of the Formulation of Nonlinear Terms on Aliasing Errors in Spectral Methods*, Applied Numerical Mathematics, 21 (1996), pp. 207–219.
- [21] M. E. BRACHET, D. L. MERION, S. A. ORSZAG, B. G. NICKEL, R. H. MORF, AND U. FRISCH, *Small-Scale Structure of the Taylor-Green Vortex*, Journal of Fluid Mechanics, 130 (1983), pp. 411–452.
- [22] A. BRANDT, *Multi-Level Adaptive Solutions to Boundary-Value Problems*, Mathematics of Computation, 31 (1977), pp. 333–390.
- [23] T. BRANDVIK AND G. PULLAN, *An Accelerated 3D Navier–Stokes Solver for Flows in Turbomachines*, Journal of Turbomachinery, 133 (2009), pp. 1–9.
- [24] S. C. BRENNER AND L. RIDGWAY-SCOTT, *The Mathematical Theory of Finite Element Methods*, Springer-Verlag, New York, third ed., 2008.
- [25] J. R. BULL AND A. JAMESON, *Simulation of the Compressible Taylor Green Vortex using High-Order Flux Reconstruction Schemes*, AIAA Journal, 53 (2014), pp. 1–17.
- [26] J. C. BUTCHER, *On Runge–Kutta Processes of High Order*, Journal of the Australian Mathematical Society, 4 (1964), pp. 179–194.

- [27] R. S. CANT, *SENGA2 User Guide*, Tech. Rep. CUED/ATHERMO/TR67, University of Cambridge, 2012.
- [28] M. H. CARPENTER, D. GOTTLIEB, AND S. ABARBANEL, *The Stability of Numerical Boundary Treatments for Compact High-Order Finite-Difference Schemes*, *Journal of Computational Physics*, 108 (1993), pp. 272–295.
- [29] M. H. CARPENTER AND C. A. KENNEDY, *Fourth-Order 2N-Storage Runge-Kutta Schemes*, NASA Technical Memorandum, 109112 (1994), pp. 1–26.
- [30] P. CASTONGUAY, *High-order Energy Stable Flux Reconstruction Schemes For Fluid Flow Simulations on Unstructured Grids*, PhD thesis, Stanford University, 2012.
- [31] P. CASTONGUAY, P. E. VINCENT, AND A. JAMESON, *Application of High-Order Energy Stable Flux Reconstruction Schemes to the Euler Equations*, 49th AIAA Aerospace Sciences Meeting including the New Horizons Forum and Aerospace Exposition, 686 (2011).
- [32] ———, *A New Class of High-Order Energy Stable Flux Reconstruction Schemes for Triangular Elements*, *Journal of Scientific Computing*, 51 (2012), pp. 224–256.
- [33] P. CASTONGUAY, D. M. WILLIAMS, P. E. VINCENT, AND A. JAMESON, *Energy Stable Flux Reconstruction Schemes for Advection-Diffusion Problems*, *Computer Methods in Applied Mechanics and Engineering*, 267 (2013), pp. 400–417.
- [34] J.-B. CHAPELIER, M. DE LA LLAVE PLATA, AND F. RENAC, *Inviscid and Viscous Simulations of the Taylor-Green Vortex Flow Using a Modal Discontinuous Galerkin Approach*, in 42nd AIAA Fluid Dynamics Conference and Exhibit, no. June, 2012, pp. 1–17.
- [35] A. J. CHORIN, *A numerical method for solving incompressible viscous flow problems*, *Journal of Computational Physics*, 2 (1967), pp. 12–26.
- [36] F. K. CHOW AND P. MOIN, *A Further Study of Numerical Errors in Large-Eddy Simulations*, *Journal of Computational Physics*, 184 (2003), pp. 366–380.
- [37] B. COCKBURN, G. E. KARNIADAKIS, AND C. W. SHU, *The Development of Discontinuous Galerkin Methods*, in *Discontinuous Galerkin Methods* (Newport, RI, 1999), vol. 11, Springer-Verlag, Berlin, 2000, ch. 1, pp. 3–50.
- [38] B. COCKBURN, M. LUSKIN, C. W. SHU, AND E. SULI, *Post-Processing of Galerkin Methods for Hyperbolic Problems*, in *Discontinuous Galerkin Methods* (Newport, RI, 1999), Newport, 1999, Springer-Verlag, pp. 291–300.
- [39] B. COCKBURN AND C. W. SHU, *The Local Discontinuous Galerkin Method for Time-Dependent Convection-Diffusion Systems*, *SIAM*, 35 (1998), pp. 2440–2463.
- [40] R. COURANT, K. FRIEDRICHS, AND H. LEWY, *On the Partial Difference Equations of Mathematical Physics*, *IBM Journal*, 11 (1967), pp. 215–234.
- [41] S. DAVIS, *Simplified Second-order Godunov-type Methods*, *SIAM Journal on Scientific and Statistical Computing*, 9 (1988), pp. 445–473.



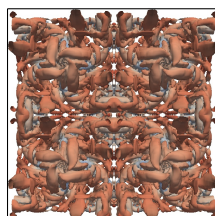
- [42] J. R. DEBONIS, *Solutions of the Taylor-Green Vortex Problem Using High-Resolution Explicit Finite Difference Methods*, 51st AIAA Aerospace Sciences Meeting including the New Horizons Forum and Aerospace Exposition, (2013).
- [43] E. H. DOHA, *On the Coefficients of Differentiated Expansions and Derivative of Jacobi Polynomials*, *Journal of Physics A: Mathematical and General*, 35 (2002), pp. 3467–3478.
- [44] J. DOUGALL, *On The Product of Two Legendre Polynomials*, *Glasgow Mathematical Journal*, 1 (1952), pp. 121–125.
- [45] M. DUBINER, *Spectral methods on triangles and other domains*, *Journal of Scientific Computing*, 6 (1991), pp. 345–390.
- [46] M. DUMBSER, D. S. BALSARA, E. F. TORO, AND C. D. MUNZ, *A Unified Framework for the Construction of One-Step Finite Volume and Discontinuous Galerkin Schemes on Unstructured Meshes*, *Journal of Computational Physics*, 227 (2008), pp. 8209–8253.
- [47] M. DUMBSER, F. FAMBRI, M. TAVELLI, M. BADER, AND T. WEINZIERL, *Efficient Implementation of Ader Discontinuous Galerkin Schemes for a Scalable Hyperbolic PDE Engine*, *Axioms*, 7 (2018), pp. 63–89.
- [48] M. DUMBSER, F. GUERCILENA, S. KÖPPEL, L. REZZOLLA, AND O. ZANOTTI, *Conformal and Covariant Z4 Formulation of the Einstein Equations: Strongly Hyperbolic First-Order Reduction and Solution with Discontinuous Galerkin Schemes*, *Physical Review D*, 97 (2018), p. 84053.
- [49] M. DUMBSER AND C. D. MUNZ, *Arbitrary High Order Discontinuous Galerkin Schemes*, in *Numerical Methods for Hyperbolic and Kinetic Problems*, S. Cordier, T. Goudon, M. Gutnic, and E. Sonnendrucker, eds., EMS Publishing House, Zurich, first ed., 2005, ch. 15, pp. 295–333.
- [50] J. GAO, *A Block Interface Flux Reconstruction Method for Numerical Simulation with High Order Finite Difference Scheme*, *Journal of Computational Physics*, 241 (2013), pp. 1–17.
- [51] B. GARFINKEL, *Addition Theorem for a Derivative of a Legendre Polynomial*, *The Astronomical Journal*, 69 (1964), pp. 567–569.
- [52] W. GAUTSCHI, *Construction of Gauss-Christoffel quadrature formulas*, *Mathematics of Computation*, 22 (1968), pp. 251–270.
- [53] ———, *A Survey of Gauss-Christoffel Quadrature Formulae*, in *E.B. Christoffel - The Influence of His Work on Mathematics and the Physical Sciences*, P. L. Butzer and F. Feher, eds., Birkhäuser Verlag, Basel, 1981, ch. 6, pp. 72–147.
- [54] S. GHOSAL, *An Analysis of Numerical Errors in Large-Eddy Simulations of Turbulence*, *Journal of Computational Physics*, 125 (1996), pp. 187–206.
- [55] J. W. GIBBS, *Fourier's Series*, *Nature*, 59 (1899), p. 606.
- [56] F. H. HARLOW, *Fluid Dynamics in Group T-3 Los Alamos National Laboratory (with Introduction)*, *Journal of Computational Physics*, 195 (2004), pp. 413–433.

- [57] A. HARTEN, *High Resolution Schemes for Hyperbolic Conservation Laws*, Journal of Computational Physics, 49 (1983), pp. 357–393.
- [58] A. HARTEN, B. ENGQUIST, S. OSHER, AND S. R. CHAKRAVARTHY, *Uniformly High-Order Accurate Essentially Non-Oscillatory Schemes, III*, Journal of Computational Physics, 71 (1987), pp. 231–303.
- [59] J. S. HESTHAVEN AND D. GOTTLIEB, *Stable spectral methods for conservation laws on triangles with unstructured grids*, Computer Methods in Applied Mechanics and Engineering, 175 (1999), pp. 361–381.
- [60] J. S. HESTHAVEN AND T. WARBURTON, *Nodal Discontinuous Galerkin Methods: Algorithms, Analysis, and Applications*, vol. 54 of Texts in Applied Mathematics, Springer New York, New York, NY, first ed., 2008.
- [61] J. T. HOLDEMAN, *Legendre Polynomial Expansions of Hypergeometric Functions with Applications*, Journal of Mathematical Physics, 11 (1970), pp. 114–117.
- [62] H. HOMANN, J. DREHER, AND R. GRAUER, *Impact of the Floating-Point Precision and Interpolation Scheme on the Results of DNS of Turbulence by Pseudo-Spectral Codes*, Computer Physics Communications, 177 (2007), pp. 560–565.
- [63] E. HOPF, *The partial differential equation $ut + uux = \mu xx$* , Communications on Pure and Applied Mathematics, 3 (1950), pp. 201–230.
- [64] F. Q. HU, M. Y. HUSSAINI, AND P. RASSETARINERA, *An analysis of the Discontinuous Galerkin method for wave propagation problems*, Journal of Computational Physics, 151 (1999), pp. 921–946.
- [65] H. T. HUYNH, *A Flux Reconstruction Approach to High-Order Schemes Including Discontinuous Galerkin Methods*, in 18th AIAA Computational Fluid Dynamics Conference, vol. 2007-4079, 2007, pp. 1–42.
- [66] ———, *A Flux Reconstruction Approach to High-Order Schemes Including Discontinuous Galerkin for Diffusion*, in 47th AIAA Aerospace Science Meeting, no. January in Fluid Dynamics and Co-located Conferences, American Institute of Aeronautics and Astronautics, jun 2009, pp. 1–34.
- [67] ———, *High-Order Methods Including Discontinuous Galerkin by Reconstructions on Triangular Meshes*, in 49th AIAA Aerospace Sciences Meeting, no. January, 2011, pp. 1–28.
- [68] E. ISAACSON AND H. B. KELLER, *Analysis of Numerical Methods*, John Wiley & Sons Ltd., New York, second ed., 1994.
- [69] A. ISERLES, *A First Course in the Numerical Analysis of Differential Equations*, Cambridge University Press, Cambridge, second ed., 2009.
- [70] M. E. H. ISMAIL, *Classical and Quantum Orthogonal Polynomials in One Variable*, Encyclopedia of Mathematics and its Applications, Cambridge University Press, first ed., 2005.
- [71] A. JAMESON, *Time Dependent Calculations Using Multigrid, with Applications to Unsteady Flows Past Airfoils and Wings*, in AIAA 10th Computational Fluid Dynamics Conference, 1991, p. 14.



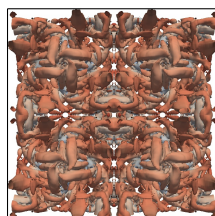
- [72] ———, *Formulation of Kinetic Energy Preserving Conservative Schemes for Gas Dynamics and Direct Numerical Simulation of One-Dimensional Viscous Compressible Flow in a Shock Tube Using Entropy and Kinetic Energy Preserving Schemes*, *Journal of Scientific Computing*, 34 (2008), pp. 188–208.
- [73] ———, *A Proof of the Stability of the Spectral Difference Method For All Orders of Accuracy*, *Journal of Scientific Computing*, 45 (2010), pp. 348–358.
- [74] A. JAMESON, W. SCHMIDT, AND E. TURKEL, *Numerical Solution of the Euler Equations by Finite Volume Methods Using Runge–Kutta Time-Stepping Schemes*, in *AIAA 14th Fluid and Plasma Dynamic Conference*, vol. 1259, 1981, pp. 1–17.
- [75] A. JAMESON, P. E. VINCENT, AND P. CASTONGUAY, *On The Non-Linear Stability of Flux Reconstruction Schemes*, *Journal of Scientific Computing*, 50 (2012), pp. 434–445.
- [76] G. E. KARNIADAKIS AND S. J. SHERWIN, *Spectral/hp Element Methods for Computational Fluid Dynamics*, Oxford University Press, Oxford, first ed., 2013.
- [77] C. A. KENNEDY, M. H. CARPENTER, AND R. M. LEWIS, *Low-Storage, Explicit Runge-Kutta Schemes for the Compressible Navier-Stokes Equations*, *Applied Numerical Mathematics*, 35 (2000), pp. 177–219.
- [78] P. K. KHOSLA AND S. G. RUBIN, *Filtering of Non-Linear Instabilities*, *Journal of Engineering Mathematics*, 13 (1979), pp. 127–141.
- [79] J. W. KIM AND D. J. LEE, *Characteristic Interface Conditions for Multiblock High-Order Computation on Singular Structured Grid*, *AIAA Journal*, 41 (2003), pp. 2341–2348.
- [80] D. A. KOPRIVA, *A Conservative Staggered-grid Chebyshev Multidomain Method for Compressible Flows. II. A Semi-Structured Method*, *Journal of Computational Physics*, 128 (1996), pp. 475–488.
- [81] D. A. KOPRIVA AND J. H. KOLIAS, *A Conservative Staggered-Grid Chebyshev Multidomain Method for Compressible Flows*, *Journal of Computational Physics*, 261 (1996), pp. 244–261.
- [82] A. G. KRAVCHENKO AND P. MOIN, *On the Effect of Numerical Errors in Large Eddy Simulations of Turbulent Flows*, *Journal of Computational Physics*, 131 (1997), pp. 310–322.
- [83] R. KRESS, *Numerical Analysis*, vol. 181 of Graduate Texts in Mathematics, Springer New York, New York, NY, first ed., 1998.
- [84] S. KUKSIN AND A. SHIRIKYAN, *Preliminaries*, in *Mathematics of Two-Dimensional Turbulence*, Cambridge University Press, Cambridge, first ed., 2012, ch. 1, pp. 1–35.
- [85] P. D. LAX, *Gibbs Phenomena*, *Journal of Scientific Computing*, 28 (2006), pp. 445–449.
- [86] P. D. LAX AND R. D. RICHTMYER, *Survey of the Stability of Linear Finite Difference Equations*, *Communications on Pure and Applied Mathematics*, IX (1956), pp. 267–293.

- [87] P. D. LAX AND B. WENDROFF, *Systems of Conservation Laws*, Communications in Pure and Applied Mathematics, XIII (1960), pp. 217–237.
- [88] ———, *Difference Schemes for Hyperbolic Equations with High Order of Accuracy*, Comm, XVII (1964), pp. 381–398.
- [89] S. K. LELE, *Compact Finite Difference Schemes With Spectral-Like Resolution*, Journal of Computational Physics, 103 (1992), pp. 16–42.
- [90] G. LEONI, *Part I: Functions of One Variable*, in A First Course in Sobolev Spaces, American Mathematical Society, Providence, RI, first ed., 2009, ch. 1-7, pp. 3–230.
- [91] R. A. LESLIE, *How Not to Repeatedly Differentiate a Reciprocal*, The American Mathematical Monthly, 98 (1991), pp. 732–735.
- [92] Y. LI AND Z. J. WANG, *A Priori and a Posteriori Evaluations of Sub-Grid Scale Models for the Burgers' Equation*, Computers and Fluids, 139 (2016), pp. 92–104.
- [93] M. S. LIOU, *A Sequel to AUSM: AUSM+*, Journal of Computational Physics, 129 (1996), pp. 364–382.
- [94] M. S. LIOU AND C. J. STEFFEN, *A New Flux Splitting Scheme*, Journal of Computational Physics, 107 (1993), pp. 23–39.
- [95] X.-D. LIU, S. OSHER, AND T. CHAN, *Weighted Essentially Non-Oscillatory Schemes*, Journal of Computational Physics, 115 (1994), pp. 200–212.
- [96] Y. LIU, M. VINOKUR, AND Z. J. WANG, *Discontinuous Spectral Difference Method for Conservation Laws on Unstructured Grids*, Computational Fluid Dynamics 2004, Proceedings of the Third International Conference on Computational Fluid Dynamics (ICCFD3), Toronto, 12-16 July 2004, i (2006), pp. 449–454.
- [97] D. P. LOCKARD, K. S. BRENTNER, AND H. L. ATKINS, *High-Accuracy Algorithms for Computational Aeroacoustics*, AIAA Journal, 33 (1995), pp. 247–251.
- [98] N. A. LOPPI, F. D. WITHERDEN, A. JAMESON, AND P. E. VINCENT, *A high-order cross-platform incompressible Navier – Stokes solver via artificial compressibility with application to a turbulent jet*, Computer Physics Communications, 233 (2018), pp. 193–205.
- [99] ———, *Locally adaptive pseudo-time stepping for high-order Flux Reconstruction*, Journal of Computational Physics, 399 (2019), p. 108913.
- [100] M. D. LOVE, *Subgrid Modelling Studies with Burgers' Equation*, Journal of Fluid Mechanics, 100 (1980), pp. 87–100.
- [101] A. MASTELLONE, F. CAPUANO, S. BENEDETTO, AND L. CUTRONE, *Problem C3 . 5 Direct Numerical Simulation of the Taylor-Green Vortex at $Re = 1600$* , tech. rep., 2015.
- [102] A. MAZAHERI AND H. NISHIKAWA, *Very Efficient High-Order Hyperbolic Schemes for Time-Dependent Advection-Diffusion Problems: Third-, Fourth-, and Sixth-Order*, Computers and Fluids, 102 (2014), pp. 131–147.



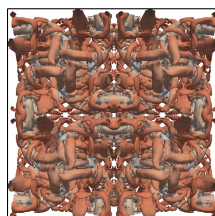
- [103] G. MENGALDO, D. DE GRAZIA, P. E. VINCENT, AND S. J. SHERWIN, *On the Connections Between Discontinuous Galerkin and Flux Reconstruction Schemes: Extension to Curvilinear Meshes*, *Journal of Scientific Computing*, 67 (2016), pp. 1272–1292.
- [104] G. MENGALDO, R. C. MOURA, B. GIRALDA, J. PEIRÓ, AND S. J. SHERWIN, *Spatial Eigensolution Analysis of Discontinuous Galerkin Schemes with Practical Insights for Under-Resolved Computations and Implicit LES*, *Computers and Fluids*, 169 (2018), pp. 349–364.
- [105] J. MILLER, *Formulas for Integrals of Products of Associated Legendre or Laguerre Functions*, *Mathematics of Computation*, 17 (1963), pp. 84–84.
- [106] R. D. MOSER, P. MOIN, AND A. LEONARD, *A Spectral Numerical Method for the Navier–Stokes Equations with Applications to Taylor–Couette Flow*, *Journal of Computational Physics*, 52 (1983), pp. 524–544.
- [107] O. NEVANLINNA AND A. H. SIPILA, *A Nonexistence Theorem for Explicit $A\bar{A}$ -Stable Methods*, *American Mathematical Society*, 28 (1974), pp. 1053–1055.
- [108] H. NISHIKAWA, *A First-Order System Approach for Diffusion Equation. I: Second-Order Residual-Distribution Schemes*, *Journal of Computational Physics*, 227 (2007), pp. 315–352.
- [109] H. NISHIKAWA AND P. L. ROE, *Third-Order Active-Flux Scheme for Advection Diffusion: Hyperbolic Diffusion, Boundary Condition, and Newton Solver*, *Computers and Fluids*, 125 (2016), pp. 71–81.
- [110] NVIDIA, *Nvidia Tesla v100 Gpu Architecture; The World’s Most Advanced Data Center Gpu*, Tech. Rep. August, 2017.
- [111] S. A. ORSZAG AND M. ISRAELI, *Numerical Simulation of Viscous Incompressible Flows*, *Annual Review of Fluid Mechanics*, 6 (1974), pp. 281–318.
- [112] K. OSSWALD, A. SIEGMUND, P. BIRKEN, V. HANNEMANN, AND A. MEISTER, *l2 Roe: A Low Dissipation Version of Roe’s Approximate Riemann Solver for Low Mach Numbers*, *International Journal for Numerical Methods in Fluids*, 81 (2016), pp. 71–86.
- [113] N. PENG AND Y. YANG, *Effects of the Mach Number on the Evolution of Vortex-Surface Fields in Compressible Taylor-Green Flows*, *Physical Review Fluids*, 3 (2018), pp. 1–21.
- [114] A. QUARTERONI, *Domain Decomposition Methods for Systems of Conservation Laws: Spectral Collocation Approximations*, *SIAM Journal on Scientific and Statistical Computing*, 11 (1990), pp. 1029–1052.
- [115] J. J. QUIRK, *A Contribution to the Great Riemann Solver Debate*, *International Journal for Numerical Methods in Fluids*, 18 (1992), pp. 555–574.
- [116] P. A. RAVIART AND THOMAS, *A Mixed Finite Element Method for 2nd Order Elliptic Problems*, in *Mathematical Aspects of Finite Element Methods*, Rome, 1977, Springer Berlin Heidelberg, pp. 292–315.

- [117] W. H. REED AND T. R. HILL, *Triangular Mesh Methods for the Neutron Transport Equation*, Tech. Rep. LA-UR-73-479, 1973.
- [118] K. V. ROBERTS AND N. O. WEISS, *Convective Difference Schemes*, *Mathematics of Computation*, 20 (1966), pp. 272–299.
- [119] M. RODRIGUES, *Sur l’Attraction des Sphéroïdes*, *Correspondence Sur l’École Impériale Polytechnique*, 3 (1816), pp. 361–385.
- [120] P. L. ROE, *Approximate Riemann Solvers , Parameter Vectors, and Difference Schemes*, *Journal of Computational Physics*, 43 (1981), pp. 357–372.
- [121] ———, *Is Discontinuous Reconstruction Really a Good Idea?*, *Journal of Scientific Computing*, 73 (2017), pp. 1094–1114.
- [122] J. ROMERO, K. ASTHANA, AND A. JAMESON, *A Simplified Formulation of the Flux Reconstruction Method*, *Journal of Scientific Computing*, 67 (2016), pp. 351–374.
- [123] J. ROMERO, F. D. WITHERDEN, AND A. JAMESON, *A Direct Flux Reconstruction Scheme for Advection–Diffusion Problems on Triangular Grids*, *Journal of Scientific Computing*, (2017).
- [124] V. RUSANOV, *The Calculation of the Interaction of Non-Stationary Shock Waves with Barriers*, *Zh. Vychisl. Mat. Mat. Fiz.*, 1 (1961), pp. 267–279.
- [125] O. SAN, *Analysis of Low-Pass Filters for Approximate Deconvolution Closure Modelling in One-Dimensional Decaying Burgers Turbulence*, *International Journal of Computational Fluid Dynamics*, 30 (2016), pp. 20–37.
- [126] A. SCILLITOE, P. G. TUCKER, AND P. ADAMI, *Numerical Investigation of Three-Dimensional Separation in an Axial Flow Compressor: The Influence of Free-Stream Turbulence Intensity and Endwall Boundary Layer State*, in *ASME Turbo Expo 2016: Turbomachinery Technical Conference and Exposition*, Seoul, South Korea, jun 2016, ASME, pp. 1–12.
- [127] A. SHESHADRI, *An Analysis of Stability of the Flux Reconstruction Formulation With Applications to Shock Capturing*, phd thesis, Stanford University, 2016.
- [128] A. SHESHADRI AND A. JAMESON, *On the Stability of the Flux Reconstruction Schemes on Quadrilateral Elements for the Linear Advection Equation*, *Journal of Scientific Computing*, 67 (2016), pp. 769–790.
- [129] C. W. SHU, *Essentially Non-oscillatory and Weighted Essentially Non-oscillatory Schemes for Hyperbolic Conservation Laws Chi-Wang*, in *Advanced Numerical Approximation of Non-Linear Hyperbolic Equations*, A. Quarteroni, A. Dold, F. Takens, and B. Teisser, eds., Springer-Verlag, Berlin Heidelberg, first ed., 1997, ch. 4, pp. 327–432.
- [130] ———, *High Order Weighted Essentially Nonoscillatory Schemes for Convection Dominated Problems*, *SIAM Review*, 51 (2009), pp. 82–126.
- [131] C. W. SHU, W. S. DON, D. GOTTLIEB, O. SCHILLING, AND L. JAMESON, *Numerical Convergence Study of Nearly Incompressible, Inviscid Taylor-Green Vortex Flow*, *Journal of Scientific Computing*, 24 (2005), pp. 569–595.



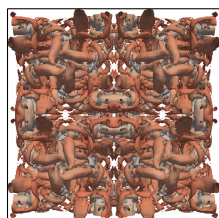
- [132] J. SLOTNICK, A. KHODADOUST, J. ALONSO, D. DARMOFAL, W. GROPP, E. LURIE, AND D. MAVRIPLIS, *CFD Vision 2030 Study: A Path to Revolutionary Computational Aerosciences*, Tech. Rep. March, NASA, 2014.
- [133] J. SMAGORINSKY, *On the Numerical Integration of the Primitive Equations of Motion for Baroclinic Flow in a Closed Region*, *Monthly Weather Review*, 86 (1958), pp. 457–466.
- [134] ———, *General Circulation Experiments with the Primitive Equations*, *Monthly Weather Review*, 91 (1963), pp. 99–164.
- [135] A. SODANI, R. GRAMUNT, J. CORBAL, H. KIM, K. VINOD, S. CHINTHAMANI, S. HUSTELL, R. AGARWAL, Y. C. LIU, AND INTEL, *Knights Landing: Second-Generation Intel Xeon Phi Product*, *IEEE Micro*, 36 (2016), pp. 34–46.
- [136] P. R. SPALART, T. B. COMPANY, M. STRELETS, AND S. R. ALLMARAS, *Comments on the Feasibility of LES for Wings, and on a Hybrid RANS/LES Approach*, in 1st AFOSR International Conference on DNS/LES, C. Liu and Z. Liu, eds., no. January, Ruston, 1997, Greyden Press.
- [137] S. C. SPIEGEL, H. T. HUYNH, AND J. R. DEBONIS, *A Survey of the Isentropic Euler Vortex Problem using High-Order Methods*, in 22nd AIAA Computational Fluid Dynamics Conference, no. June, 2015, pp. 1–21.
- [138] ———, *De-Aliasing through Over-Integration Applied to the Flux Reconstruction and Discontinuous Galerkin Methods*, in 22nd AIAA Computational Fluid Dynamics Conference, AIAA AVIATION Forum, (AIAA 2015-2744), Dallas (TX), 2015, pp. 1–22.
- [139] J. L. STEGER AND R. F. WARMING, *Flux Vector Splitting of the Inviscid Gasdynamic Equations with Application to Finite-Difference*, *Journal of Computational Physics*, 40 (1981), pp. 263–293.
- [140] Y. SUN, Z. J. WANG, AND Y. LIU, *High-Order Multidomain Spectral Difference Method for the Navier-Stokes Equations on Unstructured Hexahedral Grids I Introduction*, *Communications in Computational Physics*, 2 (2007), pp. 310–333.
- [141] A. TAFLOVE AND S. C. HAGNESS, *Computational Electrodynamics: The Finite-Difference Time Domain Method*, Artech House, Boston, MA, second ed., 2000.
- [142] C. K. W. TAM AND J. C. WEBB, *Dispersion-Relation-Preserving Finite Difference Schemes for Computational Acoustics*, *Journal of Computational Physics*, 107 (1993), pp. 262–281.
- [143] G. I. TAYLOR AND A. E. GREEN, *Mechanism of the Production of Small Eddies from Large Ones*, *Proceedings of the Royal Society A: Mathematical, Physical and Engineering Sciences*, 158 (1937), pp. 499–521.
- [144] P. D. THOMAS AND C. K. LOMBARD, *Geometric Conservation Law and Its Application to Flow Computations on Moving Grids*, *AIAA Journal*, 17 (1979), pp. 1030–1037.
- [145] E. F. TORO, *Riemann Solvers and Numerical Methods for Fluid Dynamics - A Practical Introduction*, Springer-Verlag Berlin Heidelberg, Dordrecht Berlin Heidelberg London New York, third ed., 2009.

- [146] L. N. TREFETHEN, *Finite Difference and Spectral Methods for Ordinary and Partial Differential Equations*, Ithaca, New York, first ed., 1994.
- [147] W. TROJAK, *Generalised Lebesgue Stable Flux Reconstruction*, Arxiv, 1805 (2018), pp. 1–15.
- [148] ———, *Generalised Sobolev Stable Flux Reconstruction*, Arxiv, 1804 (2018), pp. 1–19.
- [149] W. TROJAK, R. WATSON, AND P. G. TUCKER, *High Order Flux Reconstruction on Stretched and Warped Meshes*, in AIAA SciTech, 55th AIAA Aerospace Sciences Meeting, Grapevine Texas, 2017, pp. 1–12.
- [150] ———, *Temporal Stabilisation of Flux Reconstruction on Linear Problems*, in 2018 Fluid Dynamics Conference, AIAA AVIATION Forum, Atlanta, jun 2018, American Institute of Aeronautics and Astronautics.
- [151] ———, *High-Order Flux Reconstruction on Stretched and Warped Meshes*, AIAA Journal, 57 (2019), pp. 341–351.
- [152] P. G. TUCKER, *Advanced Computational Fluid and Aerodynamics*, Cambridge Aerospace Series, Cambridge University Press, New York, first ed., 2016.
- [153] P. G. TUCKER, C. L. RUMSEY, P. R. SPALART, R. E. BARTELS, AND R. T. BIEDRON, *Computations of Wall Distances Based on Differential Equations*, AIAA Journal, 43 (2005), pp. 539–549.
- [154] A. M. TURING, *The Chemical Basis of Morphogenesis THE CHEMICAL BASIS OF MOKPHOGENESIS*, Philosophical Transactions of the Royal Society of London. Series B, Biological Sciences, 237 (1952), pp. 37–72.
- [155] B. VAN LEER, *Towards the Ultimate Conservative Differnece Scheme II. Monotonicity and Conservation Combined in a second-Order Scheme*, Journal of Computational Physics, 14 (1974), pp. 361–370.
- [156] ———, *Towards the Ultimate Conservative Differnece Scheme III. Upstream-Centered Finite-Difference Schemes for Idea Compressible Flow*, Journal of Computational Physics, 23 (1977), pp. 263–275.
- [157] B. C. VERMEIRE, S. NADARAJAH, AND P. G. TUCKER, *Implicit Large Eddy Simulation Using the High-Order Correction Procedure via Reconstruction Scheme*, International Journal for Numerical Methods in Fluids, 82 (2016), pp. 231–260.
- [158] B. C. VERMEIRE AND P. E. VINCENT, *On the Properties of Energy Stable Flux Reconstruction Schemes for Implicit Large Eddy Simulation*, Journal of Computational Physics, 327 (2016), pp. 368–388.
- [159] ———, *On the Behaviour of Fully-Discrete Flux Reconstruction Schemes*, Journal of Computational Physics, 315 (2017), pp. 1053–1079.
- [160] P. E. VINCENT, P. CASTONGUAY, AND A. JAMESON, *A New Class of High-Order Energy Stable Flux Reconstruction Schemes*, Journal of Scientific Computing, 47 (2010), pp. 50–72.



- [161] ———, *Insights From von Neumann Analysis of High-Order Flux Reconstruction Schemes*, *Journal of Computational Physics*, 230 (2011), pp. 8134–8154.
- [162] P. E. VINCENT, A. M. FARRINGTON, F. D. WITHERDEN, AND A. JAMESON, *An Extended Range of Stable-Symmetric-Conservative Flux Reconstruction Correction Functions*, *Computer Methods in Applied Mechanics and Engineering*, 296 (2015), pp. 248–272.
- [163] P. E. VINCENT, F. D. WITHERDEN, B. C. VERMEIRE, J. S. PARK, AND A. IYER, *Towards Green Aviation with Python at Petascale*, in *International Conference for High Performance Computing, Networking, Storage and Analysis*, SC, no. November, Denver, 2017, IEEE, pp. 1–11.
- [164] M. R. VISBAL AND D. V. GAITONDE, *High-Order-Accurate Methods for Complex Unsteady Subsonic Flows*, *AIAA Journal*, 37 (1999), pp. 1231–1239.
- [165] M. A. WAHAB, *A Breif History of the ANSIS Package*, in *Mechanics of Adhesives in Composite and Metal Joints: Finite Element Analysis with ANSYS*, DEStech Publications, Lancaster, Pa, first ed., 2014, ch. 3, pp. 59–60.
- [166] Z. J. WANG, *Spectral (Finite) Volume Method for Conservation Laws on Unstructured Grids. Basic Formulation: Basic Formulation*, *Journal of Computational Physics*, 178 (2002), pp. 210–251.
- [167] Z. J. WANG, K. FIDKOWSKI, R. ABGRALL, F. BASSI, D. CARAENI, A. CARY, H. DECONINCK, R. HARTMANN, K. HILLEWAERT, H. T. HUYNH, N. KROLL, G. MAY, P. PERSSON, B. VAN LEER, AND M. VISBAL, *High-Order CFD Methods: Current Status and Perspective*, *International Journal for Numerical Methods in Fluids*, 72 (2013), pp. 811–845.
- [168] J. WATKINS, K. ASTHANA, AND A. JAMESON, *A Numerical Analysis of the Nodal Discontinuous Galerkin Scheme Via Flux Reconstruction for the Advection-Diffusion Equation*, *Computers and Fluids*, 139 (2016), pp. 233–247.
- [169] R. WATSON, P. G. TUCKER, Z. N. WANG, AND X. YUAN, *Towards Robust Unstructured Turbomachinery Large Eddy Simulation*, *Computers and Fluids*, 118 (2015), pp. 245–254.
- [170] A. P. S. WHEELER, R. D. SANDBERG, N. D. SANDHAM, R. PICHLER, AND G. LASKOWSKI, *Direct Numerical Simulations of a High-Pressure Turbine Vane*, *Journal of Turbomachinery*, 138 (2016), pp. 1–9.
- [171] D. M. WILLIAMS, P. CASTONGUAY, P. E. VINCENT, AND A. JAMESON, *An Extension of Energy Stable Flux Reconstruction to Unsteady, Non-linear, Viscous Problems on Mixed Grids*, in *20th AIAA Computational Fluid Dynamics Conference*, no. June, Honolulu, 2011, AIAA, pp. 1–37.
- [172] D. M. WILLIAMS AND A. JAMESON, *Energy Stable Flux Reconstruction Schemes for Advection-Diffusion Problems on Tetrahedra*, *Journal of Scientific Computing*, 59 (2014), pp. 721–759.
- [173] A. R. WINTERS, R. C. MOURA, G. MENGALDO, G. J. GASSNER, S. WALCH, J. PEIRO, AND S. J. SHERWIN, *A Comparative Study on Polynomial Dealiasing and Split Form Discontinuous Galerkin Schemes for Under-Resolved Turbulence Computations*, *Journal of Computational Physics*, 372 (2018), pp. 1–21.

- [174] F. D. WITHERDEN, A. M. FARRINGTON, AND P. E. VINCENT, *PyFR: An Open Source Framework for Solving Advection-Diffusion Type Problems on Streaming Architectures Using the Flux Reconstruction Approach*, *Computer Physics Communications*, 185 (2014), pp. 3028–3040.
- [175] F. D. WITHERDEN, J. S. PARK, AND P. E. VINCENT, *An Analysis of Solution Point Coordinates for Flux Reconstruction Schemes on Tetrahedral Elements*, *Journal of Scientific Computing*, 69 (2016), pp. 1–16.
- [176] M. YU, Z. J. WANG, AND Y. LIU, *On the Accuracy and Efficiency of Discontinuous Galerkin, Spectral Difference and Correction Procedure via Reconstruction Methods*, *Journal of Computational Physics*, 259 (2014), pp. 70–95.
- [177] V. V. ZHIKOV, *Weighted Sobolev Spaces*, *Sbornik: Mathematics*, 189 (1998), pp. 1139–1170.
- [178] P. ZWANENBURG AND S. NADARAJAH, *Equivalence between the Energy Stable Flux Reconstruction and Filtered Discontinuous Galerkin Schemes*, *Journal of Computational Physics*, 306 (2016), pp. 343–369.



Appendix A

Introductory Theory of Orthogonal Polynomials

In this appendix we will detail some of the theory of orthogonal polynomials. This is by no means exhaustive and some of the results shown in the chapter are also presented throughout the main body of the work, but collected here for the readers convenience. If a more detailed understanding of the theory of orthogonal polynomials is required then the following references are recommended [13, 18, 19, 43, 44, 51–53, 61, 70, 105].

We will begin by introducing the concept of orthogonality when applied to a function, which will lead the way for a defining orthogonal polynomials. If we have a domain such that $\Omega \subset \mathbb{R}$ and $x \in \Omega$. Then, two functions $f(x) : x \rightarrow \mathbb{R}$ and $g(x) : x \rightarrow \mathbb{R}$ are said to be orthogonal iff:

$$\int_{\Omega} f(x)g(x)dx = 0 \quad (\text{A.1})$$

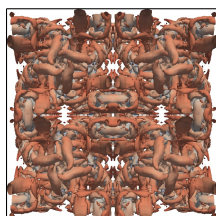
Orthogonality can then be further generalised by defining it with respect to a measure. This measure (or weight function), w is a positive function with infinite support over Ω . Furthermore, moments of the measure must exist:

$$\int_{\Omega} x^n dw(x) \in \mathbb{R} \quad (\text{A.2})$$

for $n \in \mathbb{N}$. With this established, the definition of orthogonality can then be extended to:

$$\int_{\Omega} f(x)g(x)dw(x) = 0 \quad (\text{A.3})$$

The importance of this definition is that we can then establish a set of polynomials, P , where $p_n \in P$ is a polynomial of degree n . By this we mean that the highest order monomial with a non zero coefficient is x^n . To form an orthogonal set we then require



that, again for some weight function, w , that:

$$\int_{\Omega} p_n p_m dw(x) = 0, \quad \forall n \neq m | n, m \in \mathbb{N} \quad (\text{A.4})$$

where $p_n, p_m \in P$. If we state that the polynomials are monic, i.e the coefficient of the largest largest non-zero monomial is one, this simplifies the analysis without a loss of generality. It should then be clear that we can declare the recurrence relation:

$$xp_n = p_{n+1} + \sum_{i=0}^n c_i p_i \quad (\text{A.5})$$

If we then invoke that the polynomial series, P , is orthogonal, then we are left with only three terms:

$$xp_n = p_{n+1} + a_n p_n + b_n p_{n-1}, \quad n \leq 0 \quad (\text{A.6})$$

where $p_{-1} = 0$ and $p_0 = 1$. For a full proof see Theorem 2.2 in [70]. An important contribution of Christoffel [53] was the definition of forms for a_n and b_n :

$$a_n = \frac{\langle xp_n | p_n \rangle}{\langle p_n | p_n \rangle} \quad (\text{A.7})$$

$$b_n = \frac{\langle p_n | p_n \rangle}{\langle p_{n-1} | p_{n-1} \rangle} \quad (\text{A.8})$$

where the inner-product is defined as:

$$\langle f | g \rangle = \int_{\Omega} f(x)g(x)dw(x) \quad (\text{A.9})$$

The final result that can be useful, before we present some specific instances, is Rodrigues' formula [119]. If the weight function is such that:

$$\frac{w'}{w} = \frac{A(x)}{B(x)} \quad (\text{A.10})$$

where $A(x)$ is a function with degree at most equal to one and $B(x)$ is a function of degree at most equal to two, then:

$$p_n(x) = \frac{c_n}{w(x)} \frac{d^n}{dx^n} [B(x)^n w(x)] \quad (\text{A.11})$$

where c_n is some constant. Rodrigues' formula represents an important link between orthogonal polynomials, the derivative operator and differential equations.

We will now present some useful results for some specific polynomial families.

A.1 Legendre Polynomials

Legendre polynomials, ψ_n , are a canonical set of orthogonal polynomials as they are defined with the the weight function $w(x) = 1$ with $\Omega = [-1, 1]$.

$$\int_{-1}^1 \psi_n(x)\psi_m(x)dx = \frac{2}{2n+1}\delta_{n,m} \quad (\text{A.12})$$

The terms of Rodrigues' formula are then found to be:

$$c_n = \frac{1}{2^n n!} \quad (\text{A.13})$$

$$B(x) = (x^2 - 1) \quad (\text{A.14})$$

and the three recurrence relationship is then:

$$(2n+1)x\psi_n = (n+1)\psi_{n+1} + n\psi_{n-1}. \quad (\text{A.15})$$

Combining these results, the derivative of Legendre polynomials may then be found to be:

$$\frac{d\psi_n}{dx} = (2n-1)\psi_{n-1} + (2n-3)\psi_{n-3} + (2n-5)\psi_{n-5} + \dots \quad (\text{A.16})$$

which can straightforwardly be extended to the end points as:

$$\frac{d^p \psi_n(-1)}{dx^p} = \frac{(-1)^{n-p}(n+p)!}{2^p p!(n-p)!} \quad (\text{A.17})$$

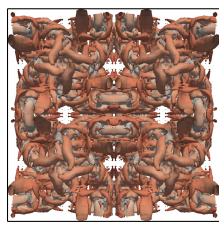
$$\frac{d^p \psi_n(1)}{dx^p} = \frac{(1)^{n-p}(n+p)!}{2^p p!(n-p)!} \quad (\text{A.18})$$

An important result for this work is that of Miller [105] for the integration of Associated Legendre polynomials. First we must introduce the set of functions called Associated Legendre polynomials. These are functions that satisfy:

$$\psi_n^{(m)} = (-1)^m (1-x^2)^{m/2} \frac{d^m \psi_n}{dx^m} \quad (\text{A.19})$$

Miller's result, then, was:

$$\int_{-1}^1 \psi_{n_1}^{(m_1)} \psi_{n_2}^{(m_2)} dx = 2\delta(\text{even}, N) \sum_{q=0}^{(M/2)} \sum_{i=0}^{I(n_1, m_1)} \sum_{j=0}^{I(n_2, m_2)} (-1)^q \binom{M/2}{q} \frac{c_i(n_1, m_1) c_j(n_2, m_2)}{N - M - 2(i+j-q) + 1} \quad (\text{A.20})$$



where $M = \sum_i m_i$, $N = \sum_i n_i$, and c is defined as:

$$c_i(n, m) = \frac{(-1)^i [2(n-i)]!}{2^n (n-m-2i)! (n-i)! i!} \quad (\text{A.21})$$

Here the meaning of $\delta(\text{even}, N)$ is:

$$\delta(\text{even}, N) = \begin{cases} 1, & \text{if } N = \text{even} \\ 0, & \text{if } N = \text{odd} \end{cases} \quad (\text{A.22})$$

Hence by using Eq. (A.19) and recognising that the first summation over q in Eq. (A.20) is due to the $(1-x^2)^{m/2}$ term, we may then write:

$$\int_{-1}^1 \frac{d^{m_1} \psi_{n_1}}{dx^{m_1}} \frac{d^{m_2} \psi_{n_2}}{dx^{m_2}} dx = 2\delta(\text{even}, N) \sum_{i=0}^{\lfloor \frac{n_1-m_1}{2} \rfloor} \sum_{j=0}^{\lfloor \frac{n_2-m_2}{2} \rfloor} \frac{c_i(n_1, m_1) c_j(n_2, m_2)}{N-M-2(i+j)+1} \quad (\text{A.23})$$

This an incredibly powerful result and will come in useful in the generalised analysis of chapter 5.

The final point that should be raised before moving on is the use of Legendre polynomials in polynomial fitting. If we wish to fit a polynomial of order p to the function, f , of order q for $q > p$, while minimising the error, then Legendre polynomial are extremely useful. If we consider the case set out and the error of interest is the L_2 error then we have the problem of finding f_a such that:

$$f_a | \min \sqrt{\int_{-1}^1 (f - f_a)^2 dx} \quad (\text{A.24})$$

If we then say that both f and its approximation f_a are expressed as polynomial series:

$$f = \sum_{i=0}^q \tilde{f}_i L_i \quad \text{and} \quad f_a = \sum_{i=0}^p \tilde{f}_{a,i} L_i \quad (\text{A.25})$$

the integral then becomes:

$$\sqrt{\int_{-1}^1 \left(\sum_{i=0}^q \tilde{f}_i L_i - \sum_{i=0}^p \tilde{f}_{a,i} L_i \right)^2 dx} \quad (\text{A.26})$$

clearly then from the Legendre polynomial orthogonality condition, the minimum is when $\tilde{f}_{a,i} = \tilde{f}_i$ for $i \leq p$. Hence, the Legendre polynomial approximation is optimal with respect to minimum least squares.

A.2 Jacobi Polynomials

Jacobi polynomials are another more general set of orthogonal polynomial sets for $\Omega = [-1, 1]$. Each set of orthogonal polynomials is uniquely defined by two parameters α and β , where $\alpha, \beta \in \{x|x \in \mathbb{R}, x < -1\}$. Jacobi polynomials have proved to be an interesting case of orthogonal polynomial, shown to contain Legendre, Chebyshev and Gegenbauer polynomials. The reason for this is clear when the orthogonality condition is considered:

$$\int_{-1}^1 J_n^{(\alpha,\beta)}(x)J_m^{(\alpha,\beta)}(x)(1-x)^\alpha(1+x)^\beta dx = \frac{2^{\alpha+\beta+1}}{2n+\alpha+\beta+1} \frac{\Gamma(n+\alpha+1)\Gamma(n+\beta+1)}{\Gamma(n+\alpha+\beta+1)n!} \delta_{n,m} \tag{A.27}$$

The terms of Rodrigues' formula are found to be:

$$c_n = \frac{(-1)^n}{2^n n!} \tag{A.28}$$

$$B(x) = (1-x^2) \tag{A.29}$$

and three term recurrence relationship is:

$$(2n+\alpha+\beta+1)(2n+\alpha+\beta+2)(2n+\alpha+\beta)xJ_n^{(\alpha,\beta)} = (2n+2)(n+\alpha+\beta+1)(n+\alpha+\beta)J_{n+1}^{(\alpha,\beta)} + (2n+\alpha+\beta+1)(\beta^2-\alpha^2)J_n^{(\alpha,\beta)} + 2(n+\alpha)(n+\beta)(2n+\alpha+\beta+2)J_{n-1}^{(\alpha,\beta)} \tag{A.30}$$

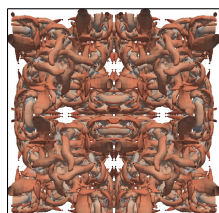
The derivative as a series of lower order Jacobi polynomials was then found by Doha [43] to be:

$$\frac{d^m J_n^{(\alpha,\beta)}}{d\xi^m}(x) = 2^{-m}(n+\alpha+\beta+1)_m \sum_{i=0}^{n-m} D_{n-m,i}(\alpha+m,\beta+m;\alpha,\beta)J_i^{(\alpha,\beta)}(x) \tag{A.31}$$

where

$$D_{j,i}(\gamma,\delta;\alpha,\beta) = \frac{(j+\gamma+\delta+1)_i(i+\gamma+1)_{j-i}\Gamma(i+\alpha+\beta+1)}{(j-i)!\Gamma(2i+\alpha+\beta+1)} \times {}_3F_2\left(\begin{matrix} i-j, & j+i+\gamma+\delta+1, & i+\alpha+1 \\ i+\gamma+1, & 2i+\alpha+\beta+2 \end{matrix}; 1\right) \tag{A.32}$$

We define here that that $(x)_i$ is the rising Pochhammer function and ${}_3F_2(\dots; z)$ is the 3-2 generalised hypergeometric function [13, 18].



A final result that will prove to be useful is that of Ismail [70] for the changing of the Jacobi polynomial basis:

$$J_n^{(\alpha,\beta)} = \sum_{i=0}^n D_{n,i}(\alpha,\beta;\gamma,\delta) J_i^{(\gamma,\delta)} \quad (\text{A.33})$$

where D is defined in Eq.(A.32).

Appendix B

Extended Range of Energy Stable Flux Reconstruction Correction Functions

After the initial definition of OSFR by Vincent et al. [160] an extension to FR was made that drew on techniques from FE and Spectral Element methods. This extension was presented by Vincent et al. [162] to give what was called Extended Range Stable FR (ESFR). This set of correction functions was far wider than those of OSFR, with more control variables. To introduce this set of corrections functions we will take the gradient of the left correction function to be:

$$\frac{dh_L}{d\xi} = g_L(\xi) = \sum_{i=0}^p \tilde{\mathbf{g}}_{L,i} \psi_i(\xi) \quad (\text{B.1})$$

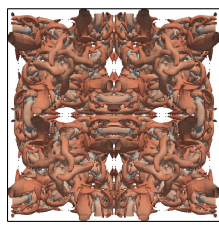
with the right correction similarly defined, and the notation of $\tilde{\bullet}$ generally used for something either in or cast into a Legendre basis. It followed that the extended range of correction function was defined by the equations:

$$\tilde{\mathbf{g}}_L = -(\tilde{\mathbf{M}} + \tilde{\mathbf{K}})^{-1} \tilde{\mathbf{l}} \quad (\text{B.2})$$

$$\tilde{\mathbf{g}}_R = (\tilde{\mathbf{M}} + \tilde{\mathbf{K}})^{-1} \tilde{\mathbf{r}} \quad (\text{B.3})$$

where $\tilde{\mathbf{l}} = [\psi_0(-1), \dots, \psi_p(-1)]^T$, $\tilde{\mathbf{r}} = [\psi_0(1), \dots, \psi_p(1)]^T$ and

$$\tilde{\mathbf{M}}_{i,j} = \int_{-1}^1 \psi_i \psi_j d\xi = \frac{2}{2j+1} \delta_{i,j}, \quad i, j \in \{0, \dots, p\} \quad (\text{B.4})$$



Here, $\tilde{\mathbf{K}}$ is a matrix dependent on the free variables $\{\kappa_0, \dots, \kappa_n\}$ where $n = \lfloor p/2 \rfloor + 1$, with some constraints imposed upon $\tilde{\mathbf{K}}$. First, it is necessary to define the following matrices:

$$\mathbf{D}_{i,j} = \frac{dl_j(\xi_i)}{d\xi} \quad (\text{B.5})$$

$$\mathbf{V}_{i,j} = \psi_j(\xi_i) \quad (\text{B.6})$$

$$\tilde{\mathbf{D}} = \mathbf{V}^{-1} \mathbf{D} \mathbf{V} \quad (\text{B.7})$$

Hence, $\tilde{\mathbf{K}}$ is a real matrix satisfying the constraints:

$$\tilde{\mathbf{K}} = \tilde{\mathbf{K}}^T \quad (\text{B.8})$$

$$\tilde{\mathbf{K}} \tilde{\mathbf{D}} + (\tilde{\mathbf{K}} \tilde{\mathbf{D}})^T = \mathbf{0} \quad (\text{B.9})$$

$$\tilde{\mathbf{M}} + \tilde{\mathbf{K}} > \mathbf{0} \quad (\text{B.10})$$

together with $h_L(-1) = h_R(1) = 1$ and $h_L(1) = h_R(-1) = 0$ and symmetry conditions, this defined a multi-parameter set of correction functions, with examples for various orders shown by Vincent et al. [162]. Further, it was demonstrated that the single parameter OSFR set of Eq.(5.30 & 5.31) was a subset of ESFR.

To illustrate the ESFR correction function set, consider the case of $p = 3$, then, the Legendre coefficients of the correction function gradient can be found to be:

$$\tilde{\mathbf{g}}_1 = - \left[\begin{array}{c} \frac{1}{2} \\ \frac{3(21\kappa_0 + 35\kappa_1 + 6)}{5} \\ \frac{5\kappa_1 + 2}{21(5\kappa_1 + 2)} \\ \frac{21(5\kappa_1 + 2)}{\nu} \end{array} \right] \quad \text{where} \quad \nu = 175\kappa_1^2 - 42\kappa_0 - 12 \quad (\text{B.11})$$

After having defined the ESFR correction functions using FE methods, the Sobolev stability was investigated and found to hold. We have included ESFR as an appendix here as it is informative to the reader to understand the form that the correction functions take. But, due to their different method of derivation and for clarity, they are not included in the main text.

Appendix C

Additonal Generalised Sobolev FR Derivation Details

Here further details around the derivation of the GSFR correction function will be given. This includes how the terms in the norm are produced and how the conditions of stability are met. Beginning by restating FR applied to 1D linear advection with unit velocity:

$$\frac{\partial \hat{u}^\delta}{\partial t} = -\frac{\partial \hat{u}^\delta}{\partial \xi} - (\hat{u}_L^{\delta I} - \hat{u}_L^\delta) \frac{dh_L}{d\xi} - (\hat{u}_R^{\delta I} - \hat{u}_R^\delta) \frac{dh_R}{d\xi} \quad (\text{C.1})$$

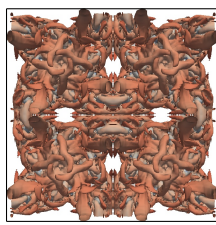
This equation can be used to form the individual terms required in Generalised Sobolev norm. Initially forming the first derivative component by spatially differentiating Eq. (C.1) and then multiplying by $\hat{u}^{\delta(1)}$ to give:

$$\begin{aligned} \frac{\partial \hat{u}^\delta}{\partial \xi} \frac{d}{dt} \left(\frac{\partial \hat{u}^\delta}{\partial \xi} \right) &= \frac{1}{2} \frac{d}{dt} \left(\frac{\partial \hat{u}^\delta}{\partial \xi} \right)^2 \\ &= -\frac{\partial \hat{u}^\delta}{\partial \xi} \frac{\partial^2 \hat{u}^\delta}{\partial \xi^2} - (\hat{u}_L^{\delta I} - \hat{u}_L^\delta) \frac{\partial \hat{u}^\delta}{\partial \xi} \frac{d^2 h_L}{d\xi^2} - (\hat{u}_R^{\delta I} - \hat{u}_R^\delta) \frac{\partial \hat{u}^\delta}{\partial \xi} \frac{d^2 h_R}{d\xi^2} \end{aligned} \quad (\text{C.2})$$

This can be simplified by further use of the product rule to:

$$\frac{1}{2} \frac{d}{dt} \left(\frac{\partial \hat{u}^\delta}{\partial \xi} \right)^2 = -\frac{1}{2} \frac{\partial}{\partial \xi} \left(\frac{\partial \hat{u}^\delta}{\partial \xi} \right)^2 - (\hat{u}_L^{\delta I} - \hat{u}_L^\delta) \frac{\partial \hat{u}^\delta}{\partial \xi} \frac{d^2 h_L}{d\xi^2} - (\hat{u}_R^{\delta I} - \hat{u}_R^\delta) \frac{\partial \hat{u}^\delta}{\partial \xi} \frac{d^2 h_R}{d\xi^2} \quad (\text{C.3})$$

Before continuing, the nature of the differentiation that is being performed here should be explained, hence explaining the validity of applying the product rule. \hat{u}^δ is being taken to mean a polynomial and, as it is continuous, so differentiation is defined here using the standard limit approach. This links to a second point, that components of the norm are attempting to be constructed and not Eq. (C.3) is not being solved in an FR framework and so each component, say $d(\hat{u}^{\delta(1)})^2/d\xi$, is not required to lie in the same p^{th}



order functional space. This is why differentiation is defined using a limit here and not a finite basis. This is the same method as was used by Vincent et al. [160].

Resuming the derivation, Eq. (C.3), can then be integrated over the reference domain and multiplied by ι_1 to give:

$$\begin{aligned} \frac{1}{2} \frac{d}{dt} \int_{-1}^1 \iota_1 (\hat{u}^{\delta(1)})^2 d\xi \\ = -\frac{\iota_1}{2} \int_{-1}^1 \frac{\partial}{\partial \xi} \left(\frac{\partial \hat{u}^\delta}{\partial \xi} \right)^2 d\xi - \iota_1 (\hat{u}_L^{\delta I} - \hat{u}_L^\delta) \int_{-1}^1 \frac{\partial \hat{u}^\delta}{\partial \xi} \frac{d^2 h_L}{d\xi^2} d\xi \\ - \iota_1 (\hat{u}_R^{\delta I} - \hat{u}_R^\delta) \int_{-1}^1 \frac{\partial \hat{u}^\delta}{\partial \xi} \frac{d^2 h_R}{d\xi^2} d\xi \quad (C.4) \end{aligned}$$

This process of differentiating, multiplying by the derivative, applying the product rule, and integrating can be repeated for all the derivatives up to the p^{th} . The result is that we may write:

$$\begin{aligned} \frac{1}{2} \frac{d}{dt} \int_{-1}^1 \iota_i (\hat{u}^{\delta(i)})^2 d\xi = -\frac{1}{2} \int_{-1}^1 \iota_i \frac{\partial}{\partial \xi} \left(\frac{\partial^i \hat{u}^\delta}{\partial \xi^i} \right)^2 d\xi \\ - (\hat{u}_L^{\delta I} - \hat{u}_L^\delta) \int_{-1}^1 \iota_i \frac{\partial^i \hat{u}^\delta}{\partial \xi^i} \frac{d^{i+1} h_L}{d\xi^{i+1}} d\xi \\ - (\hat{u}_R^{\delta I} - \hat{u}_R^\delta) \int_{-1}^1 \iota_i \frac{\partial^i \hat{u}^\delta}{\partial \xi^i} \frac{d^{i+1} h_R}{d\xi^{i+1}} d\xi \quad (C.5) \end{aligned}$$

This can then be substituted to form the Generalised Sobolev norm criterion, by summing over i from 0 to p , to give:

$$\begin{aligned} \frac{1}{2} \frac{d}{dt} \|\hat{u}^\delta\|_{W_2^{p,\iota}}^2 = \frac{1}{2} \frac{d}{dt} \int_{-1}^1 \sum_{i=0}^p \iota_i (\hat{u}^{\delta(i)})^2 d\xi = -\frac{1}{2} \underbrace{\int_{-1}^1 \sum_{i=0}^{p-1} \iota_i \frac{\partial}{\partial \xi} \left(\frac{\partial^i \hat{u}^\delta}{\partial \xi^i} \right)^2 d\xi}_{I_D} \\ - (\hat{u}_L^{\delta I} - \hat{u}_L^\delta) \int_{-1}^1 \sum_{i=0}^p \iota_i \frac{\partial^i \hat{u}^\delta}{\partial \xi^i} \frac{d^{i+1} h_L}{d\xi^{i+1}} d\xi \\ - (\hat{u}_R^{\delta I} - \hat{u}_R^\delta) \int_{-1}^1 \sum_{i=0}^p \iota_i \frac{\partial^i \hat{u}^\delta}{\partial \xi^i} \frac{d^{i+1} h_R}{d\xi^{i+1}} d\xi \quad (C.6) \end{aligned}$$

As \hat{u}^δ is a p^{th} order polynomial, the term in I_D for $i = p$ is identically zero and so the limits on the sum have been changed to reflect this. Integration by parts then allows us to

reformulate this as:

$$\begin{aligned} \frac{1}{2} \frac{d}{dt} \|\hat{u}^\delta\|_{W_2^{p,\iota}}^2 &= -\frac{1}{2} \int_{-1}^1 \sum_{i=0}^{p-1} \iota_i \frac{\partial}{\partial \xi} \left(\frac{\partial^i \hat{u}^\delta}{\partial \xi^i} \right)^2 d\xi \\ &\quad - (\hat{u}_L^{\delta I} - \hat{u}_L^\delta) \sum_{i=0}^p \iota_i \left[\left| \frac{\partial^i \hat{u}^\delta}{\partial \xi^i} \frac{d^i h_L}{d\xi^i} \right|_{-1}^1 - \int_{-1}^1 \frac{\partial^{i+1} \hat{u}^\delta}{\partial \xi^{i+1}} \frac{d^i h_L}{d\xi^i} d\xi \right] \\ &\quad - (\hat{u}_R^{\delta I} - \hat{u}_R^\delta) \sum_{i=0}^p \iota_i \left[\left| \frac{\partial^i \hat{u}^\delta}{\partial \xi^i} \frac{d^i h_R}{d\xi^i} \right|_{-1}^1 - \int_{-1}^1 \frac{\partial^{i+1} \hat{u}^\delta}{\partial \xi^{i+1}} \frac{d^i h_R}{d\xi^i} d\xi \right] \end{aligned} \quad (C.7)$$

If we apply the conditions that:

$$\sum_{i=0}^p \iota_i \int_{-1}^1 \frac{d^i h_L}{d\xi^i} \frac{\partial^{i+1} \hat{u}^\delta}{\partial \xi^{i+1}} d\xi = \sum_{i=1}^p \iota_i \left| \frac{\partial^i \hat{u}^\delta}{\partial \xi^i} \frac{d^i h_L}{d\xi^i} \right|_{-1}^1 \quad (C.8)$$

$$\sum_{i=0}^p \iota_i \int_{-1}^1 \frac{d^i h_R}{d\xi^i} \frac{\partial^{i+1} \hat{u}^\delta}{\partial \xi^{i+1}} d\xi = \sum_{i=1}^p \iota_i \left| \frac{\partial^i \hat{u}^\delta}{\partial \xi^i} \frac{d^i h_R}{d\xi^i} \right|_{-1}^1 \quad (C.9)$$

then the remaining components are:

$$\begin{aligned} \frac{1}{2} \frac{d}{dt} \|\hat{u}^\delta\|_{W_2^{p,\iota}}^2 &= -\frac{1}{2} \int_{-1}^1 \sum_{i=0}^{p-1} \iota_i \frac{\partial}{\partial \xi} \left(\frac{\partial^i \hat{u}^\delta}{\partial \xi^i} \right)^2 d\xi \\ &\quad - \iota_0 (\hat{u}_L^{\delta I} - \hat{u}_L^\delta) |\hat{u}^\delta h_L|_{-1}^1 - \iota_0 (\hat{u}_R^{\delta I} - \hat{u}_R^\delta) |\hat{u}^\delta h_R|_{-1}^1 \end{aligned} \quad (C.10)$$

After the enforcement of the boundary conditions on h_L and h_R it can be written that:

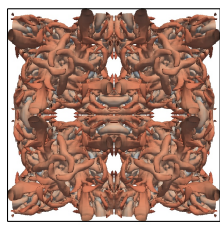
$$\frac{1}{2} \frac{d}{dt} \|\hat{u}^\delta\|_{W_2^{p,\iota}}^2 = \frac{1}{2} \iota_0 \left((\hat{u}_L^{\delta I} - \hat{u}_L^\delta) \hat{u}_L^\delta - (\hat{u}_R^{\delta I} - \hat{u}_R^\delta) \hat{u}_R^\delta \right) - \frac{1}{2} \sum_{i=0}^{p-1} \iota_i \left[(\hat{u}_R^{\delta(i)})^2 - (\hat{u}_L^{\delta(i)})^2 \right] \quad (C.11)$$

By then considering the Sobolev criterion cast in the reference domain, we see that in order for the scheme to be stable the problem is reduced to proving:

$$\iota_0 (\hat{u}_L^{\delta I} - \hat{u}_L^\delta) \hat{u}_L^\delta - \iota_0 (\hat{u}_R^{\delta I} - \hat{u}_R^\delta) \hat{u}_R^\delta \leq 0 \quad (C.12)$$

This statement was explored by Vincent et al. [160] and found to be true for upwinded to centrally differenced interfaces.

We shall now go on to show the symmetry of the correction functions defined by Eq. (C.8 & C.9). As was shown in section 5.3.3 we may cast these conditions into a



matrix problem, with each row corresponding to a value of \tilde{u}_i .

$$\mathbf{L}_p \tilde{\mathbf{h}}_l = \begin{bmatrix} 0 & \dots & 0 & 1 \end{bmatrix}^T = \mathbf{b}_l \quad (\text{C.13})$$

where the penultimate two entries of \mathbf{L}_p and \mathbf{b}_l are due to the enforcement of the boundary conditions on h_l . Hence, because of these boundary conditions, \mathbf{L}_p is a square matrix. For the right correction function, we may similarly write:

$$\mathbf{L}_p \tilde{\mathbf{h}}_r = \begin{bmatrix} 0 & \dots & 1 & 0 \end{bmatrix}^T = \mathbf{b}_r \quad (\text{C.14})$$

Symmetry implies the condition that:

$$\tilde{\mathbf{h}}_l = \text{diag}(-1, 1, -1 \dots) \tilde{\mathbf{h}}_r = \mathbf{\Lambda} \tilde{\mathbf{h}}_r. \quad (\text{C.15})$$

Hence, substituting Eq. (5.62), we may write:

$$\mathbf{L}_p \mathbf{\Lambda} \tilde{\mathbf{h}}_r = \mathbf{b}_l \quad (\text{C.16})$$

As all but the final two values of \mathbf{b} are always zero it can be seen that solving this is equivalent to solving Eq. (C.14). Therefore, GSFR defines a symmetric set of correction functions. Due to this, we may focus on the left correction function, with the right straightforwardly recovered through Eq. (C.15).

Appendix D

Burgers' Turbulence and GJFR

Here, an additional investigation into the behaviour of GJFR is included. This will investigate the behaviour of the GJFR correction function set when applied to the 1D turbulent viscous Burgers's equation [100]. The 1D viscous Burgers' equation is defined as:

$$\frac{\partial u}{\partial x} + \frac{1}{2} \frac{\partial u^2}{\partial x} = \mu \frac{\partial^2 u}{\partial x^2} \quad (\text{D.1})$$

Here μ is the diffusivity and, following the investigations of San [125] and Alhawwary et al. [7], it is set as $\mu = 2 \times 10^{-4}$. The solution of this equation, due to the diffusion term, experiences a cascade of energy from the large scales to the small scales [100]. This energy cascade can subsequently be derived from the closed form of the solution of Hopf [63]. This case is of importance as it can give some indication of the behaviour of the numerical scheme when applied to Navier–Stokes turbulence, due to analogies in the mechanisms. The energy spectra used to derive the initial velocity field is defined as:

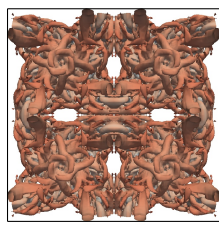
$$E(k, t = 0) = \frac{Ak^4}{k_0^5} \exp(-(k/k_0)^2) \quad (\text{D.2})$$

with

$$A = \frac{2}{3\sqrt{\pi}} \quad \text{and} \quad k_0 = 10 \quad (\text{D.3})$$

on a 1D periodic domain $\Omega = [0, 2\pi]$. This leads to $E(k, 0)$ having a maximum value at $k = 13$, where $k \in \mathbb{N}$. This initial condition is chosen as it is known to transition to a clear $-k^2$ energy cascade. Therefore, the velocity field in the spatial domain may be written as:

$$u(x) = \sum_{k=0}^{k_{\max}} \sqrt{2E(k, 0)} \cos(kx + 2\pi\Phi(k)) + \bar{u} \quad (\text{D.4})$$



where $2\pi\Phi(k) \in (0, 2\pi]$ is a random phase angle, k_{\max} is that maximum wavenumber set here to 2048, and \bar{u} is the mean velocity. For the recovery of an initial turbulence intensity of 0.66%, we will set $\bar{u} = 75$ [92, 7]. To maintain a constant temporal filter width with RK44 integration, the initial CFL number ($\bar{u}\Delta t/\Delta x$) will be held at 0.057. This CFL number is equivalent to $\Delta t = 2 \times 10^{-5}$ for $n = 1200$, $p = 4$ as was used by Alhawwary et al. [7].

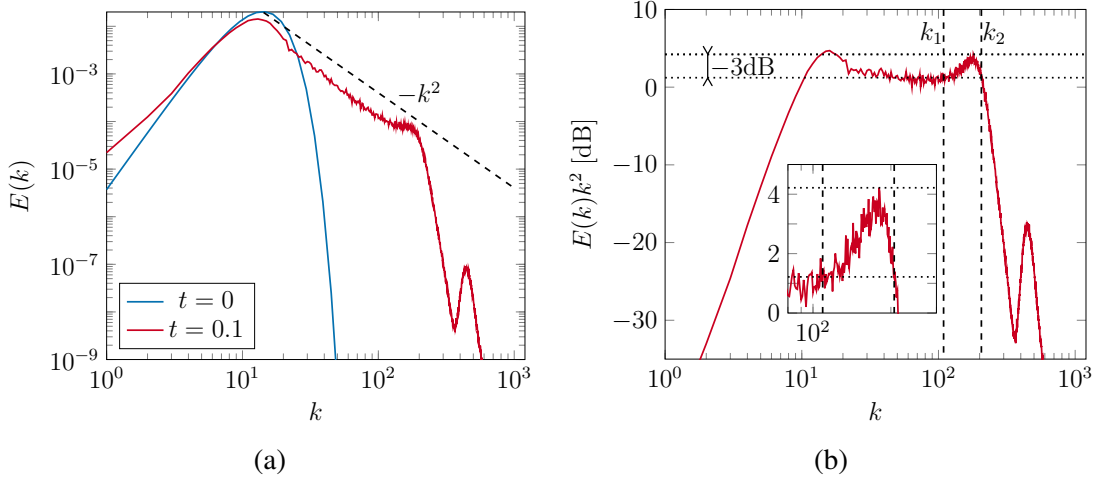


Fig. D.1 Burgers' turbulence energy spectra of FR, $p = 4$, with SD correction functions $\alpha = \beta = 0$, DoF = 1200, $\Delta t = 2 \times 10^{-5}$.

The primary means of evaluating schemes for this case will be through the energy spectra. In order to reduce variability due to the random phases, spectra are averaged over runs from 100 unique initialisations. Studying Figure D.1a, it can be seen that after 0.1 s the expected energy cascade has become established. A feature that is commonly seen when numerical solving this equation with ILES is the resonant peak—in this case at $k \approx 100$. This peak has previously been explained [125] as a pile up of energy at the smallest scales due to under-dissipation. Therefore, if a scheme is to be used for implicit LES, it is advantageous to reduce the size of this resonant peak.

In order to understand the impact of the correction function on this resonance behaviour we shall begin by taking the energy spectra $E(k)$ and multiplying it by k^2 . Any resonance will therefore show itself as a peak in what should otherwise be a flat line, see Figure D.1b. This peak is then parameterised by Q-factor, drawn from stability theory, which is defined as:

$$Q = \frac{k_0}{k_2 - k_1} \quad (\text{D.5})$$

Here k_0 is the wavenumber of the resonance peak, and k_1 and k_2 are the half power wavenumbers i.e. the wavenumbers for the peak -3dB . An example of the modified energy spectra, together with the locations of k_1 and k_2 , is shown in Figure D.1b. The

Q-factor of this example is 1.845. Q-factor is an indicator of the dissipation that is occurring within the system, with higher Q-factors implying less dissipation and vice versa. A second parameter we will examine is the cut-off wavenumber, which is defined as the wavenumber at which the value of $E(k)k^2$ drops by 3dB from the level of the plateau.

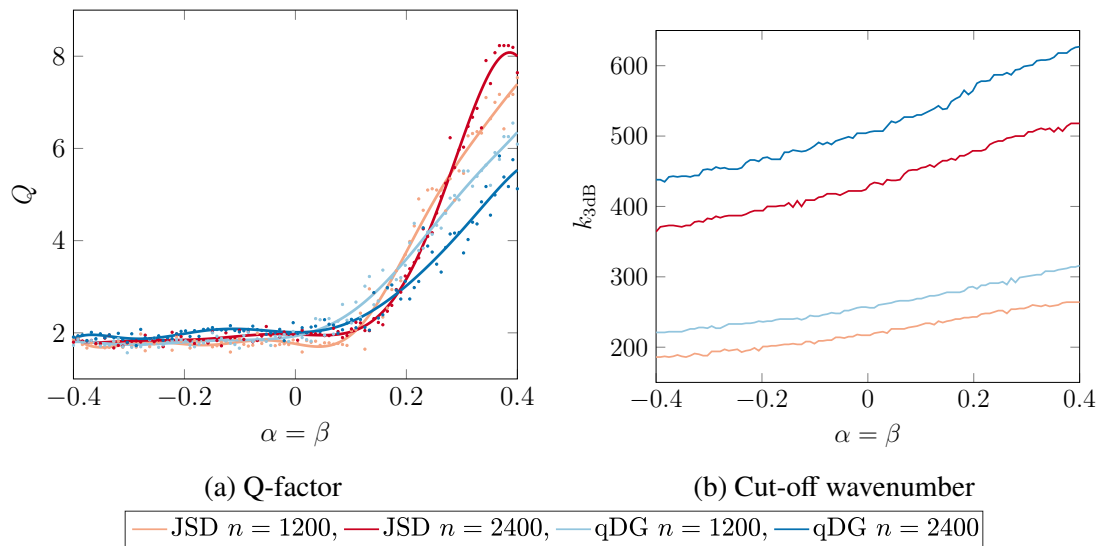
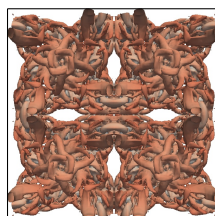


Fig. D.2 Burgers' turbulence parametrization for FR, $p = 4$, at $t = 0.1$ for various correction functions.

Figure D.2 displays the Q-factor and cut-off wavenumber for qDG and SD, exploring the behaviour of $\alpha = \beta$ for two different degree of freedom counts; $n = 1200$ and $n = 2400$. Studying Figure D.2a there is a region $-0.4 < (\alpha = \beta) < \approx 0.1$ where the Q-factor is largely invariant with the correction function. Then, as $\alpha = \beta$ is increased the Q-factor rises, with qDG rising slightly sooner than SD. However, around $\alpha = \beta \approx 0.2$ the Q-factor for SD overtakes that of qDG. The findings of the cut-off wavenumber are displayed in Figure D.2b. These show that qDG has a higher cut-off wavenumber than SD and that, within the range tested, the cut-off frequency rises as $\alpha = \beta$ is increased. These two findings suggest that, for the simulation of turbulent phenomena, a good correction function is in the vicinity where $0 < \alpha = \beta < 0.2$. However, the exact position of an optimal correction function for Navier–Stokes turbulence will be dependent on the relative importance of Q-factor and cut-off wavenumber.



Appendix E

Correction Function Pseudo Code

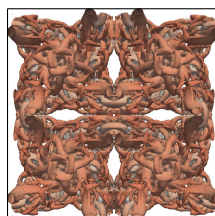
Presented in chapter 5 were several families of correction functions. For ease of implementation we will set up the algorithms for generating some of the correction function. Namely Generalised Sobolev and Lebesgue Stable FR. We only include these as Generalised Jacobi correction functions are just a task of precisely implementing Eq.(5.49).

E.1 Generalised Sobolev Stable FR

Of concern when trying to calculate the GSFR correction function is the calculation of the matrix \mathbf{L}_p , hence we will outline the technique for calculating \mathbf{L}_p . The method shown will be valid for the first $p-2$ rows of \mathbf{L}_p and, as can be seen from Eqs.(5.67,5.69,5.72), the penultimate two row enforce the boundary conditions of the left correction function. Therefore, we have:

Algorithm 1 Process for calculating the value of $\mathbf{L}_p[m-1][n]$ for a $\mathbf{I}_p = [t_0 \dots t_p]$. The method of calculating $I_{i,m,n}$ is given in Algorithm 2.

Require: p, m, n, \mathbf{I}_p
 $L[m-1][n] \leftarrow 0$
for $0 \leq i \leq p$ **do**
 $L[m-1][n] \leftarrow L[m-1][n] + t_i I_{i,m,n}$
end for
for $1 \leq i \leq p$ **do**
 $a \leftarrow \frac{(n+i)!(m+i)!}{2^{2i}(i!)^2(n-i)!(m-i)!} (1 - (-1)^{n+m-2i})$
 $L[m-1][n] \leftarrow L[m-1][n] - at_i$
end for
return $L[m-1][n]$



Algorithm 2 Algorithm for calculating the integral of Eq.(5.64) where $b_i(m, n)$ is defined by Eq.(5.65).

Require: m, n, k

```

 $I_{m,n,k} \leftarrow 0$ 
for  $0 \leq i \leq \lfloor \frac{n-m}{2} \rfloor$  do
  for  $0 \leq j \leq \lfloor \frac{k-m-1}{2} \rfloor$  do
     $c \leftarrow \frac{b_i(m,n)b_j(m+1,k)}{n+k-2(m+i+j)} [1 - (-1)^{n+k-2(m+i+j)}]$ 
     $I_{m,n,k} \leftarrow I_{m,n,k} + c$ 
  end for
end for
return  $I_{m,n,k}$ 

```

E.2 Generalised Lebesgue Stable FR

We will now present a short piece of pseudo-code to calculate the left correction functions Legendre polynomial coefficients, \tilde{h}_L . In this example we use % to mean the modulus or remainder operator, *i.e.* $a \% b = a \bmod b$. Here the input is an array \mathbf{q} with $p - 2$ entries that control the shape of h_L .

Algorithm 3 Calculate left GLSFR correction Legendre coefficients

Require: $p, q[p-2]$

```

 $\tilde{h}_L[p-1] \leftarrow 0$ 
 $\tilde{h}_L[p-2] \leftarrow 0$ 
for  $0 \leq i \leq p-3$  do
   $\tilde{h}_L[i] \leftarrow q[i]$ 
   $\tilde{h}_L[p-1] \leftarrow \tilde{h}_L[p-1] - (i + p \% 2)q[i]$ 
   $\tilde{h}_L[p-2] \leftarrow \tilde{h}_L[p-2] - (i + p - 1 \% 2)q[i]$ 
end for
 $\tilde{h}_L[p] \leftarrow 0.5(-1)^p$ 
 $\tilde{h}_L[p+1] \leftarrow 0.5(-1)^{p+1}$ 
return  $\tilde{h}_L$ 

```
